Tailoring the Properties of Two-dimensional Systems by Molecular Adsorption and Defect Engineering: Density Functional Theory Studies

A Thesis

Submitted to the
Jawaharlal Nehru Center for Advanced Scientific Research, Bengaluru
for the Degree of Doctor of Philosophy

by

Sourav Mondal

Jawaharlal Nehru Center for Advanced
Scientific Research, Bengaluru,India.

DECEMBER 2020

To my Mother & Father

DECLARATION

I hereby declare that the matter embodied in the thesis entitled "**Tailoring the Properties of Two-dimensional Systems by Molecular Adsorption and Defect Engineering: Density Functional Theory Studies**" is the result of investigations carried out by me at the Theoretical Science Unit, Jawaharlal Nehru Centre for Advanced Scientific Research, Bangalore, India under the supervision of Prof. Shobhana Narasimhan and that it has not been submitted elsewhere for the award of any degree or diploma.

In keeping with the general practice in reporting scientific observations, due acknowledgement has been made whenever the work described is based on the findings of other investigators. Any omission that might have occurred by oversight or error of judgement is regretted.

Sourav Mondal

Sourav Mondal

CERTIFICATE

I hereby certify that the matter embodied in this thesis entitled "**Tailoring the Properties of Two-dimensional Systems by Molecular Adsorption and Defect Engineering: Density Functional Theory Studies**" has been carried out by Mr. Sourav Mondal at the Theoretical Science Unit, Jawaharlal Nehru Centre for Advanced Scientific Research, Bangalore, India under my supervision and that it has not been submitted elsewhere for the award of any degree or diploma.

Shobhana Narasimhan

Prof. Shobhana Narasimhan
(Research Supervisor)

Acknowledgements

First of all, I would like to thank my Ph.D. supervisor Prof. Shobhana Narasimhan for introducing me to this wonderful world of nanoscience. She has helped me understand the basics of nanoscience and guided me to choose different problems for my Ph.D. thesis. Her ideas of looking at a problem from different perspectives enriched my problem-solving skills and inspired me a lot to become a good researcher. I owe her a lot of gratitude for listening to my problems very patiently and correcting my mistakes at every stage of the work. She has provided me plenty of opportunities to visit different research groups in Paris and collaborate with renowned scientists in our field. All these visits have enriched me both academically and non-academically. Moreover, her motherly caring has helped me a lot to overcome my hard times in my entire Ph.D. life.

I would like to thank all of my experimental and theoretical collaborators: Prof. Vincent Repain, Dr. Jérôme Lagoute, Prof. Sylvie Rousset, Dr. Yannick J. Dappe, Dr. Alexander Smogunov, Prof. Cyrille Barreteau, Dr. Rishav Harsh, Dr. Rajdeep Banerjee, Dr. Devina Sharma, Dr. Debdipto Acharya and Mehdi Bouatou.

I would like to give a special thanks to Prof. Vincent Repain for providing me the best facilities for my work and making my stay in Paris memorable. I will always remember your praise about my cooking. Not to forget the wonderful trip we had in Coorg.

I am thankful to Prof. Michele Lazzeri for his help in modifying the constant current STM code.

I thank all of my course instructors Prof. U. V. Waghmare, Prof. Meher K. Prakash, Prof. N. S. Vidhyadhiraja, and Prof. Balasubramanian. I want to thank all the faculties from TSU. I want to acknowledge the present and past chairpersons of TSU.

I acknowledge the financial help from the UGC, Indo-French CEFIPRA grant, CEA-Saclay, and JNCASR for supporting my research.

I thank everyone in the Academic Section, especially Dr. Princy. I want to thank Mr. Joydeep Deb, Mr. Jayachandra, Mrs. Jayamangala, and all others in the Administrative Section for their help with all the administrative procedures. I thank Dr. Archana and all the Dhanvantari staff for the medical assistance they provided. I am grateful to the past & present CCMS staff Vijay, Anoop, and Suresh for their help and support with computing facilities. I want to thank all the library staff and the hostel staff.

I thank all my past and present labmates: Prasenjit, Jaita, Mighfar, Madhura, Nisha, Kanchan, Sananda, Vasudevan, Bulumoni, Debarati, Debdipto, Sukanya, Rajiv, Devina, Somesh, Saikat, Rajdeep, Nandana, Arpan, and Abhishek for providing a lively and pleasant environment in the lab.

I thank my friends Krisnendu, Shantanu, and Subhajit for our unplanned trips to explore different parts of Southern India, which gave me an escape from my Ph.D. routine life. I thank my past and present friends in JNC, especially Soumalya, Sandhya, Arka, Suman, Shuvam, Pawan, Abhirup, Madulika, and Manoj, for the wonderful time we had together, which made the time I spent in JNCASR more enjoyable.

My respectful gratitude to Prof. C. N. R. Rao for providing excellent research facilities and the scientific environment in the institute.

Finally, I thank my parents, my sisters, and Sanchita for their love, constant support, and motivation, which made it possible to finish my Ph.D.

Synopsis

In this thesis, I have tailored the properties of two-dimensional systems by molecular adsorption and defect engineering. I have worked on low-dimensional materials which have technological applications. I have solved puzzles that arose from experimental observations, which can be solved using first-principles calculations.

In **Chapter 1**, I have given a brief introduction to the problems that I have considered for study in this thesis. I have focused on two types of systems: organic molecules on surfaces, and two dimensional systems with impurities and/or defects. These systems have in common certain features: (i) they are low-dimensional, (ii) they have applications in fields such as spintronics, and device physics, (iii) the system properties accordingly have to be tailored so that they are optimal for the desired applications, (iv) frequently, strong correlations and/or non-covalent interactions play an essential role.

I have studied organic molecules on surfaces in the first part of this thesis. For example, I have studied spin- crossover molecules on a metallic substrate in Chapter 3. The electro-acceptor F_4TCNQ molecule on different non-metallic surfaces has been studied in Chapters 4, 5 and 6. I have also studied an organo-metallic catalyst, the CoPc molecule, on nitrogen-doped graphene in Chapter 5. The second part of this thesis, i.e., Chapter 7, discusses the defects found in few-layer black phosphorene.

The experimental parts of all the problems discussed in this thesis have been performed by the team of Prof. Vincent Repain and Dr. Jérôme Lagoute in the MPQ Laboratory of the University of Paris - Diderot.

In **Chapter 2**, I have discussed the underlying theoretical formalism and the computational techniques that I have used in this thesis. These include non-spin-polarized and spin-polarized density functional theory (DFT), the DFT-D2 technique to incorporate dispersion interactions, the DFT+U method to describe strong correlations, and the Tersoff-Hamann approach to simulate scanning tunneling microscopy (STM) images.

In **Chapter 3**, I have studied partial spin crossover in an ordered two-dimensional (2D) monolayer of Fe((3,5-$(CH_3)_2C_3N_2H)_3BH)_2$ (or IPB) molecules deposited on Au(111). Spin crossover is a phenomenon of changing spin state induced by external stimuli such as light, pressure, or temperature. IPB molecules are found in the low-spin (LS) ground state in its crystalline form. However, recent STM experiments have shown that an ordered superlattice of two types of molecules is formed when they are deposited on an Au(111) substrate. One can guess that these two types of molecules could be in two different spin states, i.e., high-spin (HS) and low-spin (LS) states, but this has not been proven experimentally. Using DFT, I show that the IPB molecules are indeed arranged in an ordered mixed spin state, forming an LS-HS-HS superlattice. We are the first to report this two dimensional ordered spin-state superlattice. I also show that the driving force for the formation of this 2D spin-state lattice is the epitaxial strain that arises due to the lattice mismatch between the substrate and the monolayer of the IPB. A toy model fitted with DFT parameters has been developed to understand the strain-induced spin crossover.

In **Chapter 4**, I have studied the F_4TCNQ molecule, which is an electron acceptor by nature, on twisted bilayer graphene (TBLG), to explore the molecule-substrate interaction in the F_4TCNQ/TBLG system. STM experiments performed by Dr. Harsh and Dr. Lagoute show that F_4TCNQ prefers to avoid the AA-stacked region of the Moiré (formed by the TBLG) at lower coverage. The STM experiments also show that F_4TCNQ forms a linear chain on twisted bilayer graphene (TBLG) at higher coverage. My DFT calculations have validated the experimental findings. I have found that a comparatively strong non-covalent van der Waals type of interaction between the molecule and the locally concave surface of the AB-stacked region of the Moiré stabilizes the adsorption of the molecule on the AB-stacked region, instead of it adsorbing on the electron-rich AA-stacked region. I have also found that the energy landscape for a charged dimer of F_4TCNQ molecules can explain the strong intermolecular interactions among the F_4TCNQ molecules along a particular direction, leading to the formation of a one-dimensional F_4TCNQ chain on TBLG at higher coverage.

In **Chapter 5**, I have tuned the magnetic moments and charge on organic molecules adsorbed on a graphene substrate. In the first part of this chapter, I have discussed how one could induce magnetism in the F_4TCNQ-graphene system. I have shown two different ways to do this. One way is by applying an external electric field to the system, and another way is by doping the graphene substrate with nitrogen atoms. I have also shown that both approaches can hugely increase the electron transfer from graphene to the molecule. In addition, I have found a nice correlation among the magnetism, charge transfer, and the external electric field, which could be useful to guess the magnetism and the charge transfer of the system just by noting the direction and magnitude of the electric field. In the second part of this chapter, I have discussed the tuning of the charge on a CoPc molecule in the CoPc/graphene system. CoPc is a potential catalyst for the CO_2 reduction reaction. Thus, if we can reduce the oxidation state of the molecule it is expected to show enhanced catalytic performance. I have shown that high charge transfer from pairs of nitrogen atoms in N-doped graphene to the CoPc molecule can explain the experimental observation of reduction (redox reaction) of the CoPc molecule on N-doped graphene.

In **Chapter 6**, I have shown that one can tune the electronic and magnetic properties of black phosphorene (BP) by using molecular doping combined with the application of an external electric field. Unlike defect creation and chemical functionalization, this approach for tuning the electronic properties is advantageous because molecular doping does not damage the phosphorene's structure. Using DFT calculations, I have shown that an external negative electric field can induce magnetism in the F_4TCNQ/BP system. This can be explained in terms of the splitting of the impurity band introduced by the molecule. F_4TCNQ creates p-type doping in the BP by introducing a band (corresponding to its LUMO) in the band gap of BP which gets split into one unoccupied spin down (SUMO) band and one partially occupied spin up (SOMO) band at negative electric fields. I have also shown that the electronic and magnetic properties of this system will evolve in interesting ways as the temperature increases. In addition to this, I have also explained a puzzle regarding the origin of streaks found in STM images of this system. These streaks are found to occur along the zigzag direction but not the armchair direction. I have found that the diffusion barrier for F_4TCNQ on phosphorene is highly anisotropic, being low/high along the zigzag/armchair directions. Thus the features observed in STM images can be explained as arising from the F_4TCNQ molecules' diffusion along the zigzag direction during the scan time.

In **Chapter 7**, I have studied defects in few-layer black phosphorene. The presence of various defects causes different changes in the electronic properties, and hence these can be exploited (or maybe disadvantageous) for different possible applications. I have built up a library of several kinds of defects and their simulated STM images. Some of these simulated images are in good agreement with the experiments. For example, STM experiments performed by Dr. Lagoute and his team on few-layer black phosphorene show a unique dumbbell shape; this feature displays a change of contrast and shape upon reversal of the bias potential. The origin of this feature remains a puzzle. Previously, other groups also tried to address the same problem of the origin of this ubiquitous feature, but could not find entirely satisfactory solutions. We are the first to show that an Sn substitutional defect can explain the shape and change of contrast on reversal of bias, seen in STM experiments. I have also developed a simple post-processing technique that provides insight into the origin of features such as these in STM images. In addition to this, I have also explained the effect of an electric pulse on defects, observed in the experiments. Application of an electric pulse is shown to cause Sn and P atoms leading to a new kind of defect.

In **Chapter 8**, the conclusions of each chapter are summarized and possible directions for future work are discussed.

List of Publications

1. "Direct Observation of the Reduction of a Molecule on a Nitrogen pair in Doped Graphene", M. Bouatou, S. Mondal, C. Chacon, F. Joucken, Y. Girard, V. Repain, A. Bellec, S. Rousset, R. Sporken, Y. J. Dappe, S. Narasimhan and J. Lagoute, *Nano Lett.* **20**, 6908 (2020).

2. "Importance of Epitaxial Strain at a Spin-Crossover Molecule-Metal Interface", C. Fourmental, S. Mondal, R. Banerjee, A. Bellec, Y. Garreau, A. Coati, C. Chacon, Y. Girard, J. Lagoute, S. Rousset, M. L. Boillot, T. Mallah, C. Enachescu, C. Barreteau, Y. Dappe, A. Smogunov, S. Narasimhan, and V. Repain, *J. Phys. Chem. Lett.* **10**, 4103 (2019).

3. "Symmetry aspects of spin filtering in molecular junctions: Hybridization and quantum interference effects", D. Li, R. Banerjee, S. Mondal, I. Maliyov, M. Romanova, Y. J. Dappe, and A. Smogunov, *Phys. Rev. B* **99**, 115403 (2019).

4. "Enhanced hydrogen evolution reactivity on Mo_2C-Mo_2N composites", D. Acharya , K. Ojha, N. Mamen , P. Dagar, S. Mondal, A. K. Ganguli and S. Narasimhan, *Bull. Mater. Sci.*, **43**, 321, (2020)

5. "Defects in few layer black phophorene", R. Harsh, S. Mondal, D. Sharma,, V. Repain, S. Rousset, C. Barreteau, Y. Dappe, A. Smogunov, J. Lagoute, and

S. Narasimhan, (manuscript under preparation).

6. "F_4TCNQ on Nitrogen Doped Graphene systems", S. Mondal, R. Harsh, V. Repain, S. Rousset, C. Barreteau, Y. Dappe, A. Smogunov, J. Lagoute, and S. Narasimhan, (manuscript under preparation).
7. "Self organisation F_4TCNQ on twisted bilayer graphene systems", R. Harsh, S. Mondal, V. Repain, S. Rousset, C. Barreteau, Y. Dappe, A. Smogunov, J. Lagoute, and S. Narasimhan, (manuscript under preparation).
8. "F_4TCNQ doping on black phosphorene", S. Mondal, R. Harsh, V. Repain, S. Rousset, C. Barreteau, Y. Dappe, A. Smogunov, J. Lagoute, and S. Narasimhan, (manuscript under preparation).

List of Abbreviations

ΔH	Change of Enthalpy
ΔQ	Charge Transfer
Δ	Pairing Energy
Δ_0	Crystal Field Spliting Energy
ϵ	Electric field
ρ	Charge density
E_F	Fermi energy
E_g	Band Gap
S_G	Structure Factor
U	Onsite Coulomb Energy
1D	One-dimensional
2D	Two-dimensional
3D	Three-dimensional

3L-BP	Three Layer Thick Black Phosphorene
BE	Binding Energy
BP	Black Phosphorene
BZ	Brillouin Zone
CoPc	Cobalt Phthalocyanine
DCD	Differential Charge Density
DFE	Defect formation energy
DFT	Density Functional Theory
DOS	Density of states
DV	Divacancy
EB	Energy Barrier
F_4TCNQ	Tetrafluoro Tetracyano-quinodimethane
GGA	Generalized Gradient Approximation
GIXD	Grazing Incident X-ray Diffraction
HOMO	Highest Occupied Molecular Orbital
HS	High Spin
IPB	$Fe((3, 5\text{-}(CH_3)_2C_3N_2H)_3BH)_2$
KS	Kohn Sham
LDA	Local Density Approximation

LS	Low Spin
LUMO	Lowest Unoccupied Molecular Orbital
ML	Monolayer
MV	Monovacancy
N-Gr	Nitrogen-doped Graphene
N-TBLG	Nitrogen-doped Twisted Bilayer Graphene
PBE	Perdew, Burke and Ernzerhof
PDOS	Projected Density of States
PZ	Perdew and Zunger
QE	Quantum ESPRESSO
SCO	Spin Crossover
SOMO	Singly Occupied Molecular Orbital
STM	Scanning Tunneling Microscopy
STS	Scanning Tunneling Spectroscopy
SUMO	Singly Unoccupied Molecular Orbital
SW	Stone Wales
TBLG	Twisted Bilayer Graphene
TCNQ	Tetracyano-quinodimethane
XAS	X-ray Adsorption Spectroscopy

Contents

Acknowledgements **v**

Synopsis **ix**

List of Publications **xv**

List of Abbreviations **xvii**

1 Introduction **1**

1.1 Design of Materials at the Nanoscale for Technological Applications 1

1.2 Motivation of this thesis: Organic molecules on substrates 5

1.3 Outline of this thesis 10

2 Methods and Formalism **27**

2.1 The Schrödinger Equation and Many-Body Problem 27

2.1.1 The Born-Oppenheimer Approximation 28

2.1.2 Density Functional Theory 29

2.1.3 Exchange-Correlation Functional 34

2.1.4 Plane Wave Basis Sets 35

2.1.5 Pseudopotential Approximation 37

2.1.6 k-point Sampling and Smearing 38

2.1.7 Hellmann-Feynman theorem: Calculation of Forces 39

2.1.8 Spin-Polarized Density Functional Theory 40

2.2 Dispersion Interactions: DFT-D2 Method 41

2.3 Strong correlations: The DFT+U Method 42

2.4 Tersoff-Hamann Approach: Simulation of STM image 44

2.5 Codes Used 48

3 Ordered Partial Spin Crossover Transition in IPB/Au(111) Triggered by Epitaxial Strain 55

3.1 Introduction 55

3.2 Experimental background 60

3.3 Systems under study 62

3.4 Computational details 63

3.5 Results and discussion 64

3.5.1 Optimized structure of isolated molecule in HS and LS 66

3.5.2 Determining an approximate value of U 66

3.5.3 Finding the molecular orientaion on the substrate 68

3.5.4 Determining spin states as a function of U in $S_{1/3}$ 71

3.5.5 Comparison with STM data 73

3.5.6 Mechanoelastic model 73

3.6 Conclusions 79

4 Linear Self Organization of F_4TCNQ on Twisted Bilayer Graphene 87

4.1 Introduction 87

4.2 Experimental Background 91

4.3 Systems under study 92

4.3.1 Twisted Bilayer Graphene 92

4.3.2 F_4TCNQ on TBLG 95
4.4 Computational details 98
4.5 Results and discussion 100
4.5.1 Site preference of F_4TCNQ molecule at low coverage 100
4.5.2 Formation of a linear chain at higher coverage 105
4.5.3 Explanation for the linear chain at higher coverage 106
4.5.4 F_4TCNQ on N-doped TBLG 113
4.6 Conclusions 120

5 Tuning of Magnetism and Charge Transfer: F_4TCNQ and CoPc Adsorbed on Graphene 129
5.1 Introduction 129
5.2 Computational details 134
5.3 Results and discussion for F_4TCNQ/Gr 135
5.3.1 Adsorption geometry of F_4TCNQ on Gr 135
5.3.2 Tuning of molecular magnetism in F_4TCNQ/Gr system using an external electric field 138
5.3.3 Adsorption of F_4TCNQ on nitrogen-doped graphene 145
5.3.4 N-doping in graphene induces molecular magnetism in F_4TCNQ/Gr system 156
5.4 Results and discussion for CoPc on doped graphene 161
5.4.1 Experimental results 161
5.4.2 Adsorption geometry of CoPc on doped Gr 162
5.4.3 Tuning of charge upon CoPc molecule on the doped graphene 164
5.5 Conclusions 168

6 F_4TCNQ Molecules on Black Phosphorene 179
6.1 Introduction 179

6.2 Experimental Background 183
6.3 Systems under study 184
6.4 Computational details 187
6.5 Results and discussion 188
  6.5.1 Benchmark calculations on monolayer and few-layer black phosphorene 188
  6.5.2 Adsorption geometry and effect of thickness in determining the adsorption geometry 189
  6.5.3 Charge transfer in F_4TCNQ/BP systems 191
  6.5.4 Effect of electric fields: Magnetic moment at $T = 0$ 193
  6.5.5 Effect of electric field on band structure 198
  6.5.6 Directional anisotropy in molecular diffusion 202
6.6 Conclusions 203

7 Defects in Few-layer Black Phosphorene 213

7.1 Introduction 213
7.2 Experimental results 217
7.3 Systems under study 221
  7.3.1 Intrinsic Defects 221
  7.3.2 Extrinsic Defects 223
7.4 Computational details 227
7.5 Results and Discussion 227
  7.5.1 Benchmark calculations: lattice parameters and band gap of pristine few-layer black phosphorene 228
  7.5.2 Defect Formation Energies 229
  7.5.3 Simulated constant-current STM images for intrinsic and extrinsic defects in 3L-BP 230

7.5.4 Origin of the shape and contrast in feature **A** and feature **B** . 237
7.5.5 Effect of the electric pulse 243
7.6 Conclusions 249

8 Summary & Future Outlook 257

List of Figures

1.1 Top views of the three substrates considered in this thesis: (a) Au(111), (b) graphene, and (c) black phosphorene. Color code for atoms: golden yellow (Au), gray (C), purple (P). The black lines indicate the boundaries of the primitive surface unit cell. 5

1.2 Optimized geometry of isolated (a) spin crossover IPB molecule [Color code for atoms is red (iron), blue (nitrogen), green (boron), orange (carbon), violet (hydrogen)], (b) F_4TCNQ molecule [Color code for atoms: red (F), yellow (C), blue (N)] and (c) CoPc molecule [Color code for atoms: red (F), yellow (C), blue (N), green (Co), and turquoise (H)] in the gas phase. 8

2.1 Flow chart showing the self-consistency loop for the iterative solution of the KS equation. Superscripts indicate the iteration. 33

2.2 Idealized schematic of an STM experiment. Reproduced from Ref. 49 with permission of the Licensor through PLSclear. 45

2.3 Schematic diagram showing the energy level alignment between the tip and the sample (a) in absence of any bias volatge, no electron tunnels and (b) when the bias voltage V is applied. E_{F} and E_{vacuum} are the Fermi energy and vacuum energy, respectively. Φ_{WF} is the work function and $d_{\mathrm{T-S}}$ is the tip-sample distance. 46

2.4 Schematic diagram showing the geometry of the STM tip. The tip is assumed to be spherical in shape. R is the radius of curvature, d is the nearest tip-sample distance and r_0 is the center of curvature of the tip. The shaded region shows the surface of the sample. Thia figure is taken with permission from ref. 51 ©American Physical Society . . 47

3.1 (a) d orbitals split into t_{2g} and e_g in an octahedral field. There are two possibilities for filling t_{2g} and e_g depending on crystal field splitting energy (Δ_0) and pairing energy (Δ) (b) $\Delta_0 < \Delta$, both t_{2g} and e_g are partially filled (c) $\Delta_0 > \Delta$, t_{2g} is completely filled, no electrons in e_g. 56

3.2 Schematic diagram for pairing energy (Δ). 56

3.3 Low temperature (4.6 K) experimental STM images (a) STM image, recorded at -1.5 V, $I = 50$ pA shows all the IPB molecules imaged as bright (red) spots (b) STM image, recorded at 0.3 V, $I = 50$ pA shows only one out of three molecules imaged as a bright (red) spot. The positions of the two 'missing' molecules (imaged dark) have been shown using dotted white circles. In both panels, the $S_{1/3}$ unit cells have been drawn using solid yellow lines. This figure is reprinted with the permission from Ref. 2 ©2016, Nature Publishing Group. 61

3.4 (a) Optimized geometry of IPB molecule in gas phase. Color code for atoms is red (iron), blue (nitrogen), green (boron), orange (carbon), violet (hydrogen). (b) $S_{1/2}$ cell (highlighted area) on Au(111) surface, red oval shapes schematically indicate IPB molecules in HS state (C) highlighted area is $S_{1/3}$ supercell on Au(111) surface; black, purple and green ovals represent the three IPB molecules in unknown (to be determined) spin states.The small gray spheres in panels (b) and (c) indicate gold atoms in the topmost layer. 62

3.5 DFT+U results, at $U = 6.55$ eV, for the variation in the total energy of an IPB molecule in the gas-phase, as a function of Fe-N bond distance (d_{Fe-N}), averaged over the six Fe-N bonds. The blue and red curves are results for the HS state and LS state, respectively. The zero of energy is set at the minimum of the LS state. 67

3.6 DFT results for total energies of HS (red) and LS (blue) IPB in gas-phase as a function of on-site Coulomb potential U. IPB shows HS ground state above ∼6.87 eV and LS ground state below it. 68

3.7 Top and side views of three possible adsorption geometries for IPB on Au(111) in a $S_{1/2}$ supercell. The three orientations considered correspond to different planes of the bulk HS crystal a) (01-1) b) (010) c) (001). Color code for atoms is red (iron), blue (nitrogen), green (boron), orange (carbon), violet (hydrogen) and yellow grey (gold). Reprinted with permission from Ref 4. ©2019 American Chemical Society. 69

3.8 Determination of the molecular orientation using theoretically computed (from DFT) and experimentally measured (from GIXD) structure factors. Comparison between measured (black half-disk) and calculated (white half-disk) structure factors for three different orientations of the molecule on the surface. a) (01-1). b) (010). c) (001). $\vec{A}^*$ and $\vec{B}^*$ are the reciprocal lattice vector of the $S_{1/2}$ cell. Reprinted with permission from Ref 4. ©(2019) American Chemical Society. . 71

3.9 Total energies of different spin configurations of a monolayer of IPB in the $S_{1/3}$ unit cell on Au(111) (shown in Fig. 3.4(c)) supercell as a function of Hubbard U. Pure LS phase, i.e., LS-LS-LS, is favored for $U <$ 6.47 eV. Pure HS phase, i.e., HS-HS-HS, is favored for $U >$ 6.60 eV. Mixed-spin phase (either HS-LS-LS or LS-HS-HS) is favored for $6.47 < U < 6.60$. 72

3.10 Comparison of simulated STM images with experiments, for a monolayer of IPB on Au(111). (a) Experimental, and simulated STM images of (c) LS-HS-HS and (e) HS-LS-LS at −1.5 V. We see all three molecules within the unit cell, in both theory and experiment. (b) Experimental and simulated STM images of (d) LS-HS-HS and (f) HS-LS-LS at 0.3 V. We see only only one out of three molecules within the experimental unit cell; simulation predicts the same only for LS-HS-HS (we see only LS molecules at positive bias). STM simulations have been performed using Tersoff-Hamann approach in constant height mode (h = 5.6 Å). 74

3.11 (a) Schematics of the hard sphere mechanoelastic model. Above: all the molecules are in HS states (red spheres). Below: Chain of mixed phase where both HS (red) and LS (blue) are present. Mixed phase arises because of the substrate-imposed epitaxial strain. k_{sub} and k_{mol} are the spring constant for molecule-substrate interaction and intermolecular interaction. (b) Inter-atomic potential of a periodic chain of LS molecules as a function of their intermolecular distance (black dots). The solid black line is a fit based on a Morse potential. The dotted red line is the closest parabolic potential. Adapted with permission from Ref 4. ©2019 American Chemical Society. 77

3.12 Energetics and phase diagram using the mechanoelastic model. $\mathrm{E_{LS\text{-}LS}}$, $\mathrm{E_{HS\text{-}HS}}$ and $\mathrm{E_{HS\text{-}LS}}$ as function of a for $\Delta_{SCO} = 108$ meV. In this graph, the model parameters are set at $k_{mol} = 1.38$ eV.Å^{-2}, $2r_{LS} = 6.1$ Å and $2r_{HS} = 6.52$ Å and l_0=2.5 Å. The three phases, LS-LS, HS-LS and HS-HS, have been shown using three colors, blue, pink, and orange, respectively. 79

4.1 Simulated STM image of the Moiré pattern found in the TBLG unit cell. The image has been simulated at the height of 2.73 Å from the surface and at the bias of +0.27 V. 89

4.2 Optimized geometry of F_4TCNQ molecule in the gas phase. Color code for atoms: red (F), yellow (C), and blue (N). 90

4.3 Experimental STM images recorded at bias voltage of + 2.0 V, I= 10 pA at 4 K temperature. STM image of the F_4TCNQ molecule at (a) lower coverage, (b) higher coverage. The images are reused with permission from Ref. 30. 92

4.4 (a) $\mathbf{a}_1$ and $\mathbf{a}_2$ are the primitive lattice vectors for the unrotated graphene. (b) Twisted bilayer graphene (TBLG) supercell we used for our calculations. Lattice vectors $\mathbf{T} = 6\mathbf{a}_1 + 7\mathbf{a}_2$ and $\mathbf{V} = -7\mathbf{a}_1 + 13\mathbf{a}_2$ are used to construct this TBLG supercell. We have rotated bottom layer using a twist angle (ϕ) of 5.085° with respect to the top layer to make this TBLG supercell. Color code: gray (top layer), turquoise (bottom layer) 93

4.5 Various relaxed adsorption geometries, from DFT, for a single F_4TCNQ molecule on TBLG. We have chosen six different sites (a) site–1 (b) site–2 (c) site–3 (d) site–4 (e) site–5 and (f) site–6 to calculate the adsorption energy. Color code: Yellow (C atom of molecule), blue (N), red (F), gray (top layer graphene), turquoise (bottom layer graphene). The black lines show the boundaries for the unit cell of the TBLG. . 96

4.6 Different lateral positions considered for the molecule's hexagonal ring, relative to the substrate, for the site–1. The center of the hexagonal ring of the molecule is on top of (a) the C atom of the toplayer graphene, (b) hexagonal ring of the top layer graphene (c) shifted C atom of the toplayer graphene, (d) C-C bond of the top layer graphene. Color code: Yellow (C atom of molecule), blue (N), red (F), gray (top layer graphene), turquoise (bottom layer graphene). 97

4.7 Optimized geometry of (a) 1D linear chain passing through AA and AB regions, (b) 1D linear chain passing through AB regions but avoiding AA regions, and (c) 2D monolayer on TBLG. Color code: Yellow (C atom of molecule), blue (N), red (F), gray (top layer graphene), turquoise (bottom layer graphene). 99

4.8 (a) Electron density plot for the pristine TBLG, at a plane at a height oft 0.33 Å. Corrugation of the top layer of the pristine TBLG (b) top view and (c) side view. 101

4.9 (a) $[F_4TCNQ]_2$ dimer, showing the separations d_x and d_y. (b) Binding energy (BE) of $[F_4TCNQ]_2$ as a function of d_x and d_y. BE for the dimer has been calculated usnig the Eq. (4.6) 107

4.10 Binding energy of the dimer of two anions as a function of d_x and d_y. 109

4.11 Binding energy (BE_{anions}) of the dimer of two anions as a function of d_x and d_y. BE_{anions} has been calculated using Eq. (4.7) with $s = 0.58$. 110

4.12 Predicted linear chain based on the DFT calculations of the energy landscape for a charged molecular dimer. We have marked d and θ in the chain where d is the intermolecular distance and θ is the angle between the two molecules. Color code: Yellow (C atom of molecule), blue (N), red (F). 112

4.13 Nitrogen is doped in (a) AA stacked region, (b) AB stacked region, and (c) in between AB region of the nitrogen doped TBLG (N-TBLG). Color code: blue (N), gray (top layer graphene), and turquoise (bottom layer graphene). The solid black lines show the boundaries of the TBLG unit cell. 114

4.14 Optimized geometries of F_4TCNQ on different positions of the nitrogen doped TBLG. Position of the N dopant has been shown using a solid blue circle. Color code: Yellow (C atom of molecule), blue (N), red (F), gray (top layer graphene), turquoise (bottom layer graphene). 116

4.15 Calculated differential charge densities (DCD) for the site–2 [see Fig. 4.5(b)] of the F_4TCNQ/TBLG (a) top-view (c) side-view and for the Fig. 4.14(c) configuration of F_4TCNQ/N-TBLG (b) top-view (d) side-view. In all cases, the isosurface value of 0.0015 e/Bohr^3 has been plotted. Red and blue lobes represent electron accumulation and depletion, respectively. The upper and lower graphene layers are shown in gray and turquoise, respectively. 118

4.16 (a) Non spin-polarized density of states of F_4TCNQ molecule on the TBLG for site–2 [see Fig. 4.5(b)]. Black line represents the total up & down spins DOS for TBLG and green line represents the total up & down spins DOS for F_4TCNQ molecule. (b) spin polarized density of states of F_4TCNQ molecule on the N-site of the N-TBLG [see Fig. 4.14(c)]. Golden yellow line represents the DOS for N-TBLG, blue line represents up spin DOS and red line down spin DOS for F_4TCNQ molecule. 119

5.1 Plots of differential charge density, $\Delta\rho$ for TCNQ monolayer on bare graphene, for three values of the electric field, plotted at iso-surfaces value of 0.0007 e/Bohr^3. Red and blue lobes correspond to electron accumulation and depletion, respectively. A, B and C represent the conditions when $\epsilon = -1.0$V/Å, 0 V/Å and +1.0 V/Å. The insetsshow the position of the Fermi level with respect to the graphene Dirac cone, for each case. This figure is reused with permission from Ref. 25 ©2019 Springer Nature Limited. 131

5.2 Optimized geometry of (a) F_4TCNQ molecule and (b) CoPc molecule in the gas phase. Color code for atoms: red (F), yellow (C), blue (N), green (Co), and turquoise (H). 133

5.3 Zoomed in views of five starting adsorption configurations considered for a single F_4TCNQ molecule on undoped graphene; a $\sqrt{127} \times \sqrt{127}$ graphene supercell was used in the calculaitons. As a result, periodic images of molecules are > 12 Å away from each other. Color codes for atoms are red (F), yellow (C), blue (N), and gray (C of graphene). 136

5.4 The magnetic moment μ_B has been plotted as a function of the applied external electric field. The insets show the direction of the electric field (a negative electric field is pointed downwards, while a positive electric field pointed upwards, i.e., towards the molecule). A negative electric field ($\epsilon < 0$) gives rise to a magnetic moment in the F_4TCNQ/Gr system. 139

5.5 (a) ΔQ (charge transfer from substrate to the molecule) as a function of external electric field (b) Total magnetic moment μ_B of the system as a function of ΔQ. 141

5.6 Top and side views of F_4TCNQ/Gr, showing isosurfaces of the spin polarization $\left[n^{\uparrow}(\mathbf{r}) - n^{\downarrow}(\mathbf{r})\right]$. (a),(c) ϵ =-0.3 V/Å, (b),(d) ϵ =-0.5 V/Å. Green lobes: $n^{\uparrow}(\mathbf{r}) > n^{\downarrow}(\mathbf{r})$, purple lobes: $n^{\uparrow}(\mathbf{r}) < n^{\downarrow}(\mathbf{r})$ Isosurface value: 0.00095 e/Bohr^3 142

5.7 (a) Position of the LUMO peak (in a non-spin-polarized calculation) of the F_4TCNQ molecule with respect to the Fermi energy of the F_4TCNQ/Gr system for different external electric fields (b) Position of the LUMO peak (in a non-spin-polarized calculation) of the F_4TCNQ molecule with respect to the Fermi energy of the F_4TCNQ/Gr system as a function ΔQ (charge transfer from substrate to the molecule). 143

5.8 Projected density of states (PDOS) for F_4TCNQ/Gr system at (a) ϵ = -0.5 V/Å, and (b) ϵ = 0.5 V/Å. Black and green lines represent the PDOS for graphene and F_4TCNQ, respectively. The Fermi level has is shown using a violet line. 144

5.9 Constant current STM images simulated at (a) -0.5 V and (b) $+0.5$ V for the F_4TCNQ/Gr shown in Fig. 5.3(d). All the simulations have been performed applying an external electric field (ϵ) of -0.5 V/Å perpendicular to the graphene sheet. We have plotted the isosurface values of 1×10^{-8} e/Bohr^3 to plot the constant current images (c) LUMO of F_4TCNQ molecule in the gas phase. Isosurface value of 0.00015 e/Bohr^3 is used to plot the LUMO of the molecule. 145

5.10 Zoomed in view of graphene doped with single N atom (N-Gr). A $\sqrt{127} \times \sqrt{127}$ graphene (Gr) supercell was used for N doping. Color code: blue (N), and gray (C of graphene). 146

5.11 Zoomed in views of graphene doped with N pair (2N-Gr). A $\sqrt{127} \times \sqrt{127}$ graphene (Gr) supercell was used for N doping where we have replaced 2 C atoms of Gr with 2 N atoms. (a)–(i) are the configurations we considered for the different positions N atoms in 2N-Gr. Color codes for atoms are blue (N), and gray (C of graphene). 148

5.12 Zoomed in views of various optimized geometries of single F_4TCNQ on N-Gr. The positions of the single dopant N atom have been highlighted using a red circle. Color code for atoms is red (F), yellow (C), blue (N), and gray (C of graphene). 151

5.13 Optimized geometry of single F_4TCNQ adsorbed at a C-site of the doped graphene, far away from the dopant N atom. Color code for atoms is red (F), yellow (C), blue (N), and gray (C of graphene). The positions of the single dopant N atom have been highlighted using a red circle. 153

5.14 Experimental STM images for (a) F_4TCNQ/N-Gr (b) after removal of F_4TCNQ molecules from F_4TCNQ/N-Gr. The two bright circles in (b) indicate the position of dopant N atoms where formerly F_4TCNQ molecules were present. Both the images recorded at bias voltage of +1.5 V and at I = 5 pA. The figures are reprinted with permission from Ref. 54. 153

5.15 Zoomed in views of optimized geometry of single F_4TCNQ on 2N-Gr. We have doped $\sqrt{127} \times \sqrt{127}$ supercell of graphene with a N pair. Different positions for dopant N have been shown using red circle. Color code for atoms are red (F), yellow (C), blue (N), and gray (C of graphene). 155

5.16 Side views showing isosurfaces of the spin polarization density $\left[n^{\uparrow}(\mathbf{r}) - n^{\downarrow}(\mathbf{r})\right]$, for (a) bare N-Gr, (b) F_4TCNQ/N-Gr [configuration Fig. 5.12(e)], and (c) bare 2N-Gr, (d) F_4TCNQ/2N-Gr [configuration Fig. 5.15(i)]. Isovalue of 0.0007 e/Bohr^3 has been used to plot the iso-surfaces. Color code for atoms: gray – C of graphene, blue – N, yellow – C of molecule, red – F, turquoise – H. Green lobes: $n^{\uparrow}(\mathbf{r}) > n^{\downarrow}(\mathbf{r})$ and purple lobes: $n^{\uparrow}(\mathbf{r}) < n^{\downarrow}(\mathbf{r})$. 158

5.17 (a) Projected density of states for F_4TCNQ/N-Gr, and (b) F_4TCNQ/2N-Gr. Color code: Golden yellow (substrate N-Gr), turquoise (substrate 2N-Gr), and green (F_4TCNQ). The position of the Fermi level has been indicated using solid purple line. 158

5.18 Calculated differential charge densities (DCD) for F_4TCNQ/Gr (a) top-view (b) side-view, for F_4TCNQ/N-Gr [for config. Fig. 5.12(e)] (c) top-view (d) side-view and for F_4TCNQ/2N-Gr [for config. Fig. 5.15(i)] (e) top-view (f) side-view. In all cases, the isosurface value of 0.0015 e/Bohr^3 has been plotted. Red and blue lobes indicate electron accumulation and depletion, respectively. 160

5.19 (a) STM image of CoPc molecule adsorbed on single nitrogen (encircled with green circle) and on the nitrogen pair (encircled with red circle) of the N-doped graphene. Dark blue dots represents the position of the nitrogen below the CoPc molecule. The images have been recorded at I = 50 pA and V = 1.0 V. (b) dI/dV spectra of CoPc molecule on single nitrogen of the doped graphene. (c) dI/dV spectra of CoPc molecule on the nitrogen pair of the doped graphene. The figures are reprinted with permission from Ref. 35. 162

5.20 Zoomed in views of optimized geometry of CoPc on (a) Gr (b) N-Gr and (c) 2N-Gr. We have substituted one C atom of the 15×15 graphene supercell by one N atom to make N-Gr and two C atoms by two N atoms to make the 2N-Gr. The position of the dopant nitrogen has been encircled in red in (b) and (c). Color code: yellow (C), blue (N), green (Co), turquoise (H), and gray (graphene). 163

5.21 Projected density of states (PDOS) for isolated CoPc on (a) Gr, (b) N-Gr, and (c) 2N-Gr. Color code: red (up spin of the CoPc), blue (down spin of the CoPc, gray (PDOS of the Gr), orange (PDOS of the N-Gr), and turquoise (PDOS of the 2N-Gr). The Fermi level is shown using a purple dotted line. The figures are reprinted with permission from Ref. 35. 165

5.22 Charge redistribution that occurs on placing a CoPc molecule on (a),(d) pristine graphene, (b),(e) N-Gr, and (c),(f) 2N-Gr. Red and blue lobes represent electron gain and loss, respectively. The isosurfaces shown correspond to (a),(b)(c) 0.0015 e/Bohr^3 and (d),(e),(f) 0.00055 e/Bohr^3. Color code: C (yellow), blue (N), purple (Co), light blue (H). The red circles indicate the positions of dopant N atoms in the graphene substrate. The gray lines indicate nearest neighbor bonds between C atoms in graphene. The figures are reprinted with permission from Ref. 35. 167

5.23 Distance between the Co atom (of CoPc) and the substrate as a function of charge transferred from the substrate to the molecule. 167

6.1 (a) and (b) are the top and side views of the black phosphorene (BP) 3x3 unit cell. **a** and **b** are the unit cell lattice parameters. The stacking along x-axis (armchair direction) is different from the y-axis (zigzag direction). 179

6.2 Field dependent band gaps of BP, TCNQ/BP, TCNE/BP, and TTF/BP. The direction of the applied positive E-field is labeled inside by taking TCNQ/BP as an example. Republished with permission of IOP Publishing Ltd, from 24; permission conveyed through Copyright Clearance Center, Inc. 182

6.3 (a) Experimental STM image of F_4TCNQ molecules deposited on few-layer black phosphorene at very low concentration. (b) Experimental STM image at a small length scale shows that single F_4TCNQ molecules are far apart from each other on few-layer black phosphorene. Both the STM images recorded at -2.0 V and I= 10 pA. White bars show the length scale of the STM images. The images are taken with permission from Ref 25. 184

6.4 Optimized geometry of F_4TCNQ molecule in gas phase. Color code for atoms: red (F), yellow (C), and blue (N).The long axis of F_4TCNQ, which passes through C atoms attached to CN^- groups, is shown using a dark red dashed line. 185

6.5 Optimized geometries of F_4TCNQ/BP systems, (a) to (g) are the top views of the seven configurations we considered. All the configurations are different from each other in terms of the position of hexagonal ring of the F_4TCNQ molecule on BP. (h) side view of F_4TCNQ/BP. Color code for atom is red (F), yellow (C), blue (N), maroon (P at the interface), purple (rest of the P). 186

6.6 Side view of optimized geometry of F_4TCNQ/3L-BP. Two extra layers are added at the bottom of the F_4TCNQ/BP systems shown in Fig. 6.5(h). Color code for atom is red (F), yellow (C), blue (N), maroon (P at the interface), and purple (rest of the P). 187

6.7 (a) Density of states (DOS) for the bare BP substrate. The black dashed line shows the position of the Fermi level. 189

6.8 Calculated differential charge densities for Fig. 6.5(d) (a) top-view (b) side-view. (c) LUMO of the isolated F_4TCNQ molecule. To plot (a), (b) and (c) we have used iso-surface value of 0.00015 e-bohr^{-3}. (d) Planar averaged differential charge density, $\Delta\rho(z)$ is plotted as a function of z. Color code: purple (electron accumulation), and turquoise (electron depletion) 192

6.9 μ_B has been plotted as a function of external electric fields. Inset shows the direction of the electric field. Negative electric field pointed downwards—positive electric field pointed upwards, i.e., towards the molecule. The negative electric field ($\epsilon < 0$) gives rise to a stable magnetic phase in F_4TCNQ/BP system. Color code: pale green (magnetic phase) blue (non-magnetic phase). 194

6.10 Charge transfer from BP to the molecule, as a function of the applied external electric field. 195

6.11 μ_B as a function of charge transfer from BP to the F_4TCNQ molecule. 196

6.12 Top and side views of the F_4TCNQ/BP system, showing isosurfaces of the spin-polarized charge density $\left[n^{\uparrow}(\mathbf{r}) - n^{\downarrow}(\mathbf{r})\right]$, for (a),(c) $\epsilon = -0.3$ V/Å, and (b),(d) $\epsilon = -0.5$ V/Å. Green and purple lobes correspond to positive and negative values, respectively, i.e., green: $n^{\uparrow}(\mathbf{r}) > n^{\downarrow}(\mathbf{r})$ and purple: $n^{\uparrow}(\mathbf{r}) < n^{\downarrow}(\mathbf{r})$. Isosurface value 0.00046 e/bohr^3. 197

6.13 Projected band structures for F_4TCNQ/BP systems along the **k**-path $\overline{X}$–$\overline{S}$–$\overline{Y}$–$\overline{G}$–$\overline{X}$ at different external electric fields (a) ϵ= +0.5 V/Å (b) ϵ= +0.3 V/Å, (c) ϵ= 0.0 V/Å. Note that we have projected the bands on the molecule. Color bar indicates the contribution from the molecule. Red color implies that full contribution of the molecule. Blue color indicates zero contribution of the molecule. Fermi energy has been drawn using black dashed line. (d) The full **k**-path inside the Brillouin zone. 199

6.14 Projected spin polarized band structures for F_4TCNQ/BP systems along the **k**-path $\overline{X}$–$\overline{S}$–$\overline{Y}$–$\overline{G}$–$\overline{X}$ at (e) ϵ= -0.3 V/Å (f) ϵ= -0.5 V/Å. Note that we have projected the bands on the molecule. Color bar indicates the contribution from the molecule. Red color implies that full contribution of the molecule. Blue color indicates zero contribution of the molecule. Fermi energy has been drawn using black dashed line. 200

6.15 Magnetic moment of the F_4TCNQ/BP system as function of temperature T. 202

6.16 (a) Diffusion of the molecule along the armchair (magenta arrow) and along the zigzag direction (orange arrow). (b) Experimental STM image shows streaks along zigzag direction. The STM recorded at -2.0 V bias voltage and at I= 10 pA. The image is taken with permission from Ref 25. (c) Barrier heights for both the directions calculated using constrained optimization method. To calculate the diffusion barrier, we have interpolated equidistant images between two equivalent sites. Plot shows the variation of the total energy of the images as a function of d_{path}. 204

7.1 Orthorhombic crystal structure of bulk black phosphorus (a) top view of x-y plane, (b) side view of x-z plane, and (c) side view of x-z plane slightly tilted along y-direction for better visual clarity of lattice vectors **a**, **b** and **c**. It can be seen that **a** is the lattice vector along the armchair (x) direction, **b** is the lattice vector along the zigzag (y) direction , and **c** represents the lattice vector along the z direction. Phosphorus atoms are indicated by purple spheres. 214

7.2 Experimental STM images of few-layer phosphorene from Kiraly et al.[27] (a) is the constant-current STM image for the monovacancy A which has been shown in the insets of the (b). The point defect A has been created by removing single P atom from the upper sublayer of the topmost layer of the three-layer black phosphorene (3L-BP). The STM image recorded at -0.1 V bias voltage. scale bar = 2 nm. (b) is charge density plots for A simulated using a tight binding model, scale bar = 1 nm. Reprinted with permission from Ref. 27©2017 American Chemical Society. 216

7.3 Experimental constant current STM images of black phosphorus surface recorded at (a) 0.11 V and (b) -0.2 V, scale bar = 1 nm. Reprinted with permission from Ref. 28 ©2017 American Chemical Society. 217

7.4 Experimental STM images recorded for the same area on the surface of few-layer black phosphorene before (left) and after (right) applying an electric pulse at bias voltage of -0.4 V and $I = 100$ pA. scale bar = 5 nm. Feature **A** remains unchanged after application of the electric pulse. However, feature **B** is transformed into **B'** after the electric pulse is applied. **a** and **b** represent the armchair and zigzag directions of the few-layer BP. The colored ellipses have been drawn to highlight the features of interest. The figures are reprinted with permission from Ref. 30. 218

7.5 Line scan profile for the features **A** (green line) and **B'** (red line). Scanning for both the features has been performed along the axis **a** shown in the right-hand side of Fig. 7.4. This image is reused with permission from Ref. 30. 219

7.6 Experimental STM images for feature **A**. The top panel shows STM image recorded at -1.0 V bias voltage and I = 100 pA. The bottom panel is the STM image recorded at $+1.0$ V bias voltage and I = 100 pA. Dumbbell shape can be observed at negative bias (top panel), and dumbbell changes to a dark circle at positive bias (bottom panel) This figure is reprinted with permission from Ref. 30. 220

7.7 Top and side views of (3×3) unit cell of (a),(d) monolayer (BP), (b),(e) bilayer (2L-BP), and (c),(f) trilayer (3L-BP) of black phosphorene, respectively. a and b are the lattice parameters, and d is the interlayer distance between two consecutive layers. SL-1 and SL-2 are the upper and lower sublayers of the topmost BP layer. SL-3 is the upper sublayer of the second BP layer. Purple spheres indicate phosphorus atoms. The rectangles in (a), (b) and (c) indicate the boundaries of (1×1) cells. 222

7.8 Optimized geometries of intrinsic defects in 3L-BP: Top views of (a) 59-MV, (b) 5757-DV, (c) 5757-SW, (d) 5656-MV-1/2. Note that we have shown one geometry for both the top views of 5656-MV-1 and 5656-MV-2 because they look the same. (e) and (f) are the side views of 5656-MV-1 and 5656-MV-2. Filled black circle in (e) and (f) represents the position of the single vacancy in the case of 5656-MV-1/2. Color code: purple (P), we have used yellow for the P atoms near vacancy to show the vacancy more clearly. 224

7.9 Optimized geometries of extrinsic defects in 3L-BP: (a) and (d) are the top view and side view of Sn-1, (b) and (e) are the top view and side view of Sn-2, (c) and (f) are top view and side view of Sn-3. For the top views shown in (a) and (b) we have shown only the top layer of the 3L-BP for visual clarity. Similarly, for (c) we have shown the middle layer of the 3L-BP to show the substitution in SL-3. Color code: purple (P) and red (Sn). 225

7.10 Optimized geometries of extrinsic defects in 3L-BP: (a) and (c) are top view and side view of Au-2. (b) and (d) are top view and side view of Sn-int. For the top views shown in (a) and (b), we have shown only the top layer of the 3L-BP for visual clarity. Color code: purple (P), red (Sn) and golden yellow (Au). 226

7.11 Simulated constant current STM images: (a) and (b) for 59-MV at bias voltage -0.15 V and $+1.0$ V, (c) and (d) for DV at bias voltage -0.65 V and $+1.0$ V, (e) and (f) for SW at bias voltage -0.3 V and $+1.0$ V, (g) and (h) for 5656-MV-1 at bias voltage -0.16 V and $+1.0$ V, (i) and (j) 5656-MV-2 at bias voltage -0.20 V and $+1.0$ V. We have fixed the isosurface value at 1×10^{-8} e/Bohr^3 to plot STM images. Scale bar = 1 nm 233

7.12 Simulated constant-current STM images: (a) and (c) for Sn-1 at bias voltage -0.24 V and $+1.0$ V, (b) and (d) for Sn-2 at bias voltage -0.10 V and $+1.0$ V. We have fixed the isosurface value at 1×10^{-8} e/Bohr^3 to plot STM images. Scale bar = 1 nm 234

7.13 (a) and (c) are experimental STM images at V = -0.022 V, I = 200 pA and V = $+1.0$ V, I = 400 pA, respectively (b) and (d) are simulated STM images for Sn-2 at bias voltage -0.10 V and $+1.0$ V. We have fixed the isosurface value at $1{\times}10^{-8}$ e/Bohr^3 to plot (b) and (d). scale bar = 1 nm. 235

7.14 Simulated constant-current STM images: (a) and (d) for Sn-3 at bias voltage -0.15 V and $+1.0$ V, (b) and (e) for Au-2 at bias voltage -0.07 V and $+1.0$ V, (c) and (d) for Sn-int at bias voltage -0.88 V and $+0.53$ V. We have fixed the isosurface value at 1×10^{-8} e/Bohr^3 to plot the STM images. Scale bar = 1 nm. 236

7.15 Charge density plot for (a) 5656-MV-1, and (b) Sn-2. The variation of the isosurface is shown for the plane placed at 2.57 Å above from the topmost layer. Scale bar = 1nm. 237

7.16 Distribution of atomic charges in the Sn-2 system, i.e., a 3L-BP system with a Sn atom substituted in the lower sublayer of the topmost BP layer. The atoms are colored according to the value of the calculated Löwdin charge (Q_i^L) computed according to Eq. (7.4), for (a) top layer, (b) middle layer, and (c) bottom layer. 238

7.17 $\log(\Delta_i)$ for the atoms in (a) top layer, (b) middle layer, and (c) bottom layer of the Sn-2 system for the energy window ϵ_F to $\epsilon_F - 0.10$ eV. $\log(\Delta_i)$ for the atoms in (d) top layer, (e) middle layer, and (f) bottom layer of the Sn-2 system for the energy window ϵ_F to $\epsilon_F + 1.0$ eV. . . 240

7.18 log($D_{i,j}$) for (a) p_z, (b) p_x+p_y, and (c) s orbitals of the atoms present in top layer layer of the Sn-2 system for the energy window ϵ_F to ϵ_F − 0.10 eV. log($D_{i,j}$) for (d) p_z, (e) p_x+p_y, and (f) s orbitals of the atoms present in top layer layer of the Sn-2 system for the energy window ϵ_F to ϵ_F + 1.0 eV. 241

7.19 log(Δ_i) for the atoms in (a) top layer, (b) middle layer, and (c) bottom layer of the Sn-int system for the energy window ϵ_F to ϵ_F −0.88 eV. log(Δ_i) for the atoms in (d) top layer, (e) middle layer, and (f) bottom layer of the Sn-int system for the energy window ϵ_F to ϵ_F +0.53 eV. . 242

7.20 log(Δ_i) for the p_z orbitals of the atoms in (a) top layer and (b) middle layer of the Sn-int system for the energy window ϵ_F to ϵ_F − 0.88 eV. log(Δ_i) for the p_z orbitals of the atoms in (c) top layer and (d) middle layer of the Sn-int system for the energy window ϵ_F to ϵ_F + 0.53 eV. 243

7.21 log(Δ_i) for the s orbitals of the atoms in (a) top layer and (b) middle layer of the Sn-int system for the energy window ϵ_F to ϵ_F − 0.88 eV. log(Δ_i) for the s orbitals of the atoms in (c) top layer and (d) middle layer of the Sn-int system for the energy window ϵ_F to ϵ_F + 0.53 eV. 244

7.22 Three possible scenarios considered for effect of electric pulse on the Sn interstitial defect: (a) Sn-int switches to Sn-2 + P-vac (or Sn-2), (b) Sn-int switches to Sn-2 + P-adatom, (c) Sn-int switches to Sn-2+P-int. Color code: purple (P), red (Sn) 246

7.23 Simulated constant-current STM images: (a) and (d) for Sn-2 + P-vac (or Sn-2) at at bias voltages −0.10 V and +1.0 V, (b) and (e) for Sn-2 + P-adatom at bias voltages −0.06 V and +0.91 V, (c) and (f) for Sn-2 + P-int at bias voltages +0.05 V and +0.91 V. Scale bar = 1nm 247

7.24 Change in enthalpy for the three switchover paths discussed in Figs. 7.22(a)–(c). 249

List of Tables

3.1 Adsorption energy (in eV/molecule), as calculated using DFT, for a monolayer of HS IPB in $S_{1/2}$ supercell on Au(111), for orientations corresponding to different molecular planes of the bulk HS crystal, (01-1), (010) and (001) (see Fig. 3.7) at U= 6.55 eV. 70

4.1 Calculated values of adsorption energies in eV, for all the F_4TCNQ/TBLG sites. 102

4.2 Total energies in meV for site–1 and site–2 in 'bridge' position. The values in the second and third columns represent the total energy calculated when incorporating and not incorporating dispersion interactions, respectively. The zero of energy is set at the value for site-1. 103

4.3 Adsorption energies in eV/molecule for the linear chains and monolayer of the molecules on TBLG substrate. Linear chains of different numbers of molecules have been considered on TBLG. 106

4.4 Total energy in meV for the nitrogen doped twisted bilayer graphene (N-TBLG). We have calculated total energy using DFT for the configurations shown in Fig. 4.13(a)–(c). 115

4.5 Adsorption energy in eV for F_4TCNQ on the nitrogen-doped twisted bilayer graphene (N-TBLG). We have calculated adsorption energy for the configurations corresponding to Figs. 4.14(a)-(f) using Eq. (4.11). 119

5.1 Computed formation energy ($E^{\text{form}}_{\text{doped Gr}}$) for the graphene doped with nitrogen pair (2N-Gr) and for the graphene doped with single nitrogen (N-Gr). We have substituted one C atom of $\sqrt{127} \times \sqrt{127}$ graphene supercell by a single N atom for N-Gr and two C atoms by two N atoms in case of 2N-Gr. For 2N-Gr, we can have more than one configuration depending on the position of the two N atoms with respect to each other. The formation energies have been computed using Eq. (5.2). For ease of reference, the values corresponding to the lowest-energy configuration have been boxed. 149

5.2 Calculated values for the adsorption energy $E^{\text{N-Gr}}_{\text{ads}}$ for the various adsorption geometries considered for F_4TCNQ on graphene with a single N atom. The values are computed using Eq. (5.3). For ease of reference, the value corresponding to the lowest-energy geometry has been boxed. 152

5.3 Computed adsorption energy ($E^{\text{2N-Gr}}_{\text{ads}}$) for various configurations considered for F_4TCNQ/2N-Gr. We have substituted two C atoms of the ($\sqrt{127} \times \sqrt{127}$) graphene supercell with two N atoms and adsorbed a F_4TCNQ molecule on it. The adsorption energy is computed using Eq. (5.4). The boxed value corroesponds to the lowest energy configuration. 157

6.1 Lattice parameters for BP (1L-BP) and 3L-BP calculated using PBE+DFT-D2. 188

6.2 Adsorption energies (in eV) calculated using Eq. (6.1) for all the F_4TCNQ/nL-BP configurations shown in Fig. 6.5, for both monolayer and 3L phosphorene substrates. The boxed values correspond to the lowest energy configurations on the two substrates. 190

7.1 Lattice parameters of bulk and few layer of black phosphorene (nL-BP, where n = 1, 2, and 3) calculated using PBE + DFT-D2. 228

7.2 DFT results for calculated band gap (E_g) of few-layer black phosphorene and bulk black phosphorus. The second column contains our results computed using PBE + DFT-D2, the remaining columns contain previous values in the literature obtained using different techniques. The experimental values for the band gap in bulk black phosphorus range from 0.31 to 0.35 eV.[40–43] 229

7.3 Calculated values of defect formation energy for all the types of intrinsic and extrinsic defects in 3L-BP considered by us. The positive E_{DFE} value of intrinsic defects suggests that formation of these defects is energetically unfavorable, whereas the negative E_{DFE} value of extrinsic defects suggests that formation of these defects is energetically favorable. 231

Chapter 1

Introduction

1.1 Design of Materials at the Nanoscale for Technological Applications

From sending a rocket to space to our daily life usage, technology is everywhere. It is needless to say that we live in an age driven by technology. The demands posed by technological applications drive the search for new materials with novel properties. For example, the need for a material that shows high carrier mobility like graphene (an allotrope of carbon consisting of a single layer of atoms arranged in a two-dimensional honeycomb lattice), but simultaneously offers a sizeable band gap for applications in the semiconductor industry, has provided the motivation for the synthesis of black phosphorene (a single layer of black phosphorus, the most stable allotrope of phosphorus).[1;2]

The success of graphene has accelerated the search for new two dimensional (2D) materials. This has led to the discovery of other new 2D materials such as germanene (a single layer of germanium atoms),[3] phosphorene,[1;4] hexagonal boron nitride (boron and nitrogen atoms arranged in a two-dimensional honeycomb lattice like graphene),[5] and van der Waals stacked heterostructures.[6;7] It is thought that these materials may replace the current silicon-based electronics in the future. These new 2D materials are not only attractive because of their technological applications due to their extraordinary electronic properties such as high carrier mobility, but are also interesting from the viewpoint of fundamental physics. For example, graphene shows exotic properties like the integer and fractional quantum Hall effects,[8;9] and a remarkably high electrical conductivity.[10] Black phosphorene is also known to show interesting physical properties. For example, black phosphorene shows anisotropy in hole mobility, i.e., it shows very high/low hole mobility along the zigzag/armchair direction.[11] It also shows a sizeable band gap of 1.50 eV.[11–13] The combination of these two properties is rarely observed in the same material, making black phosphorene very attractive in the semiconductor industry.

Technological applications have got a massive boost with the incorporation of nanomaterials. For example, the electronics industry requires effective ways of nanostructuring materials that can lead to a large density of electronic components on a chip.[14–16] Nanomaterials are restricted in nanometric dimensions. One can have zero, one, two, or three dimensional nanomaterials. Molecules and nanoclusters are examples of zero dimensional nanomaterials.[17;18] Similarly, nanowires and nanotubes are examples of one-dimensional nanomaterials.[19–22] Examples of two-dimensional nanomaterials include monolayers, thin films and heterostructures.[23;24] An example of a three-dimensional nanomaterial is a nanostructured alloy. In recent years, nanomaterials have drawn huge attention owing to the variety of novel and technologically desirable properties that one can get out of materials by reducing the size. For example, some materials like Pt and Au are well known to be noble metals, which display very low chemical reactivity. However nanoparticles of these elements show catalytic properties and are becoming increasingly used in applications. Gold nanoparticles are also known to show magnetism, in contrast to the nonmagnetic bulk counterpart.[25]

A new revolutionary field in which nanoscience and nanotechnolgy play an important role is molecular electronics,[26] where one or more molecules are designed to be used as components such as conducting wires, switches or rectifiers.[27] Another area where the use of organic molecules in electronics is popular is that of exploiting the spin degree of freedom of the electron. This leads to the new field of molecular spintronics, which combines both electronics and spintronics.[28;29] Spin crossover molecules are one class of molecules that find application in spintronics.[30;31] This is because of their switchable spin states (e.g., two possible spin states exist for the $\mathrm{Fe}^{\mathrm{II}}$ complexes) which can be switched using external stimuli like light, pressure, or electric field. A significant opportunity for research can be foreseen in this field, for developing a basic understanding as well as probing and improving spin-dependent properties for the applications.

Designing a nanomaterial which can give us desirable properties for technological applications is one of the very first steps of the materials research. The next step is the synthesis of the material. Then the material goes for characterization, which tells us how much it deviates from the desired properties. Scanning tunneling microscopy[32;33] (STM) and atomic force microscopy[34] (AFM) are two of the techniques used very frequently for the characterization part. If the characterization shows significant deviation from the properties we wanted, we may have to repeat the whole process. This is often very challenging, because repeating the entire process requires a lot of extra effort and time. Sometimes it is very expensive in terms of cost. This is where first principles calculations play a significant role, and can guide us in designing materials with desired properties.

The term 'first principles calculations' is used to describe theoretical methods that allow one to calculate the electronic and physical properties of a material using quantum mechanical principles, within no empirical input apart from atomic numbers and atomic masses. *Ab initio* density functional theory[35;36] (DFT), *ab initio* molecular dynamics[37] (AIMD), and Quantum Monte Carlo[38] (QMC) are a few examples of first principles methods that are frequently used to compute the material properties. The charm of these computational techniques is that they do not require any experimental data as input. This is where the strength of the first principles calculations lies. They can also help us gain a detailed understanding into the underlying reasons why a material possesses the properties it does, in a way that is not accessible to experiments. Such knowledge can then be leveraged to further design an even more suitable material for the desired application. Once a suitable material has been finally made by such a combined theoretical and experimental approach, one can then move on to device fabrication.

In this thesis, we have used *ab initio* density functional theory (DFT) to compute the properties of the systems under investigation, as well as to gain insight into why they possess the properties that they do. DFT simplifies the complexity of handling the quantum many-body problem by mapping it onto an equivalent problem formulated in terms of the three-dimensional electron density; this is then mapped in turn onto an equivalent one-electron problem. Hence, to compute or explain the properties of a material, we do not need to compute the complicated many-body electronic wave-function; instead, we can get essentially the same information by solving instead the one-electron Kohn-Sham equations.

Sometimes, computations based on first principles calculations can become rather expensive; in such scenarios, one can still, however, make progress with models that capture the essential physics at play, with the model parameters being fitted to simpler first principles calculations.

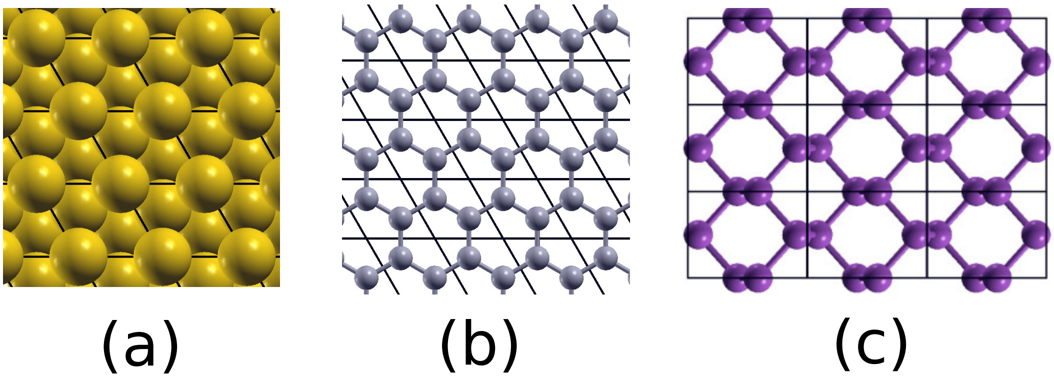

Figure 1.1: Top views of the three substrates considered in this thesis: (a) Au(111), (b) graphene, and (c) black phosphorene. Color code for atoms: golden yellow (Au), gray (C), purple (P). The black lines indicate the boundaries of the primitive surface unit cell.

1.2 Motivation of this thesis: Organic molecules on substrates

In this thesis, we have explored the possibility of tailoring the properties of two dimensional systems by molecular adsorption. We have studied organic molecules on surfaces in many chapters of this thesis. Molecule-substrate interfaces are of interest for materials science, as placing a molecule on a substrate can tune the properties of both the molecule and the substrate, and can even introduce novel phenomena. For example, it has been shown that non-magnetic TCNQ molecules develop a magnetic moment when deposited on a non-magnetic substrate comprised of graphene grown on Ru(0001).[39] On the other side, a thin film of Cu, a diamagnetic system, shows ferromagnetism upon adsorption of C_{60} molecules.[40]

We now give a brief introduction to the substrates that we have considered for the deposition of organic molecules. In this thesis, we have considered three different kinds of substrates, viz., Au(111) (a metal), graphene (a semimetal), and black phosphorene (an insulator), see Figs. 1.1(a) to (c).

Bulk gold has the face centered cubic (fcc) structure, and accordingly atoms on the bulk-terminated Au(111) surface are arranged in a triangular lattice where each atom has six nearest neighbors [see Fig. 1.1(a)]. However, this bulk terminated structure reconstructs into a structure that is known as the herringbone pattern,[41–43] which results from the formation of elastic stress domains that relieve surface stress.[44] We note that when considering the Au(111) surface in Chapter 3, we have not taken into account the herringbone reconstruction. This is because it has a unit cell that is prohibitively large for DFT calculations; in any case, over large regions of the surface, the herringbone reconstruction can be viewed as a minor perturbation to the unreconstructed structure, and we do not believe it plays an important role in the physics of the spin crossover transition studied in Chapter 3.

Graphene was first discovered and isolated by Andre Geim and Konstantin Novoselov in 2004.[45] It has drawn a great deal of attention since its discovery due to its spectacular mechanical and electronic properties, which open up spaces for its possible application in modern technologies.[6;46;47] Pristine graphene is a semimetal, i.e., it has a zero band gap, which makes it unsuitable for many applications in electronics. Ways of effectively tuning graphene's electronic properties, such as opening up a band gap in graphene, have been among the most discussed topics in physics in the last two decades.[48–50] Graphene also displays several unusual properties such as room temperature quantum Hall effect,[8;9] ambipolar electric field effect,[45] and extremely high electrical conductivity.[10] In this thesis, we have tuned the charge and magnetic moment of organic molecules such as F_4TCNQ (tetrafluoro-tetracyano-quinodimethane) and CoPc (cobalt phthalocyanine) by adsorbing them on graphene and nitrogen doped graphene. We have also studied the self-organization of F_4TCNQ molecules deposited on twisted bilayer graphene. Twisted bilayer graphene (TBLG) is a system composed of two monolayers of graphene deposited atop each other, such that the atomic rows of one layer are misoriented with respect to those of the other layer by a twist angle. As a result of the twist between the successive layers, in TBLG, in different regions of the unit cell, the stacking changes from AA to AB to in-between. The electronic properties of TBLG are not the same as those of single-layer graphene; they are much more complicated and largely depend on stacking and the twist angle between layers. For example, at small twist angles, twisted bilayer graphene (TBLG) shows appealing properties such as very low Fermi velocity, highly localized electron density, and van Hove singularities in the electronic density of states near the Fermi energy.[51]

Black phosphorene, a monolayer of black phosphorus, was first prepared by mechanical exfoliation by Lu *et al.*[2] It has drawn much attention because of its fascinating electronic properties. In particular, its high charge carrier mobility, direct band gap semiconducting characteristics, and strong anisotropies in electro-optical and thermo-mechanical properties are opening up new opportunities for its application in electronics[52] and optical devices.[53] We have studied the effect of external electric fields on electronic and magnetic properties of black phosphorene doped by the deposition of F_4TCNQ molecules.

Next, we give a brief introduction of the three organic molecules we considered for adsorption. We have studied the adsorption of the spin crossover molecule Fe((3, 5-$(CH_3)_2C_3N_2H)_3BH)_2$ (IPB) on Au(111) in Chapter 3, and the adsorption of the electron acceptor F_4TCNQ on twisted bilayer graphene, pristine graphene, and N-doped graphene in Chapters 4 and 5. Adsorption of F_4TCNQ on black phosphorene has been studied in Chapter 6. We have studied the adsorption of another electron acceptor type molecule, cobalt phthalocyanine, (CoPc) on pristine and N-doped graphene in Chapter 5. The three molecules have been shown in Figs. 1.2(a)–(c).

Spin crossover molecules can show switching between two spin states – a low-spin (LS) and a high-spin (HS) state – under the application of external stimuli such as electric field, light, or heat.[54] IPB is a classic example of this category; see

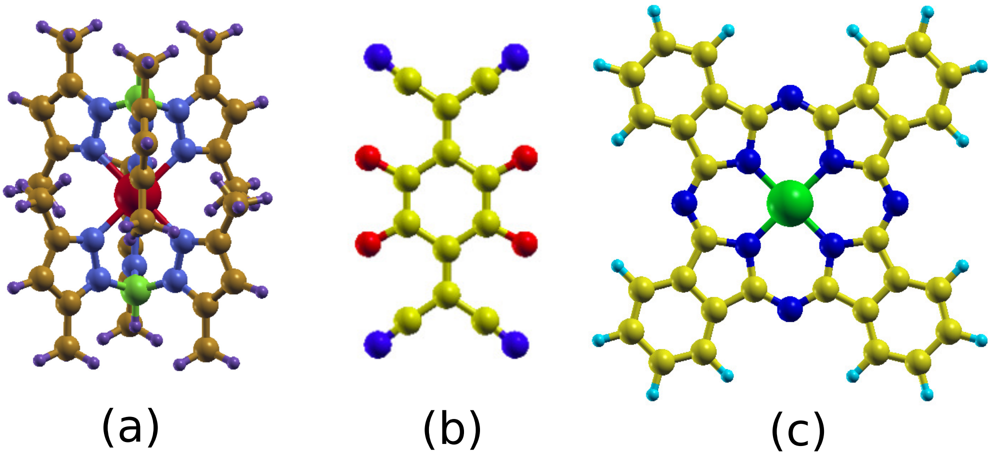

Figure 1.2: Optimized geometry of isolated (a) spin crossover IPB molecule [Color code for atoms is red (iron), blue (nitrogen), green (boron), orange (carbon), violet (hydrogen)], (b) F_4TCNQ molecule [Color code for atoms: red (F), yellow (C), blue (N)] and (c) CoPc molecule [Color code for atoms: red (F), yellow (C), blue (N), green (Co), and turquoise (H)] in the gas phase.

Fig. 1.2(a). Spin crossover molecules[55] are particularly attractive compounds in molecular spintronics as they can display a different conductance in the two spin states. They can also find applications in magnetic memory devices,[56] where spin states are used as classical bits. The study of interfaces between spin crossover molecules and metal substrates is important because such interfaces will be present in devices, and one needs to understand how the presence of the interface may alter the spin crossover properties of the molecules. For example, we will see that we find that epitaxial strain imposed by the substrate [Au(111) in our case] can alter the spin state of the spin crossover molecule.

The electron acceptor type molecule F_4TCNQ has drawn considerable attention because of its possible application in molecular electronics. One can tune the electronic properties of a substrate by adsorbing F_4TCNQ on it. For example, it has been shown that F_4TCNQ creates p-type doping when deposited on a black phosphorene[57] or graphene[58] substrate. One can also change the p-type doping to a n-type doping by replacing the F_4TCNQ molecule with an electron donor type molecule such as tetrathiafulvalene (TTF).[58] In this thesis, we show that it in addition to p-type doping, one can also induce a magnetic moment, by applying an external electric field to a system consisting of a F_4TCNQ molecule adsorbed on graphene or black phosphorene.

Metal phthalocyanines are the third class of molecules considered in this thesis. These are particularly attractive for their catalytic activity.[59] For example, cobalt phthalocyanine or CoPc is a potential catalyst for CO_2 conversion reactions.[59–61] Enhanced catalytic activity for CoPc has been observed on nitrogen-doped graphene when the molecule binds to a pyridinic or pyrrolic site.[62] It has been suggested that changing the oxidation state of the Co center in the CoPc molecule, from 0 state to a -1 state, by a redox reaction, should result in improved catalytic performance.[60;61] We will show that such a change in charge state due to a redox reaction occurs for the CoPc molecule when it is adsorbed on a nitrogen pair in N-doped graphene.

Above, we have mentioned that molecular adsorption can affect structural, electronic, and magnetic properties. The next question is, what are the driving forces which result in a change in properties on bringing the molecule and substrate together? One important driving force could be charge transfer between the substrate and molecule. Another driving force could be the epitaxial strain imposed by the substrate on the molecular overlayer. For example, we will see in Chapter 3 that epitaxial strain induces spin-crossover between low-spin and high-spin states of the molecule deposited on the substrate.[63] In addition to such intrinsic mechanisms, extrinsic factors such as an applied electric field could be used to further tune the properties of the system. There is a lot of room left in this field, which requires rigorous research to have a better idea of the driving forces that can be exploited to tune the properties of the molecules and/or substrate for technological applications.

1.3 Outline of this thesis

In Chapter 1, we have given a brief introduction to the problems we have considered in this thesis. This thesis has focused on two types of systems: organic molecules on surfaces, and two dimensional systems with impurities and/or defects. These systems have in common certain features, (i) they are low-dimensional, (ii) they have applications in fields such as spintronics, and device physics, (iii) the system properties accordingly have to be tailored so that they are optimal for the desired applications, (iv) frequently, strong correlations and/or non-covalent interactions play an essential role.

We have studied organic molecules on surfaces in the first part of this thesis. Spin crossover molecules on a metallic substrate have been discussed in Chapter 3. Electron acceptor type organic molecules on different non-metallic surfaces have been studied in the next three chapters. The problems have been discussed in the following order: electron acceptor type molecule F_4TCNQ on twisted bilayer graphene in Chapter 4, F_4TCNQ on pristine and nitrogen doped graphene in Chapter 5, and F_4TCNQ molecule on black phosphorene in Chapter 6. We have also studied an organo-metallic catalyst, the cobalt phthalocyanine (CoPc) molecule, on nitrogen-doped graphene in Chapter 5.

The second part of this thesis, i.e., Chapter 7, discusses the defects found in few-layer black phosphorene. The experimental parts of all the problems discussed in this thesis have been performed by the group of Prof. Vincent Repain and Dr. Jérôme Lagoute in the MPQ Laboratory of the University of Paris - Diderot.

In Chapter 2, we have discussed the underlying theoretical formalism and the computational techniques that we have used in this thesis. This includes non-spin-polarized and spin-polarized density functional theory[35;36] (DFT), the DFT-D2[64;65] technique to incorporate dispersion interactions, the DFT+U[66–68] method for describing strong correlations, and the Tersoff-Hamann[69] approach to simulate scanning tunneling microscopy (STM) images.

In Chapter 3, we have studied spin crossover molecules deposited on a metallic gold substrate. Spin crossover is a phenomenon of changing spin state induced by external stimuli such as light, pressure, or temperature. Spin crossover molecules (SCM) have drawn considerable attention in the field of spintronics because of their unique ability of controllable spin switching.[30;31] $Fe((3, 5-(CH_3)_2C_3N_2H)_3BH)_2$ (or IPB) is one of the classic examples of this category. IPB molecules are found in the low-spin (LS) ground state in their crystalline phase.[70] However, recent STM experiments show that an ordered superlattice of two types of molecules is formed when they are deposited on a Au(111) substrate.[71] One can guess that these two types of molecules could be in two different spin states, i.e., high-spin (HS) and low-spin (LS) states, but this has not been proven experimentally. Using DFT, we show that the SCM molecules are indeed arranged in an ordered mixed spin state, forming a LS-HS-HS superlattice.[63] We have simulated STM images for this ground state structure, and compared with experiment. The simulated and experimental STM images show excellent agreement. We are the first to report this two dimensional ordered spin-state superlattice. We also show that the driving force for the formation of this 2D spin-state lattice is the epitaxial strain that arises due to the lattice mismatch between the substrate and the monolayer of the IPB. A mechanoelastic model fitted with the DFT parameters has been developed to understand the strain-induced spin crossover. This finding opens up a new space for the spin crossover molecules because one can control the spin states of the molecule at the metallic interfaces by tuning the lattice mismatch between the molecular monolayer and the substrate. This is possible if one considers different substrates for the same molecule.

In the next few chapters, we have studied the interaction of organic molecules with different non-metallic interfaces. For example, we have studied F_4TCNQ on graphene, nitrogen-doped graphene and phosphorene in Chapters 4, 5 and 6. We have studied CoPc on graphene and nitrogen-doped graphene in Chapter 5. F_4TCNQ on different non-metallic surfaces has drawn considerable attention in the field of device physics, because one can tune the electronic properties of the substrate by doping with an organic molecule. So, molecular doping can be a game-changer in the semiconductor industries where we can use different organic molecules as dopants to get the desired properties during device fabrication.

One should also have a complete understating of the molecule-substrate interaction before applying such systems for the device fabrication, because the molecules can sometimes react with the substrate and form chemical bonds. Sometimes, they can show different self assemblies depending on the substrates we are using. For example, F_4TCNQ molecules form very densely packed 2D-islands on graphene grown on the hexagonal-BN substrate.[72] In Chapter 4, we have studied the F_4TCNQ molecule on twisted bilayer graphene (TBLG). STM experiments performed by Dr. Harsh and Dr. Lagoute show that F_4TCNQ avoids the comparatively electron-rich AA-stacked regions of the Moiré (formed by the TBLG); this is counter-intuitive since the molecule is an electron acceptor.[73] The STM experiments also show that F_4TCNQ self assembles into one-dimensional linear chains on twisted bilayer graphene (TBLG) at higher coverage.[73] Our DFT calculations have validated and explained the experimental findings. We have found that relatively weak van der Waals interactions between the molecule and the substrate when it sits at the locally convex AA-stacked regions of the Moiré cause adsorption at these sites to be disfavored. We have also found that strong intermolecular interactions among the F_4TCNQ molecules along a particular direction leads to the formation of the linear chain on TBLG at higher coverage. These findings could conceivably be of interest in molecular electronics, where one would like to make molecular wires.

F_4TCNQ-graphene systems can be very special if one can add magnetic functionalities to them, thus raising the possibility of them being used in spintronic devices. In the first part of Chapter 5, we are interested in showing how one can add magnetism to the F_4TCNQ-graphene system. We have shown two different ways to do this. One way is applying an external electric field to the system, and another is doping the graphene substrate with nitrogen atoms. We have also shown that both approaches can hugely increase the electron transfer from graphene to the molecule. Our calculations show that the LUMO (lowest unoccupied molecular orbital) of the molecule splits into two orbitals, majority spin SOMO (singly occupied molecular orbital) and minority spin SUMO (singly unoccupied molecular orbital) with different filling ratio which induces magnetism. We find a good correlation among the magnetism, charge transfer, and the external electric field; these correlations could be useful to predict the magnetism and the charge transfer of a system for a given direction and magnitude of the electric field. In the second part of Chapter 5, we have tuned the charge of the CoPc molecule on nitrogen-doped graphene. It is expected to show enhanced catalytic performance in its reduced state. However, in the earlier study[62] which discussed enhanced catalytic activity for the CoPc on the nitrogen-doped graphene, the molecule was in the “0" oxidation state. Recently, STM experiments led by our collaborator Dr. Lagoute, have shown that CoPc is in the reduced -1 state on nitrogen pairs in nitrogen-doped graphene.[74] Using DFT, we have shown that high charge transfer from the nitrogen pair to the CoPc molecule shifts the LUMO of the CoPc molecule below the Fermi level, a signature of the reduction reaction. This explains the experimental $\mathrm{d}I/\mathrm{d}V$ spectra, where they have found that the LUMO of the CoPc molecule shifts to below the Fermi level when deposited on N-pairs in graphene.

In another work on F_4TCNQ, we have used F_4TCNQ to dope black phosphorene (BP). Black phosphorene has gained major popularity owing to its spectacular electronic properties, which are ideal for technological applications. One can tune the electron properties of the black phosphorene by chemical doping[75;76], defect creation[77;78], applying external electric field[57] or by applying bi-axial or uni-axial strain.[79;80] In Chapter 6, we have shown that one can tune the electronic ans magnetic properties of BP by using molecular doping combined with application of an external electric field. Unlike defect creation and chemical functionalization, our approach for tuning the electronic properties is advantageous because molecular doping does not damage the phosphorene's structure. Using DFT calculations, we have shown that an external negative electric field can induce magnetism in the F_4TCNQ/BP system. This can be explained in terms of the splitting of the impurity band introduced by the molecule. F_4TCNQ creates *p*-type doping in the BP by introducing a band (corresponding to its LUMO) in the band gap of BP which gets split into one unoccupied spin down (SUMO) band and one partially occupied spin up (SOMO) band at negative electric fields. We have also shown that the electronic and magnetic properties of this system will evolve in interesting ways as the temperature increases.

In addition to this, we have also explained a puzzle regarding the origin of unidirectional streaks that were found in STM images of this system. These streaks are found to occur along the zigzag direction but not the armchair direction.[73] We have found that the diffusion barrier for F_4TCNQ on phosphorene is highly anisotropic, being low/high along the zigzag/armchair directions. Thus the features observed in STM images can be explained as arising from the diffusion of F_4TCNQ molecules along the zigzag direction during the scan time.

In the second part of this thesis, we have studied defects in a two-dimensional material. Few-layer phosphorene has gained enormous popularity among 2D materials because both the band gap and charge carrier mobility can be tuned by varying the thickness (numer of layers). This makes few-layer phosphorene a potential candidate for use in electronic and photonic devices.[11;81] The presence of various defects causes different changes in the electronic properties, and hence these can be exploited (or may be disadvantageous) for different possible applications. For example, a divacancy reduces the carrier mobility due to increased electron-hole recombination and therefore impairs the performance of electronic devices.[75] Therefore, it is crucial to understand the nature and impact of the presence of different kinds of defects. In Chapter 7, we have built up a library of several kinds of defects and their simulated STM images. Some of these simulated images are in good agreement with experiments. For example, STM experiments performed by Prof. Lagoute and his team on few-layer black phosphorene show a unique dumbbell shape; this feature displays a change of contrast and shape upon reversal of the bias potential.[73] The origin of this feature remains a puzzle. Previously, other groups also tried to address the same problem of the origin of this ubiquitous feature, but could not find entirely satisfactory solutions.[82;83] We show that a Sn substitutional defect can explain the shape and change of contrast observed in these STM experiments. We have also developed a simple post-processing technique that provides insight into the origin of features such as these in STM images.

In addition to this, a second kind of feature has also been observed in the STM experiments, which inititally shows a bright circular shape but changes to a dumbbell shape after being subjected to an electric pulse.[73] However, this dumbbell shape differs from the 'native' dumbbell shape (the dumbbell which was there even before applying the pulse). Using DFT, we have shown that this second kind of feature arises from the presence of a Sn intercalation defect. To understand the effect of the electric pulse, we have also proposed a mechanism where the Sn intercalation defect changes to a third kind of Sn defect, Sn-2 + P-adatom (Sn substituted in the lower sub-layer of the topmost layer + a P atom adsorbed on the upper sub-layer over the Sn atom) owing to the breaking of Sn-P bond, due to the effect of an external electric pulse. Our STM simulation results for this third kind of Sn defect also show a dumbbell shape and at the same time, some difference from the ‘native’ dumbbell, as in the STM experiments.

In Chapter 8, the conclusions of each chapter are summarized and possible directions for future work are discussed.

Bibliography

[1] H. Liu, A. T. Neal, Z. Zhu, Z. Luo, X. Xu, D. Tománek, and P. D. Ye, "Phosphorene: an unexplored 2D semiconductor with a high hole mobility," *ACS Nano*, vol. 8, p. 4033, 2014.

[2] W. Lu, H. Nan, J. Hong, Y. Chen, C. Zhu, Z. Liang, X. Ma, Z. Ni, C. Jin, and Z. Zhang, "Plasma-assisted fabrication of monolayer phosphorene and its raman characterization," *Nano Res.*, vol. 7, p. 853, 2014.

[3] S. Cahangirov, M. Topsakal, E. Aktürk, H. Şahin, and S. Ciraci, "Two-and one-dimensional honeycomb structures of silicon and germanium," *Phys. Rev. Lett.*, vol. 102, p. 236804, 2009.

[4] L. Li, Y. Yu, G. J. Ye, Q. Ge, X. Ou, H. Wu, D. Feng, X. H. Chen, and Y. Zhang, "Black phosphorus field-effect transistors," *Nat. Nanotechnol.*, vol. 9, p. 372, 2014.

[5] L. Ci, L. Song, C. Jin, D. Jariwala, D. Wu, Y. Li, A. Srivastava, Z. Wang, K. Storr, L. Balicas, *et al.*, "Atomic layers of hybridized boron nitride and graphene domains," *Nat. Mater*, vol. 9, p. 430, 2010.

[6] K. S. Novoselov, V. Fal, L. Colombo, P. Gellert, M. Schwab, K. Kim, *et al.*, "A roadmap for graphene," *Nature*, vol. 490, p. 192, 2012.

[7] A. K. Geim and I. V. Grigorieva, “van der Waals heterostructures,” *Nature*, vol. 499, p. 419, 2013.

[8] V. Gusynin and S. Sharapov, “Unconventional integer quantum Hall effect in graphene,” *Phys. Rev. Lett.*, vol. 95, p. 146801, 2005.

[9] Y. Zhang, Y.-W. Tan, H. L. Stormer, and P. Kim, “Experimental observation of the quantum Hall effect and Berry’s phase in graphene,” *Nature*, vol. 438, p. 201, 2005.

[10] J. H. Chen, C. Jang, S. Xiao, M. Ishigami, and M. S. Fuhrer, “Intrinsic and extrinsic performance limits of graphene devices on SiO_2,” *Nat. Nanotechnol*, vol. 3, p. 206, 2008.

[11] J. Qiao, X. Kong, Z.-X. Hu, F. Yang, and W. Ji, “High-mobility transport anisotropy and linear dichroism in few-layer black phosphorus,” *Nat. Commun.*, vol. 5, p. 4475, 2014.

[12] A. N. Rudenko, S. Yuan, and M. I. Katsnelson, “Toward a realistic description of multilayer black phosphorus: From *gw* approximation to large-scale tight-binding simulations,” *Phys. Rev. B*, vol. 92, p. 085419, 2015.

[13] Y. Cai, G. Zhang, and Y.-W. Zhang, “Layer-dependent band alignment and work function of few-layer phosphorene,” *Sci. Rep.*, vol. 4, p. 6677, 2014.

[14] M. Chander, Y. Z. Li, D. Rioux, and J. H. Weaver, “Pattern of Si(100): Spontaneous etching with Br_2,” *Phys. Rev. Lett.*, vol. 71, p. 4154, 1993.

[15] Y. Cui and C. M. Lieber, “Functional nanoscale electronic devices assembled using silicon nanowire building blocks,” *Science*, vol. 291, p. 851, 2001.

[16] J. Chai, D. Wang, X. Fan, and J. M. Buriak, “Assembly of aligned linear metallic patterns on silicon,” *Nat. Nanotechnol*, vol. 2, p. 500, 2007.

[17] H. Kroto, J. Heath, S. C. O'Brien, R. F. Curl, and R. Smalley, "C_{60}: Buckminsterfullerene," *Nature*, vol. 318, p. 22, 1985.

[18] W. A. De Heer, "The physics of simple metal clusters: experimental aspects and simple models," *Rev. Mod. Phys.*, vol. 65, p. 611, 1993.

[19] S. Ijima, "Helical microtubes of graphitic carbon," *Nature*, vol. 354, p. 56, 1991.

[20] H. Ohnishi, Y. Kondo, and K. Takayanagi, "Quantized conductance through individual rows of suspended gold atoms," *Nature*, vol. 395, p. 780, 1998.

[21] X. Li, X. Wang, L. Zhang, S. Lee, and H. Dai, "Chemically derived, ultrasmooth graphene nanoribbon semiconductors," *Science*, vol. 319, p. 1229, 2008.

[22] J. Cai, P. Ruffieux, R. Jaafar, M. Bieri, T. Braun, S. Blankenburg, M. Muoth, A. P. Seitsonen, M. Saleh, X. Feng, *et al.*, "Atomically precise bottom-up fabrication of graphene nanoribbons," *Nature*, vol. 466, p. 470, 2010.

[23] K. S. Novoselov, A. K. Geim, S. V. Morozov, D. Jiang, M. I. Katsnelson, I. V. Grigorieva, S. V. Dubonos, and A. A. Firsov, "Two-dimensional gas of massless Dirac fermions in graphene," *Nature*, vol. 438, p. 197, 2005.

[24] J. Tersoff, "Surface-confined alloy formation in immiscible systems," *Phys. Rev. Lett.*, vol. 74, p. 434, 1995.

[25] Y. Nakae, Y. Seino, T. Teranishi, M. Miyake, S. Yamada, and H. Hori, "Anomalous spin polarization in pd and au nano-particles," *Physica B: Condensed Matter*, vol. 284-288, p. 1758, 2000.

[26] A. Aviram and M. A. Ratner, "Molecular rectifiers," *Chem. Phys. Lett.*, vol. 29, p. 277, 1974.

[27] C. Joachim, J. K. Gimzewski, and A. Aviram, “Electronics using hybrid-molecular and mono-molecular devices,” *Nature*, vol. 408, p. 541, 2000.

[28] E. G. Emberly and G. Kirczenow, “Molecular spintronics: spin-dependent electron transport in molecular wires,” *Chem. Phys.*, vol. 281, p. 311, 2002.

[29] A. R. Rocha, V. M. García-Suárez, S. Bailey, C. J. Lambert, J. Ferrer, and S. Sanvito, “Towards molecular spintronics,” *Nat. Mater*, vol. 4, p. 335, 2005.

[30] K. Moth-Poulsen and T. Bjørnholm, “Molecular electronics with single molecules in solid-state devices,” *Nat. Nanotechnol*, vol. 4, p. 551, 2009.

[31] A. Fert, “Nobel lecture: Origin, development, and future of spintronics,” *Rev. Mod. Phys.*, vol. 80, p. 1517, 2008.

[32] G. Binnig and H. Rohrer, “Scanning tunneling microscopy,” *Surf. Sci.*, vol. 126, p. 236, 1983.

[33] G. Binnig, H. Rohrer, C. Gerber, and E. Weibel, “Surface studies by scanning tunneling microscopy,” *Phys. Rev. Lett.*, vol. 49, p. 57, 1982.

[34] M. F. Crommie, C. P. Lutz, and D. M. Eigler, “Confinement of electrons to quantum corrals on a metal surface,” *Science*, vol. 262, p. 218, 1993.

[35] P. Hohenberg and W. Kohn, “Inhomogeneous electron gas,” *Phys. Rev.*, vol. 136, p. B864, 1964.

[36] W. Kohn and L. J. Sham, “Self-consistent equations including exchange and correlation effects,” *Phys. Rev.*, vol. 140, p. A1133, 1965.

[37] A. Rahman, “Correlations in the motion of atoms in liquid argon,” *Phys. Rev.*, vol. 136, p. A405, 1964.

[38] D. M. Ceperley, "Path integrals in the theory of condensed helium," *Rev. Mod. Phys.*, vol. 67, p. 279, 1995.

[39] M. Garnica, D. Stradi, S. Barja, F. Calleja, C. Díaz, M. Alcamí, N. Martín, A. L. V. de Parga, F. I. Martín, and R. Miranda, "Long-range magnetic order in a purely organic 2D layer adsorbed on epitaxial graphene," *Nat. Phys.*, vol. 9, p. 368, 2013.

[40] F. Al MáMari, T. Moorsom, G. Teobaldi, W. Deacon, T. Prokscha, H. Luetkens, S. Lee, G. E. Sterbinsky, D. A. Arena, D. A. MacLaren, *et al.*, "Beating the Stoner criterion using molecular interfaces," *Nature*, vol. 524, p. 69, 2015.

[41] J. V. Barth, H. Brune, G. Ertl, and R. Behm, "Scanning tunneling microscopy observations on the reconstructed Au (111) surface: Atomic structure, long-range superstructure, rotational domains, and surface defects," *Phys. Rev. B*, vol. 42, p. 9307, 1990.

[42] K. Huang, D. Gibbs, D. Zehner, A. Sandy, and S. Mochrie, "Phase behavior of the Au (111) surface: Discommensurations and kinks," *Phys. Rev. Lett.*, vol. 65, p. 3313, 1990.

[43] A. Sandy, S. Mochrie, D. Zehner, K. Huang, and D. Gibbs, "Structure and phases of the Au (111) surface: X-ray-scattering measurements," *Phys. Rev. B*, vol. 43, p. 4667, 1991.

[44] S. Narasimhan and D. Vanderbilt, "Elastic stress domains and the herringbone reconstruction on au (111)," *Phys. Rev. Lett.*, vol. 69, p. 1564, 1992.

[45] K. S. Novoselov, A. K. Geim, S. V. Morozov, D. Jiang, Y. Zhang, S. V. Dubonos, I. V. Grigorieva, and A. A. Firsov, "Electric field effect in atomically thin carbon films," *Science*, vol. 306, p. 666, 2004.

[46] P. Avouris, “Graphene: electronic and photonic properties and devices,” *Nano Lett.*, vol. 10, p. 4285, 2010.

[47] F. Schwierz, “Graphene transistors,” *Nature Nanotechnol.*, vol. 5, p. 487, 2010.

[48] Y. W. Son, M. L. Cohen, and S. G. Louie, “Half-metallic graphene nanoribbons,” *Nature*, vol. 444, p. 347, 2006.

[49] Y. Zhang, T.-T. Tang, C. Girit, Z. Hao, M. C. Martin, A. Zettl, M. F. Crommie, Y. R. Shen, and F. Wang, “Direct observation of a widely tunable bandgap in bilayer graphene,” *Nature*, vol. 459, p. 820, 2009.

[50] H. Liu, Y. Liu, and D. Zhu, “Chemical doping of graphene,” *J. Mater. Chem.*, vol. 21, p. 3335, 2011.

[51] G. Li, A. Luican, J. L. Dos Santos, A. C. Neto, A. Reina, J. Kong, and E. Andrei, “Observation of van Hove singularities in twisted graphene layers,” *Nat. Phys.*, vol. 6, p. 109, 2010.

[52] L. Li, Y. Yu, G. J. Ye, Q. Ge, X. Ou, H. Wu, D. Feng, X. H. Chen, and Y. Zhang, “Black phosphorus field-effect transistors,” *Nat. Nanotechnol*, vol. 9, p. 372, 2014.

[53] M. Buscema, D. J. Groenendijk, G. A. Steele, H. S. Van Der Zant, and A. Castellanos-Gomez, “Photovoltaic effect in few-layer black phosphorus pn junctions defined by local electrostatic gating,” *Nat. Commun.*, vol. 5, p. 4651, 2014.

[54] J. A. Real, A. B. Gaspar, and M. C. Muñoz, “Thermal, pressure and light switchable spin-crossover materials,” *Dalton Trans.*, p. 2062, 2005.

[55] A. Bousseksou, G. Molnár, L. Salmon, and W. Nicolazzi, “Molecular spin crossover phenomenon: recent achievements and prospects,” *Chem. Soc. Rev.*, vol. 40, p. 3313, 2011.

[56] C. Lefter, V. Davesne, L. Salmon, G. Molnár, P. Demont, A. Rotaru, and A. Bousseksou, “Charge Transport and Electrical Properties of Spin Crossover Materials: Towards Nanoelectronic and Spintronic Devices,” *Magnetochemistry*, vol. 2, p. 18, 2016.

[57] Y. Jing, Q. Tang, P. He, Z. Zhou, and P. Shen, “Small molecules make big differences: molecular doping effects on electronic and optical properties of phosphorene,” *Nanotechnology*, vol. 26, p. 095201, 2015.

[58] H. Pinto, R. Jones, J. Goss, and P. Briddon, “p-type doping of graphene with F4-TCNQ,” *J. Phys: Condens. Matter*, vol. 21, p. 402001, 2009.

[59] G. F. Manbeck and E. Fujita, “A review of iron and cobalt porphyrins, phthalocyanines and related complexes for electrochemical and photochemical reduction of carbon dioxide,” *J. Porphyr. Phthalocya.*, vol. 19, p. 45, 2015.

[60] Z. Zhang, J. Xiao, X.-J. Chen, S. Yu, L. Yu, R. Si, Y. Wang, S. Wang, X. Meng, Y. Wang, *et al.*, “Reaction mechanisms of well-defined metal–N4 sites in electrocatalytic CO_2 reduction,” *Angew. Chem. Int. Ed.*, vol. 57, p. 16339, 2018.

[61] D.-H. Nam, P. De Luna, A. Rosas-Hernández, A. Thevenon, F. Li, T. Agapie, J. C. Peters, O. Shekhah, M. Eddaoudi, and E. H. Sargent, “Molecular enhancement of heterogeneous CO_2 reduction,” *Nat. Mater.*, vol. 19, p. 266, 2020.

[62] M. Zhu, C. Cao, J. Chen, Y. Sun, R. Ye, J. Xu, and Y.-F. Han, “Electronic tuning of cobalt porphyrins immobilized on nitrogen-doped graphene for CO_2 reduction,” *ACS Appl. Energy Mater.*, vol. 2, p. 2435, 2019.

[63] C. Fourmental, S. Mondal, R. Banerjee, A. Bellec, Y. Garreau, A. Coati, C. Chacon, Y. Girard, J. Lagoute, S. Rousset, M.-L. Boillot, T. Mallah, C. Enachescu, C. Barreteau, Y. J. Dappe, A. Smogunov, S. Narasimhan, and V. Repain, “Importance of epitaxial strain at a spin-crossover molecule–metal interface,” *J. Phys. Chem. Lett.*, vol. 10, p. 4103, 2019.

[64] S. Grimme, “Accurate description of van der waals complexes by density functional theory including empirical corrections,” *J. Comput. Chem.*, vol. 25, p. 1463, 2004.

[65] S. Grimme, “Semiempirical GGA-type density functional constructed with a long-range dispersion correction,” *J. Comput. Chem.*, vol. 27, p. 1787, 2006.

[66] V. I. Anisimov, J. Zaanen, and O. K. Andersen, “Band theory and mott insulators: Hubbard U instead of Stoner i,” *Phys. Rev. B*, vol. 44, p. 943, 1991.

[67] A. I. Liechtenstein, V. I. Anisimov, and J. Zaanen, “Density-functional theory and strong interactions: Orbital ordering in Mott-Hubbard insulators,” *Phys. Rev. B*, vol. 52, p. R5467, 1995.

[68] V. I. Anisimov, I. V. Solovyev, M. A. Korotin, M. T. Czyżyk, and G. A. Sawatzky, “Density-functional theory and Nio photoemission spectra,” *Phys. Rev. B*, vol. 48, p. 16929, 1993.

[69] J. Tersoff and D. R. Hamann, “Theory of the scanning tunneling microscope,” *Phys. Rev. B*, vol. 31, p. 805, 1985.

[70] K. Bairagi, A. Bellec, C. Fourmental, O. Iasco, J. Lagoute, C. Chacon, Y. Girard, S. Rousset, F. Choueikani, E. Otero, P. Ohresser, P. Sainctavit, M.-L. Boillot, T. Mallah, and V. Repain, “Temperature, Light, and Soft X-ray-induced Spin crossover in a Single Layer of $\mathrm{Fe}^{\mathrm{II}}$-Pyrazolylborate Molecules in Direct Contact with Gold,” *J. Phys. Chem. C*, vol. 122, p. 727, 2018.

[71] K. Bairagi, O. Iasco, A. Bellec, A. Kartsev, D. Li, J. Lagoute, C. Chacon, Y. Girard, S. Rousset, F. Miserque, Y. J. Dappe, A. Smogunov, C. Barreteau, M.-L. Boillot, T. Mallah, and V. Repain, "Molecular-scale dynamics of light-induced spin cross-over in a two-dimensional layer," *Nat. Comm.*, vol. 7, p. 12212, 2016.

[72] H.-Z. Tsai, A. A. Omrani, S. Coh, H. Oh, S. Wickenburg, Y.-W. Son, D. Wong, A. Riss, H. S. Jung, G. D. Nguyen, *et al.*, "Molecular self-assembly in a poorly screened environment: F4TCNQ on graphene/BN," *ACS Nano*, vol. 9, p. 12168, 2015.

[73] R. Harsh, *Electronic interaction of organic molecules with low dimensional materials: a scanning tunneling microscopy study on graphene and black phosphorus.* Université de Paris, 2019.

[74] M. Bouatou, S. Mondal, C. Chacon, F. Joucken, Y. Girard, V. Repain, A. Bellec, S. Rousset, S. Narasimhan, R. Sporken, Y. J. Dappe, and J. Lagoute, "Direct observation of the reduction of a molecule on nitrogen pairs in doped graphene," *Nano Lett.*, vol. 20, p. 6908, 2020.

[75] V. Wang, Y. Kawazoe, and W. Geng, "Native point defects in few-layer phosphorene," *Phys. Rev. B*, vol. 91, p. 045433, 2015.

[76] X. Peng and Q. Wei, "Chemical scissors cut phosphorene nanostructures," *Mater. Res. Express*, vol. 1, p. 045041, 2014.

[77] T. Hu and J. Dong, "Geometric and electronic structures of mono-and divacancies in phosphorene," *Nanotechnology*, vol. 26, p. 065705, 2015.

[78] Y. Guo and J. Robertson, "Vacancy and doping states in monolayer and bulk black phosphorus," *Sci. Rep.*, vol. 5, p. 14165, 2015.

[79] X. Peng, Q. Wei, and A. Copple, “Strain-engineered direct-indirect band gap transition and its mechanism in two-dimensional phosphorene,” *Phys. Rev. B*, vol. 90, p. 085402, 2014.

[80] A. Carvalho, A. S. Rodin, and A. H. Castro Neto, “Phosphorene Nanoribbons Cornell univ,” 2014.

[81] V. Tran, R. Soklaski, Y. Liang, and L. Yang, “Layer-controlled band gap and anisotropic excitons in few-layer black phosphorus,” *Phys. Rev. B*, vol. 89, p. 235319, 2014.

[82] Z. Qiu, H. Fang, A. Carvalho, A. Rodin, Y. Liu, S. J. Tan, M. Telychko, P. Lv, J. Su, Y. Wang, *et al.*, “Resolving the spatial structures of bound hole states in black phosphorus,” *Nano Lett.*, vol. 17, p. 6935, 2017.

[83] B. Kiraly, N. Hauptmann, A. N. Rudenko, M. I. Katsnelson, and A. A. Khajetoorians, “Probing single vacancies in black phosphorus at the atomic level,” *Nano Lett.*, vol. 17, p. 3607, 2017.

Chapter 2

Methods and Formalism

In this thesis, I have primarily used density functional theory (DFT) to solve diverse problems. In this chapter, I will briefly review the formalism underlying this approach.

2.1 The Schrödinger Equation and Many-Body Problem

In principle, one can get any desired information about a material by solving the relevant many-body Schrödinger equation:

$$\hat{H}\Psi(\mathbf{R},\mathbf{r}) = E\Psi(\mathbf{R},\mathbf{r}). \tag{2.1}$$

Here, Ψ is the wavefunction of all the participating particles, i.e, electrons and nuclei; it is a function of all the nuclear coordinates $\{\mathbf{R}\}$ and all the electronic coordinates $\{\mathbf{r}\}$. $\hat{H}$ is the many-body Hamiltonian operator,[1] which can be written as:

$$\hat{H} = -\frac{1}{2M_I}\sum_I \nabla_I^2 - \frac{1}{2}\sum_i \nabla_i^2 + \frac{1}{2}\sum_{I\neq J}\frac{Z_I Z_J}{|\mathbf{R}_I - \mathbf{R}_J|} - \sum_{i,I}\frac{Z_I}{|\mathbf{r}_i - \mathbf{R}_I|} + \frac{1}{2}\sum_{i\neq j}\frac{1}{|\mathbf{r}_i - \mathbf{r}_j|}, \tag{2.2}$$

where $\mathbf{R}_I$, M_I and Z_I are the position, mass and the atomic number of the I^{th} nucleus. Similarly, $\mathbf{r}_i$ is an electronic position. It is standard practice to set $\hbar = e = m_e = 4\pi\epsilon_0 = 1$, as has been done in the equation above. Note that I will exercise this convention throughout my thesis. $\hbar$ is Planck's constant divided by 2π. One can rewrite Eq. (2.2) as:

$$\hat{H} = \hat{H}_{k,n} + \hat{H}_{k,e} + \hat{H}_{p,n-n} + \hat{H}_{p,n-e} + \hat{H}_{p,e-e} \tag{2.3}$$

$\hat{H}_{k,n}$ and $\hat{H}_{k,e}$ are the kinetic energy operators for the nuclei and electrons. $\hat{H}_{p,n-n}$, $\hat{H}_{p,n-e}$ and $\hat{H}_{p,e-e}$ are the potential energy operators for the nucleus–nucleus interaction, nucleus–electron interaction and electron–electron interaction. Except for a few special cases, it is impossible to solve Eq. (2.1) exactly and analytically for interacting many-body systems. Therefore we need to invoke various approximations to make it solvable. I discuss a few of them in the sections below.

2.1.1 The Born-Oppenheimer Approximation

Within this approximation, one can decouple the electronic degrees of freedom from the nuclear degrees of freedom, because electrons being much lighter, move much faster than the nuclei.[2] So for a given set of nuclear positions, the electrons adjust their position almost instantaneously, i.e., before the nuclei move. Hence we can separate the nuclear and electronic coordinates:

$$\Psi(\mathbf{R}, \mathbf{r}) = \Psi_n(\mathbf{R})\Psi_e. \tag{2.4}$$

This approximation simplifies the many-body electronic Schrödinger equation into the form[3] shown below:

$$(\hat{H}_{k,e} + \hat{H}_{p,n-e} + \hat{H}_{p,e-e})\Psi_e(\mathbf{R}, \mathbf{r}) = E_e(\mathbf{R})\Psi_e(\mathbf{R}, \mathbf{r}) \tag{2.5}$$

The second term on the left-hand-side of Eq. (2.5) tells us that the electrons are experiencing the effects of the nuclear positions only through the electrostatic interactions between the electrons and the nuclei. In the Born-Oppenheimer approximation,[2] we solve Eq. (2.5) for a set of nuclear positions and then calculate the total energy using the following equation:

$$E = E_e(\mathbf{R}) + \frac{1}{2}\sum_{I \neq J} \frac{Z_I Z_J}{|\mathbf{R}_I - \mathbf{R}_J|}. \tag{2.6}$$

Subsequently, we could do the same for a second set of nuclear positions, which leads to a new value for the total energy. By doing this repeatedly, we can ultimately we hope to determine the ground state structure, i.e., the particular set of nuclear positions that gives the lowest energy according to Eq. (2.6).

2.1.2 Density Functional Theory

So far, we have seen that the solution of the many-body Schrödinger equation of the N-electron system depends on $3N$ position-space coordinates and N spin coordinates. Therefore, Ψ_e is an extremely complicated function even for a small molecule like water or methane, which suggests that it is nearly impossible to solve the many-body Schrödinger equation. The unparalleled success of density functional theory (DFT) comes in this context, which simplifies the problem by mapping the solution in terms of the $3N$-dimensional electronic wavefunction, into a solution instead of the 3-dimensional electron density. Hence, in explaining the properties of the material, it is unnecessary to compute the complicated many-body electronic wavefunction Ψ_e; instead, we can get the same information by solving another equation, which is a functional of the electron density $n(\mathbf{r})$. The formalism of DFT is built on two underlying principles which we discuss in the following two sections, viz., the Hohenberg-Kohn Theorems[4] and the Kohn-Sham Ansatz.[5]

Hohenberg-Kohn Theorems

The entire field of DFT stands upon two fundamental theorems given by Hohenberg and Kohn (HK).[4]

Theorem I: For any system of interacting particles in an external potential $V_{ext}(\mathbf{r})$, the potential $V_{ext}(\mathbf{r})$ is determined uniquely, up to an additive constant, by the ground state particle density $n_0(\mathbf{r})$.[1]

This theorem states that once we know the ground state electron density, we can construct the term V_{ext} as well as the other terms in the Hamiltonian operator. Then, solving the Schrödinger equation can give us the N-electron wavefunction of the ground-state, from which we can compute any desired property.

Theorem II: A universal functional for the energy $E[n]$ in terms of $n(\mathbf{r})$ can be defined, valid for any external potential $V_{ext}(\mathbf{r})$. For any particular $V_{ext}(\mathbf{r})$, the exact ground state energy of the system is the global minimum value of this functional, and the density $n(\mathbf{r})$ that minimizes the functional is the exact ground state density $n_0(\mathbf{r})$.[1]

The second HK theorem states that we can define the total energy $E[n]$, which is a functional of the density $n(\mathbf{r})$. This can be written as:[6]

$$E[n] = F[n] + \int V_{ext}(\mathbf{r})n(\mathbf{r})d\mathbf{r}, \tag{2.7}$$

with a universal functional $F[n]$:

$$F[n] = \big\langle \Psi_e(n) | \hat{H}_{k,e} + \hat{H}_{p,e-e} | \Psi_e(n) \big\rangle. \tag{2.8}$$

$F[n]$ depends on the kinetic energy of the electrons and the potential energy due to the electron-electron interaction. Minimizing Eq. (2.7) with respect to $n(\mathbf{r})$ enables us to find the ground state energy and the ground state electronic density.

However, the real challenge of the DFT is that we don't know the exact functional form of $F[n]$. The accuracy of the method depends on how good are the approximations that can be made for the functional $F[n]$. An ansatz proposed by Kohn and Sham deals wonderfully with this problem, which has made DFT very much popular in the community.

Kohn-Sham Ansatz

The ansatz[5] simplifies the many-body problem by mapping a system of N interacting particles onto a system of N non-interacting particles. The idea was that if one can find a system of N non-interacting electrons which can produce the same electron density as of N interacting electrons, the total energy of the system can be expressed as follows:

$$E_{KS}[n] = T[n] + \frac{1}{2}\int \frac{n(\mathbf{r})n(\mathbf{r}')}{|\mathbf{r}-\mathbf{r}'|}d\mathbf{r}d\mathbf{r}' + \int V_{ext}(\mathbf{r})n(\mathbf{r})d\mathbf{r} + E_{xc}[n]. \tag{2.9}$$

$T[n]$, the kinetic energy of the single-particle non-interacting system can be expressed using Eq. (2.10) below,

$$T[n] = -\frac{1}{2}\sum_{i}^{N}\langle\psi_i|\nabla^2|\psi_i\rangle, \tag{2.10}$$

where ψ_i is the single-particle orbital or Kohn-Sham orbital[1] which can be filled up following Pauli's exclusion principle. $\frac{1}{2}\int \frac{n(\mathbf{r})n(\mathbf{r}')}{|\mathbf{r}-\mathbf{r}'|}d\mathbf{r}d\mathbf{r}'$ is the Hartree term or E_H, arising due to Coulombic repulsion of the electron density with itself. The interaction between nuclei and electrons can be replaced by an external potential V_{ext}. $E_{xc}[n]$ is the exchange-correlation energy that accounts for the kinetic energy difference between the many-electron interacting system and the N single-electron non-interacting system, and also the residual energy contributions due to the exchange asymmetry and correlations.

Comparing Eq. (2.7) with Eq. (2.9), we can rewrite the universal functional in the following way:

$$F_{KS}[n] = T[n] + \frac{1}{2}\int \frac{n(\mathbf{r})n(\mathbf{r}')}{|\mathbf{r}-\mathbf{r}'|}d\mathbf{r}d\mathbf{r}' + E_{xc}[n]. \tag{2.11}$$

Alternatively, we can write the Kohn-Sham equations in the form of the Schrödinger equation as follows:[5]

$$\left\{ -\frac{1}{2}\nabla^2 + V_{\mathrm{KS}}(\mathbf{r}) \right\}\psi_i(\mathbf{r}) = \epsilon_i\psi_i(\mathbf{r}), \tag{2.12}$$

where

$$V_{\mathrm{KS}}(\mathbf{r}) = V_H(\mathbf{r}) + V_{xc}(\mathbf{r}) + V_{ext}(\mathbf{r}). \tag{2.13}$$

Here ϵ_i is the one-electron energy, $V_H(\mathbf{r}) = \frac{\delta E_H}{\delta n(\mathbf{r})}$ is the Hartree potential and $V_{xc}(\mathbf{r}) = \frac{\delta E_{xc}}{\delta n(\mathbf{r})}$ is the exchange-correlation potential. To solve Eq. (2.12), we need the potential V_{KS}. Since the potential V_{KS} depends on $n(\mathbf{r})$, which is however what we are solving for, it needs to be found self-consistently, with the resulting density given as:

$$n(\mathbf{r}) = 2\sum_{s=1}^{N/2} |\psi_i(\mathbf{r})|^2. \tag{2.14}$$

A flowchart describing the self-consistent procedure to solve Eqs. (2.12)- (2.14) has been shown in Fig. 2.1.

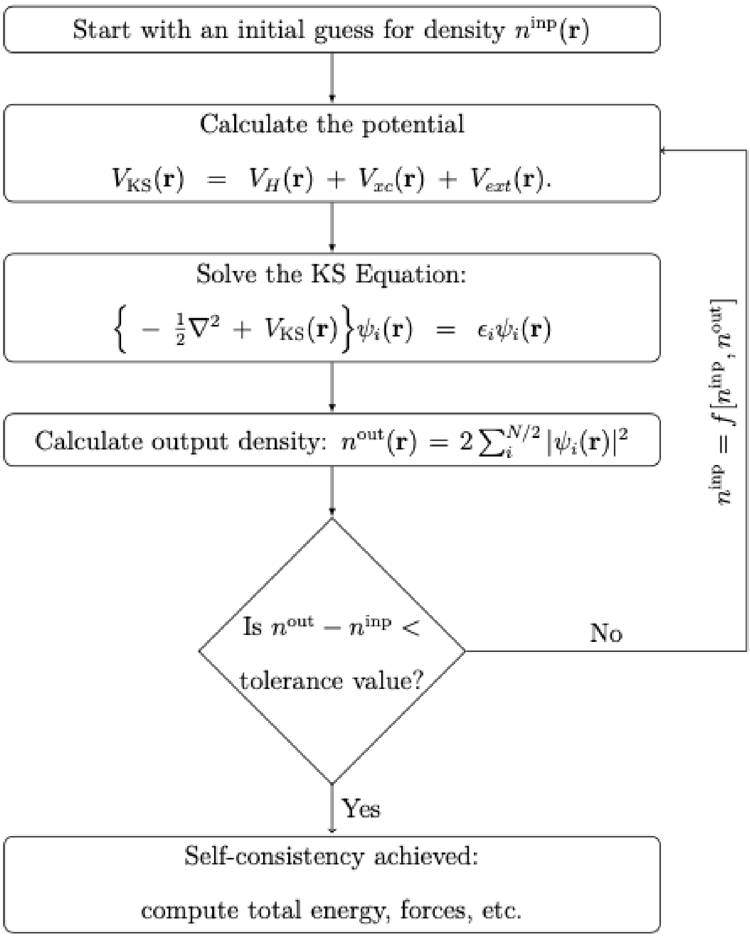
Start with an initial guess for density $n^{\text{inp}}(\mathbf{r})$
Calculate the potential
$V_{\text{KS}}(\mathbf{r}) = V_H(\mathbf{r}) + V_{xc}(\mathbf{r}) + V_{ext}(\mathbf{r})$.
Solve the KS Equation:
$\left\{ -\frac{1}{2}\nabla^2 + V_{\text{KS}}(\mathbf{r}) \right\} \psi_i(\mathbf{r}) = \epsilon_i \psi_i(\mathbf{r})$
Calculate output density: $n^{\text{out}}(\mathbf{r}) = 2\sum_i^{N/2} |\psi_i(\mathbf{r})|^2$
Is $n^{\text{out}} - n^{\text{inp}} <$
tolerance value?
No
$n^{\text{inp}} = f[n^{\text{inp}}, n^{\text{out}}]$
Yes
Self-consistency achieved:
compute total energy, forces, etc.

Figure 2.1: Flow chart showing the self-consistency loop for the iterative solution of the KS equation. Superscripts indicate the iteration.

2.1.3 Exchange-Correlation Functional

The exchange-correlation potential (V_{xc}) is the only big unknown when writing down the form of the Hamiltonian for the Kohn-Sham equations. Unfortunately, we need this term to account for all the many-body effects in the system. Electrons are fermions by nature. Electrons with the same spin repel each other and want to stay apart from each other. This spatial separation causes extra stabilization to the system (due to the reduction of the Coulomb energy), which is known as the exchange energy. The correlation is a complicated quantity that is the result of many-body interactions among the electrons, where electrons try to reduce the Coulomb repulsion by screening themselves. The correlation energy is defined as the difference between the exact energy of the many-body system and its energy as calculated by the Hartree-Fock approximation.

It is impossible to calculate the exact form of the exchange-correlation potential, although there are several approximations available, which I discuss in the next two paragraphs.

Local Density Approximation

This is the simplest method of describing the exchange-correlation energy. In the local density approximation (LDA),[7–9] the exchange-correlation energy of the electronic system is constructed by assuming that exchange and correlation are purely local in nature as a functional of the electron density. According to this approximation, the exchange-correlation energy can be written as:

$$E_{xc}^{LDA} = \int n(\mathbf{r})\epsilon_{xc}^{hom}\big(n(\mathbf{r})\big)d\mathbf{r}, \tag{2.15}$$

where $\epsilon_{xc}^{hom}(n)$ is the exchange-correlation energy per particle of an interacting homogeneous electron gas at the density $n(\mathbf{r})$. $\epsilon_{xc}^{hom}\big(n(\mathbf{r})\big)$ has been calculated, e.g., using Quantum Monte Carlo simulations.[8] Several parametrizations also exist for the form of the exchange-correlation functional in the LDA. One of the most popular is by Perdew and Zunger.[10] Though the LDA works surprisingly well for many systems, it has a tendency to overbind.

Generalized Gradient Approximations

In a real system, it is not necessarily true that the electron density is always homogeneous. In fact, in most of the cases it is inhomogeneous. In order to capture the non-local nature of the electron density, one considers the gradient of the density with its local density, which is known as the generalized gradient approximation (GGA).[11;12] The exchange correlation energy for a GGA functional can be expressed as:

$$E_{xc}^{\mathrm{GGA}} = \int d\mathbf{r}\; n(\mathbf{r})\epsilon_{xc}\big(n(\mathbf{r}), |\nabla n(\mathbf{r})|\big), \tag{2.16}$$

where $\epsilon_{xc}(n(\mathbf{r}), |\nabla n(\mathbf{r})|)$ is the exchange-correlation energy per electron, that depends on the local electron density $n(\mathbf{r})$ as well as the gradient of the density $|\nabla n(\mathbf{r})|$. Like LDA, several distinct forms of GGA functionals are available. Two of the most widely used forms are the Perdew-Burke-Ernzerhof functional (PBE)[11] and the Perdew-Wang functional (PW91).[12] The GGA usually corrects the over-binding problem of the LDA. However, the GGA is known to often underbind.

2.1.4 Plane Wave Basis Sets

In order to solve the Kohn-Sham equations, we often expand the Kohn-Sham orbitals, $\psi_i(\mathbf{r})$, in terms of a suitable basis set $\{\phi_j(\mathbf{r})\}$:

$$\psi_i(\mathbf{r}) = \sum_j c_j \phi_j(\mathbf{r}). \tag{2.17}$$

$\phi_j(\mathbf{r})$ can be of different types, such as plane waves,[13;14] localized atomic orbitals,[15] Muffin Tin Orbitals,[16] etc. In this thesis, we have used a plane wave basis set, which is briefly described below.

Bloch's theorem states that in a periodic system like a crystalline solid, the electronic wavefunction $\psi_\mathbf{i}$ can be written as:[17]

$$\psi_\mathbf{i}(\mathbf{r}) = f_i(\mathbf{r})e^{i\mathbf{k}.\mathbf{r}}, \tag{2.18}$$

where $f_i(\mathbf{r})$, which shows periodicity in terms of cell vectors, can be expanded using a discrete (in principle infinite) set of plane waves whose vectors are reciprocal lattice vectors of the crystal:

$$f_i(\mathbf{r}) = \sum_{\mathbf{G}} c_{i,\mathbf{G}} e^{i\mathbf{G}.\mathbf{r}}. \tag{2.19}$$

Combining Eq. (2.18) and (2.19), we can rewrite the electronic wavefunction as a sum of plane waves:

$$\psi_i(\mathbf{r}) = \sum_{\mathbf{G}} c_{i,\mathbf{k}+\mathbf{G}} e^{i(\mathbf{k}+\mathbf{G}).\mathbf{r}}. \tag{2.20}$$

The number of plane waves is determined by introducing a kinetic energy cutoff (E_{cut}), so that we retain only those plane waves $e^{i(\mathbf{k}+\mathbf{G}).\mathbf{r}}$, such that $(\hbar^2/2m_e)|\mathbf{k} + \mathbf{G}|^2 \leq E_{\text{cut}}$ (note that in the atomic units used in this thesis, $\hbar = m_e = 1$). One real advantage of using a plane wave basis set is that a single parameter, E_{cut}, controls the convergence of the basis set. However, if one tries to expand the wavefunctions in the core region using plane waves, one needs a massive number of plane waves, resulting in a high computational cost. This problem is resolved by the use of pseudopotentials, which are described below.

2.1.5 Pseudopotential Approximation

By Bloch's theorem, the Kohn-Sham wavefunctions for a periodic system can be expanded using a discrete set of plane waves. However, this is a poor choice of basis for all-electron calculations because a very large number of plane waves are required to expand the tightly-bound core electrons and to follow the rapid oscillations of valence wavefunctions near the core region; this costs a vast amount of computational time and memory, making such calculations prohibitively expensive.

It is a well-known fact that the physical and chemical properties of materials are primarily dependent on valence electrons. We are going to exploit this fact by replacing the tightly bound core electrons and the strong ionic potential by a weaker potential that acts on pseudo wavefunctions rather than true wavefunctions. This is known as the pseudopotential approximation.[18–20] In this way we can drastically reduce the computational expense. A good pseudopotetial should have the following properties:

1. *Smoothness:* the pseudo-wavefunctions and their first and second derivatives should match smoothly after a cutoff radius which separates core regions from the valence region.

2. *Transferability:* the same pseudopotential can be used in different chemical and structural environments.

3. *Softness:* It should require a low energy cutoff for the expansion using plane waves. The lower the cutoff, the softer it is.

In addition, it was believed that the pseudo wavefunction should possess the same norm (squared amplitude of the wavefunction) as the true wavefunction in both the core and valence regions to meet the good transferability criteria. This is known as the norm-conservation criterion.[19] However, norm-conserving pseudopotentials still require a fairly large number of plane waves, especially for those cases where the valence wavefunction is nodeless, such as for the elements in the first row of the periodic table. The condition of norm-conservation in the core region is relaxed in ultrasoft pseudopotentials,[20] and the computational cost is reduced further. Charge loss due to the relaxing of the norm-conserving condition is compensated for by adding an extra charge, known as the “augmentation charge", in the core region of the pseudopotential.

2.1.6 k-point Sampling and Smearing

Physical quantities such as the magnetic moment, the total energy, or the density of states are obtained by integrating over all the wavevectors (**k**) in the first Brillouin zone (1^{st} BZ). Numerically, the integration is performed using a finite mesh of **k**-points. The most commonly used **k**-point sampling method is a Monkhorst-Pack grid,[21] where the grid is generated using the formula:

$$\mathbf{k}_{n_1,n_2,n_3} = \sum_{\beta=1}^{3} \frac{2n_\beta - N_\beta - 1}{2N_\beta}\mathbf{b}_\beta, \qquad (n_\beta = 1, 2, 3, ..., N_\beta), \tag{2.21}$$

where N_β is the number of divisions in reciprocal space along the βth direction ($\beta =$ 1, 2, 3) and $\mathbf{b}_1, \mathbf{b}_2$ and $\mathbf{b}_3$ are the primitive reciprocal lattice vectors. If we increase the number of **k**-points, the accuracy of the numerical integration (and hence the accuracy of the result) increases, but at the same time, it is computationally more expensive. However, we can still choose a high number of **k**-points if we can reduce the BZ by applying symmetry operations.

For insulators and semiconductors, the Fermi level lies in between conduction band (CB) and valence band (VB). In the case of metals, the VB and CB overlap and at $T = 0$, there is a sharp discontinuity in **k** space on going from occupied states to the unoccupied states. One, therefore, needs to introduce a step function in order to reproduce the Fermi surface accurately, to capture which would, on the other hand, require a large number of **k**-points. Using the smearing technique, one can replace the step function with a smoothly varying function for the occupation of states near the Fermi energy. As a result fewer **k**-points are required. Some of the existing smearing techniques are Gaussian smearing,[22] Methfessel-Paxton smearing,[23] and Marzari-Vanderbilt cold smearing.[24] The larger the smearing width, the faster is the convergence with respect to **k** points, but the lower is the accuracy.

2.1.7 Hellmann-Feynman theorem: Calculation of Forces

To obtain the lowest energy structure, i.e., the optimized geometry, we need to minimize the forces and stresses in the system. In principle, for the ground state geometry, the force on all atoms in the system should be zero. We can calculate forces using the Hellmann-Feynman (HF) theorem,[25] which states that one can calculate the force by computing the expectation value of the derivative of the Hamiltonian $\hat{H}$. Alternatively, the force on each ion I could also have been calculated by taking the first derivative of the total energy with respect to the ionic position R_I, but this would require the computation of the total energy at many configurations. In contrast the HF theorem shows that a calculation at a single configuration would be sufficient to compute the force.

$$\mathbf{F_I} = -\frac{\partial E(\mathbf{R}_I)}{\partial \mathbf{R}_I} = -\langle\Psi|\frac{\partial \hat{H}}{\partial \mathbf{R}_I}|\Psi\rangle\,, \tag{2.22}$$

where $E(\mathbf{R_I})$ is the total energy for a given set of nuclear co-ordinates $\{\mathbf{R}_I\}$ and Ψ is the eigenfunction of the Hamiltonian $\hat{H}$. Eq. (2.22) holds true only when the basis set is complete or position-independent, as in the case of a plane wave basis set. If the basis is not complete or position-dependent, e.g., for localized orbital basis sets like a Gaussian basis, one gets additional terms, known as Pulay forces. Also Ψ has to be an eigenstate of $\hat{H}$.

2.1.8 Spin-Polarized Density Functional Theory

In order to extend Kohn-Sham theory to spin-polarized systems, we need to consider the electron density decomposed over two different spin states. The total electron density of the spin-polarized system is the sum of the spin up and spin down electron densities: $n(\mathbf{r}) = n^{\uparrow}(\mathbf{r}) + n^{\downarrow}(\mathbf{r})$. The magnetic moment of the spin-polarized system is given by: $m(\mathbf{r}) = n^{\uparrow}(\mathbf{r}) - n^{\downarrow}(\mathbf{r})$. For the spin-polarized system, the Kohn-Sham equations are solved self consistently for each spin density, with a coupling term. Therefore, the non-spin-polarized Kohn-Sham equations i.e., Eqs. (2.12) to (2.14) now become instead:

$$\left\{ -\frac{1}{2}\nabla^2 + V^s_{\mathrm{KS}}(\mathbf{r}) \right\} \psi^s_i(\mathbf{r}) = \epsilon^s_i \psi^s_i(\mathbf{r}), \tag{2.23}$$

$$V^s_{\mathrm{KS}}(\mathbf{r}) = V_H(\mathbf{r}) + V_{xc}(\mathbf{r}) + V_{ext}[n^{\uparrow}, n^{\downarrow}](\mathbf{r}), \tag{2.24}$$

and

$$n^s(\mathbf{r}) = \sum_{i=1}^{N^s} \psi^{s*}_i(\mathbf{r}) \psi^s_i(\mathbf{r}), \tag{2.25}$$

where $s = \{\uparrow, \downarrow\}$ is the spin of the electron. V^s_{KS} is the Kohn-Sham potential. The spin dependence in V^s_{KS} arises only from the exchange-correlation potential which depends on $n^{\uparrow}(\mathbf{r})$ and $n^{\downarrow}(\mathbf{r})$:

$$V^s_{xc}(\mathbf{r}) = \frac{\delta E_{xc}[n^{\uparrow}(\mathbf{r}), n^{\downarrow}(\mathbf{r})]}{\delta n^s(\mathbf{r})}. \tag{2.26}$$

2.2 Dispersion Interactions: DFT-D2 Method

So far, we have discussed local and semi-local properties of systems that can be described accurately using LDA and GGA functionals. However, long-range or non-local interactions[26] are often observed in real systems due to the interaction between the local dipoles arising because of the local charge fluctuations in the system. These are called dispersion interactions. They are also known as van der Waals interactions[27] or London interactions.[28] Dispersion interactions play an essential role in many systems such as self-assembled molecular layers on surfaces, layered materials, and biomolecules such as DNA or proteins.

Dispersion interactions can be incorporated in DFT calculations at varying levels of sophistication, e.g., using semi-empirical corrections (e.g., DFT-D2[29]) or through non-empirical methods (e.g., vdw-DF).[30] The latter are more expensive computationally, but do not necessarily guarantee greater accuracy (in terms of agreement with experiment). For example, vdW-DF overestimates and DFT-D2 underestimates the adsorption energy of the pyridine-graphene system when compared with the experimental value.[31] In the case of multilayer black phosphorene, DFT-D2 produces better agreement with experimental values for the lattice parameters when it compared with results obtained using vdW-DF.[32] Therefore, in this thesis, I have used the semi-empirical DFT-D2 approach introduced by Grimme,[29;33] whenever it is believed that dispersion interactions may be significant.

In the DFT-D2 method, the dispersion-corrected total energy is given as:

$$E_{\text{DFT-D2}} = E_{\text{DFT}} + E_{disp}, \tag{2.27}$$

where E_{DFT} is the total energy from DFT calculations and E_{disp} is computed using the formula:

$$E_{disp} = -s_6 \sum_{I=1}^{N_{atom}-1} \sum_{J=I+1}^{N_{atom}} \frac{C_6^{IJ}}{R_{IJ}^6} f_{damp}(R_{IJ}). \tag{2.28}$$

Here N_{atom} is the total number of atoms present in the system, C_6^{IJ} is the dispersion coefficient for a pair of atoms I and J:

$$C_6^{IJ} = \sqrt{C_6^I C_6^J}. \tag{2.29}$$

s_6 is a global scaling factor which is 0.75 for GGA functionals[34] and depends only on the exchange-correlation functional used. R_{IJ} is the interatomic distance between the atoms I and J. $f_{damp}(R_{IJ})$ is a damping function used to avoid singularity at small R_{IJ}, given as:

$$f_{damp}(R_{IJ}) = \frac{1}{1 + e^{-d(\frac{R_{IJ}}{R_r}-1)}}, \tag{2.30}$$

where R_r is the sum of the atomic van der Waals radii, and d is a damping parameter with a typical value of 20.[29]

2.3 Strong correlations: The DFT+U Method

Transition metal and rare earth elements are characterized by localized d or f orbitals. In molecules or compounds containing such elements, if we want to put a second electron in a site that is already occupied by a localized electron, it costs an additional energy, U, because of the strong on-site Coulomb repulsion.[6] Such materials are known as strongly correlated systems. In most of the cases, the local and semi-local functionals fail to describe the strongly correlated systems because of the over-delocalization of d and f electrons. The Hubbard model (which is a field by itself, used to study the strongly correlated electrons) has been combined with DFT by supplementing LDA or GGA with a Hubbard-type on-site repulsion term (LDA+U or GGA+U).[35–37]

In this method, the corrected total energy[35] is given as:

$$E_{\mathrm{DFT+U}} = E_{\mathrm{DFT}} + E_{\mathrm{HUB}} - E_{\mathrm{dc}}. \tag{2.31}$$

E_{DFT} is the total energy from the DFT calculation. E_{HUB} is the Hubbard-type on-site repulsion term calculated using mean field theory:

$$E_{\mathrm{HUB}} = \frac{1}{2} U \sum_{i \neq j} \alpha_i \alpha_j. \tag{2.32}$$

Here, α_i are orbital occupancies for the d and f electrons. E_{dc} is a double-counting term that arises because we count the same d and f electrons twice, once at the time of calculating E_{DFT} and second at the time of calculating E_{HUB}. E_{dc} is expressed as:

$$E_{\mathrm{dc}} = \frac{1}{2} U N_c \Big(N_c - 1 \Big), \tag{2.33}$$

where

$$N_c = \sum_i \alpha_i. \tag{2.34}$$

We have used both LDA+U and GGA+U methods in this thesis to treat the strongly correlated systems. We note that the value of U depends on the type of exchange-correlation functional used, typically U is larger when used with the LDA than when used with the GGA.[38]

One should note that DFT+U is not an exact method. While the DFT+U method does deal with strongly correlated systems, it is still a mean-field approach because dynamical correlations are not considered. The DFT+U limit can be regarded as the mean-field extreme of strong interactions.

The DFT+U approach is particularly popular for studies on the transition metal oxides.[39–41] It is known to fail in certain cases, especially if the system has a mixture of localized and delocalized electronic states.[40] For example, the DFT+U often fails in correctly describing Li-ion cathode materials with dopants;[42] such systems are particularly important because dopants can improve the performance of battery materials.

However, the most challenging job is to determine the appropriate U value that has to be used. Most of the time, the value of U is tuned semi-empirically, so as to obtain good agreement with experimental or higher level computational results. However, one could also attempt to determine U from first principles.[43] In these approaches, the U parameter can generally be calculated using a self-consistent procedure. These different *ab initio* approaches for calculating U have been applied to different material systems, where the U value is calculated for individual atoms. For each atom, the U value has been found to be dependent on the material specific parameters, including its position in the lattice and the structural and magnetic properties of the crystal, and also dependent on the localized basis set employed to describe the on-site occupation in the Hubbard functional.[44;45] Therefore, the value of effective interactions should be re-computed for each type of material. In this thesis, the approach we have followed is to limit the range of U so as to be consistent with known experimental information, and then see how calculated properties vary when U is varied within this limited range.

2.4 Tersoff-Hamann Approach: Simulation of STM image

The scanning tunneling microscope (STM) is a very powerful experimental tool for probing the surface structure at the atomic scale. Binnig and Rohrer[46] (1982) developed the STM for the first time; this marked an explosive new era in the field of surface science. One of the distinctive aspects of the STM is that it can be used to investigate a variety of systems, ranging from atomically sharp surfaces to molecular

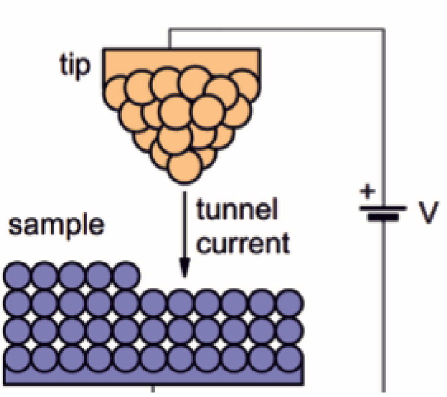

Figure 2.2: Idealized schematic of an STM experiment. Reproduced from Ref. 49 with permission of the Licensor through PLSclear.

adsorbates and molecular assemblies at the nanoscale.[47;48] Also, it can be used for directly manipulating atoms and molecules at the nanoscale.

In STM experiments (see Fig. 2.2), a metallic tip (e.g. Au, Pt) is placed in close proximity ($\sim 5 - 8$ Å) to a conducting surface. Upon applying a bias voltage, the electrons belonging to the tip can tunnel into the surface or vice-versa, depending on the polarity of the bias. The resulting tunneling current is very sensitive to the tip-sample distance. Hence a constant current measurement provides direct information on the surface topography.

In this section we simply discuss those aspects which are essential for understanding how to simulate STM images using DFT, and how to perform meaningful comparisons with experiment. In 1961, Bardeen[50] introduced a formula which allows us to calculate the tunneling current from the tip to the surface separated by a vacuum. This can be expressed as:

$$I = 2\pi \sum_i \sum_j f(E_{T,i} - E_{T,F})[1 - f(E_{S,j} - E_{S,F})]|M_{i,j}|^2 \delta(E_{T,i} - E_{S,j}). \qquad (2.35)$$

Here, $E_{T,i}$ and $E_{S,j}$ are the single-particle electronic eigenvalues of the tip (T) and

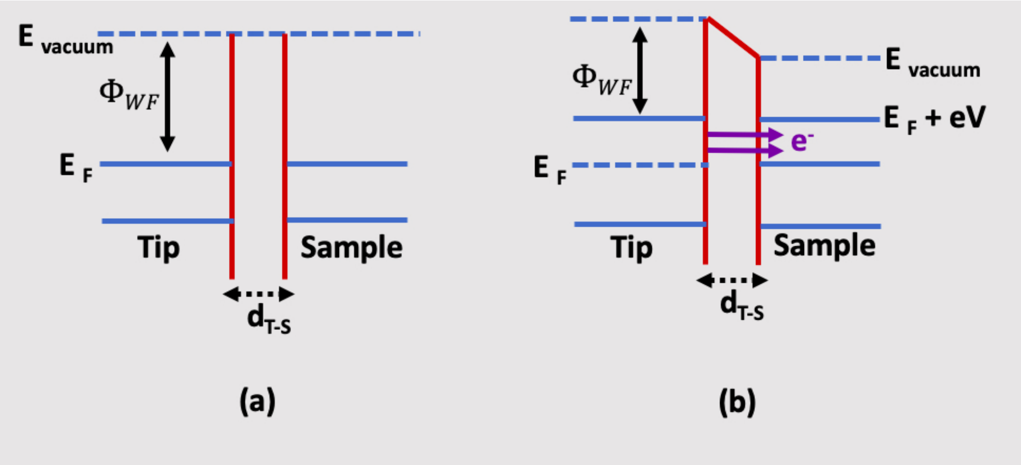

Figure 2.3: Schematic diagram showing the energy level alignment between the tip and the sample (a) in absence of any bias volatge, no electron tunnels and (b) when the bias voltage V is applied. E_{F} and E_{vacuum} are the Fermi energy and vacuum energy, respectively. Φ_{WF} is the work function and $d_{\mathrm{T-S}}$ is the tip-sample distance.

the sample (S). Bardeen theory[50] relates the tunneling current (I) to the position of the Fermi levels of the tip ($E_{T,F}$) and sample ($E_{S,F}$), the respective electronic density of states, and the spatial overlap between their electronic wavefunctions ($M_{i,j}$). $f(E) = [exp(E - E_F)/k_BT + 1]^{-1}$ is the Fermi-Dirac (F-D) distribution function. The current tunnels only when one of the Fermi levels is offset from theother by a voltage, V. When a bias voltage, V is applied, the Fermi levels of the tip and the sample become shifted with respect to each other, depending on the polarity of the voltage applied. In the schematic diagram shown in Fig. 2.3(b), the bias voltage is applied from tip to sample, which shifts E_{F} of the tip above E_{F} of the sample. Therefore, the tip becomes more occupied than the sample and thus electrons can flow from the tip to the sample, causing a net tunneling current. At temperature $T = 0$ K, the Eq. (2.35) simplifies to the Eq. (2.36) below, because Fermi-Dirac distribution, $f(E) = 1$:

$$I = 2\pi \sum_i \sum_j |M_{i,j}|^2 \delta(E_{T,i} - E_{S,j}). \tag{2.36}$$

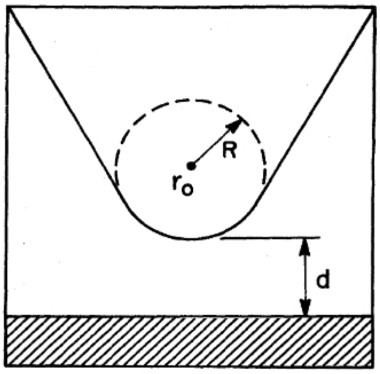

Figure 2.4: Schematic diagram showing the geometry of the STM tip. The tip is assumed to be spherical in shape. R is the radius of curvature, d is the nearest tip-sample distance and r_0 is the center of curvature of the tip. The shaded region shows the surface of the sample. Thia figure is taken with permission from ref. 51 ©American Physical Society

Now, the important and challenging part of calculating the tunneling current, is to evaluate the matrix element, M_{ij}, which measures the overlap between tip wavefunctions and sample wavefunctions. It is impossible to determine the exact form of wavefunctions of the tip at the time of the experiment, which makes M_{ij} undetermined. To tackle this problem, Tersoff and Hamann[51] proposed a way, by assuming a spherical tip. In that case, the matrix element, M_{ij}, becomes proportional to the magnitude of the wavefunction of the sample at the centre $r_{\mathbf{0}}$ of the sphere (see Fig: 2.4):

$$M_{i,j} = \text{const.} \times \psi_{S,j}(r_{\mathbf{0}}). \tag{2.37}$$

In simple words, one can say that the wavefunction of the outermost tip atom is assumed to be an atomic s-wavefunction, which is spherical in shape. Using Eq. (2.37) we can rewrite Eq. (2.36) as:

$$I = \text{const.} \sum_j |\psi_{S,j}(r_{\mathbf{0}})|^2 \delta(E_{T,i} - E_{S,j}). \tag{2.38}$$

The summation given in the Eq. (2.38) is the local density of states (LDOS) of the sample at the Fermi level. The tunneling current (I) in the final and simplified form can be written as:

$$I \propto \mathrm{LDOS}(r_0, E_{S,F}). \tag{2.39}$$

In this thesis, I have used the Tersoff-Hamann[51] approach to simulate the constant current as well as constant height STM images.

2.5 Codes Used

Quantum mechanical density functional theory as implemented in the Quantum ESPRESSO pwscf package,[13] is used in this thesis for obtaining various properties of materials, such as optimized structure, adsorption energies, charge states, magnetism, and densities of states, as described in the later chapters in this thesis.

The atomistic structures of the systems, charge redistribution plots, molecular orbital plots, and simulated STM images reported in this thesis, are obtained using the software packages XCrySDen[52] and VESTA.[53] All two or three-dimensional graphs used in the thesis are either plotted using the Xmgrace software package or obtained using gnuplot.

Bibliography

[1] R. M. Martin and R. M. Martin, *Electronic structure: basic theory and practical methods.* Cambridge University Press, 2004.

[2] M. Born and R. Oppenheimer, "Zur quantentheorie der molekeln," *Annalen der physik*, vol. 389, p. 457, 1927.

[3] M. Springborg, *Methods of electronic-structure calculations: from molecules to solids.* John Wiley & Sons, 2000.

[4] P. Hohenberg and W. Kohn, "Inhomogeneous electron gas," *Physical review*, vol. 136, p. B864, 1964.

[5] W. Kohn and L. J. Sham, "Self-consistent equations including exchange and correlation effects," *Physical review*, vol. 140, p. A1133, 1965.

[6] J. Kohanoff, *Electronic structure calculations for solids and molecules: theory and computational methods.* Cambridge University Press, 2006.

[7] R. O. Jones and O. Gunnarsson, "The density functional formalism, its applications and prospects," *Rev. Mod. Phys.*, vol. 61, p. 689, 1989.

[8] D. M. Ceperley and B. Alder, "Ground state of the electron gas by a stochastic method," *Phys. Rev. Lett.*, vol. 45, p. 566, 1980.

[9] S. H. Vosko, L. Wilk, and M. Nusair, "Accurate spin-dependent electron liquid correlation energies for local spin density calculations: a critical analysis," *Can. J. Phys.*, vol. 58, p. 1200, 1980.

[10] J. P. Perdew and A. Zunger, "Self-interaction correction to density-functional approximations for many-electron systems," *Phys. Rev. B*, vol. 23, p. 5048, 1981.

[11] J. P. Perdew, K. Burke, and M. Ernzerhof, "Generalized gradient approximation made simple," *Phys. Rev. Lett.*, vol. 77, no. 18, p. 3865, 1996.

[12] J. P. Perdew and Y. Wang, "Pair-distribution function and its coupling-constant average for the spin-polarized electron gas," *Phys. Rev. B*, vol. 46, p. 12947, 1992.

[13] P. Giannozzi, S. Baroni, N. Bonini, M. Calandra, R. Car, C. Cavazzoni, D. Ceresoli, G. L. Chiarotti, M. Cococcioni, I. Dabo, *et al.*, "Quantum espresso: a modular and open-source software project for quantum simulations of materials," *J. Phys. Condens. Matter*, vol. 21, p. 395502, 2009.

[14] X. Gonze, J.-M. Beuken, R. Caracas, F. Detraux, M. Fuchs, G.-M. Rignanese, L. Sindic, M. Verstraete, G. Zerah, F. Jollet, *et al.*, "First-principles computation of material properties: the abinit software project," *Comput. Mater. Sci.*, vol. 25, pp. 478–492, 2002.

[15] J. M. Soler, E. Artacho, J. D. Gale, A. García, J. Junquera, P. Ordejón, and D. Sánchez-Portal, "The siesta method for ab initio order-n materials simulation," *J. Phys. Condens. Matter*, vol. 14, p. 2745, 2002.

[16] H. Dreyssé, *Electronic structure and physical properties of solids.* Springer, 2000.

[17] N. W. Ashcroft and N. D. Mermin, *Solid State Physics.* Cengage Learning, 1976.

[18] W. E. Pickett, "Pseudopotential methods in condensed matter applications," *Comput. Phys. Commun.*, vol. 9, p. 115, 1989.

[19] D. Hamann, M. Schlüter, and C. Chiang, "Norm-conserving pseudopotentials," *Phys. Rev. Lett.*, vol. 43, p. 1494, 1979.

[20] D. Vanderbilt, "Soft self-consistent pseudopotentials in a generalized eigenvalue formalism," *Phys Rev. B*, vol. 41, p. 7892, 1990.

[21] H. J. Monkhorst and J. D. Pack, "Special points for brillouin-zone integrations," *Phys. Rev. B*, vol. 13, p. 5188, 1976.

[22] C.-L. Fu and K.-M. Ho, "First-principles calculation of the equilibrium ground-state properties of transition metals: Applications to Nb and Mo," *Phys. Rev. B*, vol. 28, p. 5480, 1983.

[23] M. Methfessel and A. Paxton, "High-precision sampling for Brillouin-zone integration in metals," *Phys. Rev. B*, vol. 40, p. 3616, 1989.

[24] N. Marzari, D. Vanderbilt, A. De Vita, and M. Payne, "Thermal contraction and disordering of the Al (110) surface," *Phys. Rev. Lett.*, vol. 82, p. 3296, 1999.

[25] R. P. Feynman, "Forces in molecules," *Physical Review*, vol. 56, p. 340, 1939.

[26] O. A. Vydrov and T. Van Voorhis, "Nonlocal van der Waals density functional made simple," *Phys. Rev. Lett.*, vol. 103, p. 063004, 2009.

[27] M. Dion, H. Rydberg, E. Schröder, D. C. Langreth, and B. I. Lundqvist, "Van der Waals density functional for general geometries," *Phys. Rev. Lett.*, vol. 92, p. 246401, 2004.

[28] F. London, "Uber einige eigenschaften und anwendungen der molekularkräfte," *Z. Phys. Chem.*, vol. B11, p. 222, 930.

[29] S. Grimme, "Accurate description of van der Waals complexes by density functional theory including empirical corrections," *J. Comput. Chem.*, vol. 25, p. 1463, 2004.

[30] M. Dion, H. Rydberg, E. Schröder, D. C. Langreth, and B. I. Lundqvist, "Van der Waals density functional for general geometries," *Phys. Rev. Lett.*, vol. 92, p. 246401, 2004.

[31] D. Mollenhauer, C. Brieger, E. Voloshina, and B. Paulus, "Performance of dispersion-corrected dft for the weak interaction between aromatic molecules and extended carbon-based systems," *J. Phys. Chem. C*, vol. 119, p. 1898, 2015.

[32] J. Qiao, X. Kong, Z.-X. Hu, F. Yang, and W. Ji, "High-mobility transport anisotropy and linear dichroism in few-layer black phosphorus," *Nat. Commun.*, vol. 5, p. 4475, 2014.

[33] S. Grimme, "Semiempirical GGA-type density functional constructed with a long-range dispersion correction," *J. Comput. Chem.*, vol. 27, p. 1787, 2006.

[34] R. Peverati and K. K. Baldridge, "Implementation and performance of dft-d with respect to basis set and functional for study of dispersion interactions in nanoscale aromatic hydrocarbons," *J. Chem. Theory Comput.*, vol. 4, p. 2030, 2008.

[35] V. I. Anisimov, J. Zaanen, and O. K. Andersen, "Band theory and mott insulators: Hubbard U instead of stoner I," *Phys. Rev. B*, vol. 44, p. 943, 1991.

[36] A. I. Liechtenstein, V. I. Anisimov, and J. Zaanen, "Density-functional theory and strong interactions: Orbital ordering in mott-hubbard insulators," *Phys. Rev. B*, vol. 52, p. R5467, 1995.

[37] V. I. Anisimov, I. V. Solovyev, M. A. Korotin, M. T. Czyżyk, and G. A. Sawatzky, "Density-functional theory and NiO photoemission spectra," *Phys. Rev. B*, vol. 48, p. 16929, 1993.

[38] C. Loschen, J. Carrasco, K. M. Neyman, and F. Illas, "First-principles LDA+U and GGA+U study of cerium oxides: Dependence on the effective U parameter," *Phys. Rev. B*, vol. 75, p. 035115, 2007.

[39] L. Wang, T. Maxisch, and G. Ceder, "Oxidation energies of transition metal oxides within the GGA+U framework," *Phys. Rev. B*, vol. 73, p. 195107, 2006.

[40] A. Jain, G. Hautier, S. P. Ong, C. J. Moore, C. C. Fischer, K. A. Persson, and G. Ceder, "Formation enthalpies by mixing GGA and GGA+ U calculations," *Phys. Rev. B*, vol. 84, p. 045115, 2011.

[41] A. Jain, S. P. Ong, G. Hautier, W. Chen, W. D. Richards, S. Dacek, S. Cholia, D. Gunter, D. Skinner, G. Ceder, *et al.*, "Commentary: The Materials Project: A materials genome approach to accelerating materials innovation," *APL Materials*, vol. 1, p. 011002, 2013.

[42] J. A. Santana, J. Kim, P. Kent, and F. A. Reboredo, "Successes and failures of Hubbard-corrected density functional theory: The case of Mg doped LiCoO2," *J. Chem. Phys.*, vol. 141, p. 164706, 2014.

[43] T. Miyake and F. Aryasetiawan, "Screened coulomb interaction in the maximally localized wannier basis," *Phys. Rev. B*, vol. 77, p. 085122, 2008.

[44] V. I. Anisimov, F. Aryasetiawan, and A. Lichtenstein, “First-principles calculations of the electronic structure and spectra of strongly correlated systems: the LDA+ U method,” *J. Phys. Condens. Matter*, vol. 9, p. 767, 1997.

[45] S. L. Dudarev, G. A. Botton, S. Y. Savrasov, C. J. Humphreys, and A. P. Sutton, “Electron-energy-loss spectra and the structural stability of nickel oxide: An LSDA+U study,” *Phys. Rev. B*, vol. 57, p. 1505, 1998.

[46] G. Binnig and H. Rohrer, “Scanning tunneling microscopy,” *Surf. Sci.*, vol. 126, p. 236, 1983.

[47] G. Binnig, H. Rohrer, C. Gerber, and E. Weibel, “Surface studies by scanning tunneling microscopy,” *Phys. Rev. Lett.*, vol. 49, p. 57, 1982.

[48] G. Binnig, H. Rohrer, C. Gerber, and E. Weibel, “7× 7 reconstruction on Si (111) resolved in real space,” *Phys. Rev. Lett.*, vol. 50, p. 120, 1983.

[49] F. Giustino, *Materials Modelling using Density Functional Theory Properties and Predictions.* Oxford Publishing Limited, 2014.

[50] J. Bardeen, “Tunnelling from a many-particle point of view,” *Phys. Rev. Lett.*, vol. 6, p. 57, 1961.

[51] J. Tersoff and D. R. Hamann, “Theory of the scanning tunneling microscope,” *Phys. Rev. B*, vol. 31, p. 805, 1985.

[52] A. Kokalj, “Xcrysden:(x-window) crystalline structures and densities,” *Comp. Mater. Sci.*, vol. 28, p. 155, 2003.

[53] K. Momma and F. Izumi, “Vesta 3 for three-dimensional visualization of crystal, volumetric and morphology data,” *J. Appl. Crystallogr.*, vol. 44, p. 1272, 2011.

Chapter 3

Ordered Partial Spin Crossover Transition in IPB/Au(111) Triggered by Epitaxial Strain

3.1 Introduction

One of the many reasons that the study of transition metal (TM) complexes is so fascinating, is that the same compound can sometimes show different physical and chemical properties, depending on how the *d* orbitals are filled. As an example, Fe in Fe[CN]$_6$ shows two different spin states, i.e., two states with different magnetic moments.[1] In this chapter, we consider possible transitions between two spin states of Fe in the octahedral complex $\mathrm{Fe^{II}((3,\ 5\text{-}(CH_3)_2C_3N_2H)_3BH)_2}$.[2–5] Therefore, we would like first to review the filling of Fe *d* orbitals in an octahedral environment.

In an octahedral environment, the d_{z^2} and $d_{x^2-y^2}$ orbitals bind with six ligands, whereas the d_{xy}, d_{zx} and d_{yz} orbitals do not participate in bond formation. This causes a splitting of the *d* orbitals into two sets: t_{2g} (d_{xy}+d_{zx}+d_{xy}) and e_g ($d_{x^2-y^2}$ + d_{z^2}).[1] The energy difference between the t_{2g} and e_g levels is commonly referred to as

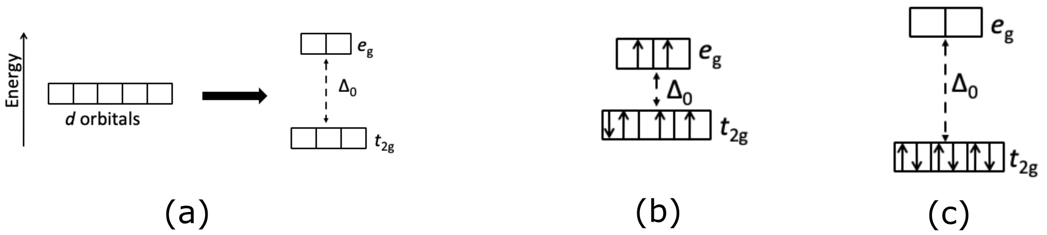

Figure 3.1: (a) d orbitals split into t_{2g} and e_g in an octahedral field. There are two possibilities for filling t_{2g} and e_g depending on crystal field splitting energy (Δ_0) and pairing energy (Δ) (b) $\Delta_0 < \Delta$, both t_{2g} and e_g are partially filled (c) $\Delta_0 > \Delta$, t_{2g} is completely filled, no electrons in e_g.

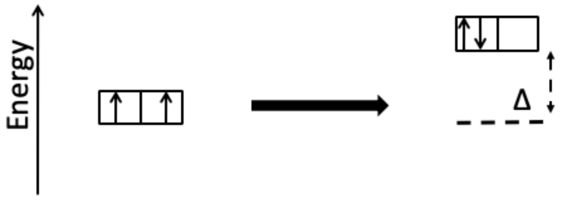

Figure 3.2: Schematic diagram for pairing energy (Δ).

the crystal field splitting energy (Δ_0), as shown in Fig. 3.1(a). We can fill the t_{2g} and e_g levels in two possible ways, shown in Figs. 3.1(b) and 3.1(c). In Fig. 3.1(b), the orbitals are filled following Hund's rule, which says that the electronic configuration with the maximum spin multiplicity (S) is lowest in energy. The spin multiplicity S is equal to 2 for the configuration shown in Fig. 3.1(b). In contrast, S is calculated to be 0 for the configuration shown in Fig. 3.1(c), which means Hund's rule is violated in Fig. 3.1(c). To explain why sometimes $S = 0$ may be favored over $S = 2$, we introduce another parameter called the "pairing energy" (Δ), which is the energy required to place two electrons in the same orbital (see Fig. 3.2). When $\Delta_0 < \Delta$, we get Fig. 3.1(b) as the favored state, where four electrons are unpaired, giving rise to a total magnetic moment of 4 μ_B. We refer to this configuration as the high spin (HS) state. In contrast, when $\Delta_0 > \Delta$, we get filled t_{2g} and no electrons in e_g. If we want to fill the e_g state in Fig. 3.1(c), we need to supply a very high energy ($> \Delta_0$), which makes this configuration unfavorable. We refer to this configuration as the low spin (LS) state, because it contains no unpaired electrons, i.e., the total magnetic moment is zero.

One can switch between the two spin states (LS and HS) by applying external stimuli such as electric field, light, or heat.[6] This phenomenon is known as spin crossover. Spin crossover molecules[7] are particularly attractive compounds in the field of molecular spintronics as they can display a different conductance as a function of their spin state. Spin crossover molecules (SCM) can also find applications in magnetic memory devices,[8] with one spin state being assigned to the binary number 1, and the other spin state to 0. One can thereby use different combinations of HS and LS molecules (or domains of molecules) to encrypt data. Similarly, SCM can be used in display devices,[9] where one spin state is used to pass light (bright region) and the other is used to stop light (dark region).

To fabricate devices, an ultrathin SCM layer[10] is deposited on a substrate, which can modify the properties of the SCM.[11] However, surprisingly little is known about such molecule-substrate effects. In this regard, the study of interfaces between Fe-SCM and metal substrates is particularly important. We note that a well-ordered bilayer of [Fe(bispyrazolyl)$_2$(phenanthroline)] on Au(111) was the first system where reversible and selective spin state switching at the single-molecule level was shown.[12] The study showed that low temperature STM topography could be used to distinguish between the different spin states because of their different shapes. Further, the existence of the two spin states was confirmed by observing the two distinguishable spectra using surface tunneling spectroscopy (STS). However, the exact structure of this system is still unclear, as it has been shown that this molecule dissociates when in contact with gold, and patches of intact molecules coexist with ordered phenanthroline phases.[13] Another STM study in combination with conductance measurements by Pronschinske *et al.* showed the coexistence of temperature independent spin states for bilayer films of [Fe($H_2B(Pz)_2)_2$bpy] on Au(111).[14] Here, Pz denotes pyrazole (C_3N_2H) and bpy denotes the bipyridine ligand. This modification of bulk behavior was attributed in part to the unique packing of the bilayer film that causes deviations from bulk behavior. Temperature and light-induced SCO was also seen for another complex of iron, [Fe($H_2B(Pz)_2)_2$bpy] on the Au substrate.[15] The experiment reported reversible and selective spin switching of the single molecule. Miyamachi *et al.* studied another Fe-SCO compound, [Fe(1,10-phenanthroline)$_2$(NCS)$_2$] on a Cu substrate, and found coexistence of HS and LS states at very low coverage on the Cu(100) surface, using STS and conductance measurements.[16] Introducing an interfacial CuN layer allowed one to switch between the HS and LS states by applying an electric field, although the same was not observed for a pristine Cu substrate. It was concluded that the strong interaction of the NCS groups of the molecule with the Cu substrate prevented the spin transition, whereas the reduced substrate-molecular interaction in the presence of the interfacial CuN layer allowed the spin switching to occur. Another STM experiment performed by Gruber *et al.* showed a thickness-dependent spin crossover for a bilayer of the [Fe(1,10-phenanthroline)$_2$(NCS)$_2$] molecule on the Cu(100) substrate.[17] They found that both HS and LS states coexisted in the first layer (i.e., the layer immediately on top of the Cu substrate) because of the strong coupling between the molecules and substrate, but there were only HS molecules in the second layer (the layer on top of the first layer). The coupling strength decreases in the second layer, which allows LS molecules to crossover into the HS state, due to the voltage difference applied during STM scanning.

We note that it is also challenging to find the true ground state spin configuration of such systems using density functional theory (DFT), due to the strongly correlated d electrons of the TM. This problem can be dealt with by adding a term in the Hamiltonian, corresponding to an on-site Coulomb repulsion, for d electrons.[18–20] Lebègue *et al.*[18] made use of the DFT+U method to model SCO, and correctly predicted the magnetic states of the two spin crossover molecules, [Fe(1,10-phenanthroline)$_2$(NCS)$_2$], and [Fe(bis-triazole)$_2$(NCS)$_2$(H$_2$O)]. They showed that the total energies of the different spin configurations vary linearly as a function of the value of the Hubbard U parameter, but with different slopes, resulting in a spin crossover at a certain value of U. Thus, in order to determine the correct spin state, finding the appropriate value of U is crucial. In another theoretical study, Gueddida *et al.* offered an explanation of the experiment performed by Miyamachi *et al.* (mentioned above), using the GGA+U method.[21] They showed that using an on-site Coulomb potential $U = 3$ eV can correctly reproduce the structure and magnetic moment of the HS state of the [Fe(1,10-phenanthroline)$_2$(NCS)$_2$] molecule. Their total energy calculations showed that the difference in energy between the HS and LS states is much lower on the CuN(001) surface compared to pristine Cu(001). This low energy difference facilitates switching between one spin state and the other on the CuN(001) surface. This modification happens because strong van der Waals interactions between the NCS group of the molecule and the Cu(001) substrate are absent in the presence of CuN(001), due to insertion of the interfacial CuN monolayer. Paulsen[19] estimated an interaction parameter for the [Fe(phenanthroline)$_2$(NCS)$_2$] molecular crystal based on first principles calculations performed for its molecular crystal, taking different combinations of spin states. This parameter allows one to describe the cooperativity of the spin crossover in the [Fe(phenanthroline)$_2$(NCS)$_2$] molecular crystal.

A few studies have shown that mechanoelastic models of SCO complexes can explain their temperature-induced spin transitions, when used together with Monte Carlo simulations.[22–27] In this regard, a study by Delgado *et al.*, on [Fe(pyrazine)Pt(CN)$_4$] nanoparticles dispersed on the sapphire surface, needs to be mentioned. It was shown that interactions with the substrate were the driving force for the appearance of a residual HS fraction during the thermal transition.[24] They used a mechanoelastic model to describe the molecule-substrate interaction. This model was first developed by Enachescu *et al.* for two-dimensional (2D) systems,[22] and then the same was transferred to three-dimensional (3D) spin crossover problems.[25]. In this model, the interaction of the molecules with the substrate is described by a set of springs, while a second set of springs models the interactions between molecules.

In this chapter, we will show the importance of the substrate in stabilizing spin states of the SCO molecules; this is an important factor that one needs to keep in mind at the time of device fabrication, when the SCO molecules are deposited on a substrate. We will confirm and explain the reason for a surprising experimental observation, viz., that a SCM was shown (for the first time) to form an ordered monolayer comprised of two kinds of molecules on a metal substrate, which moreover displays a well-defined epitaxial relationship. Using density functional theory and a mechanoelastic model fitted with DFT parameters, we will show how the epitaxial strain imposed by the substrate plays a significant role in determining the spin states of the SCM monolayer grown on an Au substrate. Many of the results presented in this chapter have been published in Ref. 4.

3.2 Experimental background

In this section, we discuss the experiments performed by our experimental colleagues in the MPQ laboratory of the University of Paris – Diderot. They have studied a monolayer of $\mathrm{Fe^{II}((3,5-(CH_3)_2Pz)_3BH)_2}$ (henceforth referred to as ‘IPB’) grown on Au(111), using scanning tunneling microscopy (STM) and grazing incidence X-ray diffraction (GIXD).[2;4] By determining the structure of IPB at the Au interface in combination with STM experiments and conductance measurements, they have

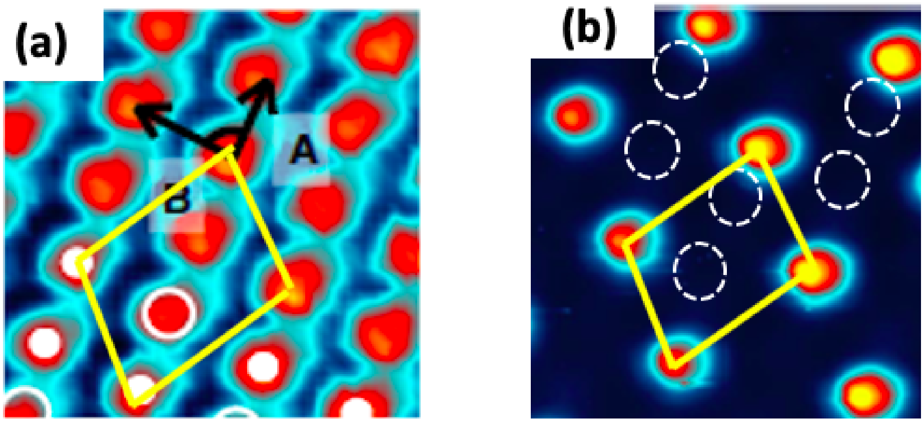

Figure 3.3: Low temperature (4.6 K) experimental STM images (a) STM image, recorded at -1.5 V, I = 50 pA shows all the IPB molecules imaged as bright (red) spots (b) STM image, recorded at 0.3 V, I = 50 pA shows only one out of three molecules imaged as a bright (red) spot. The positions of the two 'missing' molecules (imaged dark) have been shown using dotted white circles. In both panels, the $S_{1/3}$ unit cells have been drawn using solid yellow lines. This figure is reprinted with the permission from Ref. 2 ©2016, Nature Publishing Group.

shown that there are two types of molecules when IPB is deposited on Au(111). Low temperature STM experiments show that the unit cell has a periodicity of three molecules ($S_{1/3}$), see Fig. 3.3.[2] Fig. 3.3(a) shows that all the three molecules within the unit cell (yellow parallelogram) are imaged as bright (red) blobs at a bias voltage of −1.5 V, but only one out of three molecules is imaged bright (red) at a bias of +0.3 V, as shown in Fig. 3.3(b). Based on the STM results, they deduced the presence of two kinds of molecules on the surface. This can further be confirmed from conductance measurements, which show two different values of molecular conductance. As this is a known SCO molecule, one might guess that the unit cell of the $S_{1/3}$ superstructure consists of two molecules in one spin state and one molecule in the other spin state (either HS-LS-LS or LS-HS-HS); however, in the initial study, no direct experimental proof of this was obtained. Later X-ray adsorption spectroscopy (XAS) measurements found that HS and LS are in a 2:1 ratio.

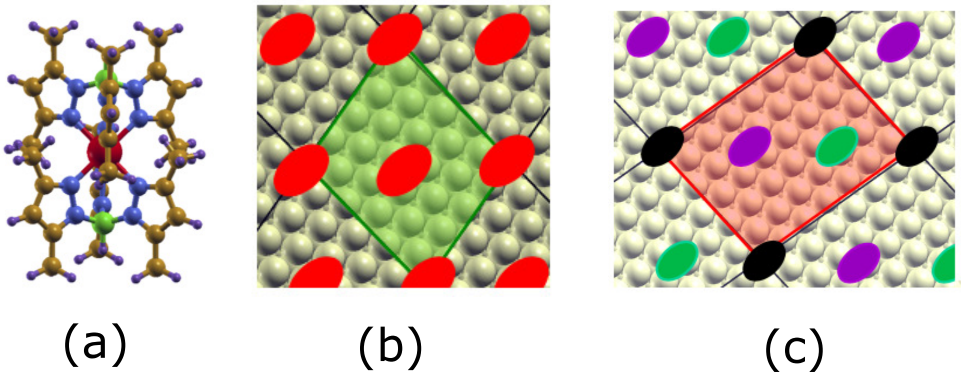

Figure 3.4: (a) Optimized geometry of IPB molecule in gas phase. Color code for atoms is red (iron), blue (nitrogen), green (boron), orange (carbon), violet (hydrogen). (b) $S_{1/2}$ cell (highlighted area) on Au(111) surface, red oval shapes schematically indicate IPB molecules in HS state (C) highlighted area is $S_{1/3}$ supercell on Au(111) surface; black, purple and green ovals represent the three IPB molecules in unknown (to be determined) spin states.The small gray spheres in panels (b) and (c) indicate gold atoms in the topmost layer.

However, at room temperature, a different superstructure was observed. A periodic superstructure containing two high spin IPB molecules within the unit cell has been found from the room temperature STM experiment, which we refer to as the $S_{1/2}$ supercell. At room temperature, IPB in bulk shows the HS ground state, and apparently the same spin state is retained in a monolayer at room temperature, even if it is on Au(111).[3;28]

The aim of our calculations is to confirm that indeed the two kinds of molecules in the $S_{1/3}$ unit cell correspond to two different spin states, and to understand why such a mixed-spin state is favored on Au(111) at low temperatures.

3.3 Systems under study

To compare our DFT results with the experiments, we first calculated the electronic properties of the IPB molecule in the gas phase [see Fig. 3.4(a)]. To model the experiments, we considered two supercells $S_{1/2}$ and $S_{1/3}$. We have first used the $S_{1/2}$ supercell to determine the adsorption geometry of IPB on the Au substrate (because GIXD data is only available for room temperature, to enable a comparison between experimental and theoretical results on adsorption geometries). In the slab model, we put the monolayer of IPB on top of $S_{1/2}$ supercell of Au(111) slab which is defined by the matrix $\begin{pmatrix} -1 & -5 \\ 6 & 3 \end{pmatrix}$ with respect to the lattice vectors of the Au(111) plane ($|a_{Au(111)}| = 2.87$ Å). The $S_{1/2}$ supercell is shown in Fig. 3.4(b), and the positions of the IPB molecules are shown schematically by drawing the ovals. Each $S_{1/2}$ unit cell contains two HS IPB molecules (represented by red-colored ovals), because the molecules are known to exist in the HS state, as the ground state at room temperature.

Similarly, we have used the $S_{1/3}$ supercell (shown in Fig. 3.4(c)) to explain the low-temperature experiment, which indicates the existence of two types of IPB molecules. The $S_{1/3}$ unitcell is defined by the matrix $\begin{pmatrix} 1 & -6 \\ 6 & 3 \end{pmatrix}$ with respect to the lattice vectors of the Au(111) plane ($a_{Au(111)}$). We have used black, purple and green colored ovals to represent three IPB molecules of unknown spin states, that are to be determined by performing calculations.

3.4 Computational details

The calculations are performed using spin polarized quantum mechanical density functional theory as implemented in the Quantum ESPRESSO package.[29;30] The interactions between ions and valence electrons are described using ultrasoft pseudopotentials.[31] The exchange-correlation potential is treated using the Perdew-Zunger[32] (PZ) parametrization of the local density approximation (LDA).[33] (Here we comment that we found that making use instead of the GGA leads to a larger error in the lattice constant of Au, as well as unphysical reconstructions of the Au(111) surface upon placing the IPB molecules on it). The plane wave cutoff is chosen to be 30 Ry for wavefunctions and 300 Ry for charge densities. In order to describe better the localization of the $3d$ electrons of Fe, the LDA+U method[34;35] is used. The gold substrate is modeled by a slab containing three layers stacked in the face-centered-cubic (111) orientation, of which the bottom two layers of Au are held fixed at bulk-like positions. All other atomic coordinates are relaxed, until the forces are less than 10^{-3} Ry/Bohr. Brillouin zone sampling is restricted to the zone center, as the unit cells are large. For all the calculations used in this chapter, we have used Gaussian broadening[36] to aid convergence, with a width equal to 0.005 Ry. The simulated STM images are obtained using the Tersoff-Hamann approach.[37]

For the calculations on a monolayer of IPB on the Au(111) substrate, we found that if the spin degrees of freedom are kept totally unconstrained, it was difficult to converge to the global minimum in spin space because of the presence of a large number of local minima. Therefore, the procedure followed was to first set the system in a given magnetic configuration by initially constraining the magnetization on the Fe atoms using a penalty functional, as implemented in the Quantum ESPRESSO package.[29;30] After performing some iterations, the penalty functional was removed. This procedure was repeated for different initial spin configurations, so as to ensure a search among different spin configurations.

3.5 Results and discussion

When studying the phenomenon of spin crossover, it is common to use the DFT+U method to capture the strong correlation of transition metals such as Fe, which results in a competition between different spin states in SCO complexes. In this section, we show our results obtained from LDA+U calculations, and a mechanoelastic model fitted with DFT parameters. There are several problems one faces when trying to perform DFT calculations on this system: (i) the existence of multiple minima in spin space, (ii) the fact that it is difficult to determine the orientation of the IPB molecule with respect to the Au(111) substrate, (iii) what value of the on-site Coulomb interaction parameter U to use. The problem of multiple minima in spin space is dealt with by initially placing the system in a certain spin state, and first performing a few iterations with constrained spin (using a penalty functional) before relaxing this constraint, and repeating this for various spin states. The problem of the unknown molecular orientation is dealt with by coming up with a shortlist of candidate orientations by slicing the bulk crystal in various directions, and looking for an approximate match with the experimentally measured lattice parameter of the IPB monolayer on Au(111). Out of these, the lowest energy orientation is determined by performing DFT calculations on the adsorbed molecular monolayer on the substrate for each candidate orientation. The correctness of this result is verified by comparing with the results of GIXD experiments. The value of U is a problem: it is known that the appropriate value can vary from system to system, even for the same atomic species. Here, we follow a semi-empirical approach, where we come up with reasonableness criteria by comparison with experiment.

We now explain our approach in greater detail. In the first step, we optimize the geometry of the isolated IPB molecule in the gas phase, in both HS and LS states. In the following step, we have estimate an approximate value for U using an empirical approach, i.e., by computing a physical observable and comparing with experiment. Then we use this value of U while determining the favored adsorption geometry of IPB in the $S_{1/2}$ cell. Further, we compare our adsorption geometry with X-ray diffraction data obtained from GIXD experiments. Then, making use of the orientation with the lowest energy, in the next step we generate a phase diagram as a function of U, for different spin configurations in the $S_{1/3}$ supercell. We use this to determine the range of values of U which are consistent with the experimental suggestion of a mixed spin phase, i.e., a phase with either HS-LS-LS or LS-HS-HS molecules in the $S_{1/3}$ supercell. We can further narrow down the range of values of U, to discriminate between the two possibilities (HS-LS-LS and LS-HS-HS) by computing simulated STM images, and comparing them with experimental data. In the last step, we use a mechanoelastic model that is fitted with parameters obtained from *ab initio* DFT calculations to explain why the mixed spin phase occurs. Our model helps us to understand that it is epitaxial strain-induced spin crossover which results in the mixed spin phase.

3.5.1 Optimized structure of isolated molecule in HS and LS

The IPB molecule has 89 atoms and among them, Fe is octahedrally coordinated by six nitrogen atoms. The two spin states, HS and LS, differ from each other in the Fe-N bond distances in the isolated molecule. The Fe-N bond distance is longer in the HS configuration, this is the well-known magnetovolume effect. We have optimized both HS and LS geometries of an isolated IPB molecule in the gas-phase, at different Fe-N bond distances (see Fig. 3.5). The optimized geometry of the LS molecule is shown in Fig. 3.4(a). Note that in the gas phase, the ground state corresponds to LS. In Fig. 3.5, we have shown the variation of the total energy of the molecule as a function of the Fe-N bond distance (averaged over the six Fe-N bonds). In the two optimal geometries, the average Fe-N bond distance (d_{Fe-N}) for HS is 2.17 Å, and for LS is 1.96 Å. In other words, we can say one can switch between the two spin states by tuning the Fe-N bond distances, d_{Fe-N}.

3.5.2 Determining an approximate value of U

To estimate a reasonable value for the on-site Coulomb interaction parameter (Hubbard parameter) U, we have plotted the total energy of isolated HS and LS molecules

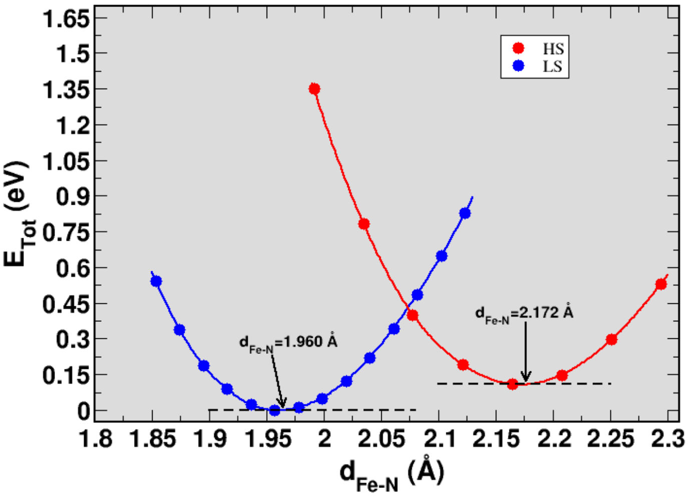

Figure 3.5: DFT+U results, at $U = 6.55$ eV, for the variation in the total energy of an IPB molecule in the gas-phase, as a function of Fe-N bond distance (d_{Fe-N}), averaged over the six Fe-N bonds. The blue and red curves are results for the HS state and LS state, respectively. The zero of energy is set at the minimum of the LS state.

as a function of U (see Fig. 3.6(a)). For $U = 0$, the LS is the ground state; it is favored by 2.38 eV as compared to HS. However, the energy of the LS state increases faster with U than that of the HS state, so that HS is favored above $U = 6.87$ eV. In order to obtain an estimate of the value of U, we are guided by experimental data.

We compare the data in Fig. 3.6(a) with experimental calorimetric data that suggests that the enthalpy difference between the HS and LS states is ~100 meV.[4] From the plot of our DFT data, we get such a difference between the HS and LS molecules for $U = 6.55$ eV. Note, however, that this experimental data is for the three-dimensional condensed phase of the molecule, whereas our DFT calculations are for isolated molecules in the gas phase. We have chosen not to perform DFT calculations on the condensed phase, as the bulk crystals undergo complicated structural transitions between the LS and HS phases.

In any case, any value of U determined would be only approximate; note that we

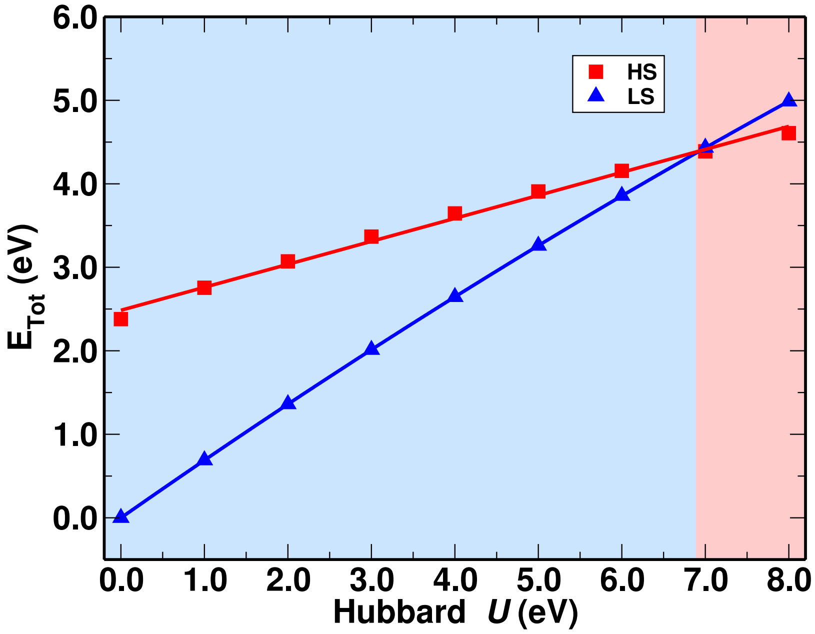

Figure 3.6: DFT results for total energies of HS (red) and LS (blue) IPB in gas-phase as a function of on-site Coulomb potential U. IPB shows HS ground state above ∼6.87 eV and LS ground state below it.

are actually interested in neither the gas phase nor the bulk crystalline phase, but a two-dimensional monolayer of the molecules on the Au(111) surface. Thus, we will keep $U = 6.55$ eV in mind as a reasonable guess, but nevertheless sweep values of U, so as to check how the behavior of the system varies with U.

3.5.3 Finding the molecular orientaion on the substrate

It is vital to know the adsorption geometry of IPB on Au(111) in order to understand the effect of the substrate on the SCO complex. To obtain a shortlist of possible orientations, we consider the three-dimensional molecular crystal of IPB, whose structure is known experimentally. We find that the lattice parameters for three low-index planes of the IPB molecular crystal are in reasonably close agreement with the experimental lattice parameters ($|\vec{A}| = 9.01 \pm 0.04$ Å, $|\vec{B}| = 11.02 \pm 0.02$ Å, $|(\vec{A}, \vec{B})| = 81.0 \pm 0.2°$) of the $S_{1/2}$ cell. The three planes are (001), (010) and (01-1); in the bulk crystal, these three planes have lattice parameters of $|\vec{A}_{(001)}| =$

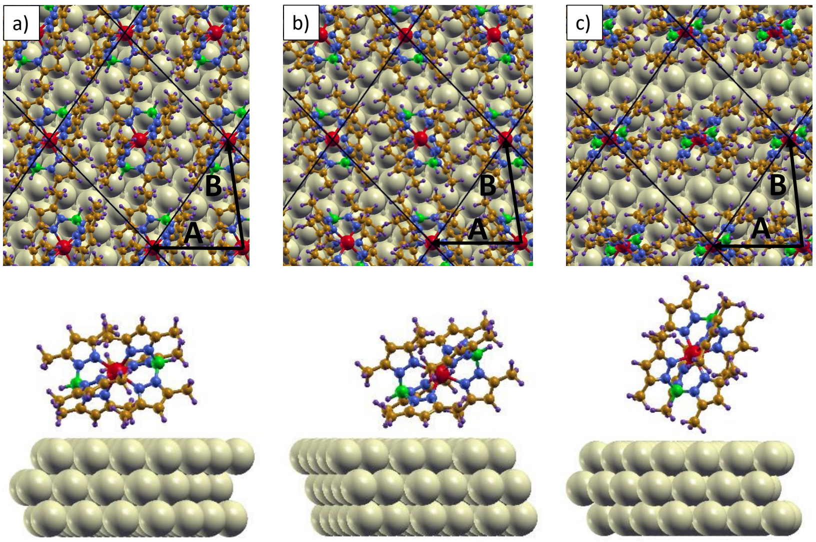

Figure 3.7: Top and side views of three possible adsorption geometries for IPB on Au(111) in a $S_{1/2}$ supercell. The three orientations considered correspond to different planes of the bulk HS crystal a) (01-1) b) (010) c) (001). Color code for atoms is red (iron), blue (nitrogen), green (boron), orange (carbon), violet (hydrogen) and yellow grey (gold). Reprinted with permission from Ref 4. ©2019 American Chemical Society.

8.82 Å, $|\vec{B}_{(001)}| = 10.21$ Å, $|(\vec{A}_{(001)},\vec{B}_{(001)})\ | = 100.09°$, $|\vec{A}_{(010)}| = 8.82$ Å, $|\vec{B}_{(010)}| = 10.79$ Å, $|(\vec{A}_{(010)},\vec{B}_{(010)})| = 85.24°$ and $|\vec{A}_{(01-1)}| = 8.82$ Å, $|\vec{B}_{(01-1)}| = 11.10$ Å, $|(\vec{A}_{(01-1)}, \vec{B}_{(01-1)})| = 85.37°$ respectively. These values may be compared with the values of $|\vec{A}|$ and $|\vec{B}|$ of the experimental lattice. Setting $U = 6.55$ eV, we have computed adsorption energies, for molecular orientations of IPB corresponding to these three planes, on top of the Au(111) substrate in the $S_{1/2}$ supercell (see Fig. 3.7), with both IPB molecules within the unit cell in the HS state.

The adsorption energy E_{ads} of the IPB/Au(111) systems can be calculated using the following formula:

$$E_{\text{ads}} = \frac{1}{n_{IPB}} \left(E_{\text{IPB/Au(111)}} - E^{\text{bare}}_{\text{Au(111)}} - n_{IPB} E^{\text{iso}}_{\text{IPB}} \right), \tag{3.1}$$

where E_{ads} is the adsorption energy per molecule, n_{IPB} is the total number of IPB

Table 3.1: Adsorption energy (in eV/molecule), as calculated using DFT, for a monolayer of HS IPB in $S_{1/2}$ supercell on Au(111), for orientations corresponding to different molecular planes of the bulk HS crystal, (01-1), (010) and (001) (see Fig. 3.7) at U= 6.55 eV.

Molecular Orientation	(01-1)	(010)	(001)
E_{ads} (eV/molecule)	-1.718	-1.646	-0.959

molecules contained within the unit cell (which is 2 in the case of the $S_{1/2}$ supercell). $E_{\text{IPB/Au(111)}}$, $E^{\text{bare}}_{\text{Au(111)}}$ and $E^{\text{iso}}_{\text{IPB}}$ are the total energies of IPB/Au(111), bare Au(111) substrate and an isolated IPB molecule in the gas phase. From the results in Table 3.1, we see that of the three orientations considered by us, the (01-1) orientation is energetically the most favorable on the Au(111) substrate.

To further confirm the orientation, we compute the structure factor from DFT calculations and compare with data obtained from the GIXD experiment. The structure factor $S_{\mathbf{G}}$ (i.e., Fourier transform of the atomic coordinates of the optimized geometry) is calculated using the following equation:

$$S_{\mathbf{G}} = \sum_j f_j e^{i\mathbf{G}\cdot\mathbf{r}_j}, \tag{3.2}$$

where $\mathbf{G}$ is the reciprocal lattice vector, f_j is the atomic form factor, and $\mathbf{r}_j$ is the position of j^{th} basis atom in real space. f_j depends on electron densities of the basis atoms. Note that $S_{\mathbf{G}}$ which is defined in Eq. (3.2) is, in general, a complex number.

Similarly, we can compute $|S_{\mathbf{G}}|$ from GIXD experiment by taking the square root of the X-ray intensity (I), since $I \propto |S_{\mathbf{G}}|^2$. Fig. 3.8 shows a comparison of magnitudes of $|S_{\mathbf{G}}|$ calculated from DFT (white half-disks) and from GIXD, at various points in reciprocal space. (The larger the size of the half disk, the larger the intensity of the corresponding spot). Note that there is no black half-disk present at

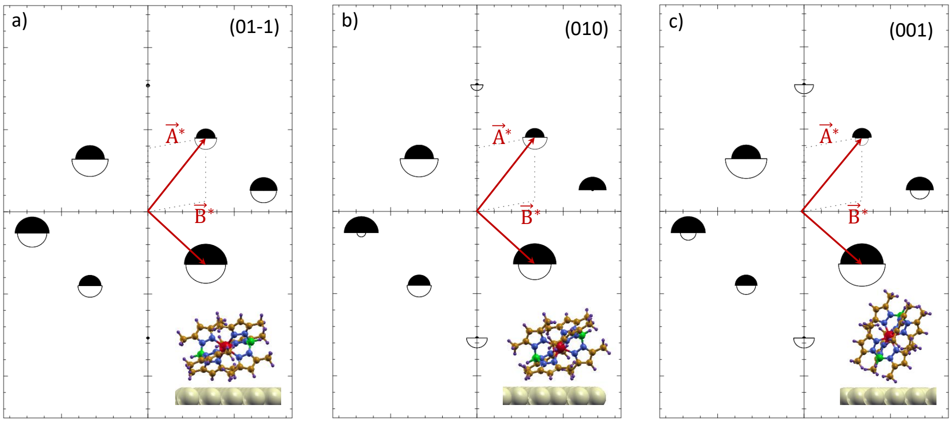

Figure 3.8: Determination of the molecular orientation using theoretically computed (from DFT) and experimentally measured (from GIXD) structure factors. Comparison between measured (black half-disk) and calculated (white half-disk) structure factors for three different orientations of the molecule on the surface. a) (01-1). b) (010). c) (001). $\vec{A}^*$ and $\vec{B}^*$ are the reciprocal lattice vector of the $S_{1/2}$ cell. Reprinted with permission from Ref 4. ©(2019) American Chemical Society.

$\pm k_z$ [see Figs. 3.8(a)-(c)] which means experiment finds zero intensity at $\pm k_z$. We see that the theoretically computed data agree very well with the experimentally measured data only for the (01-1) orientation, because the sizes of the black and white half-disks match very well; in particular, the calculated intensity vanishes along the z direction [see Fig. 3.8(a)]. More quantitatively, we find a χ^2 deviation of 2.4 for the (01-1) orientation, 41.8 for the (010) and 16.4 for the (001). We can therefore, unambiguously, conclude that the (01-1) orientation is the favored one for the IPB molecule on Au(111), based upon both theoretically computed adsorption energies and a comparison between experimental and theoretical structure factors.

We use this (01-1) orientation in the next subsections to continue our study.

3.5.4 Determining spin states as a function of U in $S_{1/3}$

We will now fix the molecular orientation on the substrate as that determined to have the lowest energy in the previous section. We will however now investigate the low-temperature $S_{1/3}$ structure, so as to determine its spin state. We will do this

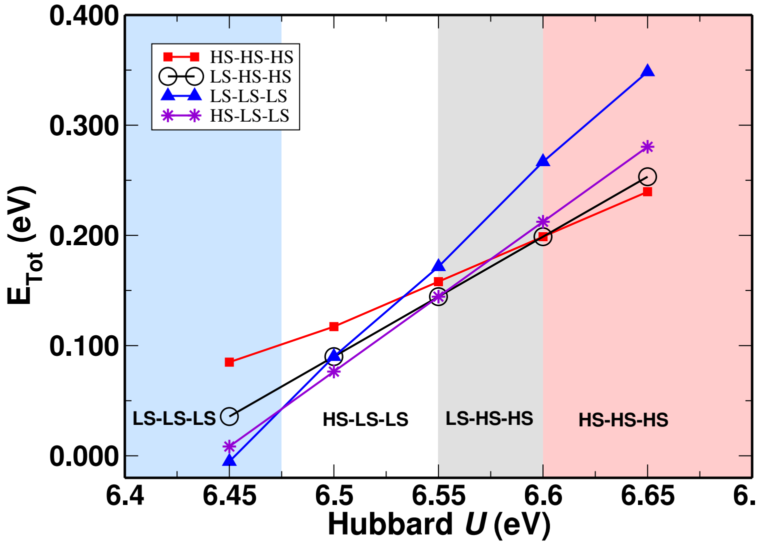

Figure 3.9: Total energies of different spin configurations of a monolayer of IPB in the $S_{1/3}$ unit cell on Au(111) (shown in Fig. 3.4(c)) supercell as a function of Hubbard U. Pure LS phase, i.e., LS-LS-LS, is favored for $U <$ 6.47 eV. Pure HS phase, i.e., HS-HS-HS, is favored for $U >$ 6.60 eV. Mixed-spin phase (either HS-LS-LS or LS-HS-HS) is favored for $6.47 < U < 6.60$.

for several values of U.

Fig. 3.9 shows the variation of total energy for different spin configurations with on-site Coulomb potential, U on Fe. The total energy calculations have been carried out using the $S_{1/3}$ supercell [see Fig. 3.4(c)], taking different combinations of HS and LS states for the three IPB molecules within the supercell. We find that a mixed spin phase (i.e., a phase where two of the molecules are in one spin state, and the third molecule is in the other spin state) is favored for U values between 6.47 eV and 6.60 eV. More specifically, HS-LS-LS is favored for U values between $6.47 < U \leq 6.55$ and LS-HS-HS for $6.55 < U < 6.60$. The pure HS phase i.e., HS-HS-HS is favored for U above 6.6 eV and pure LS phase (LS-LS-LS) is favored below 6.47 eV. This is different from the result we obtained for the isolated molecule, see Fig. 3.6(a), which shows LS ground state for the isolated molecule for $U < 6.87$ eV.

3.5.5 Comparison with STM data

In this section, we try to explain why our guess for U is the best fit for our system. Let us now fix U at our earlier mentioned guess, viz., $U = 6.55$ eV. At this value, LS-HS-HS is the lowest energy spin configuration. This suggests that the two types of molecules imaged in the STM experiments indeed correspond to two different spin states of IPB.

In order to confirm that the ground state observed in the experiments corresponds to a LS-HS-HS spin configuration, we make use of three arguments (i) as mentioned above, the calorimetric measurement is best matched with a U value of 6.55 eV, which leads to a LS-HS-HS state, (ii) we simulated STM images for both LS-HS-HS [see Figs. 3.10(c) and (d)] and HS-LS-LS [see Figs. 3.10(e) and (f)] configurations. We find that the former agrees with experimental STM images [see Figs. 3.10(a) and (b)], i.e., leads to only one out of three molecules being imaged as bright at positive bias, but all three molecules are imaged as bright at negative bias, (iii) subsequent X-ray absorption spectroscopy (XAS) experiments have suggested a 2:1 ratio of HS:LS molecules on the surface.

3.5.6 Mechanoelastic model

So far, we have shown that DFT suggests that a mixed spin configuration is energetically favored. In this subsection, we discuss the reason why such a state is favored, using a one-dimensional mechanoelastic model shown in Fig. 3.11(a). We consider each IPB molecule as a hard sphere. The red colored hard sphere is the HS state and blue colored comparatively smaller sized sphere (because of the shorter Fe-N bond distance in LS compared to HS) represents the LS state. The interaction of the molecules with the substrate is modeled by a spring with spring constant k_{sub}, while interactions between molecules are modeled by springs with a second spring

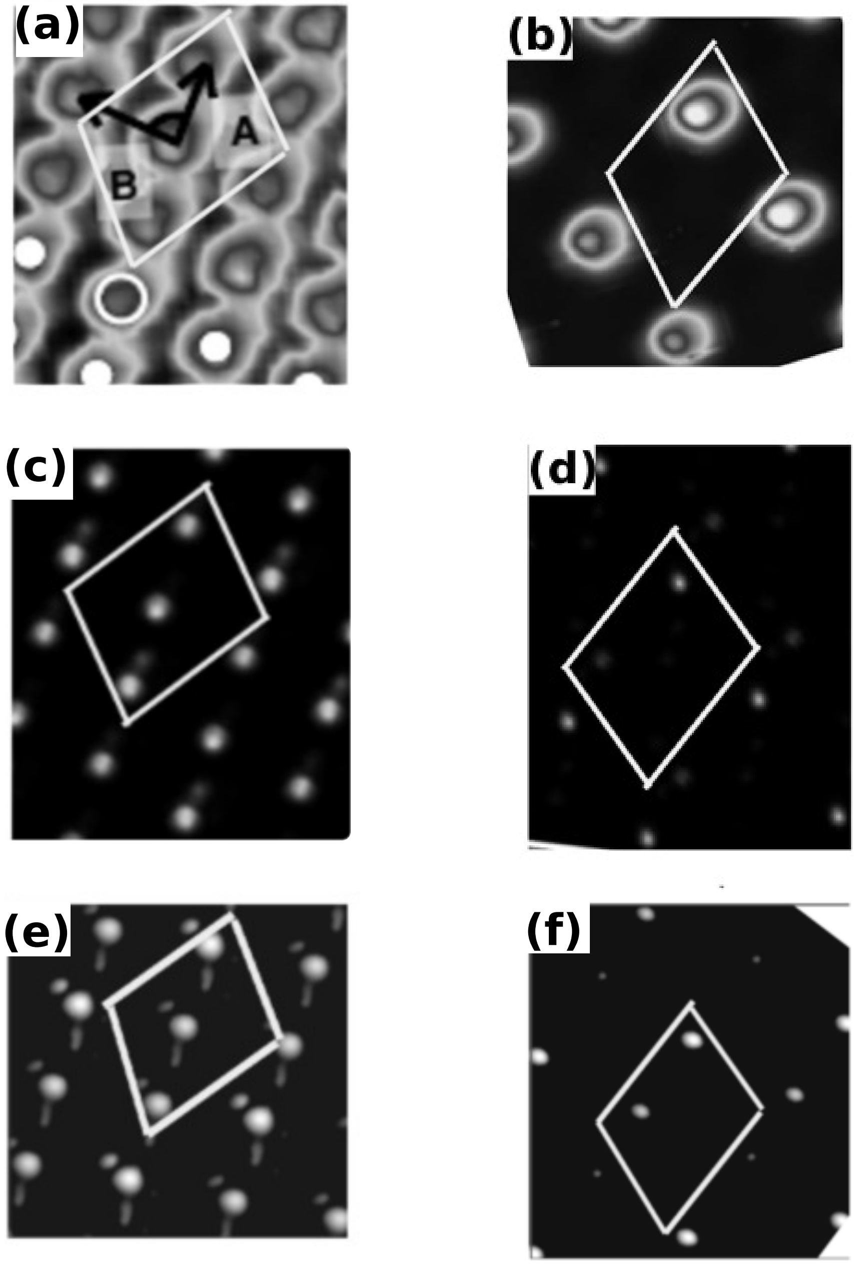

Figure 3.10: Comparison of simulated STM images with experiments, for a monolayer of IPB on Au(111). (a) Experimental, and simulated STM images of (c) LS-HS-HS and (e) HS-LS-LS at -1.5 V. We see all three molecules within the unit cell, in both theory and experiment. (b) Experimental and simulated STM images of (d) LS-HS-HS and (f) HS-LS-LS at 0.3 V. We see only only one out of three molecules within the experimental unit cell; simulation predicts the same only for LS-HS-HS (we see only LS molecules at positive bias). STM simulations have been performed using Tersoff-Hamann approach in constant height mode ($h = 5.6$ Å).

constant k_{mol}. This kind of model to treat spin crossover was first developed by Enachescu *et al.*[25] IPB molecules are strongly bound to the Au substrate due to high adsorption energy which means $k_{sub} >> k_{mol}$. Instead of directly using the k_{sub} term, we use the periodicity imposed by the substrate to incorporate the effect of the substrate. In this situation, we get a one-dimensional chain of IPB molecules with the periodicity imposed by the substrate.

Energetics of 1D-chain:

For simplicity, we consider a one-dimensional chain containing two IPB molecules in the unit cell. Hence, we can get three types of chains, HS-HS, HS-LS and LS-LS considering the two possible spin states of a single IPB molecule. The total energy of the chains depends on the internal energy of the IPB molecules and the intermolecular potential energy. The internal energy of HS and LS molecules can be described as:

$$E_{intra}^{HS} = \frac{1}{2}k_{HS}(x_{HS} - r_{HS})^2, \tag{3.3}$$

and

$$E_{intra}^{LS} = \frac{1}{2}k_{LS}(x_{LS} - r_{LS})^2, \tag{3.4}$$

where k_{HS} and k_{LS} are the internal spring constants of the HS and LS states respectively; x_{HS} and x_{LS} are the new radii of the HS and LS molecules respectively under stress; and $2r_{HS}$ and $2r_{LS}$ are the diameters respectively of the HS and LS molecules in the absence of stress. The molecules also interact with each other through a harmonic potential (V_{inter}):

$$V_{inter} = \frac{1}{2}k_{mol}(l - l_0)^2, \tag{3.5}$$

where l is the distance between the borders of two neighboring molecules and l_0 is the equilibrium length of the non-stretched spring. V_{inter} can be further simplified into the form:

$$V_{inter} = \frac{1}{2} k_{mol} (a - 2r - l_0)^2, \tag{3.6}$$

where $l = a - 2r$, r is radius of IPB molecules in the hard sphere approximation, i.e., r_{HS} for HS and r_{LS} for LS. a is the constrained lattice parameter determined by the substrate [see Fig. 3.11(a)]. The total energies (per unit cell) of the three chains can be expressed in terms of the energy of the LS-LS chain:

$$E_{LS-LS} = 2E_{intra}^{LS} + 2V_{inter}^{LS-LS}, \tag{3.7}$$

$$E_{HS-LS} = \Delta_{SCO} + 2E_{intra}^{LS} + 2V_{inter}^{HS-LS}, \tag{3.8}$$

$$E_{HS-HS} = 2\Delta_{SCO} + 2E_{intra}^{LS} + 2V_{inter}^{HS-HS}, \tag{3.9}$$

where, $\Delta_{SCO} = E_{HS} - E_{LS}$ is the energy required for a LS state to go to HS state in gas-phase.

E_{intra} and V_{inter} from DFT calculations:

It is possible to calculate the intramolecular (k_{HS} and k_{LS}) and the intermolecular (k_{mol}) spring constants from the results obtained from DFT calculations. Fig. 3.5 shows the total energy variation of the HS and LS molecules, as a function of the Fe-N bond distance d_{Fe-N}. Parabolic fits to the data plotted in Fig. 3.5 give intramolecular spring constants, $k_{HS} = 70.5$ eV Å^{-2}, and $k_{LS} = 72.2$ eV Å^{-2} respectively.

In Fig. 3.11(b), we have plotted (black dots) our results from DFT for the change in total energy of a one-dimensional (1D) chain of LS molecules, relative to the total energy of an isolated molecule, plotted as a function of the Fe-Fe bond distance

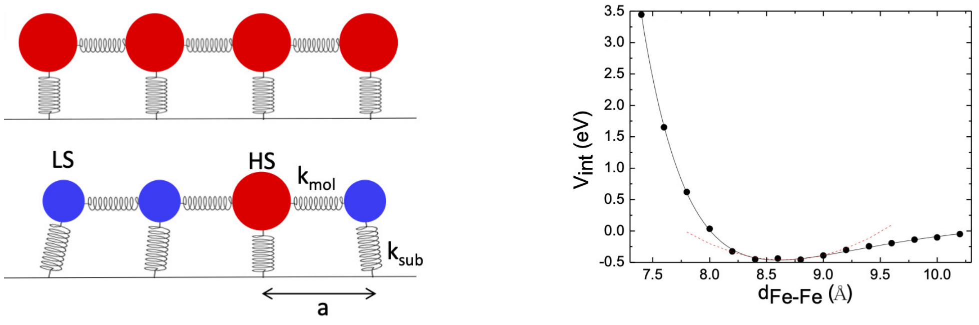

(a) (b)

Figure 3.11: (a) Schematics of the hard sphere mechanoelastic model. Above: all the molecules are in HS states (red spheres). Below: Chain of mixed phase where both HS (red) and LS (blue) are present. Mixed phase arises because of the substrate-imposed epitaxial strain. k_{sub} and k_{mol} are the spring constant for molecule-substrate interaction and intermolecular interaction. (b) Inter-atomic potential of a periodic chain of LS molecules as a function of their intermolecular distance (black dots). The solid black line is a fit based on a Morse potential. The dotted red line is the closest parabolic potential. Adapted with permission from Ref 4. ©2019 American Chemical Society.

(d_{Fe-Fe}) between neighboring molecules. V_{inter} is defined as the energy required to form such a chain from isolated molecules. We fitted the DFT results for V_{inter} in Fig. 3.11(b) with a simple Morse potential (see solid black curve in the figure), $V(r) = V(r_e) + A(1 - e^{-B(r-r_e)})^2$, and obtained the three parameters needed to describe the potential from this fit. They are $V(r_e) = -0.46$ eV, $A = 0.64$ eV and $B = 1.04$ Å^{-1}. r_e is the equilibrium distance between the LS molecules in the LS-LS chain and we got $r_e = 8.6$ Å from DFT, see Fig. 3.11(b). Close to the minimum, we can approximate this intermolecular potential by a harmonic potential with spring constant, $k_{mol} = 2AB^2 = 1.38$ eV.Å^{-2}, as shown by the dotted red line in Fig. 3.11(b).

The favored Fe-N bond distances d_{Fe-N} in the LS and HS states are 1.97 Å and 2.18 Å respectively. Therefore, in a hard sphere approximation, the difference in the radius of LS and HS is 0.21 Å. Therefore, the equilibrium distance for a HS-HS chain, r_e^{HS-HS}, can be estimated as: $r_e^{LS-LS} + (2 \times 0.21) = 9.02$ Å.

1D-chain model fitted with DFT parameters:

Eqs. (3.7) - (3.9) can be simplified to:

$$E_{LS-LS} = constant + 2 \times \frac{1}{2} k_{mol} (a - 2r_{LS} - l_0)^2, \tag{3.10}$$

$$E_{HS-LS} = \Delta_{SCO} + constant + 2 \times \frac{1}{2} k_{mol} (a - r_{HS} - r_{LS} - l_0)^2, \tag{3.11}$$

$$E_{HS-HS} = 2\Delta_{SCO} + constant + 2 \times \frac{1}{2} k_{mol} (a - 2r_{HS} - l_0)^2. \tag{3.12}$$

Note that we have replaced the internal energy of the LS-LS chain, E_{intra}^{LS} by a constant term in all three equations. l_0 can assumed to be the twice of the van der Waals radius of the H atom which is 2.5 Å. We have considered the van der Waals radius of the H atoms because the periphery of the IPB molecule has H atoms. Hence, H atoms will come into contact first when the molecules come close. Again, r_{HS} and r_{LS} can be evaluated using the relation: $r_e = 2r + l_0$. From DFT, we got r_e^{LS-LS}= 8.6 Å and r_e^{HS-HS}= 9.02 Å. So, $2r_{HS}$ and $2r_{LS}$ are 6.52 Å and 6.1 Å, respectively. If we substitute these values for r_{HS}, r_{LS}, l_0, and k_{mol} in the equations Eq (3.10) - (3.12), we get an expression for the total energy as a function of Δ_{SCO} and a, the lattice parameter constrained by the substrate. Accordingly, Fig. 3.12 shows the variation of the total energy as a function of a, at Δ_{SCO}= 108 meV. We have chosen Δ_{SCO}= 108 meV based on our DFT calculation, see Fig. 3.6(a). When $a < 8.891$ Å we get a pure LS phase (blue region of the Fig. 3.12). We get a pure HS phase (orange region of the Fig. 3.12) , when $a > 9.101$ Å. If the lattice parameter is constrained inside the range 8.891 Å to 9.101 Å i.e, 8.891 Å $> a < 9.101$ Å, we get mixed spin configurations (pink region of the Fig. 3.12).

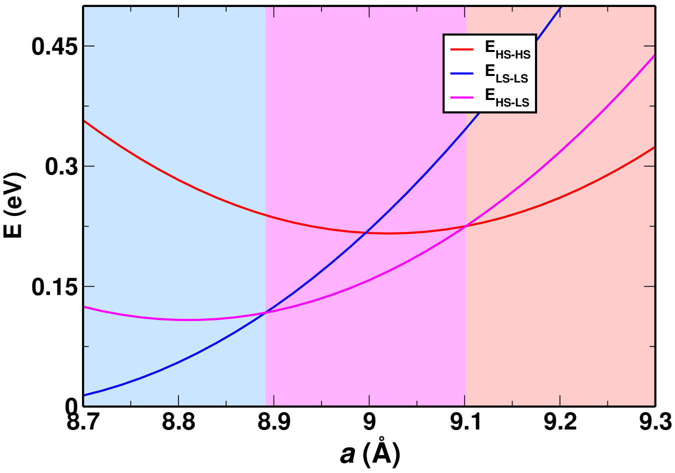

Figure 3.12: Energetics and phase diagram using the mechanoelastic model. $\mathrm{E}_{\text{LS-LS}}$, $\mathrm{E}_{\text{HS-HS}}$ and $\mathrm{E}_{\text{HS-LS}}$ as function of a for $\Delta_{SCO} = 108$ meV. In this graph, the model parameters are set at $k_{mol} = 1.38$ eV.Å^{-2}, $2r_{LS} = 6.1$ Å and $2r_{HS} = 6.52$ Å and l_0=2.5 Å. The three phases, LS-LS, HS-LS and HS-HS, have been shown using three colors, blue, pink, and orange, respectively.

The substrate constrains the lattice parameter of a molecular lattice grown on it, which therefore causes a strain inside the molecular lattice, known as epitaxial strain. The epitaxial strain induces spin crossover. It is a crossover to a mixed-spin phase. The experimental lattice parameter is 8.905 Å. One can note that there is only a very narrow range of a in which the mixed spin phase is favored, and our system just happens to fall within that range. (We also note, however, that our model is a very simple one, that is meant to capture the essential physics qualitatively and not necessarily quantitatively.)

3.6 Conclusions

We have used DFT+U calculations to study LS, HS and mixed spin configurations of IPB on Au(111). We find that for the isolated molecule, the low spin state LS is lower in energy than the high spin state HS for values of the Hubbard parameter $U < 6.87$ eV, but LS and HS become degenerate for $U = 6.87$ eV. IPB forms an ordered monolayer on Au(111), with the molecules aligned on the substrate with an orientation corresponding to the (01-1) orientation of the bulk IPB crystal. We find that both U and epitaxial strain (imposed by the Au substrate) play an important role in determining mixed spin phases. We estimated, semi-empirically, that an approximate value for U is 6.55 eV. We find that for this value of U, a configuration where the three molecules in the $S_{1/3}$ unit cell have spin states corresponding to LS-HS-HS, is the ground state. We have shown that a 1D mechanoelastic model, whose parameters are obtained from DFT calculations, can describe the substrate-imposed epitaxial strain and its effect in tuning spin states, resulting in spin crossover to the mixed-spin state.

Our results emphasize that when using spin crossover molecules in devices, the effects of the substrate may play a vital role in determining the spin switching properties. One way to tune the epitaxial strain would be to use different metallic substrates with different lattice parameters. However, note that changing the substrate species would change not just the lattice constant but also other factors such as the extent of charge transfer. Moreover, if one wanted to switch the spin states in a device by tuning the epitaxial strain, then obviously changing the substrate species is not an option. For device applications, one could think of applying mechanical strain,[38;39] e.g., by bending the substrate.

Bibliography

[1] N. N. Greenwood and A. Earnshaw, *Chemistry of the Elements.* Elsevier, 2012.

[2] K. Bairagi, O. Iasco, A. Bellec, A. Kartsev, D. Li, J. Lagoute, C. Chacon, Y. Girard, S. Rousset, F. Miserque, Y. J. Dappe, A. Smogunov, C. Barreteau, M.-L. Boillot, T. Mallah, and V. Repain, "Molecular-scale dynamics of light-induced spin cross-over in a two-dimensional layer," *Nat. Comm.*, vol. 7, p. 12212, 2016.

[3] K. Bairagi, A. Bellec, C. Fourmental, O. Iasco, J. Lagoute, C. Chacon, Y. Girard, S. Rousset, F. Choueikani, E. Otero, P. Ohresser, P. Sainctavit, M.-L. Boillot, T. Mallah, and V. Repain, "Temperature, Light, and Soft X-ray-induced Spin crossover in a Single Layer of $\mathrm{Fe}^{\mathrm{II}}$-Pyrazolylborate Molecules in Direct Contact with Gold," *J. Phys. Chem. C*, vol. 122, p. 727, 2018.

[4] C. Fourmental, S. Mondal, R. Banerjee, A. Bellec, Y. Garreau, A. Coati, C. Chacon, Y. Girard, J. Lagoute, S. Rousset, M.-L. Boillot, T. Mallah, C. Enachescu, C. Barreteau, Y. J. Dappe, A. Smogunov, S. Narasimhan, and V. Repain, "Importance of epitaxial strain at a spin-crossover molecule–metal interface," *J. Phys. Chem. Lett.*, vol. 10, p. 4103, 2019.

[5] M. Gruber, T. Miyamachi, V. Davesne, M. Bowen, S. Boukari, W. Wulfhekel,

M. Alouani, and E. Beaurepaire, “Spin crossover in Fe(phen)$_2$(NCS)$_2$ complexes on metallic surfaces,” *J. Chem. Phys.*, vol. 146, p. 092312, 2017.

[6] J. A. Real, A. B. Gaspar, and M. C. Muñoz, “Thermal, pressure and light switchable spin-crossover materials,” *Dalton Trans.*, p. 2062, 2005.

[7] A. Bousseksou, G. Molnár, L. Salmon, and W. Nicolazzi, “Molecular spin crossover phenomenon: recent achievements and prospects,” *Chem. Soc. Rev.*, vol. 40, p. 3313, 2011.

[8] C. Lefter, V. Davesne, L. Salmon, G. Molnár, P. Demont, A. Rotaru, and A. Bousseksou, “Charge Transport and Electrical Properties of Spin Crossover Materials: Towards Nanoelectronic and Spintronic Devices,” *Magnetochemistry*, vol. 2, p. 18, 2016.

[9] M. Shatruk, C. Avendano, and K. R. Dunbar, “Cyanide-bridged complexes of transition metals: A molecular magnetism perspective,” *Prog. Inog. Chem.*, vol. 56, p. 155, 2009.

[10] C. Lefter, S. Rat, J. S. Costa, M. D. Manrique-Juárez, C. M. Quintero, L. Salmon, I. Séguy, T. Leichle, L. Nicu, P. Demont, A. Rotaru, G. Molnár, and A. Bousseksou, “Current Switching Coupled to Molecular Spin-States in Large-Area Junctions,” *Adv. Mater.*, vol. 28, p. 7508, 2016.

[11] E. J. Devid, P. N. Martinho, M. V. Kamalakar, I. Šalitroš, U. Prendergast, J.-F. Dayen, V. Meded, T. Lemma, R. González-Prieto, F. Evers, T. E. Keyes, M. Ruben, B. Doudin, and S. J. van der Molen, “Spin Transition in Arrays of Gold Nanoparticles and Spin Crossover Molecules,” *ACS Nano*, vol. 9, p. 4496, 2015.

[12] T. G. Gopakumar, F. Matino, H. Naggert, A. Bannwarth, F. Tuczek, and

R. Berndt, “Electron-Induced Spin Crossover of Single Molecules in a Bilayer on Gold,” *Angew. Chem. Int. Ed.*, vol. 51, p. 6262, 2012.

[13] T. G. Gopakumar, M. Bernien, H. Naggert, F. Matino, C. F. Hermanns, A. Bannwarth, S. Mühlenberend, A. Krüger, D. Krüger, F. Nickel, W. Walter, R. Berndt, W. Kuch, and F. Tuczek, “Spin-Crossover Complex on Au(111): Structural and Electronic Differences Between Mono- and Multilayers,” *Chem. Eur. J.*, vol. 19, p. 15702, 2013.

[14] A. Pronschinske, Y. Chen, G. F. Lewis, D. A. Shultz, A. Calzolari, M. Buongiorno Nardelli, and D. B. Dougherty, “Modification of molecular spin crossover in ultrathin films,” *Nano Lett.*, vol. 13, p. 1429, 2013.

[15] B. Warner, J. C. Oberg, T. G. Gill, F. El Hallak, C. F. Hirjibehedin, M. Serri, S. Heutz, M.-A. Arrio, P. Sainctavit, M. Mannini, *et al.*, “Temperature-and light-induced spin crossover observed by x-ray spectroscopy on isolated fe (ii) complexes on gold,” *J. Phys. Chem. Lett.*, vol. 4, p. 1546, 2013.

[16] T. Miyamachi, M. Gruber, V. Davesne, M. Bowen, S. Boukari, L. Joly, F. Scheurer, G. Rogez, T. K. Yamada, P. Ohresser, *et al.*, “Robust spin crossover and memristance across a single molecule,” *Nat. Commun.*, vol. 3, p. 1, 2012.

[17] M. Gruber, V. Davesne, M. Bowen, S. Boukari, E. Beaurepaire, W. Wulfhekel, and T. Miyamachi, “Spin state of spin-crossover complexes: From single molecules to ultrathin films,” *Phys. Rev. B*, vol. 89, p. 195415, 2014.

[18] S. Lebègue, S. Pillet, and J. G. Ángyán, “Modeling spin-crossover compounds by periodic DFT + U approach,” *Phys. Rev. B*, vol. 78, p. 024433, 2008.

[19] H. Paulsen, “Periodic density functional calculations in order to assess the cooperativity of the spin transition in $Fe(phen)_2(NCS)_2$,” *Magnetochemistry*, vol. 2, p. 14, 2016.

[20] H. M. Le, T.-T. Pham, V. D. Dat, and Y. Kawazoe, "First-principles modeling of metal (ii) ferrocyanide: electronic property, magnetism, bulk moduli, and the role of C≡N-defect," *J. Phys. D*, vol. 50, p. 035004, 2016.

[21] S. Gueddida and M. Alouani, "Spin crossover in a single fe(phen)$_2$(ncs)$_2$ molecule adsorbed onto metallic substrates: An ab initio calculation," *Phys. Rev. B*, vol. 87, p. 144413, 2013.

[22] C. Enachescu, L. Stoleriu, A. Stancu, and A. Hauser, "Model for Elastic Relaxation Phenomena in Finite 2d Hexagonal Molecular Lattices," *Phys. Rev. Lett.*, vol. 102, p. 257204, 2009.

[23] K. Boukheddaden and A. Bailly-Reyre, "Towards the elastic properties of 3d spin-crossover thin films: Evidence of buckling effects," *Europhys. Lett.*, vol. 103, p. 26005, 2013.

[24] T. Delgado, C. Enachescu, A. Tissot, L. Guénée, A. Hauser, and C. Besnard, "The influence of the sample dispersion on a solid surface in the thermal spin transition of [Fe(pz)Pt(CN)$_4$] nanoparticles," *Phys. Chem. Chem. Phys.*, vol. 20, p. 12493, 2018.

[25] C. Enachescu and A. Hauser, "Study of switching in spin transition compounds within the mechanoelastic model with realistic parameters," *Phys. Chem. Chem. Phys.*, vol. 18, p. 20591, 2016.

[26] M. Bernien, H. Naggert, L. M. Arruda, L. Kipgen, F. Nickel, J. Miguel, C. F. Hermanns, A. Krüger, D. Krüger, E. Schierle, E. Weschke, F. Tuczek, and W. Kuch, "Highly Efficient Thermal and Light-Induced Spin-State Switching of an Fe(II) Complex in Direct Contact with a Solid Surface," *ACS Nano*, vol. 9, p. 8960, 2015.

[27] L. Kipgen, M. Bernien, S. Ossinger, F. Nickel, A. J. Britton, L. M. Arruda, H. Naggert, C. Luo, C. Lotze, H. Ryll, F. Radu, E. Schierle, E. Weschke, F. Tuczek, and W. Kuch, "Evolution of cooperativity in the spin transition of an iron(II) complex on a graphite surface," *Nat. Comm.*, vol. 9, p. 2984, 2018.

[28] V. Davesne, M. Gruber, M. Studniarek, W. Doh, S. Zafeiratos, L. Joly, F. Sirotti, M. Silly, A. Gaspar, J. Real, *et al.*, "Hysteresis and change of transition temperature in thin films of Fe$\{$[Me2Pyrz] 3BH$\}_2$, a new sublimable spin-crossover molecule," *J. Chem. Phys*, vol. 142, p. 194702, 2015.

[29] P. Giannozzi, S. Baroni, N. Bonini, M. Calandra, R. Car, C. Cavazzoni, Davide Ceresoli, G. L. Chiarotti, M. Cococcioni, I. Dabo, A. D. Corso, S. d. Gironcoli, S. Fabris, G. Fratesi, R. Gebauer, U. Gerstmann, C. Gougoussis, Anton Kokalj, M. Lazzeri, L. Martin-Samos, N. Marzari, F. Mauri, R. Mazzarello, Stefano Paolini, A. Pasquarello, L. Paulatto, C. Sbraccia, S. Scandolo, G. Sclauzero, A. P. Seitsonen, A. Smogunov, P. Umari, and R. M. Wentzcovitch, "QUANTUM ESPRESSO: a modular and open-source software project for quantum simulations of materials," *J. Phys.: Condens. Matter*, vol. 21, p. 395502, 2009.

[30] P. Giannozzi, O. Andreussi, T. Brumme, O. Bunau, M. B. Nardelli, M. Calandra, R. Car, C. Cavazzoni, D. Ceresoli, M. Cococcioni, *et al.*, "Advanced capabilities for materials modelling with quantum espresso," *Journal of Physics: Condensed Matter*, vol. 29, p. 465901, 2017.

[31] D. Vanderbilt, "Soft self-consistent pseudopotentials in a generalized eigenvalue formalism," *Phys. Rev. B*, vol. 41, p. 7892, 1990.

[32] J. P. Perdew and A. Zunger, "Self-interaction correction to density-functional approximations for many-electron systems," *Phys. Rev. B*, vol. 23, p. 5048, 1981.

[33] J. P. Perdew and A. Zunger, “Self-interaction correction to density-functional approximations for many-electron systems,” *Phys. Rev. B*, vol. 23, pp. 5048–5079, 1981.

[34] A. I. Liechtenstein, V. I. Anisimov, and J. Zaanen, “Density-functional theory and strong interactions: Orbital ordering in Mott-Hubbard insulators,” *Phys. Rev. B*, vol. 52, p. R5467, 1995.

[35] M. Cococcioni and S. de Gironcoli, “Linear response approach to the calculation of the effective interaction parameters in the LDA + U method,” *Phys. Rev. B*, vol. 71, p. 035105, 2005.

[36] C.-L. Fu and K.-M. Ho, “First-principles calculation of the equilibrium ground-state properties of transition metals: Applications to Nb and Mo,” *Phys. Rev. B*, vol. 28, p. 5480, 1983.

[37] J. Tersoff and D. R. Hamann, “Theory of the scanning tunneling microscope,” *Phys. Rev. B*, vol. 31, p. 805, 1985.

[38] Z. Dai, L. Liu, and Z. Zhang, “Strain engineering of 2d materials: issues and opportunities at the interface,” *Adv. Mater.*, vol. 31, p. 1805417, 2019.

[39] M. A. Bissett, M. Tsuji, and H. Ago, “Strain engineering the properties of graphene and other two-dimensional crystals,” *Phys. Chem. Chem. Phys.*, vol. 16, p. 11124, 2014.

Chapter 4

Linear Self Organization of F_4TCNQ on Twisted Bilayer Graphene

4.1 Introduction

Graphene has been a most discussed material because of its several notable properties such as high electrical conductivity,[1] room temperature quantum Hall effect,[2;3] and ambipolar electric field effect.[4] The high electrical conductivity of graphene makes it exceptional in many ways. For example, graphene can be used as a potential candidate in modern electronic devices[5–7] due to its high carrier mobility.

The canonical band structure of graphene near the Fermi level results in massless Dirac fermions, which have been used to explain the origin of several of the exotic properties observed in graphene.[8] However, many of the properties like Dirac cones go away when the graphene layers are stacked in Bernal stacking, also known as AB stacking, where the successive layers are shifted both vertically and laterally and stacked to form a graphite-like structure. Zhou et al. were the first to find Dirac fermions in multilayer graphene.[9] Recent discoveries show that the twist angle between layers can be an interesting parameter to be considered. For example, a large twist angle between the layers can preserve the Dirac cone because of the electronic decoupling between the graphene layers.[10–12] At small twist angles, twisted bilayer graphene (TBLG) shows appealing properties such as very low Fermi velocity, highly localized electron density, and van Hove singularities in the electronic density of states near the Fermi energy.[13] One can tune the position of the van Hove singularities observed in TBLG by varying the twist angle. A theoretical study by Brihuega et al. shows that the larger the twist angle, the farther the van Hove singularity is from the Fermi energy.[14]

Recent experiments have shown that graphene layers with a twist can be grown by a variety of methods, which allow one to access a range of twist angles.[15;16] However, the nature and extent of the interlayer coupling, and the consequences thereof, continue to be debated.[17] Another effect observed in multilayer graphene is that the twist angle results in different Moiré patterns at the surface, whose periodicity depends on the angle.[18] Moiré patterns can also be observed in graphene grown on metal substrates such as Au(111) and Ru(0001).[19] As a result of the twist between the successive layers, in the Moiré, in different regions of the unit cell, the stacking changes from AA to AB to in-between. In STM images, the Moire pattern of TBLG is characterized by the presence of large bright spots, which are roughly circular in shape, see Fig. 4.1. The Moiré pattern itself constitutes a triangular lattice, where each bright spot has six other bright spots as neighbors. These bright regions correspond to areas of the TBLG where the carbon atoms in the two layers of TBLG are stacked with AA stacking. Note that each AA region (bright spot) is surrounded by AB regions (darker regions). The region around the centroid of any three nearest-neighbor AA stacked regions corresponds to a region with AB stacking.

From previous work, it is clear that the electronic properties of bilayer and multilayer graphene or graphene grown on the metal substrate is not be the same as

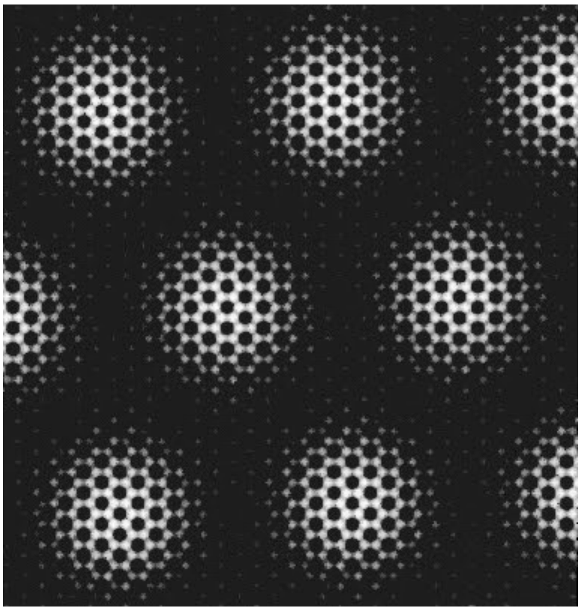

Figure 4.1: Simulated STM image of the Moiré pattern found in the TBLG unit cell. The image has been simulated at the height of 2.73 Å from the surface and at the bias of +0.27 V.

single-layer graphene; instead, it is much more complicated and largely depends on stacking. Moiré patterns show a few interesting local electronic features that can vary from one stacking region to another stacking region. For example, a recent study by Laissardière et al. shows that Dirac electrons (electrons with the energy close to the Dirac points) are localized in AA stacked regions while they are delocalized in the AB regions.[20]

One can expect to see different behavior for organic molecules when they are adsorbed on bilayer graphene or graphene grown on a metal substrate, compared to when they are adsorbed on monolayer graphene. For example, tetracyanoquinodimethane (TCNQ), an electron acceptor-type organic molecule shows molecular magnetism and Kondo resistance when it is adsorbed on graphene grown on Ru(0001).[19] However, the same molecule shows no sign of magnetism,[21] and hence no Kondo effect (Kondo effect can be observed only if the system has a magnetic impurity) when it is adsorbed on monolayer graphene.

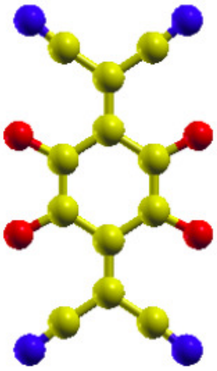

Figure 4.2: Optimized geometry of F_4TCNQ molecule in the gas phase. Color code for atoms: red (F), yellow (C), and blue (N).

In this context, it is important to note that graphene grown on Ru(0001), forms a Moiré pattern in which it shows three different types of stacking; atop, face centered cubic (FCC) and hexagonal close packed (HCP). Garnica et al.[19] showed that TCNQ avoids adsorbing on the atop regions of the Moiré pattern. Another experiment from the same group, combined with DFT, showed that TCNQ and F_4TCNQ (2,3,5,6-tetrafluoro-7,7,8,8-tetracyano-quinodimethane) molecules on the graphene/Ru(0001) Moiré pattern develop magnetism when they adsorb on the FCC stacked regions.[22] Further, the same experiment showed that the molecules adsorbed on FCC stacked area also show Kondo resistance.

Sometimes, organic molecules on the solid surface show self-assembly or self-organization. STM experiments performed by Stradi et al. showed that TCNQ and F_4TCNQ self-organize on a graphene/Ru(0001) substrate.[23] Self-organization of organic molecules on solid surfaces is itself an interesting phenomenon; it is governed primarily by two factors: the molecule-substrate interaction and the molecule-molecule interactions. Self-organization of organic molecules adsorbed on graphene/metal has been the subject of many experiments.[24;25] For example, self-assembly of TCNQ has been investigated by previous authors on graphene supported over Ir(111),[26;27] and on Au(111).[28]

In this thesis chapter, we are particularly interested in the self-assembly of F_4TCNQ molecules on TBLG. The structure of an isolated F_4TCNQ molecule is shown in Fig. 4.2. We have used *ab initio* density functional theory to solve two experimental puzzles, which are: (1) Why at lower coverages do the molecules adsorb on specific sites within the unit cell of the Moiré formed by the TBLG? More particularly, why do they not adsorb over the high-electron-density AA-stacked regions, given that they are electron acceptors? (2) Why do F_4TCNQ molecules form a linear chain on TBLG at higher (intermediate) coverages of the molecule? In this context, one can note that in contrast, F_4TCNQ forms a two-dimensional monolayer on a graphene/Ir(111) substrate,[29] and two-dimensional islands on a graphene/BN substrate at higher coverage. Using density functional theory (DFT), we show that maximizing the van der Waals interaction between the molecule and substrate favors the molecule stacking near the AB-stacked region of the Moiré at lower coverages. Our calculations also show that the strong intermolecular interaction along a particular direction solves the second puzzle. We believe these findings are of interest because chains formed by the F_4TCNQ molecule on TBLG can possibly be used as molecular wires in next-generation electronic devices.

We have also studied the adsorption of F_4TCNQ on TBLG doped with nitrogen atoms (N-TBLG). We have shown that F_4TCNQ prefers to be adsorbed on the nitrogen dopant (N-site).

4.2 Experimental Background

The experiments were carried out by our collaborators Dr. Harsh and Dr. Lagoute in the MPQ laboratory of the University of Paris-Diderot. They have studied the deposition of F_4TCNQ molecules on TBLG at very low-temperature (4 K) using scanning tunneling microscopy (STM).

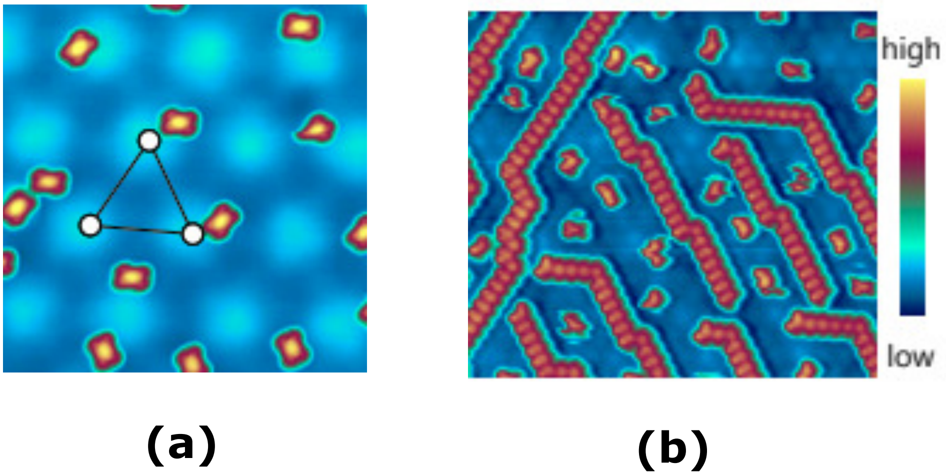

Figure 4.3: Experimental STM images recorded at bias voltage of + 2.0 V, I= 10 pA at 4 K temperature. STM image of the F_4TCNQ molecule at (a) lower coverage, (b) higher coverage. The images are reused with permission from Ref. 30.

Fig 4.3(a) is the STM image recorded for a low coverage of the molecule. We can see that at low coverages, the F_4TCNQ molecules avoid adsorbing on top of the bright AA-stacked regions. Instead, they adsorb over the dark regions of the Moiré. The very bright orange and yellow (roughly rectangular) boxes in Fig 4.3(a) correspond to the F_4TCNQ molecules.

Fig 4.3(b) shows an STM image recorded for a higher (intermediate) coverage of the molecules on TBLG. We see that the molecules form linear chains that avoid passing through the AA stacked regions of the Moiré pattern.

4.3 Systems under study

4.3.1 Twisted Bilayer Graphene

In this subsection, we discuss the TBLG supercell we have used to adsorb the F_4TCNQ molecule.

One can make twisted bilayer graphene from two graphene layers by stacking them in such a way that one layer is rotated at an angle with respect to the other.

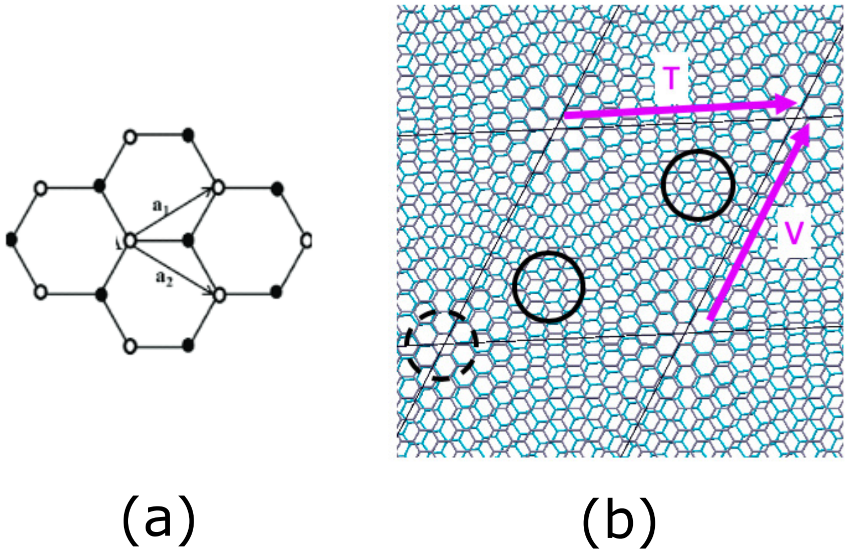

Figure 4.4: (a) $\mathbf{a}_1$ and $\mathbf{a}_2$ are the primitive lattice vectors for the unrotated graphene. (b) Twisted bilayer graphene (TBLG) supercell we used for our calculations. Lattice vectors $\mathbf{T} = 6\mathbf{a}_1 + 7\mathbf{a}_2$ and $\mathbf{V} = -7\mathbf{a}_1 + 13\mathbf{a}_2$ are used to construct this TBLG supercell. We have rotated bottom layer using a twist angle (ϕ) of 5.085° with respect to the top layer to make this TBLG supercell. Color code: gray (top layer), turquoise (bottom layer)

Modeling of TBLG in our DFT calculations requires periodic boundary conditions and hence the commensuration of the two layers. Several such commensurate supercells are possible, whose size depends on the twist angle between the two graphene layers.[31] One should note that not all angles result in commensuration.

If $\mathbf{a}_1$ and $\mathbf{a}_2$ are the primitive lattice vectors of a single graphene layer [see Fig 4.4(a)], one can make an unrotated supercell of graphene using the lattice vectors: $\mathbf{T} = m_1\mathbf{a}_1 + m_2\mathbf{a}_2$ and $\mathbf{V} = -m_2\mathbf{a}_1 + (m_2 + m_1)\mathbf{a}_2$, where m_1 and m_2 are integers. One should note that we need to use the lattice vectors $\mathbf{T}$ and $\mathbf{V}$ in the next paragraphs to construct the TBLG supercell.

TBLG can be made by putting an unrotated layer on top of a rotated layer. To construct the supercell of the rotated layer, we have rotated the primitive lattice vectors of the unrotated graphene (i.e., $\mathbf{a}_1$ and $\mathbf{a}_2$) anti-clockwise by an angle ϕ. One can easily obtain $\mathbf{a}_1^R$ and $\mathbf{a}_2^R$ using the following matrices:

$$\mathbf{a}_1^R = \begin{pmatrix} \cos\phi & -\sin\phi \\ \sin\phi & \cos\phi \end{pmatrix} \mathbf{a}_1, \text{ and } \mathbf{a}_2^R = \begin{pmatrix} \cos\phi & -\sin\phi \\ \sin\phi & \cos\phi \end{pmatrix} \mathbf{a}_2$$

$\mathbf{a}_1^R$ and $\mathbf{a}_2^R$, the primitive lattice vectors of the rotated graphene layer, are used to construct the supercell of the rotated layer using the lattice vectors: $\mathbf{T}^R = n_1\mathbf{a}_1^R + n_2\mathbf{a}_2^R$ and $\mathbf{V}^R =$ -$n_2\mathbf{a}_1^R + (n_2 + n_1)\mathbf{a}_2^R$, where n_1 and n_2 are integers.

Commensuration between the unrotated and rotated layers will be achieved if $\mathbf{T}^R = \mathbf{T}$ or

$$m_1\mathbf{a}_1 + m_2\mathbf{a}_2 = n_1\mathbf{a}_1^R + n_2\mathbf{a}_2^R, \tag{4.1}$$

for integers pairs (m_1,m_2) and (n_1,n_2). As pointed out in Ref. 31, this is a Diophantine problem, which has to be solved to find out the integer pairs (m_1,m_2) and (n_1,n_2) that satisfy Eq. (4.1). The authors of Ref. 31 solve this problem analytically; instead, we solve this using a simple numerical code to get a set of integer values for (m_1,m_2) and (n_1,n_2) for different twist angles, ϕ. For the integer pairs that satisfy the above commensuration condition, the twist angle ϕ is given by the following equation:

$$\cos\phi = \frac{2m_1n_1 + m_1n_2 + m_2n_1 + 2m_2n_2}{2(m_1^2 + m_2^2 + m_1m_2)}. \tag{4.2}$$

Ref. 20 pointed out that we can choose those rotations which can generate rotated supercell of lattice vectors: $\mathbf{T}^R = m_2\mathbf{a}_1^R + m_1\mathbf{a}_2^R$ and $\mathbf{V}^R =$ -$m_1\mathbf{a}_1^R + (m_1 + m_2)\mathbf{a}_2^R$. This means for certain twist angles ϕ, we can get $n_1 = m_2$ and $n_2 = m_1$. These conditions further reduce the Eq. (4.2) to:

$$\cos\phi = \frac{4m_1m_2 + m_1^2 + m_2^2}{2(m_1^2 + m_2^2 + m_1m_2)}. \tag{4.3}$$

The Eq. (4.3) was solved using a numerical code. As an input of the code, we have used different integer numbers for m_1 and m_2. For each pair of m_1 and m_2 we get a value of ϕ by solving the Eq. (4.3). For example a pair $m_1 = 6$ and $m_2 = 7$ gives the $\phi = 5.085°$. To perform the DFT calculations we have used $m_1 = 6$ and $m_2 = 7$ to construct a TBLG supercell with the lattice vectors: $\mathbf{T} = 6\mathbf{a}_1 + 7\mathbf{a}_2$ and $\mathbf{V} = -7\mathbf{a}_1 + 13\mathbf{a}_2$.

The resulting TBLG supercell (for $m_1 = 6$ and $m_2 = 7$) is shown in Fig. 4.4(b) where the bottom layer is rotated anticlockwise by 5.085° with respect to the top layer. It should be noted that this supercell chosen by us results in a Moiré periodicity of 27.77 Å that is approximately half of that obtained in the STM experiments. A periodicity of 54 Å has been observed in the experiment. We couldn't afford experimental unitcell due to high computational cost.

We can calculate the total number of C atoms present in the per layer of our TBLG unitcell (N_{TBLG}) using the relation $N_{TBLG} = 2(m_1^2 + m_2^2 + m_1 m_2)$. We thus obtain $N_{TBLG} = 254$ for $m_1 = 6$ and $m_2 = 7$. So, the TBLG supercell contains a total number of 508 C atoms when both the layers are considered together. Fig. 4.4(b) shows the Moiré pattern formed by this TBLG structure, with AA stacked and AB stacked regions along the long diagonal of the unit cell. The AA region has been shown using a dotted circle, and the AB region has been shown using a solid circle in Fig. 4.4(b). The size of the AA/AB stacked region is directly proportional to $\frac{1}{\phi}$ (see Ref. 20). Thus, the smaller the twist angle ϕ, the larger is the area where we have AA and AB stacking.

4.3.2 F_4TCNQ on TBLG

At low coverage of F_4TCNQ on TBLG

At low coverage, molecules are far apart from each other, so we can treat them as isolated molecules on TBLG. To model this, we have adsorbed a single F_4TCNQ molecule in the supercell shown in Fig. 4.4(b). To determine the ground state

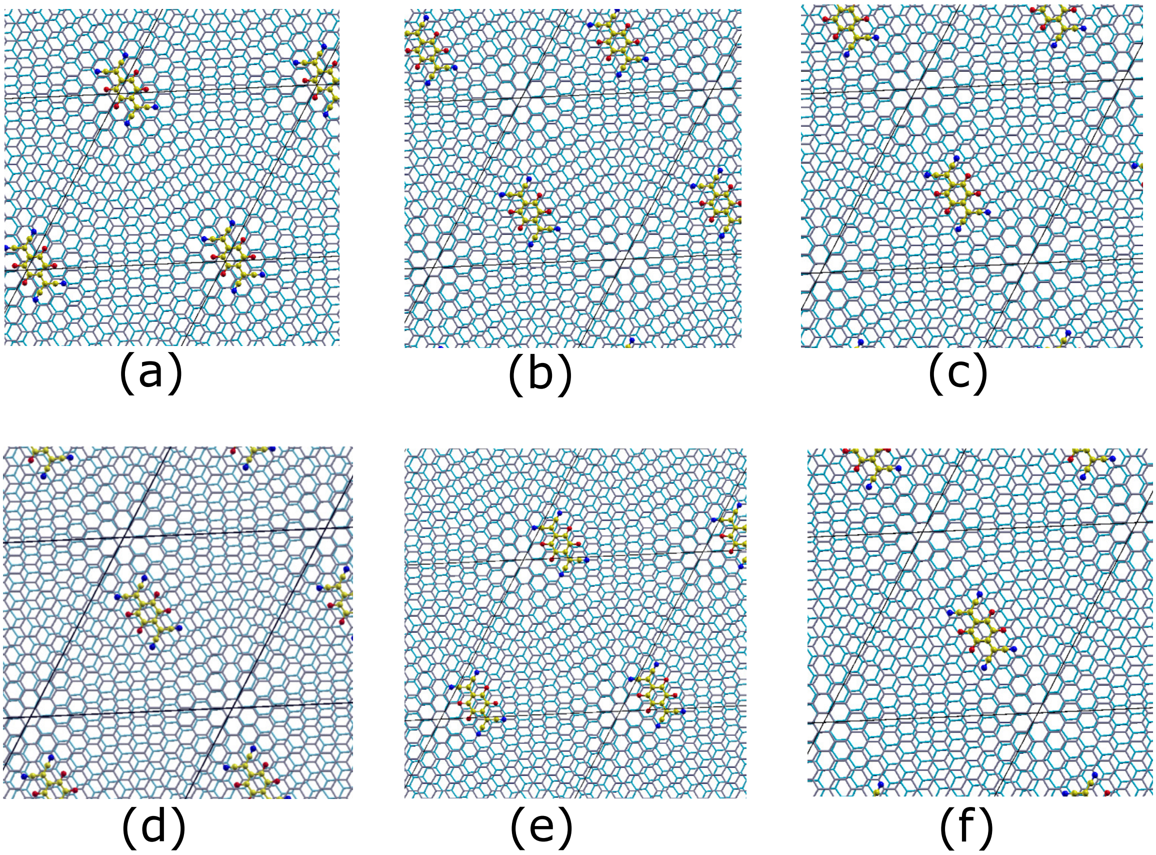

Figure 4.5: Various relaxed adsorption geometries, from DFT, for a single F_4TCNQ molecule on TBLG. We have chosen six different sites (a) site–1 (b) site–2 (c) site–3 (d) site–4 (e) site–5 and (f) site–6 to calculate the adsorption energy. Color code: Yellow (C atom of molecule), blue (N), red (F), gray (top layer graphene), turquoise (bottom layer graphene). The black lines show the boundaries for the unit cell of the TBLG.

adsorption geometry for a single molecule on TBLG, we have considered six different positions for the molecule within the TBLG unit cell. We refer to these six positions as six ‘sites’. The six sites are shown in Figs. 4.5(a)-(f). For example, F_4TCNQ is on the AA and AB stacked regions of the Moiré pattern in site-1 and site-2, respectively; see Figs. 4.5(a) and (b). Similarly, four other sites within the unit cell are shown in Figs. 4.5(c)–(f).

For each site, we also need to check where the hexagonal ring of the molecule prefers to be positioned, relative to the atoms in the upper graphene layer. As an example, various positions considered for the molecule’s hexagonal ring have been

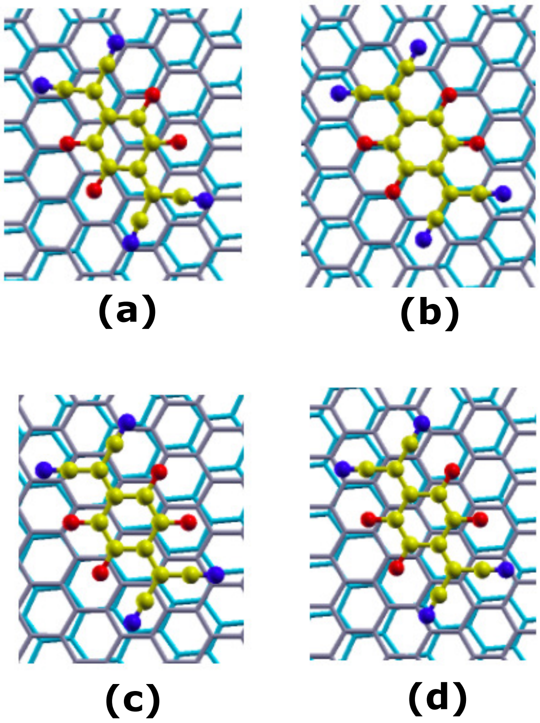

Figure 4.6: Different lateral positions considered for the molecule's hexagonal ring, relative to the substrate, for the site–1. The center of the hexagonal ring of the molecule is on top of (a) the C atom of the toplayer graphene, (b) hexagonal ring of the top layer graphene (c) shifted C atom of the toplayer graphene, (d) C-C bond of the top layer graphene. Color code: Yellow (C atom of molecule), blue (N), red (F), gray (top layer graphene), turquoise (bottom layer graphene).

shown for the site–1 in Fig. 4.6. For example, the center of the hexagonal ring of the molecule is on top of a C atom of the upper graphene layer in Fig. 4.6(a). In contrast, in Fig. 4.6(c), the center of the hexagonal ring is not exactly on top of C atom like in Fig. 4.6(a); instead, it has a lateral shift. Similarly, the hexagonal ring of the F_4TCNQ molecule lies directly on top of the hexagonal ring of the upper graphene layer in Fig. 4.6(b), but on top of a C-C bond of the upper graphene layer in Fig. 4.6(d). In a similar fashion, for all the sites considered within the TBLG unit cell, we have considered various such laterally shifted configurations to determine the lowest energy geometry for each site.

At higher (intermediate) coverage of F_4TCNQ on TBLG

Upon deposition of a higher (intermediate) coverage of F_4TCNQ, the molecules could possibly form either a two-dimensional (2D) monolayer or a one-dimensional (1D) linear chain, depending on the intermolecular interactions. We have considered both the 2D monolayer and 1D linear chain to compare their formation energies. In the case of the linear chain, we have considered two types of 1D chains, which we have shown in Figs. 4.7(a) and (b). Note that in the figure, both types of chains have been created by adsorbing three molecules within the TBLG unit cell shown in Fig. 4.4(b). We have however considered various numbers of molecules within the unit cell (i.e., various intermolecular spacings within the linear chain) and found the optimal configuration. The chain shown in Fig. 4.7(a) passes through both AA- & AB-stacked regions, whereas the one shown in Fig. 4.7(b) avoids AA-stacked regions to pass through AB-stacked regions. A 2D monolayer of F_4TCNQ is constructed by adsorbing six molecules within the same TBLG supercell. This 2D monolayer is shown in Fig. 4.7(c).

4.4 Computational details

The Quantum ESPRESSO package is used[32;33] to perform all the spin-polarized calculations using *ab initio* density functional theory. The interaction between the ions and the valence electrons has been described using ultrasoft pseudopotentials.[34] In all the cases, we have used the Perdew-Burke-Ernzerhof (PBE) form of the generalized gradient approximation (GGA) to describe the exchange-correlation interactions.[35] The Kohn-Sham equations have been expanded using a plane-wave basis set. The kinetic energy cutoff for the plane wave set is chosen to be 40 Ry and 400 Ry for the wavefunctions and charge densities, respectively. The semiempirical DFT-D2[36] method has been used to describe the van der Waals interactions. In order to obtain relaxed geometries, all the atomic coordinates are relaxed until the

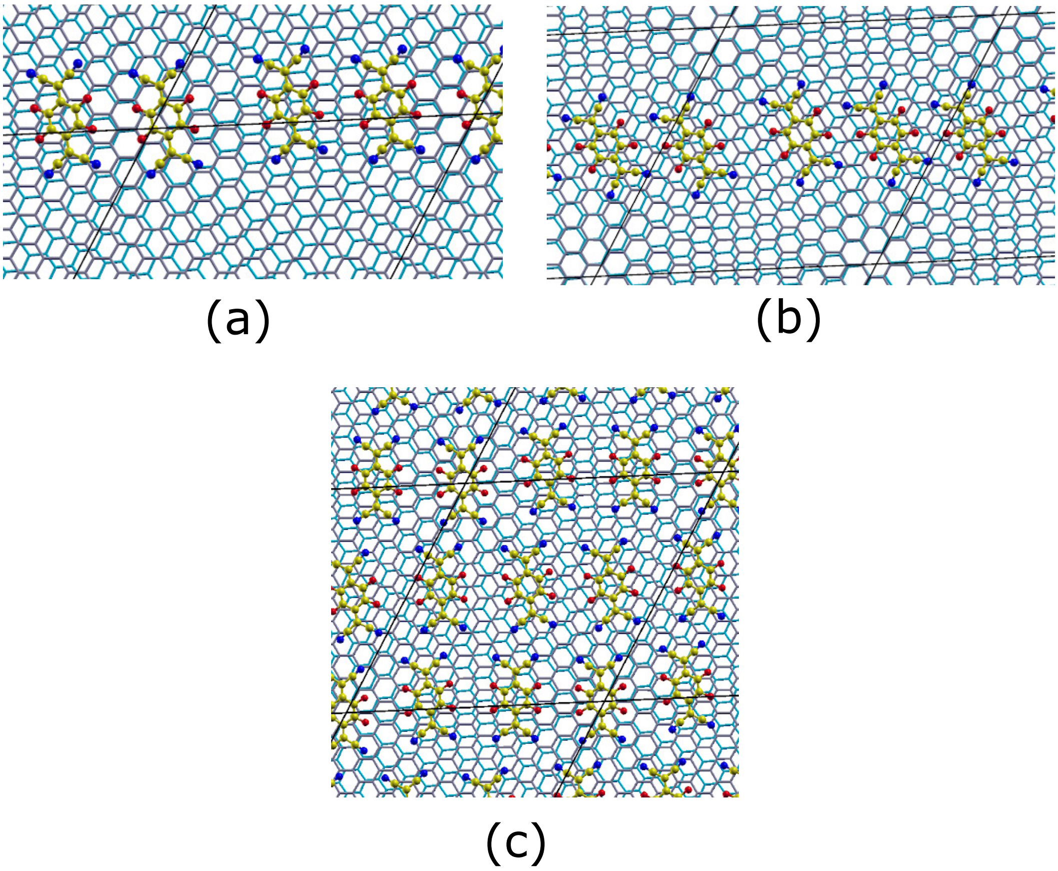

Figure 4.7: Optimized geometry of (a) 1D linear chain passing through AA and AB regions, (b) 1D linear chain passing through AB regions but avoiding AA regions, and (c) 2D monolayer on TBLG. Color code: Yellow (C atom of molecule), blue (N), red (F), gray (top layer graphene), turquoise (bottom layer graphene).

forces are less than 10^{-3} Ry/Bohr.

Brillouin zone (BZ) sampling is restricted to the zone center for the geometry optimization calculations. To generate the density of states (DOS), we have used a $9 \times 9 \times 1$ k-mesh to sample the BZ using the Monkhorst-Pack[37] sampling scheme. In order to aid convergence, we have used the Marzari-Vanderbilt[38] cold smearing function, with a width of 0.001 Ry. The electronic charge associated with each atom is obtained by using the Bader method.[39;40]

Our spin-polarized DFT calculations show that 1D linear chains and 2D monolayers of F_4TCNQ molecules are nonmagnetic. The same is true for an isolated molecule of F_4TCNQ on TBLG, except for the case where the molecule is on N-doped TBLG. The isolated molecule on N-doped TBLG shows a magnetic moment of 1.0 μ_B.

4.5 Results and discussion

4.5.1 Site preference of F_4TCNQ molecule at low coverage

We have performed total energy calculations to compare the adsorption energy for all sites shown in Figs. 4.5(a)-(f). While performing total energy calculations for each site, we have considered four possible positions of the molecule relative to the atoms in the upper layer of the substrate, see, e.g., Figs. 4.6(a)-(d). The adsorption energy ($E_{\rm ads}^{\rm TBLG}$) for each of these sites is calculated using the following formula:

$$E_{\rm ads}^{\rm TBLG} = E_{\rm F_4TCNQ/TBLG} - E_{\rm TBLG}^{\rm bare} - E_{\rm F_4TCNQ}^{\rm iso}, \tag{4.4}$$

where $E_{\rm F_4TCNQ/TBLG}$, $E_{\rm TBLG}^{\rm bare}$, and $E_{\rm F_4TCNQ}^{\rm iso}$ are the total energies of the combined F_4TCNQ/TBLG system, bare twisted bilayer graphene, and an isolated molecule in the gas phase, respectively.

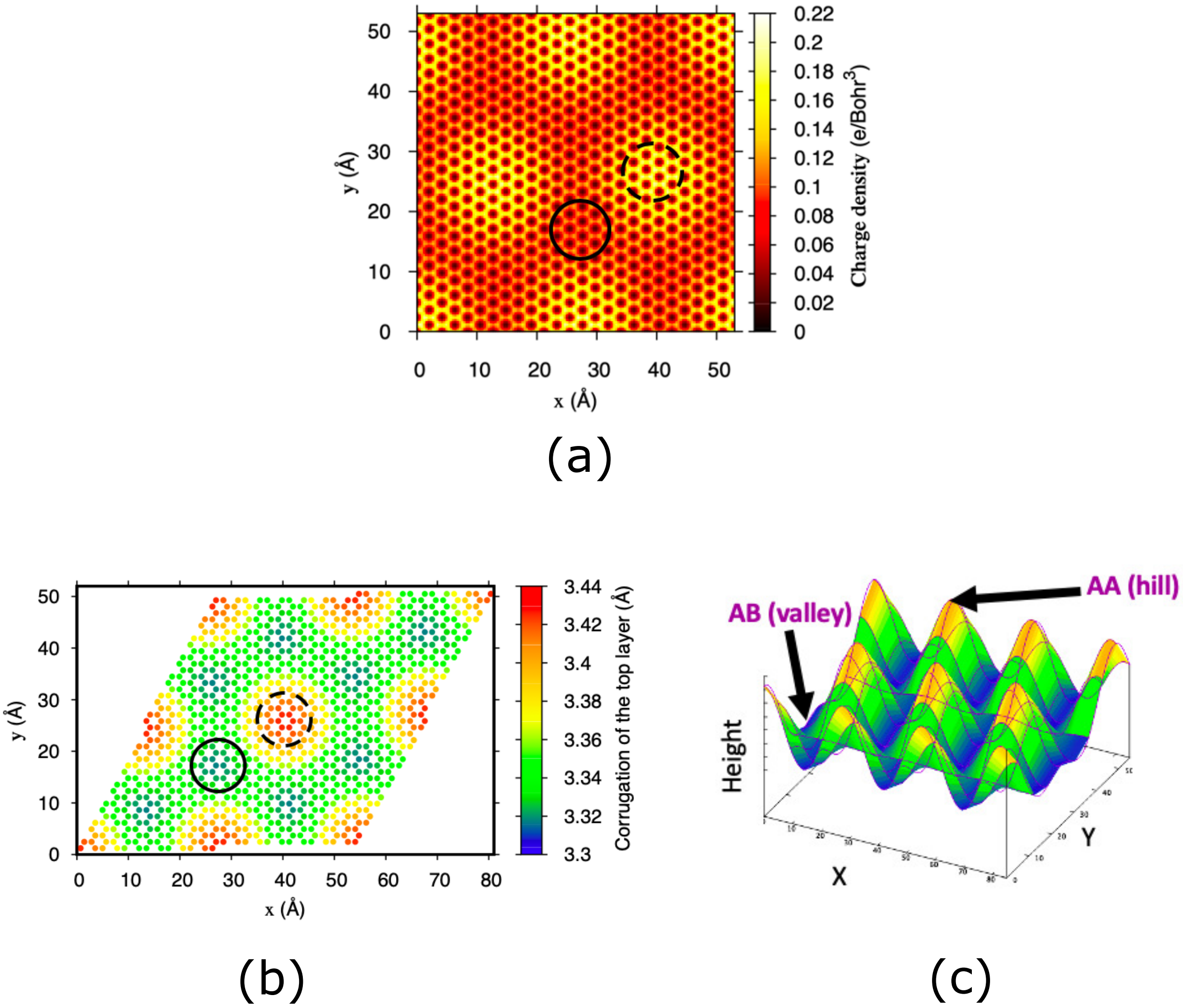

Figure 4.8: (a) Electron density plot for the pristine TBLG, at a plane at a height oft 0.33 Å. Corrugation of the top layer of the pristine TBLG (b) top view and (c) side view.

Table 4.1: Calculated values of adsorption energies in eV, for all the F_4TCNQ/TBLG sites.

Sites considered for TBLG [Corresponding figures]	$E_{\text{ads}}^{\text{TBLG}}$(eV)
site–1 [Fig. 4.5(a)]	-1.435
site–2 [Fig. 4.5(b)]	-1.446
site–3 [Fig. 4.5(c)]	-1.437
site–4 [Fig. 4.5(d)]	-1.434
site–5 [Fig. 4.5(e)]	-1.436
site–6 [Fig. 4.5(f)]	-1.437

We found that the center of the hexagonal ring of the molecule prefers to sit on top of a C-C bond of the upper graphene layer (‘bridge’ position) for all the sites within the unit cell. Similar behavior has been observed in the case of graphene.[41] Therefore, we have tabulated $E_{\text{ads}}^{\text{TBLG}}$ for all the sites in its ‘bridge’ position. Table 4.1 lists our results for the calculated adsorption energy; from these we see that site–2 at bridge position is the ground state adsorption geometry for a single F_4TCNQ molecule (low coverage) on TBLG. However, one can note that the difference in energy among the different binding sites is relatively small, which is in the order of 0.01 eV; and is possibly within the error bars of DFT calculations.

Thus, our calculations suggest that the molecule wants to preferentially adsorb on AB-stacked regions within the Moiré pattern. This is in agreement with the STM results, which suggest that the presumably electron-rich AA-stacked sites are *not* the favored adsorption sites. However, in the experiments, it would appear that the favored adsorption sites are not the centers of the AB-stacked regions, but slightly shifted away from these. We will discuss the reason for this discrepancy further below.

Table 4.2: Total energies in meV for site–1 and site–2 in ‘bridge’ position. The values in the second and third columns represent the total energy calculated when incorporating and not incorporating dispersion interactions, respectively. The zero of energy is set at the value for site-1.

Configuration	$E_{\text{DFT-D2}}$ (meV)	E_{DFT} (meV)
site–1	0.0	0.0
site–2	−11.0	+23.98

We find that the F_4TCNQ/TBLG system shows the same charge (electron) transfer between the substrate and molecule for all the sites considered ($\Delta Q = 0.54$) and no molecular magnetism upon adsorption of the molecule on TBLG. Hence, the molecules are negatively charged on the TBLG substrates. Please note that positive values of ΔQ indicate the electrons transfer from substrate to the molecule.

We have plotted the electronic charge density of bare TBLG in Fig. 4.8(a). Note that we find that the charge density is highest in the AA-stacked region, shown using a dotted circle in Fig. 4.8(a); the solid circle shows the AB-stacked region. As F_4TCNQ is an electron acceptor-type molecule, one might expect that the molecule should preferentially adsorb on the AA-stacked regions, rather than the AB-stacked regions. However, this is not the case, as has been discussed above.

To gain insight into why we find that there is preferential adsorption of the molecule on AB-stacked regions over the AA-stacked regions (i.e., on site–2 rather than site–1), we have carried out DFT calculations with and without including van der Waals (dispersion) interactions. Table 4.2 shows that site–1 is more favorable if we don’t turn on van der Waals interaction. This happens because of the high electron density on AA, which attracts the molecule to sit on it. However, the scenario changes if we turn on the van der Waals interactions, when site–2 becomes preferred. Thus, we can conclude that it is primarily the van der Waals interactions that are responsible for site–2 (AB-stacked regions) being preferred over site–1 (AA stacked regions).

To understand the origin of the preference for site–2 configuration when we turn on the van der Waals interactions, we have plotted the corrugation of the upper graphene layer of the TBLG in Figs. 4.8(b) and (c). It is clear from Fig. 4.8(b) that the AA-stacked region has a greater height, and is convex upward, than the AB-stacked region, which is concave upward. This is in good agreement with the earlier calculations reported in Ref. 14. Hills (red part in Fig. 4.8(c)) correspond to the AA-stacked regions, and valleys (blue part in Fig. 4.8(c)) correspond to the AB-stacked regions. If the adsorbed molecule sits in the concave valley, it has more carbon atoms of the substrate as close neighbors, and can form non-covalent van der Waals bonds with them. This non-covalent van der Waals interaction is significant and makes the energy lower for site–2. This situation does not appear when the molecule is on AA stacked region (site–1).The molecule on the hilltop (AA site) can also form van der Waals interaction with carbon atoms in the convex substrate; however, the interaction is very weak because most of the the atoms are further away.

Why do we find that the AB-stacked region is the most favorable adsorption site for the molecules, whereas the experiments find that this site is slightly shifted away from the AB-stacked regions? We believe that this may be due to the different twist angles and periodicities present in our calculations and in the experiments. For computational reasons, we considered a smaller periodicity than is present in the experimental sample. As a result, we have a larger corrugation of the TBLG layers; thus the effect of the van der Waals interactions dominates over that of the charge density in determining the adsorption site. In the experimental samples, since there is a lower corrugation, the effect of the van der Waals interactions is less, and there is thus a competition between the site favored by the van der Waals interactions

(AB sites) and those favored by the charge density (AA sites). A compromise is achieved by shifting the molecules slightly away from the AB sites.

4.5.2 Formation of a linear chain at higher coverage

We have performed DFT calculations on 1D linear chains and 2D monolayers of F_4TCNQ molecules on TBLG.

Table 4.3 lists our results for adsorption energy ($E_{\mathrm{ads}}^{\mathrm{TBLG}}$) for 1D linear chains of different numbers of moelcules on TBLG, as well as for a 2D monolayer on TBLG. Comparing the values of $E_{\mathrm{ads}}^{\mathrm{TBLG}}$, one can conclude that F_4TCNQ prefers to form a 1D linear chain of three molecules of the type of Fig. 4.7(b) at higher (intermediate) coverages of the molecule, as opposed to islands of the 2D monolayer. This is in agreement with the experimental observations. Note that the favored 1D chain structure is the one that avoids passing through AA-stacked regions but passes through AB-stacked regions [see Fig. 4.7(b)]; this is lower in energy compared to the one passing through AA & AB regions [see Fig. 4.7(a)]. Strong van der Waals interactions between the molecule and substrate stabilize the chain in the case of Fig. 4.7(b), as was the case for the adsorption of an isolated molecule. The average intermolecular spacing in the lowest-energy linear chain (containing 3 molecules within the TBLG unit cell considered by us) is 9.27 Å, this is slightly off from the intermolecular spacing of 8.5 Å estimated from the STM images. Recall, however, that the periodicity of the Moiré pattern for the TBLG in the calculations is smaller than that of the experimental sample by about a factor of 2; this suggests that the intermolecular spacing in the linear chain is sensitive to the periodicity of the Moiré, i.e., to the twist angle of the TBLG.

One can calculate the formation energy for a 1D linear chain from DFT (E_{chain}^{form}) using the following equation:

Table 4.3: Adsorption energies in eV/molecule for the linear chains and monolayer of the molecules on TBLG substrate. Linear chains of different numbers of molecules have been considered on TBLG.

Systems	Number of molecules present in the chain or monolayer	$E_{\mathrm{ads}}^{\mathrm{TBLG}}$(eV/molecule)
Monolayer	6	-1.238
Linear chain	3	-1.521 [a] -1.534 [b]
	4	-1.369
	5	-1.215

[a] Corresponding to Fig. 4.7(a)
[b] Corresponding to Fig. 4.7(b)

$$E_{chain}^{form} = \frac{1}{n_{\mathrm{chain}}}(E_{\mathrm{chain/TBLG}} - nE_{\mathrm{F_4TCNQ/TBLG}}), \tag{4.5}$$

where $E_{\mathrm{chain/TBLG}}$ and $E_{\mathrm{F_4TCNQ/TBLG}}$ are the total energies for the F_4TCNQ linear chain on TBLG and a single F_4TCNQ molecule on TBLG calculated from the DFT. n_{chain} is the number of F_4TCNQ molecules present per unit cell of the chain (which is 3 in our case), see Fig. 4.7(a) and 4.7(b). Eq. (4.5) gives E_{chain}^{form} = -0.09 eV/molecule.

Note that we have found zero magnetic moments for the 1D linear chains and 2D monolayers of F_4TCNQ molecules.

4.5.3 Explanation for the linear chain at higher coverage

We have seen that both DFT calculations and STM experiments show that F_4TCNQ molecules form 1D linear chains when deposited at higher coverage on TBLG. To gain insight into the reasons behind the formation of these linear chains, we need to examine the energy landscape of intermolecular interactions between F_4TCNQ

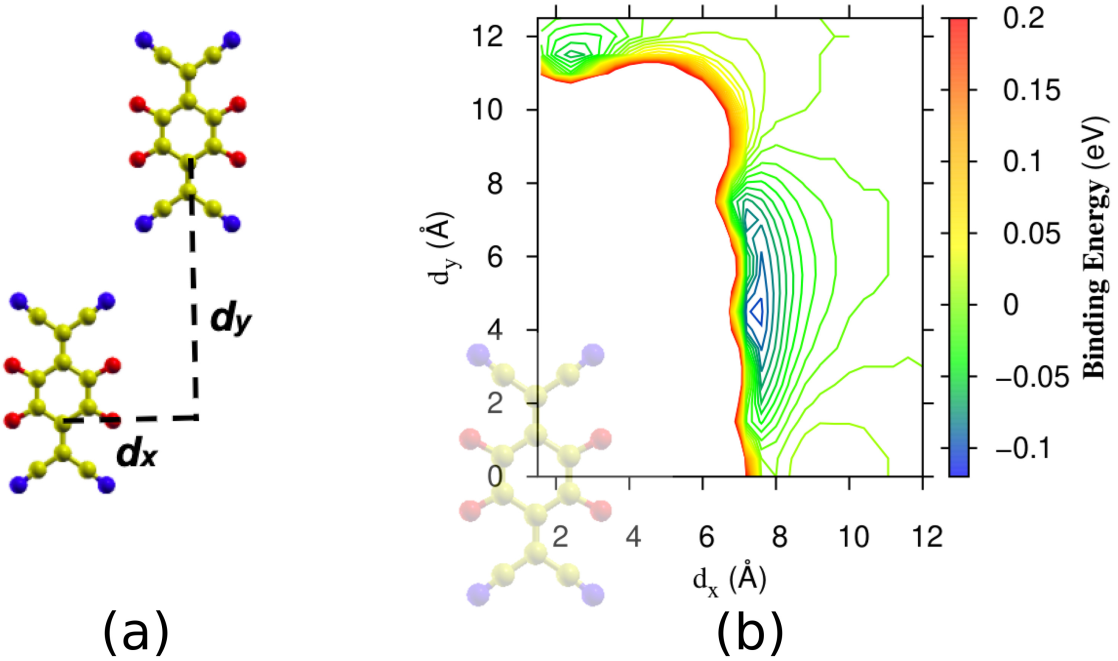

Figure 4.9: (a) $[F_4TCNQ]_2$ dimer, showing the separations d_x and d_y. (b) Binding energy (BE) of $[F_4TCNQ]_2$ as a function of d_x and d_y. BE for the dimer has been calculated usnig the Eq. (4.6)

molecules on TBLG. To study this directly, using DFT calculations, would be extremely computationally expensive. However, the essential physics of this interaction can be captured by a series of computationally less expensive calculations, as carried out below.

First, we have plotted the binding energy of a (neutral) F_4TCNQ dimer ($[F_4TCNQ]_2$) in the gas phase [see Fig. 4.9(b)] as a function of the intermolecular separation along the x and y directions. d_x and d_y are the intermolecular distance along the x axis and y axis in the $[F_4TCNQ]_2$ dimer; see Fig. 4.9(a). The binding energy (BE) of the F_4TCNQ dimer is computed using the following equation:

$$\mathrm{BE} = E_{\mathrm{dimer}} - 2E_{\mathrm{iso}}, \tag{4.6}$$

where E_{dimer} and E_{iso} are the total energies from DFT of the neutral $[F_4\mathrm{TCNQ}]_2$ dimer and an isolated molecule in the gas phase, respectively. A negative value of the BE suggests that dimer formation is energetically favorable. BE ≥ 0 suggests that the molecules do not want to form the dimer; instead, they would prefer to stay as two isolated molecules.

The origin is placed at the center of the mass of one of the two molecules, see Fig. 4.9(b). Note that there is no point falling inside a particular region in Fig. 4.9(b); this is the zone that is excluded due to steric considerations. The contour plot drawn for the binding energy of the $[F_4\mathrm{TCNQ}]_2$ as a function of d_x and d_y [see Fig. 4.9(b)] shows a deep global minimum (surrounded by blue contour lines) at $d_x = 7.4$ Å and $d_y = 4.5$ Å and a shallower local minimum around $d_x = 3.0$ Å and $d_y = 11.5$ Å. The position of the deep global minimum agrees very well with that obtained in a previous DFT study performed by Stradi et al.[23] We have computed the BE at the two minima; BE is -0.13 eV at the global minimum and -0.03 eV at the shallower local minimum. In a situation like this, where the energy at the global minimum (along one direction of intermolecular separation) is considerably lower than at the local minimum (that occurs along another direction of intermolecular separation), the formation of a one-dimensional linear chain would be favored over the formation of a two-dimensional monolayer.

However, the above calculation corresponds to the situation of F_4TCNQ molecules in the gas phase. How will the intermolecular interactions differ on the TBLG substrate? One important difference on the substrate is that the molecules become charged negatively, due to electron transfer from the substrate to the molecules. We

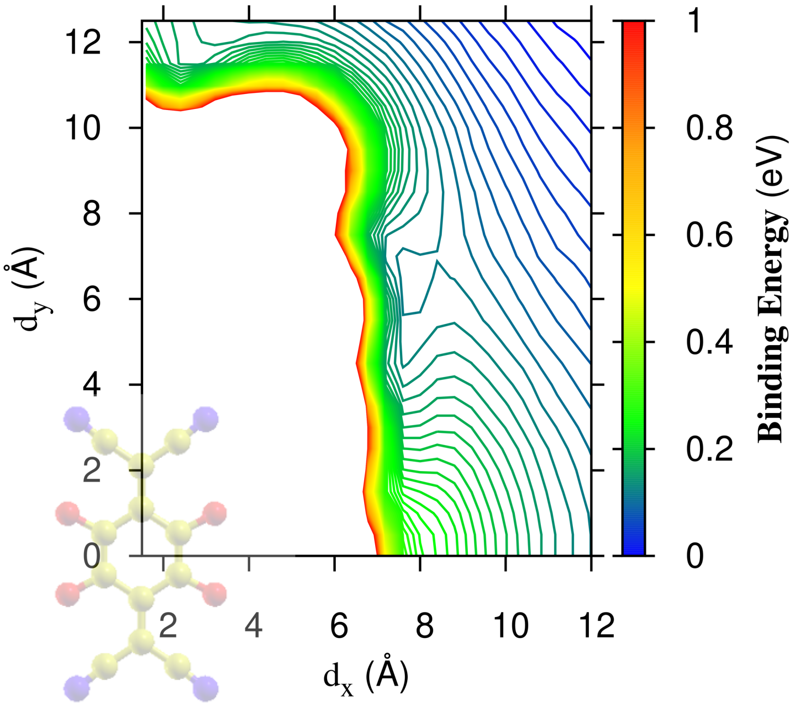

Figure 4.10: Binding energy of the dimer of two anions as a function of d_x and d_y.

have seen above that the charge on each molecule is -0.54 e. We therefore next use DFT to calculate the energy landscape for the intermolecular interaction between two F$_4$TCNQ anions (in the gas phase), with a charge of -0.54 e on each molecule; i.e., the total charge on the dimer is -1.08 e.

Fig. 4.10 shows the contour plot for the BE of this charged dimer, as obtained from DFT. We see one local minimum near $d_x = 7.5$ Å and $d_y = 6.5$ Å. Careful examination reveals that BE > 0 at the local minimum which suggest a meta-stable state for this charged dimer.

However, this interaction between charged molecules in the gas phase still differs from their interaction on the TBLG substrate. One important difference is that the Coulomb interaction between the two charged molecules on TBLG is screened by

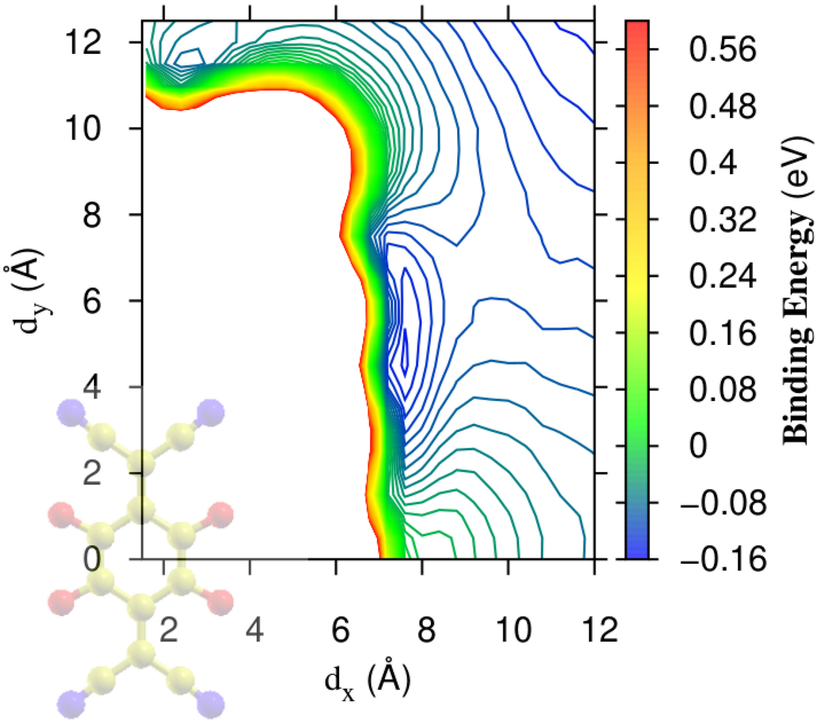

Figure 4.11: Binding energy (BE_{anions}) of the dimer of two anions as a function of d_x and d_y. BE_{anions} has been calculated using Eq. (4.7) with $s = 0.58$.

the presence of the substrate, it is lessened by a screening factor s. Accordingly, a better estimate for the BE of the charged dimer on the substrate is given by

$$\mathrm{BE}_{anions} = \left(E_{\mathrm{dimer}}^{1.08-} - s \times U_C\right) - 2E_{\mathrm{iso}}^{0.54-}, \tag{4.7}$$

where $E_{\mathrm{dimer}}^{1.08-}$, and $E_{\mathrm{iso}}^{0.54-}$ are the total energies calculated from DFT for the $[\mathrm{F_4TCNQ}]_2{}^{1.08-}$ in the gas phase and for the isolated gas-phase molecule charged with -0.54 e, respectively. U_C is the Coulomb interaction between the two charged molecules. We could approximate it as the Coulomb interaction between two point charges of -0.54 e placed at the centers of the two molecules; however, this is not a very good approximation. Instead, we consider each molecule as a charged multipole, composed of charged atoms, with the charge on each atom given by its Bader charge[39] when the molecule is deposited on the surface. U_C is then the multipole-multipole interaction at the given separation (d_x, d_y). It is given by the following equation:

$$U_C = \frac{1}{4\pi\epsilon_0}\sum_i\sum_j \frac{q_1^i q_2^j}{r_{1i,2j}}, \tag{4.8}$$

where q_1^i and q_2^j are the charges on the i^{th} atom of the first anion which is kept at the origin and j^{th} atom of the second anion. $r_{1i,2j}$ is the distance between the i^{th} atom of the first anion and the j^{th} atom of the second anion.

The only unknown in Eq. (4.7), is the value of the screening factor s. We set its value by demanding that the minimum of energy in Eq. (4.7) be equal to the DFT calculated (BE_{DFT}) value of -0.154 eV for the binding energy for the dimer on TBLG. We obtain a match for $s = 0.58$, and proceed with this value for the

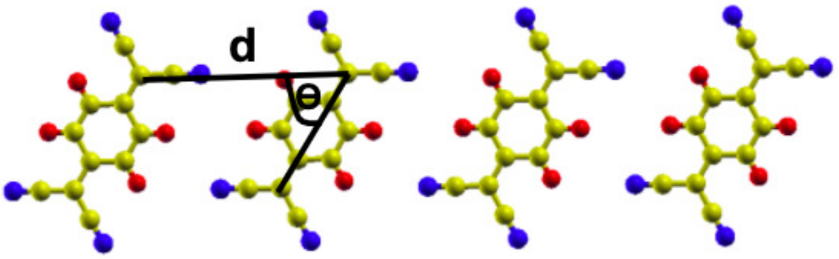

Figure 4.12: Predicted linear chain based on the DFT calculations of the energy landscape for a charged molecular dimer. We have marked d and θ in the chain where d is the intermolecular distance and θ is the angle between the two molecules. Color code: Yellow (C atom of molecule), blue (N), red (F).

screening factor. Note that we have calculated BE_{DFT} using the following equation:

$$BE_{DFT} = E^{ads}_{dimer/TBLG} - 2E^{ads}_{iso/TBLG} \tag{4.9}$$

$$= E_{dimer/TBLG} - 2E_{iso/TBLG} + E_{TBLG}, \tag{4.10}$$

where, $E^{ads}_{dimer/TBLG}$ and $E^{ads}_{iso/TBLG}$ are the adsorption energies of the $[F_4TCNQ]_2$ on TBLG, an isolated F_4TCNQ molecule on TBLG. $E_{dimer/TBLG}$, $E_{iso/TBLG}$ and E_{TBLG} are the total energies from DFT of the $[F_4TCNQ]_2$ on TBLG, an isolated F_4TCNQ on TBLG and bare TBLG, respectively.

Fig. 4.11 shows a contour plot for the energy landscape calculated using Eq. (4.7), with $s = 0.58$, We see that we have a deep global minimum at $d_x = 7.5$ Å and $d_y = 4.5$ Å and a shallower minimum at $d_x = 3.5$ Å and $d_y = 11.5$ Å.

Prediction of a linear chain based on the position of global minimum found for $[F_4TCNQ]_2{}^{1.08-}$

We can predict the structure of a linear chain (see Fig. 4.12) from the position of the deep global minimum observed in the contour plot of the $[F_4TCNQ]_2{}^{1.08-}$, see Fig. 4.11. The computed intermolecular distance ($d = \sqrt{d_x^2 + d_y^2}$) and the angle θ for the chain proposed in Fig. 4.12 are 8.74 Å and 60°, respectively. These predictions fit well with the structure of the linear chain shown obtained in our DFT calculations for F_4TCNQ on TBLG; see Fig. 4.7(b). The values of d and θ also agree very well with the experimentally measured values d= 8.5 Å and θ = 60°; note that these are approximate estimates obtained from STM images.[30] The slight disagreement in the value of d may be due to the various approximations made in obtaining the theoretically computed energy landscape, as well as due to the different structures for TBLG in the calculation and experiment.

4.5.4 F_4TCNQ on N-doped TBLG

Our DFT studies (see Table 4.1) have shown that F_4TCNQ/TBLG systems are nonmagnetic. However, F_4TCNQ/TBLG systems can be interesting if we can add magnetic functionalities to them. This can open the way for graphene systems to be used in spintronics devices. One possible way of doing this might be to dope the TBLG substrate with foreign atoms such as nitrogen. Nitrogen doping causes ferromagnetism in graphene[42;43] and the system can be used to construct selective and efficient molecular sensors.[44] N-doped graphene has also drawn much attention for its use as an efficient anode material in the field of Li-ion batteries.[45]

There exist several earlier DFT and experimental studies on nitrogen-doped graphene.[42–46] However, to the best of our knowledge, nitrogen doping in multilayer graphene or TBLG has not been explored to date. Seeing a significant opportunity in this area, we have decided to study the TBLG system doped with single nitrogen atoms (N-TBLG) using density functional theory. As noted above, the Moiré pattern of TBLG offers different stacking regions (e.g., AA stacking, AB stacking, and in between) for chemical doping. Therefore, we want to first check which stacking is a more favorable site for nitrogen doping on TBLG. Next, we want to find the preferred binding site (e.g. N-site or C-site) for the F_4TCNQ molecule on N-TBLG. This will give us an opportunity to understand the nature of the binding sites; this

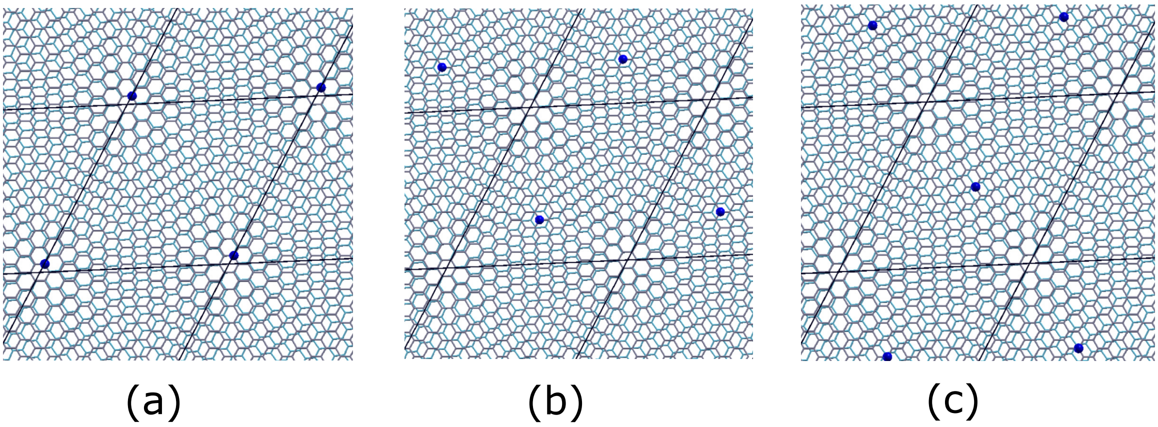

Figure 4.13: Nitrogen is doped in (a) AA stacked region, (b) AB stacked region, and (c) in between AB region of the nitrogen doped TBLG (N-TBLG). Color code: blue (N), gray (top layer graphene), and turquoise (bottom layer graphene). The solid black lines show the boundaries of the TBLG unit cell.

knowledge may also prove useful in the context of applications of N-TBLG as a molecular sensor.

Doping by single nitrogen atoms in TBLG (N-TBLG)

We have considered different configurations for nitrogen doping to find the preferable doping site, see Fig. 4.13. Comparing the total energy (see Table 4.4) of the three systems shown in Figs. 4.13(a)-(c), one can conclude that the N dopant prefers to be in the AA stacked region. This may be because nitrogen is an electronegative element. It therefore prefers to be in the AA stacked region, since this is where the electron density is highest, see Fig 4.8 However, we note that depending on the doping technique, it may not always be possible for the N dopants to occupy their most favored sites within the Moiré.

Adsorption of single F_4TCNQ molecule on N-TBLG

To continue our study on molecular adsorption, we have adsorbed the F_4TCNQ molecule on the N-TBLG, where we doped TBLG with nitrogen in the AA stacked region, see Fig. 4.13(a). The adsorption energy ($E_{\text{ads}}^{\text{N-TBLG}}$) is calculated using the

Table 4.4: Total energy in meV for the nitrogen doped twisted bilayer graphene (N-TBLG). We have calculated total energy using DFT for the configurations shown in Fig. 4.13(a)–(c).

Figure corresponding to configuration	$E_{\text{total}}^{\text{N-TBLG}}$(meV)
Fig. 4.13(a)	0.0
Fig. 4.13(b)	37
Fig. 4.13(c)	19

following formula:

$$E_{\text{ads}}^{\text{N-TBLG}} = E_{\text{F}_4\text{TCNQ/N-TBLG}} - E_{\text{N-TBLG}}^{\text{bare}} - E_{\text{F}_4\text{TCNQ}}^{\text{iso}}, \tag{4.11}$$

where $E_{\text{F}_4\text{TCNQ/N-TBLG}}$, $E_{\text{N-TBLG}}^{\text{bare}}$, and $E_{\text{F}_4\text{TCNQ}}^{\text{iso}}$ are the total energies of the F_4TCNQ molecule on N-TBLG, bare N-doped TBLG, and an isolated molecule in the gas phase, respectively. Table 4.5 lists the computed adsorption energies for the configurations shown in Figs. 4.14(a)-(f). We find that Fig. 4.14(c) is the most favored geometry on N-TBLG. Note that F_4TCNQ gets an extra stabilization of -0.801 eV/molecule on N-TBLG compared to adsorption on undoped (pristine) TBLG. From the values shown in Table 4.5, we can conclude that the molecule prefers to be adsorbed over a nitrogen site. In the configuration corresponding to Fig. 4.14(f), where the molecule is far away from the N dopant, one might have expected to get the same result as for adsorption on undoped TBLG. However, we got a much higher (in magnitude) adsorption energy for the configuration shown in Fig. 4.14(f) than for F_4TCNQ on the undoped system, even though F_4TCNQ is far away from the dopant nitrogen. This suggests that the N dopant has an effect at quite a distance away from it, and our unit cell is small enough that the molecule sees the effect of the N-dopant even at this far away “C-site"

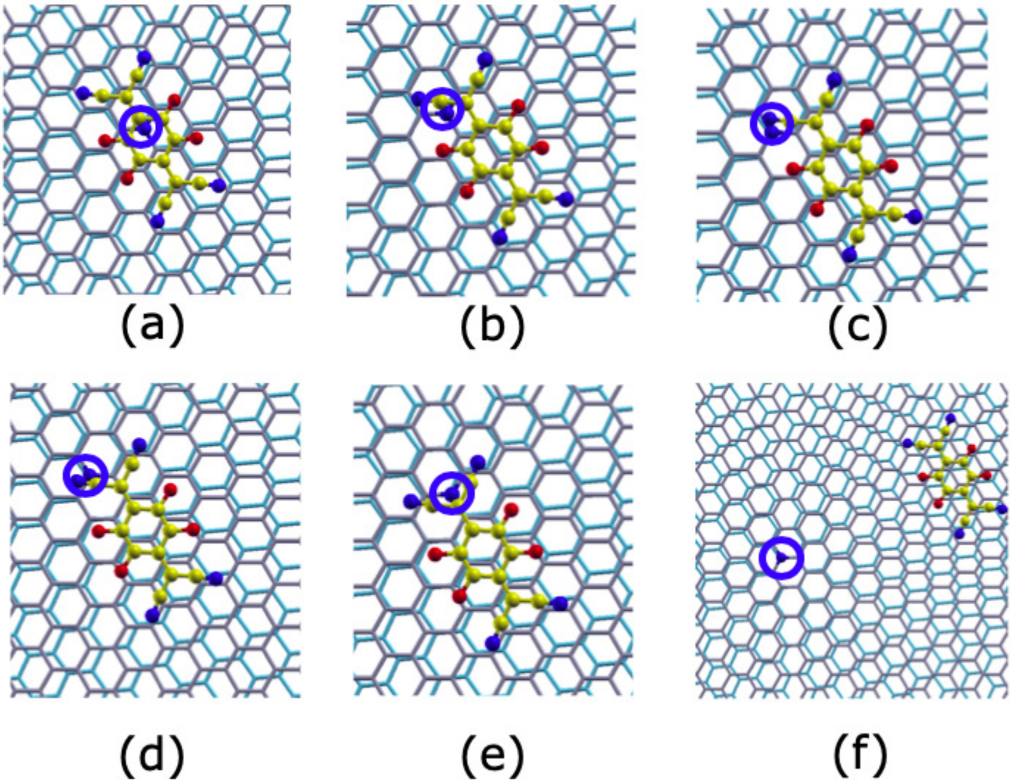

Figure 4.14: Optimized geometries of F_4TCNQ on different positions of the nitrogen doped TBLG. Position of the N dopant has been shown using a solid blue circle. Color code: Yellow (C atom of molecule), blue (N), red (F), gray (top layer graphene), turquoise (bottom layer graphene).

High electron transfer ($\Delta Q = 0.98$ e using the Bader method[39]) from the nitrogen to the molecule causes the molecule to be adsorbed on the N site whereas ΔQ was 0.54 e (using Bader[39] method) when the molecule was adsorbed on the pristine TBLG substrate. To gain further insight into the electron transfer in the F_4TCNQ/N-TBLG and F_4TCNQ/Gr systems, we have calculated the differential charge density (DCD) which is defined as:

$$\Delta\rho(\mathbf{r}) = \rho_{F_4TCNQ/sub}(\mathbf{r}) - \rho_{F_4TCNQ}(\mathbf{r}) - \rho_{sub}(\mathbf{r}), \tag{4.12}$$

where $\rho_{F_4TCNQ/sub}(\mathbf{r})$, $\rho_{F_4TCNQ}(\mathbf{r})$, and $\rho_{sub}(\mathbf{r})$ are the charge densities of combined systems, isolated F_4TCNQ molecule, and bare substrate, respectively. We considered the *sub* to be TBLG for F_4TCNQ/TBLG and N-TBLG for F_4TCNQ/N-TBLG system. Plots of isosurfaces of the DCD for F_4TCNQ/N-TBLG and F_4TCNQ/TBLG systems are shown in Fig. 4.15. This figure shows the electron accumulation on the molecule (red color). We note that the electron transfer from the substrate to the molecule is significant for N-TBLG upon comparing Fig. 4.15(c) and Fig. 4.15(d). Fig. 4.15(d) shows that depletion of electron density (large blue lobes) takes place at the N-site, which further confirms that enhanced charge transfer occurs from the N atom to the F_4TCNQ molecule. One does not see such large blue lobes in F_4TCNQ/Gr, see Fig. 4.15(c).

We have plotted the spin-polarized density of states (DOS) for F_4TCNQ on N-TBLG, see Fig. 4.16(b). The difference of DOS between the up and down spin electrons suggests a net magnetic moment. The calculated moment is 1.0 μ_B for F_4TCNQ/N-TBLG and was 0.0 μ_B for F_4TCNQ/TBLG. Therefore, single N-doping in the substrate can make the system spin-polarized. We found the magnetic moment is mainly localized on the molecule of the F_4TCNQ/N-TBLG system.

We have also plotted the DOS for F_4TCNQ/TBLG in Fig. 4.16(a). One can note

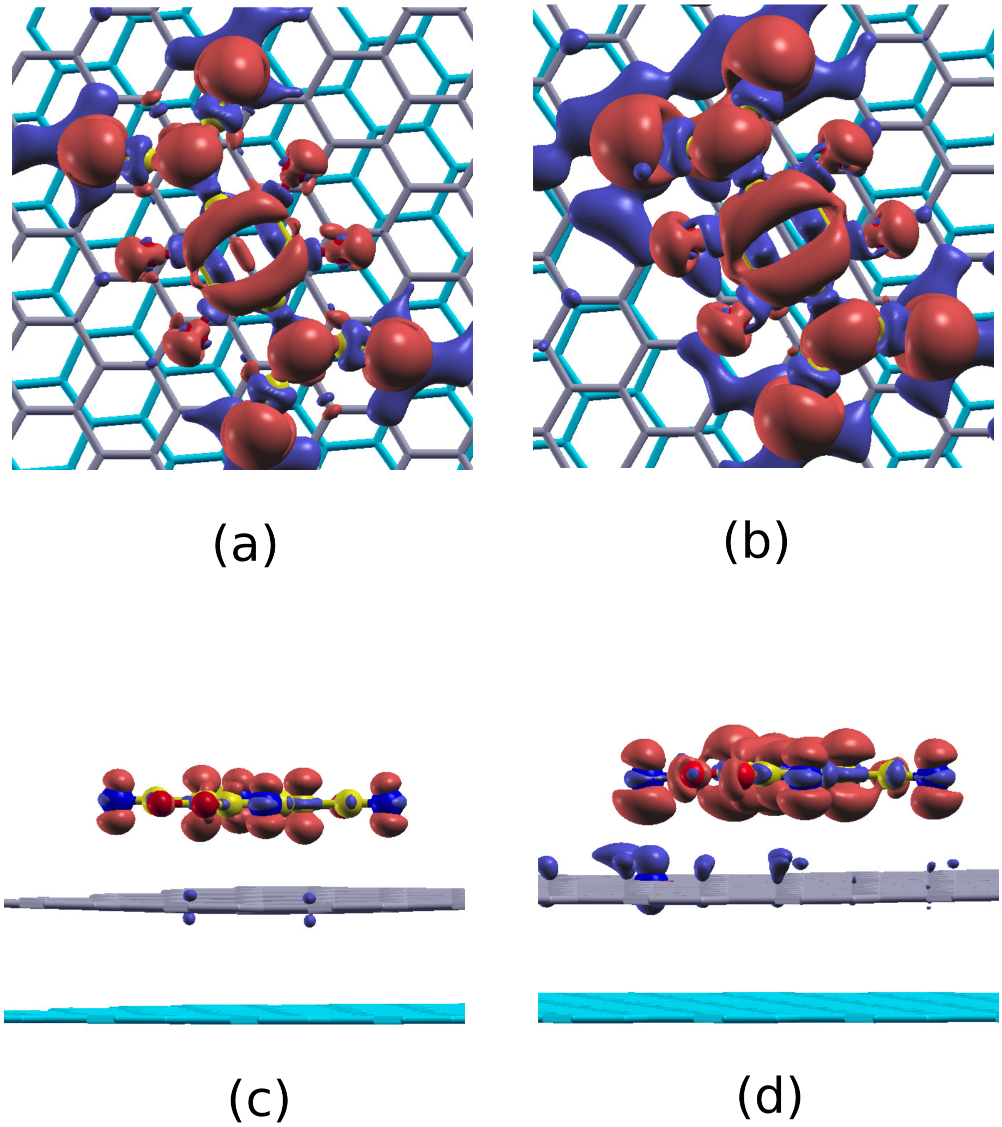

Figure 4.15: Calculated differential charge densities (DCD) for the site–2 [see Fig. 4.5(b)] of the F_4TCNQ/TBLG (a) top-view (c) side-view and for the Fig. 4.14(c) configuration of F_4TCNQ/N-TBLG (b) top-view (d) side-view. In all cases, the iso-surface value of 0.0015 e/Bohr^3 has been plotted. Red and blue lobes represent electron accumulation and depletion, respectively. The upper and lower graphene layers are shown in gray and turquoise, respectively.

Table 4.5: Adsorption energy in eV for F_4TCNQ on the nitrogen-doped twisted bilayer graphene (N-TBLG). We have calculated adsorption energy for the configurations corresponding to Figs. 4.14(a)-(f) using Eq. (4.11).

Figure corresponding to configuration	$E_{\text{ads}}^{\text{N-TBLG}}$(eV)
Fig. 4.14(a)	−2.183
Fig. 4.14(b)	−2.223
Fig. 4.14(c)	−2.248
Fig. 4.14(d)	−2.198
Fig. 4.14(e)	−2.163
Fig. 4.14(f)	−2.087

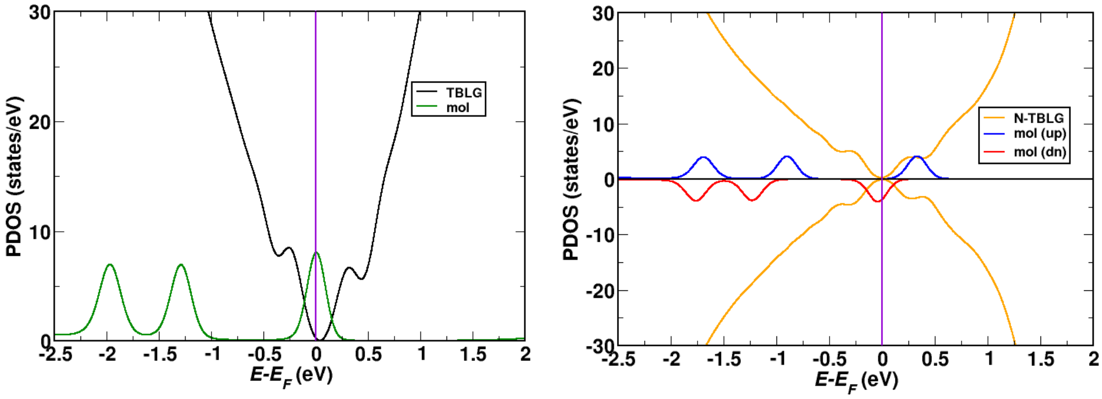

(a) **(b)**

Figure 4.16: (a) Non spin-polarized density of states of F_4TCNQ molecule on the TBLG for site–2 [see Fig. 4.5(b)]. Black line represents the total up & down spins DOS for TBLG and green line represents the total up & down spins DOS for F_4TCNQ molecule. (b) spin polarized density of states of F_4TCNQ molecule on the N-site of the N-TBLG [see Fig. 4.14(c)]. Golden yellow line represents the DOS for N-TBLG, blue line represents up spin DOS and red line down spin DOS for F_4TCNQ molecule.

that the peak at the Fermi level of Fig. 4.16(a) splits into two peaks in Fig. 4.16(b) after N-doping. The peak, which is at the Fermi level in Fig. 4.16(b) is filled with one electron due to the transfer of 1 electron (discussed above) from the N-site of the substrate to the molecule. We refer to the orbital corresponding to this peak as the SOMO (singly occupied molecular orbital) of the molecule. The other, which is above the Fermi level, is referred to as the SUMO or singly unoccupied molecular orbital.

4.6 Conclusions

We have studied the F_4TCNQ molecule on twisted bilayer graphene. At lower coverage, our calculations show that despite being an electron acceptor, the molecule avoids adsorbing on the electron-rich AA-stacked region on TBLG. This is in agreement with STM experiments performed by Harsh et al.[30] This is because the molecule can gain extra stability from van der Waals interactions with the substrate, by moving away from the convex AA-stacked regions of the corrugated substrate. At higher coverage, experiments show that molecules self assemble to form a 1D linear chain, rather than building a 2D monolayer. We have shown that the presence of a single deep global minimum in the contour of the binding energy plot of the charged dimer can explain this phenomenon. Using DFT too, we have shown that molecules prefer to form the linear chain at higher coverages, on both TBLG and monolayer graphene.

N-TBLG can be used as an efficient molecular sensor for the electron acceptor type of molecules such as F_4TCNQ. We have shown that N-doping in the substrate of the F_4TCNQ/TBLG system also adds magnetism to the system, which may conceivably have technological applications. Nitrogen doping in the TBLG system is most favored at the AA stacked region of the Moiré. When the TBLG is N-doped, the F_4TCNQ molecules preferentially adsorb over the N dopants. The molecule then gains a full electron from the N-doped substrate, and becomes spin polarized.

Bibliography

[1] J. H. Chen, C. Jang, S. Xiao, M. Ishigami, and M. S. Fuhrer, "Intrinsic and extrinsic performance limits of graphene devices on SiO_2," *Nat. Nanotechnol*, vol. 3, p. 206, 2008.

[2] V. Gusynin and S. Sharapov, "Unconventional integer quantum Hall effect in graphene," *Phys. Rev. Lett.*, vol. 95, p. 146801, 2005.

[3] Y. Zhang, Y.-W. Tan, H. L. Stormer, and P. Kim, "Experimental observation of the quantum Hall effect and Berry's phase in graphene," *Nature*, vol. 438, p. 201, 2005.

[4] K. S. Novoselov, A. K. Geim, S. V. Morozov, D. Jiang, Y. Zhang, S. V. Dubonos, I. V. Grigorieva, and A. A. Firsov, "Electric field effect in atomically thin carbon films," *Science*, vol. 306, p. 666, 2004.

[5] P. Avouris, "Graphene: electronic and photonic properties and devices," *Nano Lett.*, vol. 10, p. 4285, 2010.

[6] F. Schwierz, "Graphene transistors," *Nature Nanotechnol.*, vol. 5, p. 487, 2010.

[7] K. S. Novoselov, V. Fal, L. Colombo, P. Gellert, M. Schwab, K. Kim, *et al.*, "A roadmap for graphene," *Nature*, vol. 490, p. 192, 2012.

[8] K. S. Novoselov, A. K. Geim, S. V. Morozov, D. Jiang, M. I. Katsnelson, I. V. Grigorieva, S. V. Dubonos, and A. A. Firsov, "Two-dimensional gas of massless Dirac fermions in graphene," *Nature*, vol. 438, p. 197, 2005.

[9] S. Zhou, G.-H. Gweon, J. Graf, A. Fedorov, C. Spataru, R. Diehl, Y. Kopelevich, D.-H. Lee, S. G. Louie, and A. Lanzara, "First direct observation ofDirac fermions in graphite," *Nat. Phys.*, vol. 2, p. 595, 2006.

[10] J. L. Dos Santos, N. Peres, and A. C. Neto, "Graphene bilayer with a twist: Electronic structure," *Phys. Rev. Lett.*, vol. 99, p. 256802, 2007.

[11] S. Shallcross, S. Sharma, and O. A. Pankratov, "Quantum interference at the twist boundary in graphene," *Phys. Rev. Lett.*, vol. 101, p. 056803, 2008.

[12] A. Luican, G. Li, A. Reina, J. Kong, R. Nair, K. S. Novoselov, A. K. Geim, and E. Andrei, "Single-layer behavior and its breakdown in twisted graphene layers," *Phys. Rev. Lett.*, vol. 106, p. 126802, 2011.

[13] G. Li, A. Luican, J. L. Dos Santos, A. C. Neto, A. Reina, J. Kong, and E. Andrei, "Observation of van Hove singularities in twisted graphene layers," *Nat. Phys.*, vol. 6, p. 109, 2010.

[14] I. Brihuega, P. Mallet, H. González-Herrero, G. T. De Laissardière, M. Ugeda, L. Magaud, J. Gómez-Rodríguez, F. Ynduráin, and J.-Y. Veuillen, "Unraveling the intrinsic and robust nature of van Hove singularities in twisted bilayer graphene by scanning tunneling microscopy and theoretical analysis," *Phys. Rev. Lett.*, vol. 109, p. 196802, 2012.

[15] J. Hass, F. Varchon, J.-E. Millan-Otoya, M. Sprinkle, N. Sharma, W. A. de Heer, C. Berger, P. N. First, L. Magaud, and E. H. Conrad, "Why multilayer graphene on 4-H-SiC (0001) behaves like a single sheet of graphene," *Phys. Rev. Lett.*, vol. 100, p. 125504, 2008.

[16] L. Meng, Z.-D. Chu, Y. Zhang, J.-Y. Yang, R.-F. Dou, J.-C. Nie, and L. He, “Enhanced intervalley scattering of twisted bilayer graphene by periodic AB stacked atoms,” *Phys. Rev. B*, vol. 85, p. 235453, 2012.

[17] T. Ohta, J. T. Robinson, P. J. Feibelman, A. Bostwick, E. Rotenberg, and T. E. Beechem, “Evidence for interlayer coupling and moiré periodic potentials in twisted bilayer graphene,” *Phys. Rev. Lett.*, vol. 109, p. 186807, 2012.

[18] Z. Y. Rong and P. Kuiper, “Electronic effects in scanning tunneling microscopy: Moiré pattern on a graphite surface,” *Phys. Rev. B*, vol. 48, p. 17427, 1993.

[19] M. Garnica, D. Stradi, S. Barja, F. Calleja, C. Díaz, M. Alcamí, N. Martín, A. L. V. de Parga, F. I. Martín, and R. Miranda, “Long-range magnetic order in a purely organic 2D layer adsorbed on epitaxial graphene,” *Nat. Phys.*, vol. 9, p. 368, 2013.

[20] G. Trambly de Laissardière, D. Mayou, and L. Magaud, “Localization of dirac electrons in rotated graphene bilayers,” *Nano Lett.*, vol. 10, p. 804, 2010.

[21] V. D. Pham, S. Ghosh, F. Joucken, M. Pelaez-Fernandez, V. Repain, C. Chacon, A. Bellec, Y. Girard, R. Sporken, S. Rousset, Y. J. Dappe, *et al.*, “Selective control of molecule charge state on graphene using tip-induced electric field and nitrogen doping,” *NPJ 2D Mater. Appl.*, vol. 3, no. 1, p. 1, 2019.

[22] M. Garnica, D. Stradi, F. Calleja, S. Barja, C. Díaz, M. Alcamí, A. Arnau, A. L. V. de Parga, F. Martín, and R. Miranda, “Probing the site-dependent Kondo response of nanostructured graphene with organic molecules.,” *Nano Lett.*, vol. 14, p. 4560, 2014.

[23] D. Stradi, M. Garnica, C. Díaz, F. Calleja, S. Barja, N. Martín, M. Alcamí,

A. L. V. de Parga, R. Miranda, and F. Martín, “Controlling the spatial arrangement of organic magnetic anions adsorbed on epitaxial graphene on Ru(0001),” *Nanoscale*, vol. 6, p. 15271, 2014.

[24] Q. H. Wang and M. C. Hersam, “Room-temperature molecular-resolution characterization of self-assembled organic monolayers on epitaxial graphene,” *Nat. Chem.*, vol. 1, p. 206, 2009.

[25] J. MacLeod and F. Rosei, “Molecular self-assembly on graphene,” *Small*, vol. 10, p. 1038, 2014.

[26] S. Barja, M. Garnica, J. J. Hinarejos, A. L. V. de Parga, N. Martín, and R. Miranda, “Self-organization of electron acceptor molecules on graphene,” *Chem. Commun.*, vol. 46, p. 8198, 2010.

[27] D. Maccariello, M. Garnica, M. A. Nino, C. Navío, P. Perna, S. Barja, A. L. V. de Parga, and R. Miranda, “Spatially resolved, site-dependent charge transfer and induced magnetic moment in tcnq adsorbed on graphene,” *Chem. Mater.*, vol. 26, p. 2883, 2014.

[28] I. F. Torrente, K. J. Franke, and J. I. Pascual, “Structure and electronic configuration of tetracyanoquinodimethane layers on a Au(1 1 1) surface,” *Int. J. Mass Spectrom.*, vol. 277, p. 269, 2008.

[29] A. Kumar, K. Banerjee, M. Dvorak, F. Schulz, A. Harju, P. Rinke, and P. Liljeroth, “Charge-transfer-driven nonplanar adsorption of F4TCNQ molecules on epitaxial graphene,” *ACS Nano*, vol. 11, p. 4960, 2017.

[30] R. Harsh, *Electronic interaction of organic molecules with low dimensional materials: a scanning tunneling microscopy study on graphene and black phosphorus.* Universitè de Paris, 2019.

[31] S. Shallcross, S. Sharma, E. Kandelaki, and O. Pankratov, "Electronic structure of turbostratic graphene," *Phys. Rev. B*, vol. 81, p. 165105, 2010.

[32] P. Giannozzi, S. Baroni, N. Bonini, M. Calandra, R. Car, C. Cavazzoni, Davide Ceresoli, G. L. Chiarotti, M. Cococcioni, I. Dabo, A. D. Corso, S. d. Gironcoli, S. Fabris, G. Fratesi, R. Gebauer, U. Gerstmann, C. Gougoussis, Anton Kokalj, M. Lazzeri, L. Martin-Samos, N. Marzari, F. Mauri, R. Mazzarello, Stefano Paolini, A. Pasquarello, L. Paulatto, C. Sbraccia, S. Scandolo, G. Sclauzero, A. P. Seitsonen, A. Smogunov, P. Umari, and R. M. Wentzcovitch, "QUANTUM ESPRESSO: a modular and open-source software project for quantum simulations of materials," *J. Phys.: Condens. Matter*, vol. 21, p. 395502, 2009.

[33] P. Giannozzi, O. Andreussi, T. Brumme, O. Bunau, M. B. Nardelli, M. Calandra, R. Car, C. Cavazzoni, D. Ceresoli, M. Cococcioni, *et al.*, "Advanced capabilities for materials modelling with quantum espresso," *J. Phys.: Condens. Matter*, vol. 29, no. 46, p. 465901, 2017.

[34] D. Vanderbilt, "Soft self-consistent pseudopotentials in a generalized eigenvalue formalism," *Phys. Rev. B*, vol. 41, p. 7892, 1990.

[35] J. P. Perdew, K. Burke, and M. Ernzerhof, "Generalized gradient approximation made simple," *Phys. Rev. Lett.*, vol. 77, p. 3865, 1996.

[36] S. Grimme, "Semiempirical GGA-type density functional constructed with a long-range dispersion correction," *J. Comput. Chem*, vol. 27, p. 1787, 2006.

[37] H. J. Monkhorst and J. D. Pack, "Special points for Brillouin-zone integrations," *Phys. Rev. B*, vol. 13, p. 5188, 1976.

[38] N. Marzari, D. Vanderbilt, A. De Vita, and M. C. Payne, "Thermal contraction and disordering of the Al(110) surface," *Phys. Rev. Lett.*, vol. 82, p. 3296, 1999.

[39] R. Bader, *Atoms in Molecules, X-Ray Analyses and the Structure of Organic Molecules.* Clarendon Press: Oxford, UK, 1990.

[40] W. Tang, E. Sanville, and G. Henkelman, "A grid-based bader analysis algorithm without lattice bias," *J. Phys. Condens. Matter*, vol. 21, no. 8, p. 084204, 2009.

[41] I. de Oliveira and R. Miwa, "Organic molecules deposited on graphene: A computational investigation of self-assembly and electronic structure," *J. Chem Phys.*, vol. 142, p. 044301, 2015.

[42] R. Babar and M. Kabir, "Ferromagnetism in nitrogen-doped graphene," *Phys. Rev. B*, vol. 99, p. 115442, 2019.

[43] P. Błoński, J. Tucek, Z. Sofer, M. Vlastimil, M. Petr, M. Pumera, M. Otyepka, and R. Zborill, "Doping with graphitic nitrogen triggers ferromagnetism in graphene," *J. Am. Chem. Soc.*, vol. 139, p. 3171, 2017.

[44] R. Lv, Q. Li, A. R. Botello-Méndez, T. Hayashi, B. Wang, A. Berkdemir, Q. Hao, A. L. Elías, R. Cruz-Silva, H. R. Gutiérrez, *et al.*, "Nitrogen-doped graphene: beyond single substitution and enhanced molecular sensing," *Sci. Rep.*, vol. 2, p. 586, 2012.

[45] Y.-X. Yu, "Can all nitrogen-doped defects improve the performance of graphene anode materials for lithium-ion batteries?," *Phys. Chem. Chem. Phys.*, vol. 15, p. 16819, 2013.

[46] X. Fei, J. Neilson, Y. Li, V. Lopez, S. J. Garrett, L. Gan, H.-J. Gao, and L. Gao, "Controlled synthesis of nitrogen-doped graphene on ruthenium from azafullerene," *Nano Lett.*, vol. 17, p. 2887, 2017.

Chapter 5

Tuning of Magnetism and Charge Transfer: F_4TCNQ and CoPc Adsorbed on Graphene

5.1 Introduction

Graphene, a wonder material of the last decade, has drawn a great deal of attention due to its possible application in modern technologies.[1–3] Graphene (Gr) shows several unusual properties such as high electrical conductivity, which can reach up to $2{\times}10^5$ $\mathrm{cm^2V^{-1}s^{-1}}$,[4] room temperature quantum Hall effect,[5;6] and ambipolar electric field effect.[7] Relativistic Dirac fermions, which were first experimentally observed in graphene by Zhou et al.,[8] have been invoked to explain some of the unusual phenomena observed in graphene.[9] Its high electrical conductivity dramatically increases the applicability of graphene in the field of electronic devices.

To make the manufacture of graphene-based electronic devices possible, it is necessary to control the electronic properties of the graphene. Many techniques have been proposed to modify graphene's electronic properties, such as the application of electric field,[10;11] and chemical functionalization by adsorption of molecules.[12] In this context, one should note that the adsorption of molecules not only modifies the electronic properties of graphene, the electronic properties of the organic molecule also get modified owing to charge transfer from the substrate to the molecule (or vice versa). For example, a recent experiment by Garnica et al.[13] shows that a non-magnetic organic molecule, TCNQ (tetracyanoquinodimethane), develops a magnetic moment upon adsorption on graphene/Ru(0001) and acquires long-range magnetic ordering. The same study reports a magnetic moment of 0.18 μ_B per TCNQ molecule from DFT calculations.

In particular, we are interested in tailoring the electronic and magnetic properties of organic molecules adsorbed on graphene. Organic molecules adsorbed on graphene have been the subjects of many experiments[14;15] and theoretical investigations.[16–20] For example, TCNQ has been investigated by previous authors on graphene supported over Ir(111),[21;22] and on Au(111).[23]

In this paragraph, we cite a few examples of previous results on TCNQ and F_4TCNQ molecules adsorbed on graphene. Experiments by Garnica et al. show site-dependent magnetism and the Kondo effect for TCNQ and F_4TCNQ (2,3,5,6-tetrafluoro-7,7,8,8-tetracyano-quinodimethane) molecules on graphene supported on the Ru(0001) surface.[24] DFT calculations confirmed that molecules adsorbed on the FCC stacked region of the Moiré pattern [formed by the graphene grown on Ru(0001)] show a magnetic moment and signature of the Kondo effect. These findings are significant because adding magnetic functionalities in the graphene system can promote its applicability in the field of spintronics. Charge transfer between the molecule and the substrate can play an important role in determining magnetic properties. A study by Pham et al.[25] on TCNQ on graphene is useful to mention in this context. They have shown that control over charge transfer is possible using the tip-induced electric field. Fig. 5.1 shows that the electrons transfer from the

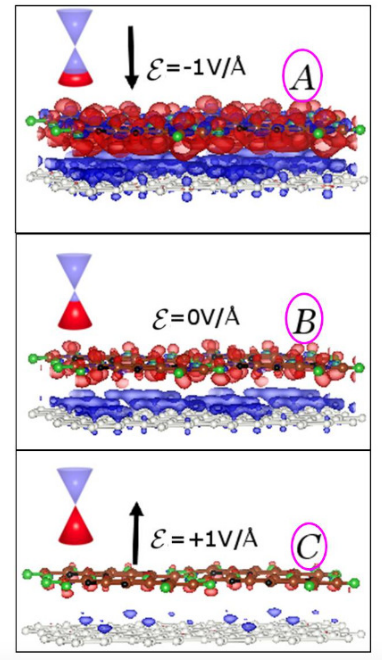

Figure 5.1: Plots of differential charge density, $\Delta\rho$ for TCNQ monolayer on bare graphene, for three values of the electric field, plotted at iso-surfaces value of 0.0007 e/Bohr^3. Red and blue lobes correspond to electron accumulation and depletion, respectively. A, B and C represent the conditions when $\epsilon = -1.0$V/Å, 0 V/Å and +1.0 V/Å. The insetsshow the position of the Fermi level with respect to the graphene Dirac cone, for each case. This figure is reused with permission from Ref. 25 ©2019 Springer Nature Limited.

graphene to the molecule for the external field (ϵ) of -1 V/Å. It also shows that there is electron transfer from the molecule to the graphene on reversing the electric field to $\epsilon = +1$ V/Å. They have also stated that an enhanced charge transfer from graphene to the molecule can be achieved by nitrogen doping in the graphene. In another study, Kumar et al. show that charge transfer can cause non-planar adsorption of the F_4TCNQ molecule on the Gr/Ir(111) surface.[26] A detailed theoretical investigation done by Oliveria et al.[27] determined the adsorption geometry of TCNQ, F_4TCNQ, and TPA (pyrenetetrasulfonic acid) on graphene. While TCNQ and F_4TCNQ cause *p*-type doping in Gr due to electron transfer from the Gr to the molecules, TPA cannot create significant doping due to the weak interaction between the molecule and the graphene. Pinto et al. have confirmed the same, i.e.,

F_4TCNQ causes *p*-type doping in graphene.[28]

So far, we have discussed F_4TCNQ or TCNQ molecules adsorbed on graphene, where we have seen that electron transfer between the molecule and the graphene can significantly modify the electronic and magnetic properties of both the molecule and graphene. Electron transfer between the molecule and the graphene can also control the organic molecule's catalytic activity adsorbed on graphene. Cobalt phthalocyanine (CoPc) is of interest in this context.[29] CoPc is an efficient catalyst for the CO_2 reduction reaction.[29–31] One can enhance the catalytic activity of CoPc by reducing the oxidation state of the molecule or by increasing the electronic density in the molecule.[32] It is observed that adsorption of CoPc on N-doped graphene can increase the electron density on it.[29;33;34] Hence, enhanced catalytic activity for the CoPc has been observed on the nitrogen-doped graphene when the molecule binds to a pyridinic or pyrrolic site.[32]

Therefore, control over the charge (electron) transfer is crucial to tailor the electronic and chemical properties of the molecule adsorbed on graphene. The interfacial charge redistribution in the molecule-graphene system depends strongly on the orientation, conformation, and nature of the adsorbed molecules on the substrate. A theoretical understanding is necessary to investigate the origin of different electronic and chemical properties.

In the first part of this thesis chapter, we show an approach toward tuning physical properties such as magnetism, by applying an external electric field to the system consisting of the organic molecule adsorbed on graphene. We have used *ab initio* density functional theory to study the behavior of the electrons of graphene doped with a F_4TCNQ molecule. The F_4TCNQ molecule is shown in Fig. 5.2(a). We have also studied the adsorption of F_4TCNQ on nitrogen-doped graphene (N-Gr). Nitrogen doping the Gr substrate makes a difference to the charge transfer between the substrate and molecule. The combined system also develops a sizeable

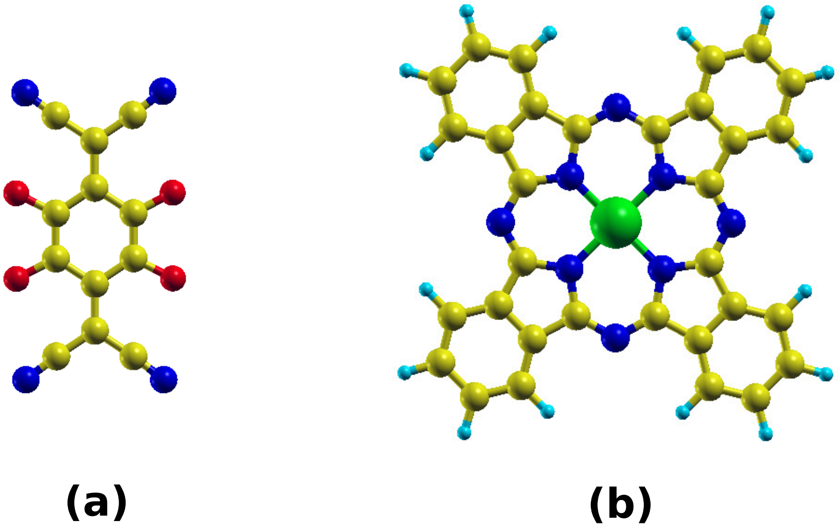

Figure 5.2: Optimized geometry of (a) F_4TCNQ molecule and (b) CoPc molecule in the gas phase. Color code for atoms: red (F), yellow (C), blue (N), green (Co), and turquoise (H).

magnetic moment. We show that N-doping can be used as an alternative route to add magnetic functionalities to the combined system. We believe that our finding will help enhance the applicability of graphene in next-generation spintronic devices.

In the second part of this thesis chapter, we have tuned the charge on the CoPc molecule, see Fig. 5.2(b), by adsorbing it on either pristine Gr, a single N dopant in Gr, or a N pair in N-doped Gr. Scanning tunneling spectroscopy (STS) shows that only for those molecules that sit on N pairs in the doped graphene, there is a complete transfer of one full electron (1 e) from the nitrogen pair to the molecule's LUMO; this is a signature of the redox reaction because the oxidation state of the Co centre in the molecule goes from 0 to -1 after receiving one electron from Gr. DFT calculations show the same trend: we find that a CoPc molecule adsorbed on a nitrogen pair of the doped graphene gains more electrons than a CoPc adsorbed on asingle nitrogen or on the pristine graphene. These results on CoPc on N-doped Gr systems have been published in Ref. 35.

5.2 Computational details

For F_4TCNQ/Gr

We have used the Quantum ESPRESSO (QE) package[36;37] to perform non-spin-polarized as well as spin-polarized density functional theory (DFT) calculations. We have used ultrasoft pseudopotentials to describe the interactions between the ions and the valence electrons.[38] In The Perdew-Burke-Ernzerhof (PBE) form of the generalized gradient approximation (GGA) is used to describe the exchange-correlation interactions.[39] The Kohn-Sham equations have been expanded using a plane-wave basis set. The kinetic energy cutoff for the wavefunctions is chosen to be 40 Ry, and 400 Ry for the charge densities. We have used the semi-empirical DFT-D2[40] method to include the van der Waals (dispersion) interactions. We have used a $\sqrt{127} \times \sqrt{127}$ supercell of graphene to adsorb a single F_4TCNQ molecule at different lateral positions, in order to determine the lowest energy adsorption site.

All the atomic coordinates are relaxed until the forces are less than 10^{-3} Ry/Bohr. For the calculations with external electric field, the electric field is applied using a sawtooth potential, which is directed normal to the plane of the F_4TCNQ/Gr system.[41;42] Brillouin zone (BZ) sampling is restricted to the zone center for the geometry relaxation calculations. We have used the Marzari-Vanderbilt[43] smearing method with functions of width of 0.001 Ry, to aid the convergence. To generate the projected density of states (PDOS), we have a used $(9 \times 9 \times 1)$ k-mesh to sample the BZ using the Monkhorst-Pack[44] sampling scheme. We have used the Tersoff-Hamann approach to simulate scanning tunneling microscopy (STM) images.[45] The electronic charge associated with each atom is obtained by using the Bader method.[46;47]

For CoPc/Gr

All our calculations have been performed within the framework of spin-polarized density functional theory, using the Quantum ESPRESSO package.[36;37] The electronic wavefunctions are expanded in a plane-wave basis set using the cutoffs set to 35 Ry for kinetic energy and 350 Ry for charge densities. The exchange correlation interactions are treated using the Perdew-Burke-Ernzerhof (PBE) form of the generalized gradient approximation.[39] The ion-electron interactions are described using ultrasoft pseudopotentials.[38]

We have used a 15×15 supercell of graphene to adsorb the CoPc molecule. van der Waals interactions between the molecule and substrate are described using the semi-empirical DFT-D2 method.[40]

All the atomic coordinates are relaxed, until the forces are less than 10^{-3} Ry/Bohr. Brillouin zone (BZ) sampling is restricted to the zone center for the geometry optimization calculations. We have used Marzari-Vanderbilt[43] broadening functions of the width of 0.001 Ry to aid the convergence. To generate the projected density of states (PDOS) plots and charge redistribution plots, we have used k-mesh of 6×6×1 to sample the BZ using the Monkhorst-Pack scheme.[44]

5.3 Results and discussion for F_4TCNQ/Gr

5.3.1 Adsorption geometry of F_4TCNQ on Gr

In order to determine the adsorption geometry of F_4TCNQ molecule on graphene, we have used density functional theory to compute the total energy for five different starting configurations shown in Figs. 5.3(a)-(e). These configurations differ in the lateral position of the molecule with respect to the graphene substrate, note in particular the position of the hexagonal ring of the molecule with respect to the graphene. For example, the centre of the hexagonal ring of the F_4TCNQ molecule is positioned on top of a C-C bond of the graphene in Figs. 5.3(a) and (d), with the molecule rotated 60° in Fig. 5.3(d) from its position in Fig. 5.3(a). Similarly,

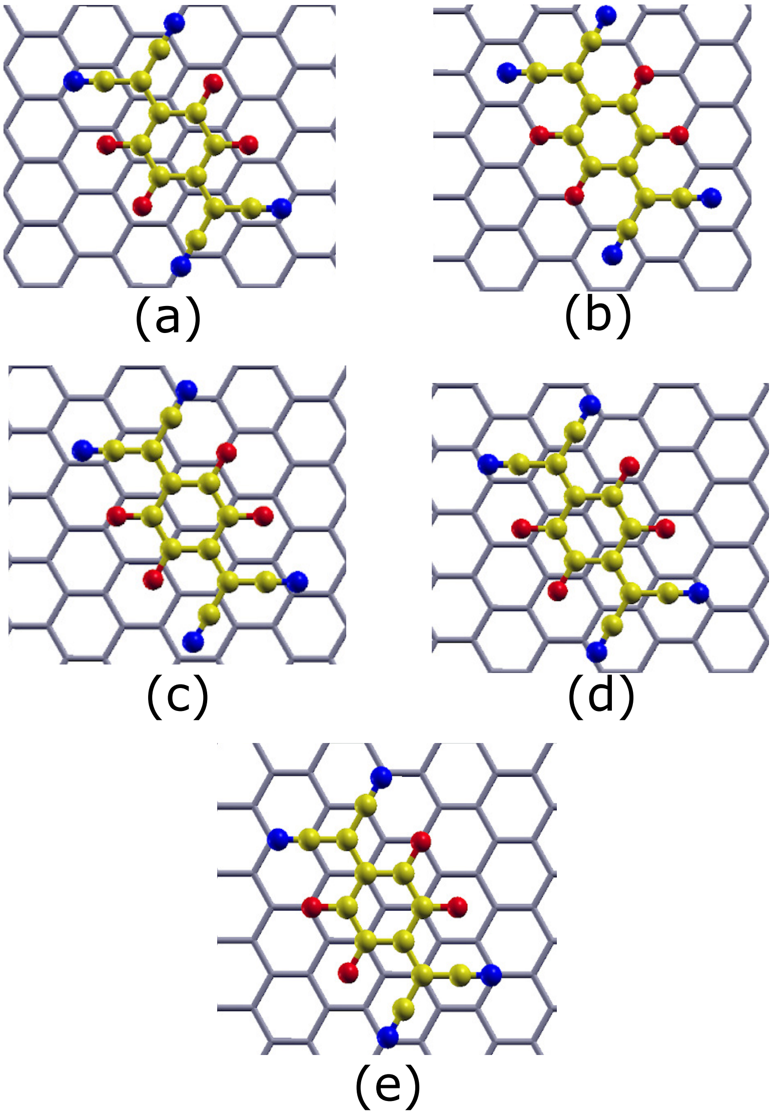

Figure 5.3: Zoomed in views of five starting adsorption configurations considered for a single F_4TCNQ molecule on undoped graphene; a $\sqrt{127}\times\sqrt{127}$ graphene supercell was used in the calculaitons. As a result, periodic images of molecules are > 12 Å away from each other. Color codes for atoms are red (F), yellow (C), blue (N), and gray (C of graphene).

the hexagonal ring of the molecule is positioned on top of the hexagonal ring of the substrate graphene in Fig. 5.3(b). In Figs. 5.3(c) and 5.3(e), the centre of the hexagonal ring of the molecule is on top of the C atom of the graphene sheet. However, the hexagonal ring in Fig. 5.3(c) is not exactly on top of a C atom as in Fig. 5.3(e) rather, it has a lateral shift. In all these configurations, we have considered a single F_4TCNQ molecule being adsorbed within a $\sqrt{127} \times \sqrt{127}$ graphene supercell. This results in an intermolecular distance (between periodic images of molecules) of more than 12 Å, as a result of which any intermolecular interactions are essentially negligible.

The adsorption energy $E_{\mathrm{ads}}^{\mathrm{Gr}}$ for each of these configurations is calculated using the following formula:

$$E_{\mathrm{ads}}^{\mathrm{Gr}} = E_{\mathrm{F_4TCNQ/Gr}} - E_{\mathrm{Gr}}^{\mathrm{bare}} - E_{\mathrm{F_4TCNQ}}^{\mathrm{iso}}, \tag{5.1}$$

where $E_{\mathrm{F_4TCNQ/Gr}}$, $E_{\mathrm{Gr}}^{\mathrm{bare}}$, and $E_{\mathrm{F_4TCNQ}}^{\mathrm{iso}}$ are the total energies of the combined F_4TCNQ/Gr system, bare graphene, and an isolated molecule in the gas phase, respectively. Comparing the adsorption energies calculated using Eq. (5.1) for all the configurations we considered, it is found that a single F_4TCNQ prefers to adsorb on the pristine graphene in the configuration shown in Fig. 5.3(d). Note that for all the starting configurations except that shown in Fig. 5.3(d), the F_4TCNQ molecule moves laterally on the graphene and relaxes to the most energetically favorable configuration, viz., that shown in Fig. 5.3(d).

The calculated value of adsorption energy ($E_{\mathrm{ads}}^{\mathrm{Gr}}$) for the configuration shown in Fig. 5.3(d) is -1.482 eV/molecule. We note that our optimized adsorption geometry is in very good agreement with that found by previous authors.[27;48]

In this context, it would be nice to compare our adsorption geometry for F_4TCNQ/Gr, with that obtained for TCNQ/Gr as reported earlier.[25;49] Both TCNQ and F_4TCNQ are electron acceptor type molecules. One can get TCNQ by replacing four fluorine (F) atoms with four hydrogens (H) in F_4TCNQ; the optimized geometry of an isolated F_4TCNQ molecule in the gas phase was shown in Fig. 5.2(a) above. The study by Pham et al.[25] showed that TCNQ adsorbs on graphene at the configuration where the centre of the ring of the TCNQ is positioned over a C-C bond of the graphene, just as we find F_4TCNQ does on graphene. Their reported value of adsorption energy for the TCNQ/Gr system was -1.27 eV/molecule.[49] Our calculations show that the magnitude of the adsorption energy for F_4TCNQ/Gr is slightly higher than that for TCNQ/Gr; this can be rationalized as being due to the enhanced charge transfer observed in the F_4TCNQ/Gr system due to the presence of the most electronegative element F. We found that charge (electron) transfer from pristine graphene to F_4TCNQ (ΔQ= 0.47 e) is higher compared to TCNQ ($\Delta Q =$ 0.30 e). In this context, we would like to mention a comparative study by Oliveira et al.[27] where they have presented a detailed discussion of the difference in charge transfer between TCNQ and F_4TCNQ molecules on graphene. We note however that we are interested in extending these previous studies, in order to explore the possibility magnetism in F_4TCNQ on graphene by using an external electric field or by doping the substrate graphene with nitrogen atoms.

5.3.2 Tuning of molecular magnetism in F_4TCNQ/Gr system using an external electric field

In this subsection, we show that one can achieve the magnetism in this organic molecule-graphene system by applying an external electric field perpendicular to the substrate. Our calculations show that F_4TCNQ/Gr develops magnetism in the presence of an applied negative electric field ($\epsilon < 0$) while it shows a magnetic to non-magnetic transition if the field is turned off or if we apply a positive electric

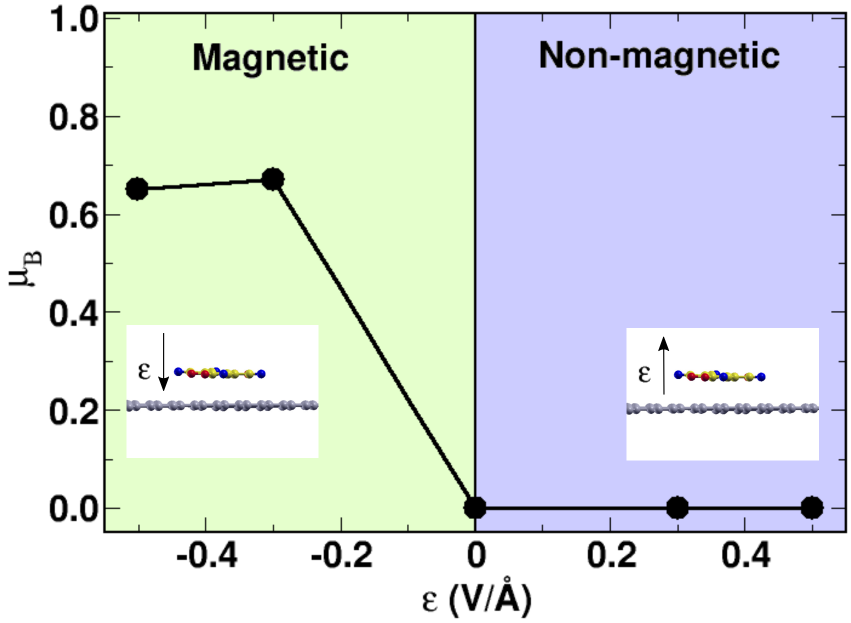

Figure 5.4: The magnetic moment μ_B has been plotted as a function of the applied external electric field. The insets show the direction of the electric field (a negative electric field is pointed downwards, while a positive electric field pointed upwards, i.e., towards the molecule). A negative electric field ($\epsilon < 0$) gives rise to a magnetic moment in the F_4TCNQ/Gr system.

field ($\epsilon > 0$), see Fig. 5.4. The pale green region in Fig. 5.4 represents the magnetic regime. The blue shaded region of the Fig. 5.4 is the non-magnetic regime. Note that we refer to the electric field as a positive electric field when the field is along $+z$ (points from graphene to molecule) and negative electric field if it is along $-z$-direction (points from molecule to graphene). Corresponding insets of Fig. 5.4 show the directions of the electric fields.

The electric-field-induced magnetism can be understood by looking at the charge transfer in the system. In Fig. 5.5(a), we have plotted the charge transferred from the Gr to the molecule, as a function of the electric field. We note that we have used the Bader method[46] to partition the charge between the molecule and the Gr substrate. We see that as the electric field is made more negative, this charge (electron) transfer ΔQ increases, in a linear fashion. The negative electric field pushes electrons from the Gr into the molecule.

In Fig. 5.5(b), we have plotted μ_B (the total magnetic moment of the system) as a function of the charge (electron) transfer (ΔQ) from Gr to the molecule. It is clear from Fig. 5.5(b) that the charge transfer induces the magnetic moment.

To see where the magnetic moment is localized in the F_4TCNQ/Gr system, in Fig. 5.6 we have plotted the isosurfaces of the spin polarization, i.e., the difference of spin-up and spin-down charge density $\left[n^{\uparrow}(\mathbf{r}) - n^{\downarrow}(\mathbf{r})\right]$ of the combined F_4TCNQ/Gr system for $\epsilon = -0.3$ V/Å and $\epsilon = -0.5$ V/Å. We can conclude from Fig. 5.6 that the magnetic moment is primarily localized on the molecule, not on the graphene. The green lobes in Fig. 5.6 correspond to a net positive spin polarization, i.e., $n^{\uparrow}(\mathbf{r}) > n^{\downarrow}(\mathbf{r})$, while the purple lobes correspond to a net negative spin polarization, i.e., $n^{\uparrow}(\mathbf{r}) < n^{\downarrow}(\mathbf{r})$.

To investigate the origin of the molecular magnetism in the F_4TCNQ molecule, we have calculated the non-spin-polarized density of states of the F_4TCNQ/Gr system for different external electric fields, and looked at the position of the LUMO peak of the F_4TCNQ molecule with respect to the Fermi energy as a function of ϵ [see Fig. 5.7(a)] and ΔQ [see Fig. 5.7(b)]. For both the cases, one finds that when the non-spin-polarized LUMO peak falls at the Fermi energy or very close to the Fermi energy, the LUMO peak splits into a spin up SOMO (singly occupied molecular orbital) and a spin down SUMO (singly unoccupied molecular orbital). This can be seen in, e.g., see Fig 5.8(a) for $\epsilon = -0.5$ V/Å. However, Figs. 5.8(b) shows no splitting of the LUMO, because the LUMO peak is far from the Fermi level for $\epsilon = +0.5$ V/Å.

One would expect that both the SOMO and the SUMO should look like the LUMO in shape as it splits into SOMO and SUMO in a negative electric field. We have simulated STM images using the Tersoff-Hamann approach[45] at two bias

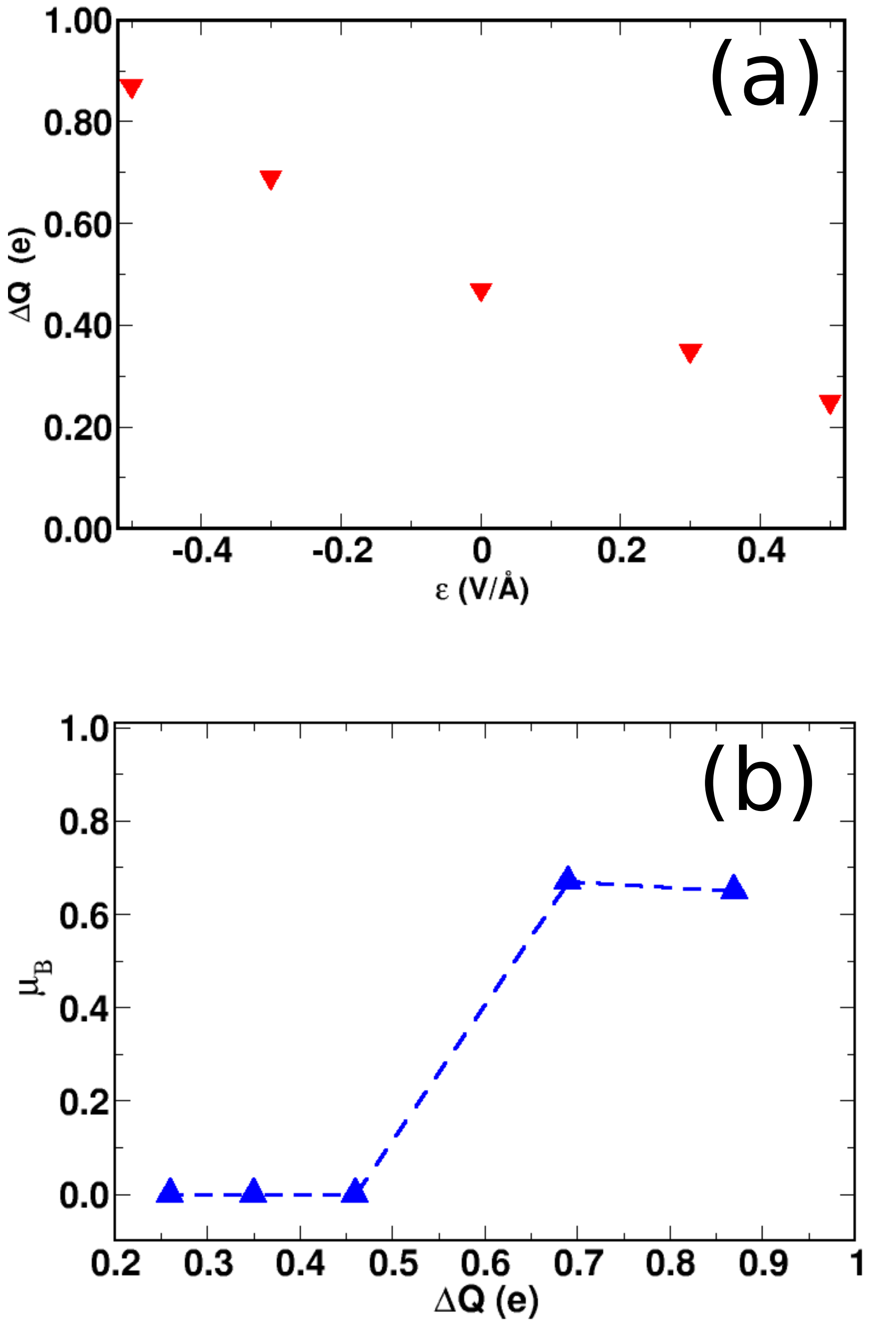

Figure 5.5: (a) ΔQ (charge transfer from substrate to the molecule) as a function of external electric field (b) Total magnetic moment μ_B of the system as a function of ΔQ.

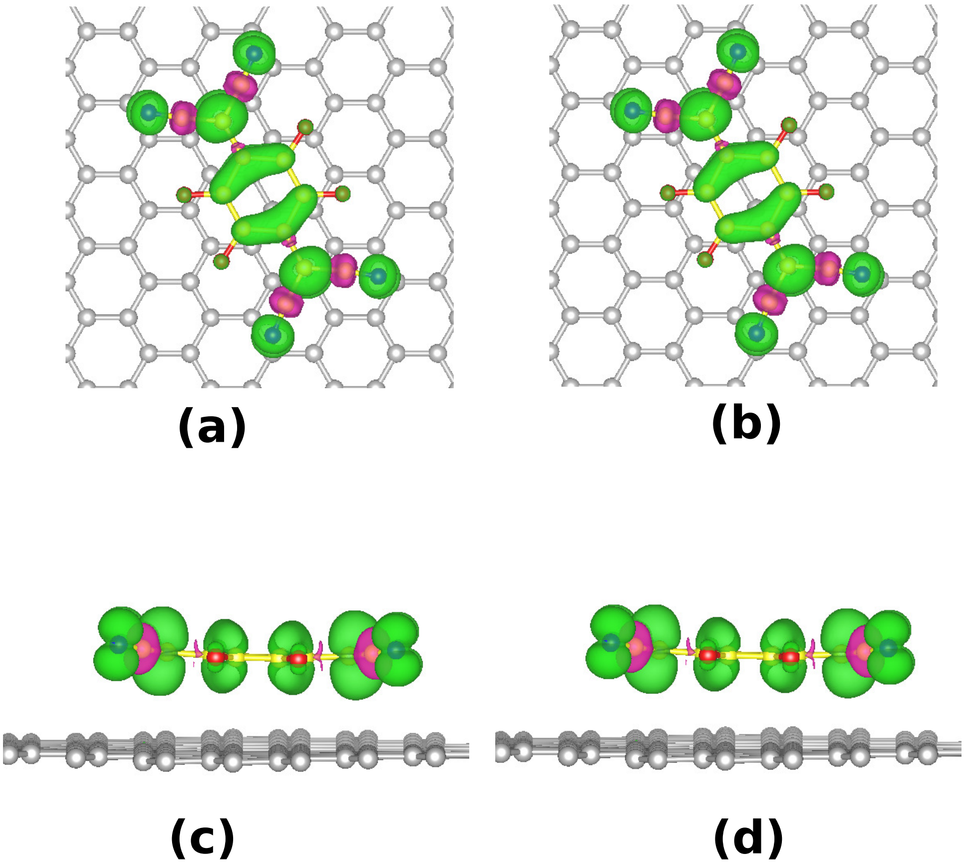

Figure 5.6: Top and side views of F_4TCNQ/Gr, showing isosurfaces of the spin polarization $\left[n^{\uparrow}(\mathbf{r})-n^{\downarrow}(\mathbf{r})\right]$. (a),(c) ϵ =-0.3 V/Å, (b),(d) ϵ =-0.5 V/Å. Green lobes: $n^{\uparrow}(\mathbf{r}) > n^{\downarrow}(\mathbf{r})$, purple lobes: $n^{\uparrow}(\mathbf{r}) < n^{\downarrow}(\mathbf{r})$ Isosurface value: 0.00095 e/Bohr^3

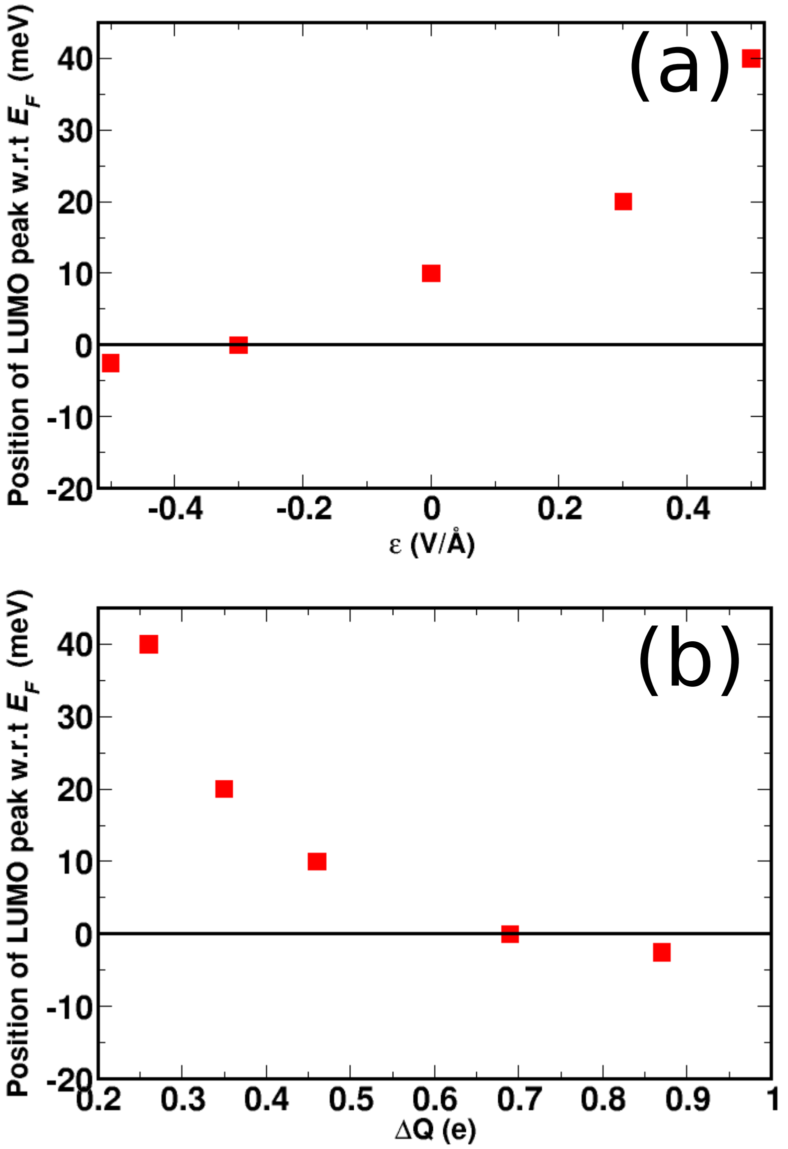

Figure 5.7: (a) Position of the LUMO peak (in a non-spin-polarized calculation) of the F_4TCNQ molecule with respect to the Fermi energy of the F_4TCNQ/Gr system for different external electric fields (b) Position of the LUMO peak (in a non-spin-polarized calculation) of the F_4TCNQ molecule with respect to the Fermi energy of the F_4TCNQ/Gr system as a function ΔQ (charge transfer from substrate to the molecule).

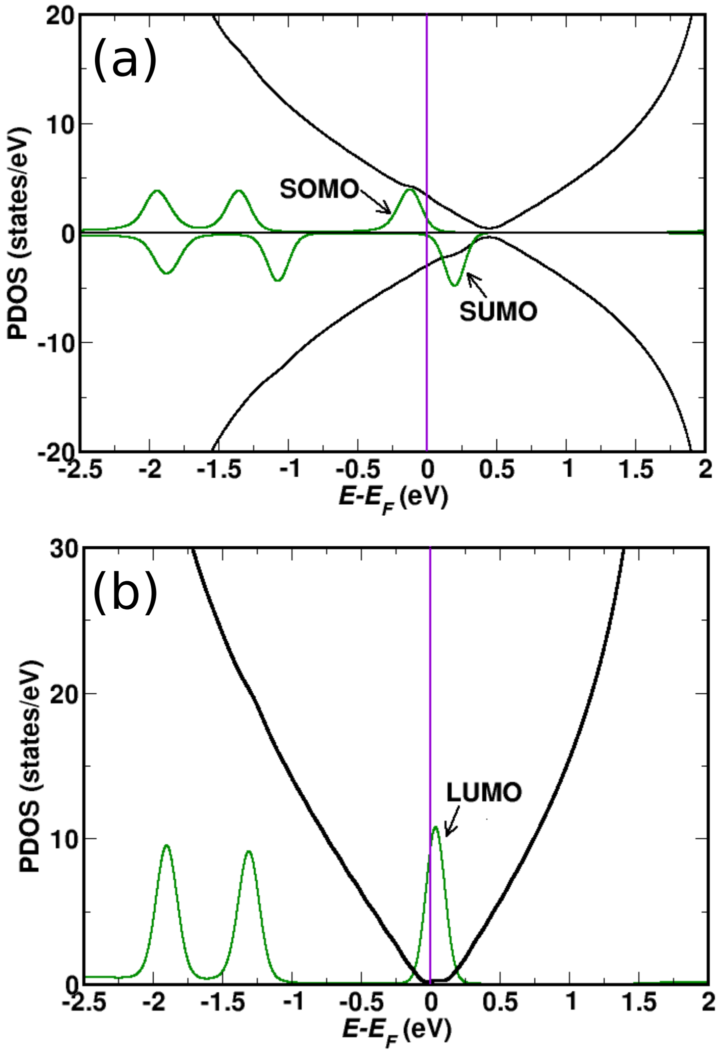

Figure 5.8: Projected density of states (PDOS) for F$_4$TCNQ/Gr system at (a) ϵ = -0.5 V/Å, and (b) ϵ = 0.5 V/Å. Black and green lines represent the PDOS for graphene and F$_4$TCNQ, respectively. The Fermi level has is shown using a violet line.

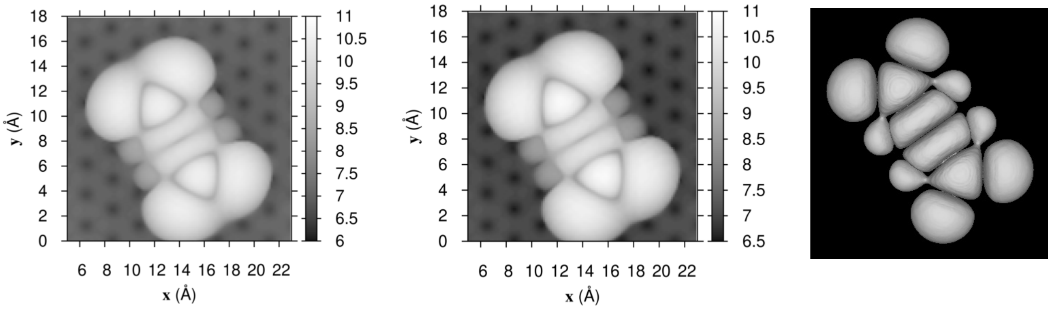

(a) (b) (c)

Figure 5.9: Constant current STM images simulated at (a) −0.5 V and (b) +0.5 V for the F_4TCNQ/Gr shown in Fig. 5.3(d). All the simulations have been performed applying an external electric field (ϵ) of −0.5 V/Å perpendicular to the graphene sheet. We have plotted the isosurface values of 1×10^{-8} e/Bohr^3 to plot the constant current images (c) LUMO of F_4TCNQ molecule in the gas phase. Isosurface value of 0.00015 e/Bohr^3 is used to plot the LUMO of the molecule.

voltages −0.5 V and +0.5 V in order to see their shapes. The STM image simulated at −0.5 V [see Fig. 5.9(a)] shows the shape of the SOMO and the STM image simulated at +0.5 V [see Fig. 5.9(b)] shows the SUMO. By comparing Fig. 5.9(a) and Fig. 5.9(b) with the ILDOS (integrated local density of states) plot for the LUMO of the gas phase molecule shown in Fig. 5.9(c), it can be concluded that the shapes of both SOMO and SUMO look like the shape of the LUMO of the gas phase molecule.

5.3.3 Adsorption of F_4TCNQ on nitrogen-doped graphene

We divide this section into three subsections. In the first subsection, we compute the formation energy of graphene doped with a nitrogen atom and a nitrogen pair, and compare these configurations with the pristine graphene. Next, we discuss the adsorption of a F_4TCNQ molecule on graphene doped with single nitrogen (N-Gr) and then on graphene doped with a nitrogen pair (2N-Gr).

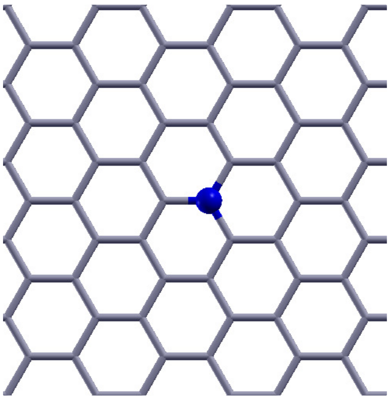

Figure 5.10: Zoomed in view of graphene doped with single N atom (N-Gr). A $\sqrt{127} \times \sqrt{127}$ graphene (Gr) supercell was used for N doping. Color code: blue (N), and gray (C of graphene).

Graphene doped with single nitrogen (N-Gr) and nitrogen pair (2N-Gr)

We have substituted one C atom of the $\sqrt{127} \times \sqrt{127}$ graphene (Gr) supercell by a single N atom to create the N-Gr supercell (see Fig. 5.10), and two C atoms by 2 N atoms to create the 2N-Gr supercell. For 2N-Gr, we can have more than one configuration depending on the positions of the two N atoms relative to each other. We have considered a few such possibilities, see Fig. 5.11. The formation energy ($E^{\text{form}}_{\text{doped Gr}}$) for graphene doped with single nitrogen/N-pair can be calculated using the following formula:

$$E^{\text{form}}_{\text{doped Gr}} = -\frac{1}{n_i}\left(E^{\text{bare}}_{\text{Gr}} - n_i(\mu_C - \mu_N) - E_{\text{doped Gr}}\right), \tag{5.2}$$

where $E^{\text{bare}}_{\text{Gr}}$ is the total energy of the bare graphene (Gr), and $E_{\text{doped Gr}}$ is the total energy of the graphene doped with single nitrogen/ N-pair. n_i is the number of C atoms substituted by N atoms from the graphene. n_i is 1 for N-Gr and 2 for 2N-Gr. μ_C and μ_N are the chemical potentials of the C and N atoms. μ_C is calculated by dividing the total energy of pristine Gr by the total number of C atoms present in the system. μ_N is half of the total energy calculated for an isolated N_2 molecule in the gas phase.

Table 5.1 lists the formation energy of N-doped graphene. First of all, we see that the formation energies are positive for N-doped graphene, which is in agreement with the results of previous DFT studies.[50;51] Note that a positive value of $E^{\text{form}}_{\text{doped Gr}}$ implies that nitrogen doping is unfavorable. So, the higher the positive value of $E^{\text{form}}_{\text{doped Gr}}$, the lower the chances of formation is. One can note from Table 5.1 that the formation of 2N-Gr is thermodynamically more likely compared to the formation of N-Gr. One can also note that the configuration corresponding to Fig. 5.11(f) is the most energetically favorable one among all the configurations we have considered for 2N-Gr, though the configuration shown in Fig. 5.11(i) is very close to the energy that of the configuration Fig. 5.11(f). Two previous groups of authors, Hou et al.,[50] and Xiang et al.,[51] reported that the latter configuration, i.e., that shown in Fig. 5.11(i), has the lowest formation energy for a N-pair. However, these previous authors did not consider the configuration shown in Fig. 5.11(f), which we find is slightly lower in energy. We note that STM experiments performed by Tison et al.[52] and Telychko et al.[53] found the configuration shown in Fig. 5.11(b) to be the most commonly seen configuration.

Table 5.1 also lists the magnetic moments for the various configurations considered for graphene doped by a single N or a N-pair. Note that N-Gr is a magnetic system. However, not all the configurations of 2N-Gr are magnetic [see Table 5.1]. We note that the most stable configuration of 2N-Gr [i.e., Fig. 5.11(f)] is a nonmagnetic system.

F_4TCNQ on single nitrogen-doped graphene (F_4TCNQ/N-Gr)

In order to determine the lowest energy adsorption geometry of F_4TCNQ molecule on N-Gr, we have computed the adsorption energy ($E^{\text{N-Gr}}_{\text{ads}}$) for all the configurations

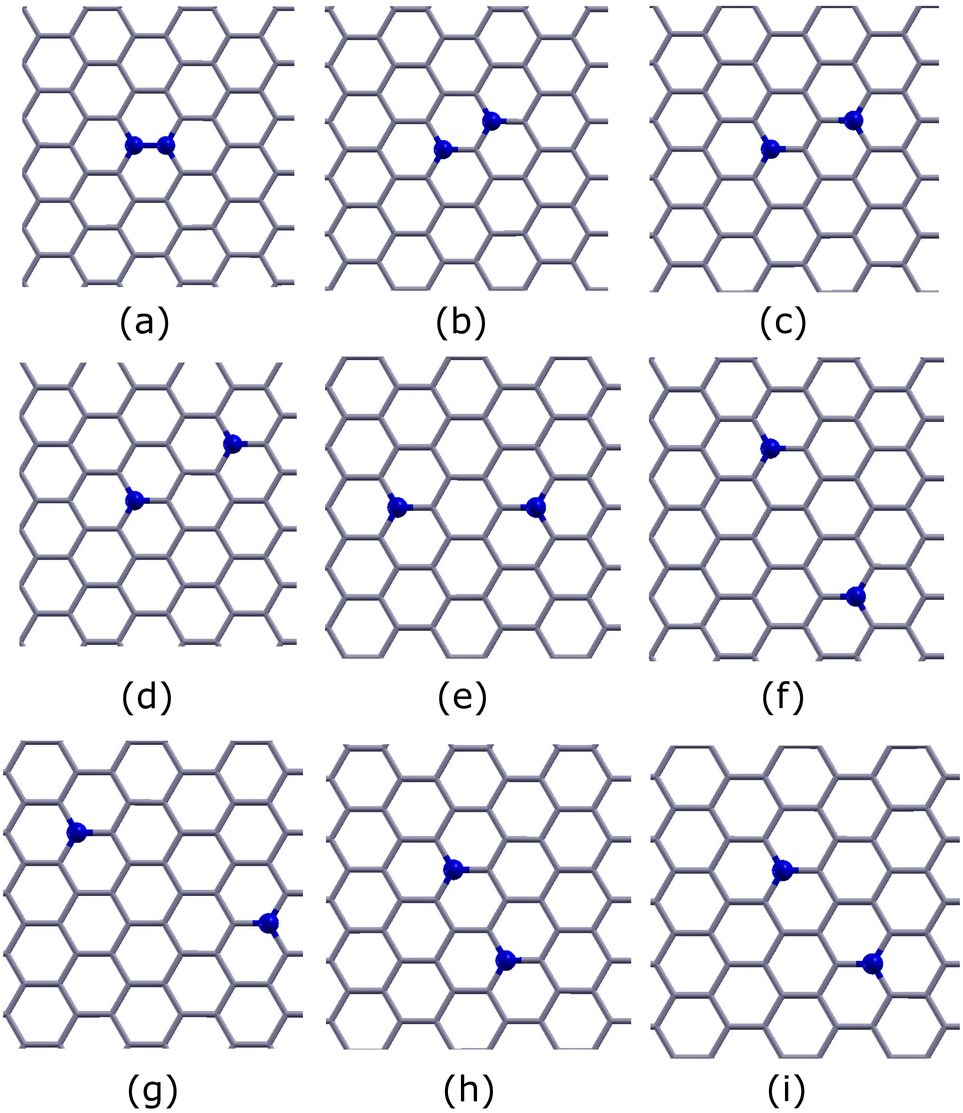

Figure 5.11: Zoomed in views of graphene doped with N pair (2N-Gr). A $\sqrt{127} \times \sqrt{127}$ graphene (Gr) supercell was used for N doping where we have replaced 2 C atoms of Gr with 2 N atoms. (a)–(i) are the configurations we considered for the different positions N atoms in 2N-Gr. Color codes for atoms are blue (N), and gray (C of graphene).

Table 5.1: Computed formation energy ($E^{\text{form}}_{\text{doped Gr}}$) for the graphene doped with nitrogen pair (2N-Gr) and for the graphene doped with single nitrogen (N-Gr). We have substituted one C atom of $\sqrt{127} \times \sqrt{127}$ graphene supercell by a single N atom for N-Gr and two C atoms by two N atoms in case of 2N-Gr. For 2N-Gr, we can have more than one configuration depending on the position of the two N atoms with respect to each other. The formation energies have been computed using Eq. (5.2). For ease of reference, the values corresponding to the lowest-energy configuration have been boxed.

Figure corresponding to configuration	$E^{\text{formation}}_{\text{doped Gr}}$(eV/N atom)	Magnetic Moment (μ_B)
pristine Gr	0.0	0.00
$\boxed{\text{N-Gr [Fig. 5.10]}}$	$\boxed{1.088}$	$\boxed{1.00}$
2N-Gr [Fig. 5.11(a)]	1.485	0.00
2N-Gr [Fig. 5.11(b)]	1.169	0.00
2N-Gr [Fig. 5.11(c)]	1.134	0.13
2N-Gr [Fig. 5.11(d)]	1.127	2.00
2N-Gr [Fig. 5.11(e)]	1.022	0.00
$\boxed{\text{2N-Gr [Fig. 5.11(f)]}}$	$\boxed{0.967}$	$\boxed{0.00}$
2N-Gr [Fig. 5.11(g)]	1.008	0.00
2N-Gr [Fig. 5.11(h)]	1.060	0.00
2N-Gr [Fig. 5.11(i)]	0.977	0.00

shown in Fig. 5.12 using the following formula:

$$E_{\text{ads}}^{\text{N-Gr}} = E_{\text{F}_4\text{TCNQ/N-Gr}} - E_{\text{N-Gr}}^{\text{bare}} - E_{\text{F}_4\text{TCNQ}}^{\text{iso}}, \tag{5.3}$$

where $E_{\text{F}_4\text{TCNQ/N-Gr}}$, $E_{\text{N-Gr}}^{\text{bare}}$, and $E_{\text{F}_4\text{TCNQ}}^{\text{iso}}$ are the total energies of the combined F_4TCNQ/N-Gr system, bare N-Gr and the isolated molecule in the gas phase. One should note that the F_4TCNQ molecule is on the nitrogen atom (N-sites) for all the configurations presented in Fig. 5.12. To see whether the molecule prefers to sit on a N-site or far from the N-site, we also have computed the adsorption energy for one configuration where the molecule is adsorbed far from the dopant nitrogen atom (i.e., on a C-site), see Fig. 5.13.

The calculated adsorption energies have been listed in Table 5.2, which suggests that configuration Fig. 5.12(e) is the most stable configuration among all those considered by us. These results for the favored adsorption geometry agree with those of a previous study in which the authors studied the adsorption of TCNQ on N-Gr.[25] The authors of this previous study found that the N atom of the TCNQ molecule lies almost directly over the N dopant atom of the N-Gr, as in our Fig. 5.12(e). Note that we find that the configurations shown in Figs. 5.12(e) and 5.12(a) are almost degenerate; this is because in both cases, the N atoms in the molecule sit almost directly over the N dopant atom.

From the results shown in Table 5.2, we can also conclude that F_4TCNQ prefers to sit over a N-site (over the dopant nitrogen atom) instead of a C-site (i.e., far from dopant N, see Fig. 5.13). This is due to the higher electron transfer (ΔQ) from the substrate to the molecule over a N-site compared to the C-site. The calculated ΔQ is 0.99 e from N-site to the molecule and 0.47 e from C-site to the molecule. We found that the configuration in Fig. 5.12(e) got extra stabilization of -0.966 eV/molecule on N-Gr compared to the undoped (pristine) Gr. In the

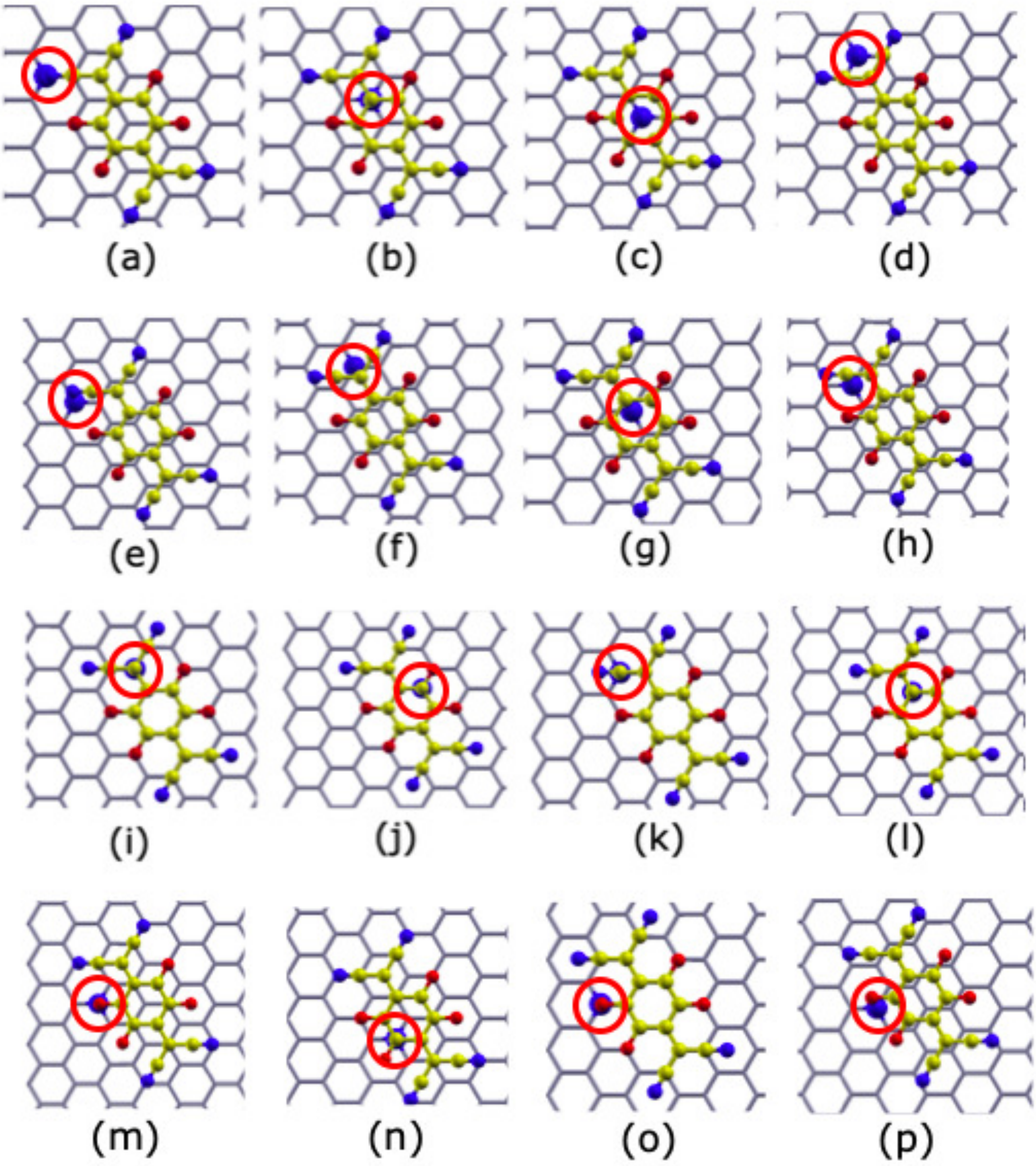

Figure 5.12: Zoomed in views of various optimized geometries of single F_4TCNQ on N-Gr. The positions of the single dopant N atom have been highlighted using a red circle. Color code for atoms is red (F), yellow (C), blue (N), and gray (C of graphene).

Table 5.2: Calculated values for the adsorption energy $E_{\text{ads}}^{\text{N-Gr}}$ for the various adsorption geometries considered for F_4TCNQ on graphene with a single N atom. The values are computed using Eq. (5.3). For ease of reference, the value corresponding to the lowest-energy geometry has been boxed.

Figure corresponding to configuration	$E_{\text{ads}}^{\text{N-Gr}}$(eV)
Fig. 5.12(a)	-2.443
Fig. 5.12(b)	-2.374
Fig. 5.12(c)	-2.379
Fig. 5.12(d)	-2.421
$\boxed{\text{Fig. 5.12(e)}}$	$\boxed{-2.448}$
Fig. 5.12(f)	-2.435
Fig. 5.12(g)	-2.378
Fig. 5.12(h)	-2.414
Fig. 5.12(i)	-2.347
Fig. 5.12(j)	-2.336
Fig. 5.12(k)	-2.390
Fig. 5.12(l)	-2.334
Fig. 5.12(m)	-2.385
Fig. 5.12(n)	-2.370
Fig. 5.12(o)	-2.345
Fig. 5.12(p)	-2.398
Fig. 5.13	-2.273

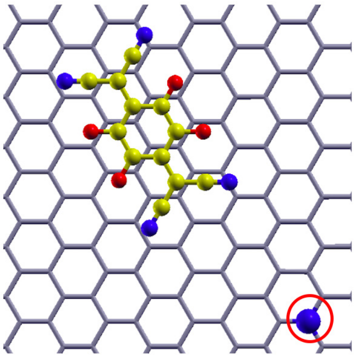

Figure 5.13: Optimized geometry of single F_4TCNQ adsorbed at a C-site of the doped graphene, far away from the dopant N atom. Color code for atoms is red (F), yellow (C), blue (N), and gray (C of graphene). The positions of the single dopant N atom have been highlighted using a red circle.

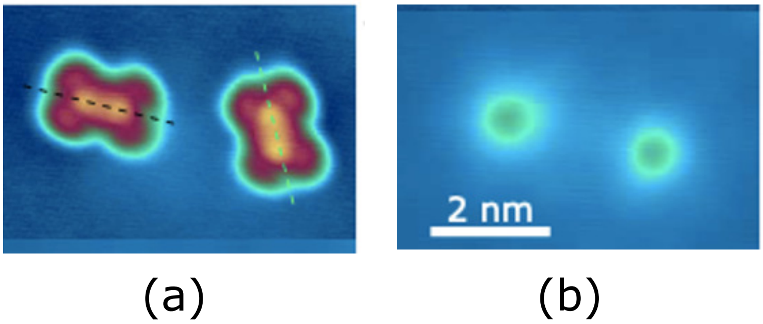

Figure 5.14: Experimental STM images for (a) F_4TCNQ/N-Gr (b) after removal of F_4TCNQ molecules from F_4TCNQ/N-Gr. The two bright circles in (b) indicate the position of dopant N atoms where formerly F_4TCNQ molecules were present. Both the images recorded at bias voltage of +1.5 V and at I = 5 pA. The figures are reprinted with permission from Ref. 54.

configuration corresponding to Fig. 5.13, where the molecule is far away from the N dopant, one might have expected to get the same result as for adsorption on pristine (undoped) graphene. However, we see that the magnitude of the adsorption energy is significantly larger for the configuration corresponding Fig. 5.13 than it was for F_4TCNQ on the undoped system (−1.482 eV/molecule), even though in the former case, the F_4TCNQ molecule is far away from the dopant nitrogen. This suggests that the effect of the dopant is felt even at quite a distance away from it, and our unit cell is small enough that the molecule sees the effect of the N-dopant even at a "C-site" that is as far away as possible from the N-dopant.

These results are in good agreement with the results of STM experiments performed by our collaborators from the University of Paris-Diderot. The experiments were performed at 4 K temperature.[54] Fig. 5.14(a) is the STM image recorded for F_4TCNQ/N-Gr system and Fig. 5.14(b) shows the image recorded in the same area after the removal of F_4TCNQ molecule from F_4TCNQ/N-Gr. The two bright spots in Fig. 5.14(b) represent the N atoms' position in N-Gr; these become visible only after removing the molecules from F_4TCNQ/N-Gr combined system, at exactly the positions where formerly F_4TCNQ molecules were present. This confirms that the molecules preferentially adsorb over N-sites.

Adsorption of F_4TCNQ on graphene doped with nitrogen pair (F_4TCNQ/2N-Gr)

In order to determine the adsorption geometry of the F_4TCNQ on 2N-Gr, we have computed the adsorption energy ($E_{\text{ads}}^{\text{2N-Gr}}$) for all the configurations shown in Fig. 5.15 using the following formula:

$$E_{\text{ads}}^{\text{2N-Gr}} = E_{\text{F}_4\text{TCNQ/2N-Gr}} - E_{\text{2N-Gr}}^{\text{bare}} - E_{\text{F}_4\text{TCNQ}}^{\text{iso}}, \tag{5.4}$$

where $E_{\text{F}_4\text{TCNQ/2N-Gr}}$, $E_{\text{2N-Gr}}^{\text{bare}}$, and $E_{\text{F}_4\text{TCNQ}}^{\text{iso}}$ are the total energies of the combined F_4TCNQ/2N-Gr system, bare 2N-Gr, and the isolated molecule in the gas phase.

Table 5.3 lists the adsorption energy of a single F_4TCNQ molecule on a N-pair of the N-doped graphene. Note that we have considered different configurations for the relative separation of the two N atoms in the N-pair, as well as for the molecule with respect to the N-pair. We see from Table 5.3 that Fig. 5.15(i) is the most stable configuration for the F_4TCNQ on 2N-Gr. Interestingly, here the 2 N atoms in the N-pair are not in their lowest energy configuration for bare 2N-Gr [see Fig. 5.11(c)]. Recall that Fig. 5.11(f) was the lowest energy configuration for bare 2N-Gr. The

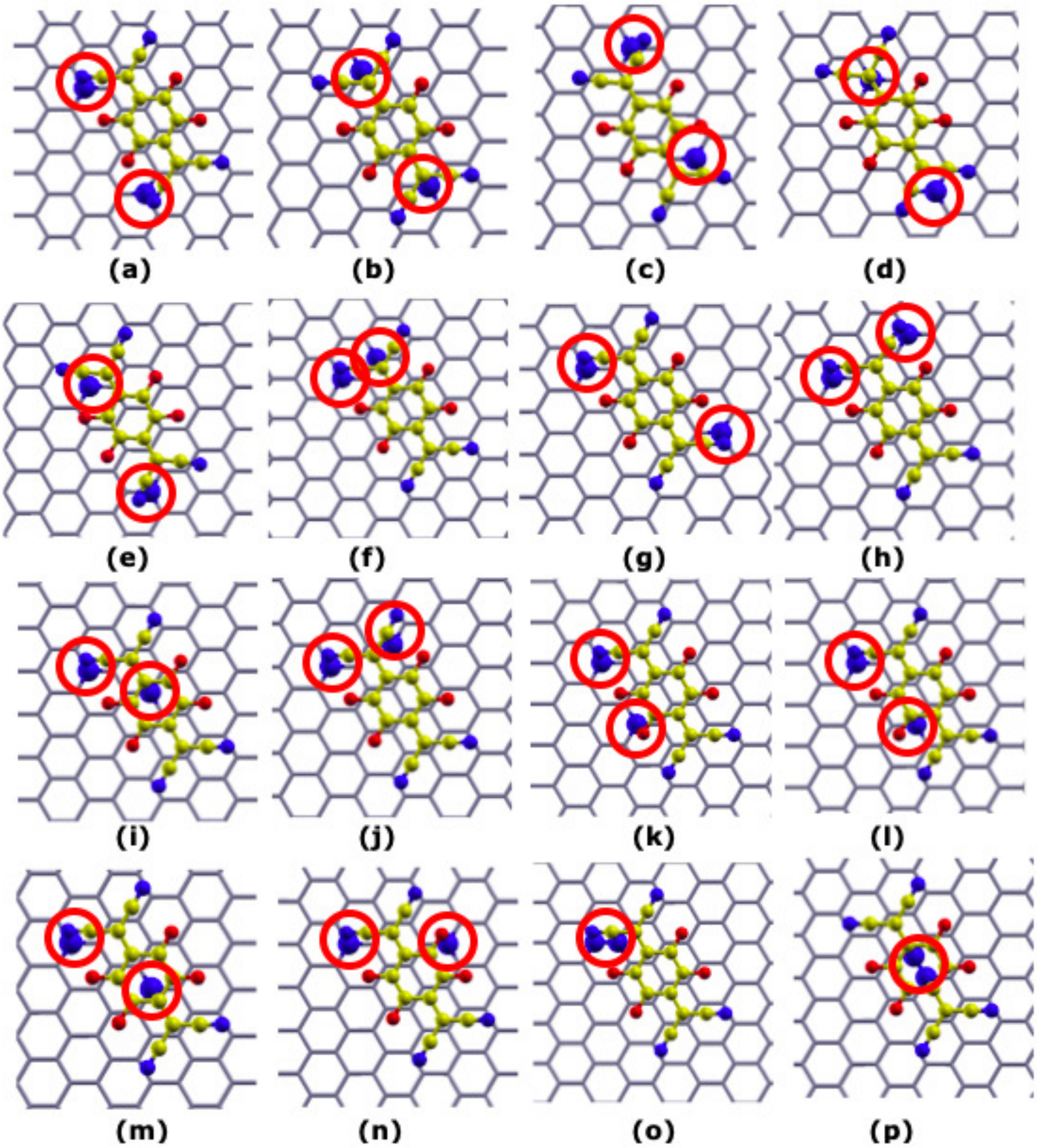

Figure 5.15: Zoomed in views of optimized geometry of single F_4TCNQ on 2N-Gr. We have doped $\sqrt{127} \times \sqrt{127}$ supercell of graphene with a N pair. Different positions for dopant N have been shown using red circle. Color code for atoms are red (F), yellow (C), blue (N), and gray (C of graphene).

charge transfer from the N-pair to the molecule is now significantly higher than it was on pristine graphene or over a single N-dopant, with ΔQ =1.20 e, favoring the molecular adsorption over a N-pair compared to over a single N or pristine graphene.

5.3.4 N-doping in graphene induces molecular magnetism in F_4TCNQ/Gr system

We have found that adsorption of the F_4TCNQ molecule on both the N-Gr & 2N-Gr induces molecular magnetism. This can be confirmed by looking at difference of spin-up & spin-down $\left[n^{\uparrow}(\mathbf{r}) - n^{\downarrow}(\mathbf{r})\right]$ charge densities for the F_4TCNQ/N-Gr [configuration Fig. 5.12(e)] and F_4TCNQ/2N-Gr [configuration Fig. 5.15(i)] systems, see Fig. 5.16. The calculated magnetic moment is 1.0 μ_B for F_4TCNQ/N-Gr and 0.44 μ_B for F_4TCNQ/2N-Gr, which can be explained by looking at their isosurfaces in Fig. 5.16(b) and 5.16(d). Prominent lobes present in the isosurface of Fig. 5.16(b) indicate high magnetic moment for F_4TCNQ/N-Gr. One can note from Fig. 5.16 that upon deposition of the molecule, the magnetic moment of 1 μ_B gets transferred from the substrate N-Gr (graphene doped with single N) to (orimarily) the molecule adsorbed on it. In the case of 2N-Gr, the bare substrate had a magnetic moment of 0.13 μ_B [for config. Fig. 5.11(c)] , but the system acquires a magnetic moment of 0.44 μ_B after adsorption of the molecule. No lobes present in the isosurface of Fig. 5.16(c) indicate very low spin polarization density for 2N-Gr after molecular adsorption. Doping induced molecular magnetism can also be confirmed by examining the density of states for F_4TCNQ/N-Gr and F_4TCNQ/2N-Gr, see Fig. 5.17.

The lowest unoccupied molecular orbital (LUMO) of the molecule splits into a spin-up SOMO (singly occupied molecular orbital) and a spin-down SUMO (singly unoccupied molecular orbital) [see Figs.5.17(a) and 5.17(b)] with different filling

Table 5.3: Computed adsorption energy ($E_{\text{ads}}^{\text{2N-Gr}}$) for various configurations considered for F_4TCNQ/2N-Gr. We have substituted two C atoms of the ($\sqrt{127} \times \sqrt{127}$) graphene supercell with two N atoms and adsorbed a F_4TCNQ molecule on it. The adsorption energy is computed using Eq. (5.4). The boxed value corroesponds to the lowest energy configuration.

Figure corresponding to configuration	$E_{\text{ads}}^{\text{2N-Gr}}$(eV/molecule)
Fig. 5.15(a)	-2.422
Fig. 5.15(b)	-2.408
Fig. 5.15(c)	-2.506
Fig. 5.15(d)	-2.467
Fig. 5.15(e)	-2.496
Fig. 5.15(f)	-2.429
Fig. 5.15(g)	-2.508
Fig. 5.15(h)	-2.560
$\boxed{\text{Fig. 5.15(i)}}$	$\boxed{-2.578}$
Fig. 5.15(j)	-2.522
Fig. 5.15(k)	-2.414
Fig. 5.15(l)	-2.358
Fig. 5.15(m)	-2.493
Fig. 5.15(n)	-2.421
Fig. 5.15(o)	-2.203
Fig. 5.15(p)	-2.134

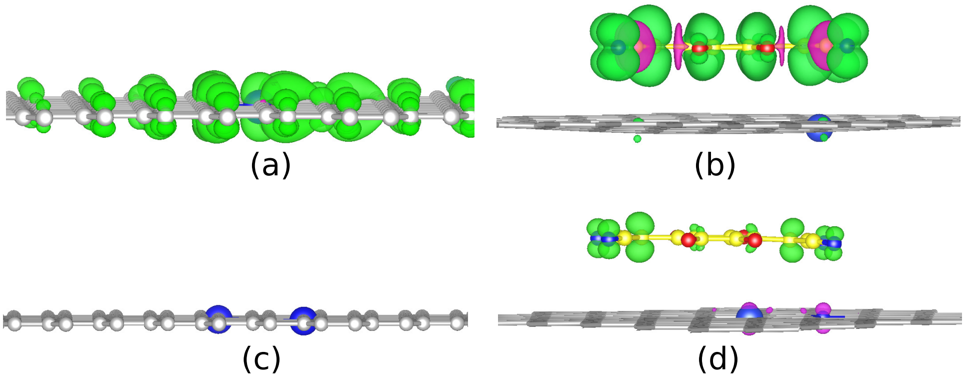

Figure 5.16: Side views showing isosurfaces of the spin polarization density $\left[n^{\uparrow}(\mathbf{r})-n^{\downarrow}(\mathbf{r})\right]$, for (a) bare N-Gr, (b) F_4TCNQ/N-Gr [configuration Fig. 5.12(e)], and (c) bare 2N-Gr, (d) F_4TCNQ/2N-Gr [configuration Fig. 5.15(i)]. Isovalue of 0.0007 e/Bohr^3 has been used to plot the iso-surfaces. Color code for atoms: gray – C of graphene, blue – N, yellow – C of molecule, red – F, turquoise – H. Green lobes: $n^{\uparrow}(\mathbf{r}) > n^{\downarrow}(\mathbf{r})$ and purple lobes: $n^{\uparrow}(\mathbf{r}) < n^{\downarrow}(\mathbf{r})$.

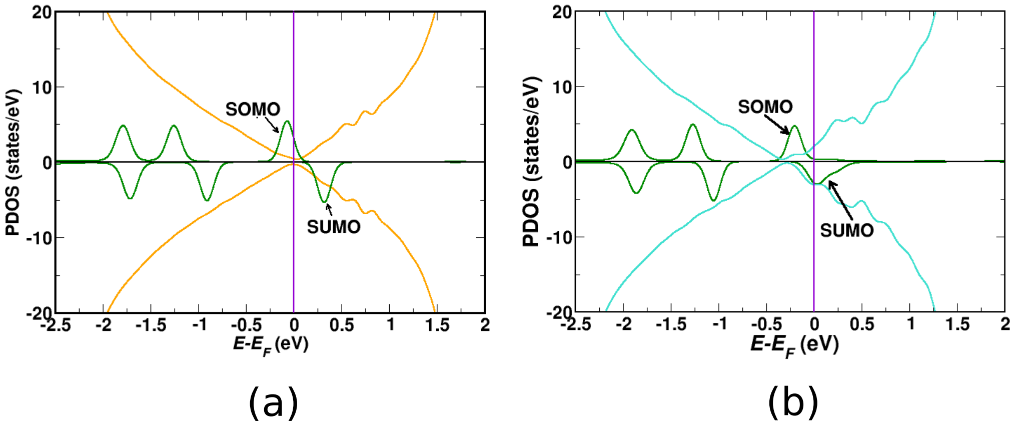

Figure 5.17: (a) Projected density of states for F_4TCNQ/N-Gr, and (b) F_4TCNQ/2N-Gr. Color code: Golden yellow (substrate N-Gr), turquoise (substrate 2N-Gr), and green (F_4TCNQ). The position of the Fermi level has been indicated using solid purple line.

ratio in the case of graphene doped with single nitrogen (N-Gr) and nitrogen pair (2N-Gr). This causes the system to have a magnetic moment.

To gain insight into the charge redistribution of F_4TCNQ on N-doped graphene, we have computed the differential charge density (DCD) for F_4TCNQ on N-Gr and 2N-Gr and compared with the corresponding results for pristine Gr. The DCD is defined as:

$$\Delta\rho(\mathbf{r}) = \rho_{F_4TCNQ/sub}(\mathbf{r}) - \rho_{F_4TCNQ}(\mathbf{r}) - \rho_{sub}(\mathbf{r}), \tag{5.5}$$

where $\rho_{F_4TCNQ/sub}(\mathbf{r})$, $\rho_{F_4TCNQ}(\mathbf{r})$, and $\rho_{sub}(\mathbf{r})$ are the charge densities of the combined system, the isolated F_4TCNQ molecule, and the bare substrate, respectively. We consider the *sub* to be Gr for F_4TCNQ/Gr, N-Gr for F_4TCNQ/N-Gr, and 2N-Gr for F_4TCNQ/2N-Gr. Plots of isosurfaces of the DCD for F_4TCNQ/Gr, F_4TCNQ/N-Gr, and F_4TCNQ/2N-Gr systems are shown in Fig. 5.18. This figure shows that electron accumulation (red color) takes place upon the F_4TCNQ molecule at the interfaces, although the amount of electron accumulation is not the same for all the systems. One can see that the charge transfer is considerably more significant for N-doped graphene upon comparing F_4TCNQ/N-Gr [see Fig. 5.18(d)] and F_4TCNQ/2N-Gr [see Fig. 5.18(f)] with F_4TCNQ/Gr [see Fig. 5.18(b)]. The blue color in Fig. 5.18(d) and (f) show the depletion of charge density at the N-site, which further confirms that the enhanced charge transfer occurs from the N-site to the F_4TCNQ molecule. One does not see such large magenta lobes in F_4TCNQ/Gr; see Fig. 5.18(b).

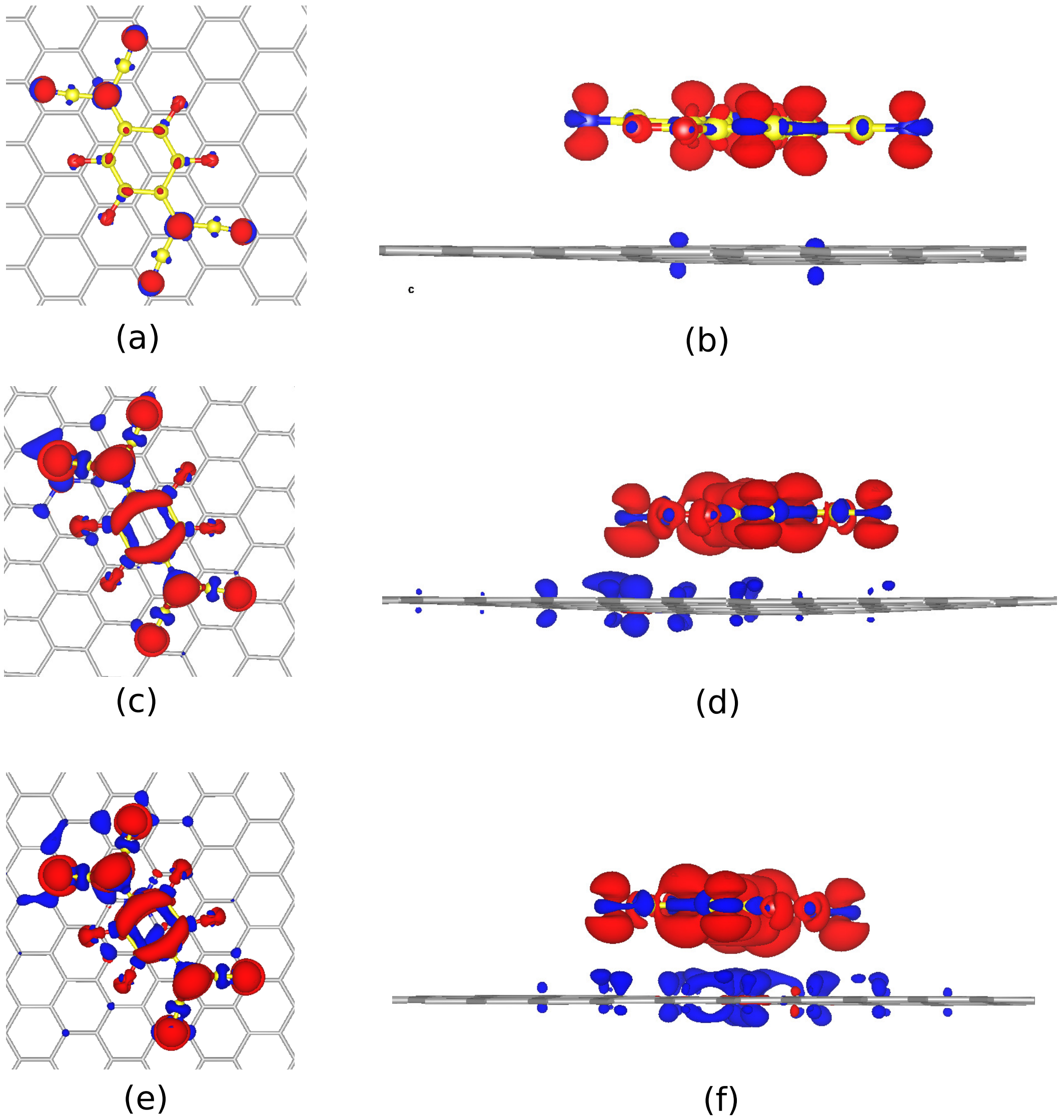

Figure 5.18: Calculated differential charge densities (DCD) for F_4TCNQ/Gr (a) top-view (b) side-view, for F_4TCNQ/N-Gr [for config. Fig. 5.12(e)] (c) top-view (d) side-view and for F_4TCNQ/2N-Gr [for config. Fig. 5.15(i)] (e) top-view (f) side-view. In all cases, the isosurface value of 0.0015 e/Bohr^3 has been plotted. Red and blue lobes indicate electron accumulation and depletion, respectively.

5.4 Results and discussion for CoPc on doped graphene

5.4.1 Experimental results

First, we discuss the low temperature (4.6 K) STM experiments performed by our experimental collaborators, Mehdi Bouatou and Dr. Jerome Lagoute in the MPQ laboratory of the University of Paris–Diderot. In the experiment, cobalt phthalocyanine (CoPc) molecules have been deposited on nitrogen-doped graphene. After deposition, it is found that a few CoPc molecules sit on single nitrogen sites, while other molecules sit on nitrogen pairs of the N-doped graphene. We show experimental STM images of the molecules adsorbed on nitrogen-doped graphene. CoPc$^-$ [i.e., the molecule on the nitrogen pair; we discuss its charge state further below] has been encircled using the red line in Fig. 5.19(a). Note that two dark blue dots represent the position of the nitrogen pair in the substrate. In Fig. 5.19(a), the CoPc molecule on a single nitrogen of the doped graphene has been encircled using green line. The position of the single nitrogen below the CoPc molecule has been shown using a dark blue dot.

From scanning tunneling spectroscopy (STS), they have found that only for those molecules that sit on nitrogen pairs in the doped graphene, there is a complete transfer of one full electron (1 e) from the nitrogen pair to the molecule's LUMO. This is a signature of the redox reaction because the oxidation state of the Co centre in the molecule goes from 0 to -1 after receiving one electron from the N-pair. Experimental $\mathrm{d}I/\mathrm{d}V$ spectra for the molecules on single nitrogen and on the nitrogen pair of the doped graphene have been shown in Figs. 5.19(b) and 5.19(c), respectively. Note that the LUMO of CoPc lies above the Fermi energy in case of CoPc on single nitrogen, whereas the LUMO lies below the Fermi energy for the molecule on nitrogen pair of the doped graphene. The shift of LUMO to below the Fermi level a indicates the high charge transfer (which is 1 e from the experiment)

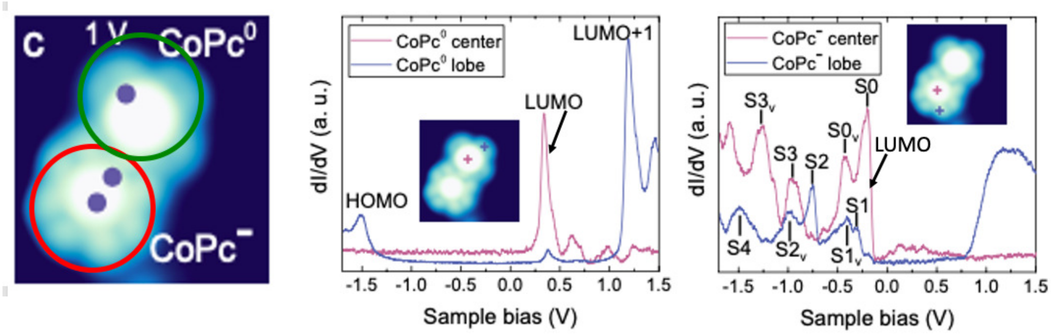

(a) (b) (c)

Figure 5.19: (a) STM image of CoPc molecule adsorbed on single nitrogen (encircled with green circle) and on the nitrogen pair (encircled with red circle) of the N-doped graphene. Dark blue dots represents the position of the nitrogen below the CoPc molecule. The images have been recorded at I = 50 pA and V = 1.0 V. (b) dI/dV spectra of CoPc molecule on single nitrogen of the doped graphene. (c) dI/dV spectra of CoPc molecule on the nitrogen pair of the doped graphene. The figures are reprinted with permission from Ref. 35.

from the N-pair to the molecule. In contrast, they found that the molecules on single nitrogen atoms are in the 0 oxidation state, i.e., there is no reduction of the CoPc molecules that sit on the doped graphene's single nitrogen dopants. Such a reduction (change in the oxidation state) of CoPc is important because it is expercted to enhance the catalytic activity of CoPc towards CO_2 reduction reaction.[32]

5.4.2 Adsorption geometry of CoPc on doped Gr

To investigate the adsorption of the CoPc molecule on nitrogen-doped graphene, we have considered a CoPc molecule on graphene doped with single nitrogen (N-Gr) or on graphene doped with a nitrogen pair (2N-Gr). We have compared these results with those obtained for a CoPc molecule adsorbed on pristine graphene. Note that we have substituted one C atom of the 15×15 graphene supercell by one N atom to make the N-Gr substrate. Similarly, we have substituted two C atoms in this supercell by two N atoms to make the 2N-Gr substrate. The optimized geometries of the CoPc molecule on Gr, N-Gr, and 2N-Gr are shown in Figs.5.20(a), (b), and

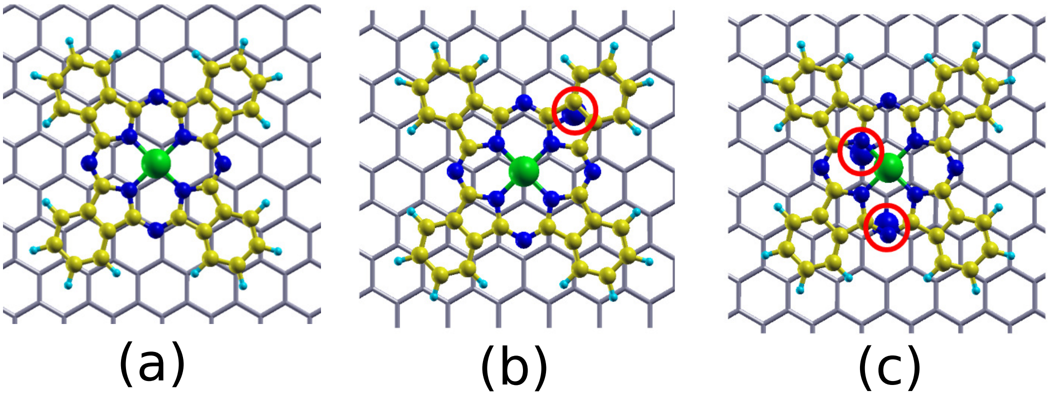

Figure 5.20: Zoomed in views of optimized geometry of CoPc on (a) Gr (b) N-Gr and (c) 2N-Gr. We have substituted one C atom of the 15×15 graphene supercell by one N atom to make N-Gr and two C atoms by two N atoms to make the 2N-Gr. The position of the dopant nitrogen has been encircled in red in (b) and (c). Color code: yellow (C), blue (N), green (Co), turquoise (H), and gray (graphene).

(c), respectively. Note that the position of the molecule with respect to the nitrogen atom/s of the doped graphene (in the cases of N-Gr and 2N-Gr) has been determined from the STM experiments, where the same area of the surface has been imaged before and after removing the molecule. We calculate the adsorption energy using the formula:

$$E^{\mathrm{ads}}_{\mathrm{CoPc/sub}} = E_{\mathrm{CoPc/sub}} - E^{\mathrm{bare}}_{\mathrm{sub}} - E^{\mathrm{iso}}_{\mathrm{CoPc}}, \tag{5.6}$$

where $E_{\mathrm{CoPc/sub}}$, $E^{\mathrm{bare}}_{\mathrm{sub}}$, and $E^{\mathrm{iso}}_{\mathrm{CoPc}}$ are the total energies of CoPc on nitrogen doped graphene substrates, bare substrates [sub is 2N-Gr for graphene doped with N-pair & N-Gr for graphene doped with single nitrogen], and the isolated CoPc molecule in the gas phase.

The calculated adsorption energy is −2.422 eV/molecule for the CoPc on pristine graphene, −2.609 eV/molecule for the CoPc on N-Gr, and −2.761 eV/molecule for the CoPc on 2N-Gr, i.e., the magnitude of the adsorption energy increases as we go from Gr to N-Gr to 2N-Gr.

We also found that the distance between the Co atom (of CoPc) and the substrate decreases on going from Gr to N-Gr to 2N-Gr, due to an increase in the interaction between the CoPc with N atoms of N-doped graphene. The calculated distance is 3.33 Å for CoPc on the pristine graphene, 3.20 Å over a single N, and 3.15 Å over a nitrogen pair in N-doped graphene. However, CoPc lies flat on the substrate in all the cases.

5.4.3 Tuning of charge upon CoPc molecule on the doped graphene

We have plotted our theoretical results for the projected density of states (PDOS) for the CoPc on pristine graphene, N-Gr, and on 2N-Gr, see Fig. 5.21. Note that the LUMO is at (or slightly the above) the Fermi energy in the case of CoPc/Gr, see Fig. 5.21(a). The same is true for CoPc/N-Gr, see Fig. 5.21(b). However, the LUMO goes below the Fermi level for CoPc/2N-Gr, see Fig. 5.21(c). Therefore, the PDOS for CoPc on the nitrogen pair agrees reasonably well with the experimental dI/dV spectra, see Fig. 5.19(c). However, one cannot always expect to see exact agreement between the PDOS (calculated from ground state theory) and dI/dV spectra obtained experimentally. For example, in our theoretical PDOS curves, we find that the molecular LUMO is present at the Fermi level in the cases of CoPc/N-Gr, and CoPc/Gr; this is in disagreement with the experimental dI/dV spectra. Note, however, that trends as a function of N-doping are reproduced correctly.

To confirm the origin of the shift of the molecular LUMO below the Fermi energy for CoPc/2N-Gr, we have computed the charge transfer from substrate to the molecule using the Bader method.[46] The charge transfer (ΔQ) is 0.20 for CoPc/Gr, 0.43 e f CoPc/N-Gr, and 0.61 e for 0 CoPc/2N-Gr. While these charge transfers differ from those estimated from the STS experiments (we do not find that a full electron is transferred on 2N-Gr), we note that we correctly predict that the charge transfer increases as one goes from Gr to N-Gr to 2N-Gr. Absolute values of charge

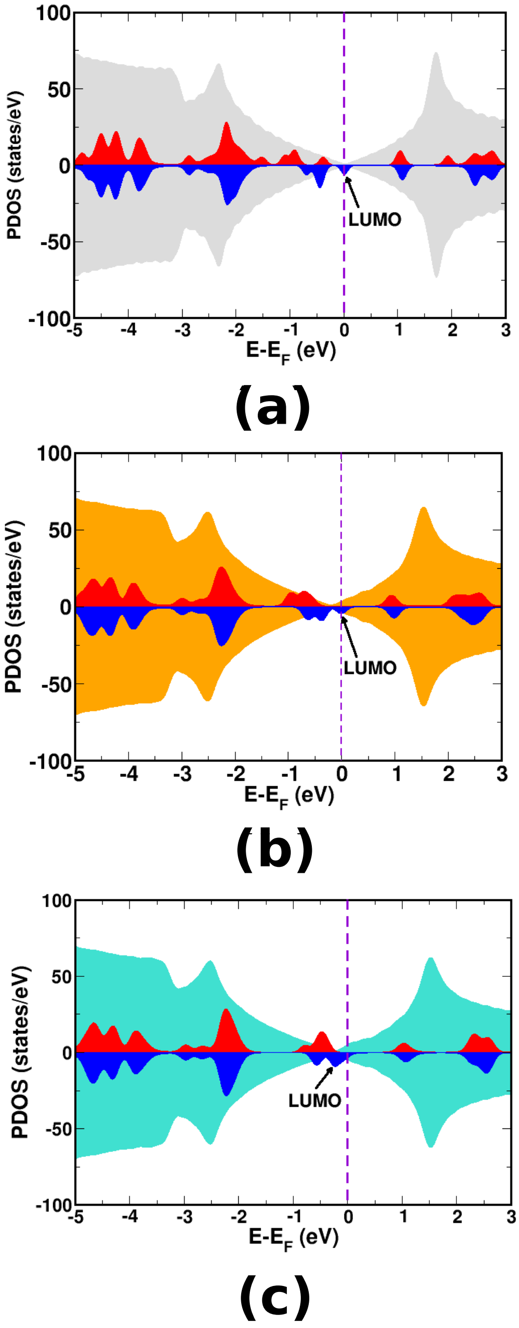

Figure 5.21: Projected density of states (PDOS) for isolated CoPc on (a) Gr, (b) N-Gr, and (c) 2N-Gr. Color code: red (up spin of the CoPc), blue (down spin of the CoPc, gray (PDOS of the Gr), orange (PDOS of the N-Gr), and turquoise (PDOS of the 2N-Gr). The Fermi level is shown using a purple dotted line. The figures are reprinted with permission from Ref. 35.

transfer evaluated from DFT are well-known to be unreliable, in part due to ambiguities inherent in charge-partitioning schemes. The high charge transfer from the N-pair to the LUMO of the CoPc shifts the LUMO of the molecule below the Fermi energy.

In addition, we have compared the charge redistribution that occurs when the CoPc molecule is placed over pristine graphene, N-Gr, and 2N-Gr. In Figs. 5.22(a),(b), and (c) the red and blue lobes show electron gain and electron loss, respectively. Notice that the electron depletion occurs markedly from the location of the nitrogen atoms. The difference between the N-Gr and 2N-Gr is more evident in Figs. 5.22(e) and (f); in these figures, for greater visual clarity, only the blue lobes corresponding to electron depletion from the substrate are shown (i.e., the red lobes are not shown, nor is the CoPc molecule). The positions of the N dopant atoms in the graphene substrate are shown using red circles. It is clear that there is less electron depletion in Fig. 5.22(e), which corresponds to adsorption over an single N dopant, than in Fig. 5.22(f), which corresponds to adsorption over a N pair. Also, in the case of the single N dopant, we see that the electron depletion occurs mostly in the vicinity of the N dopant atom (i.e., below one quadrant of the molecule only), whereas in Fig. 5.22(f), the electron depletion occurs below all four quadrants of the molecule.

Fig. 5.23 shows an inverse relationship between the charge transferred from the substrate to the molecule and the Co-substrate distance (the values of the distances and the trends in these values as a function of N-doping were discussed in the previous section).

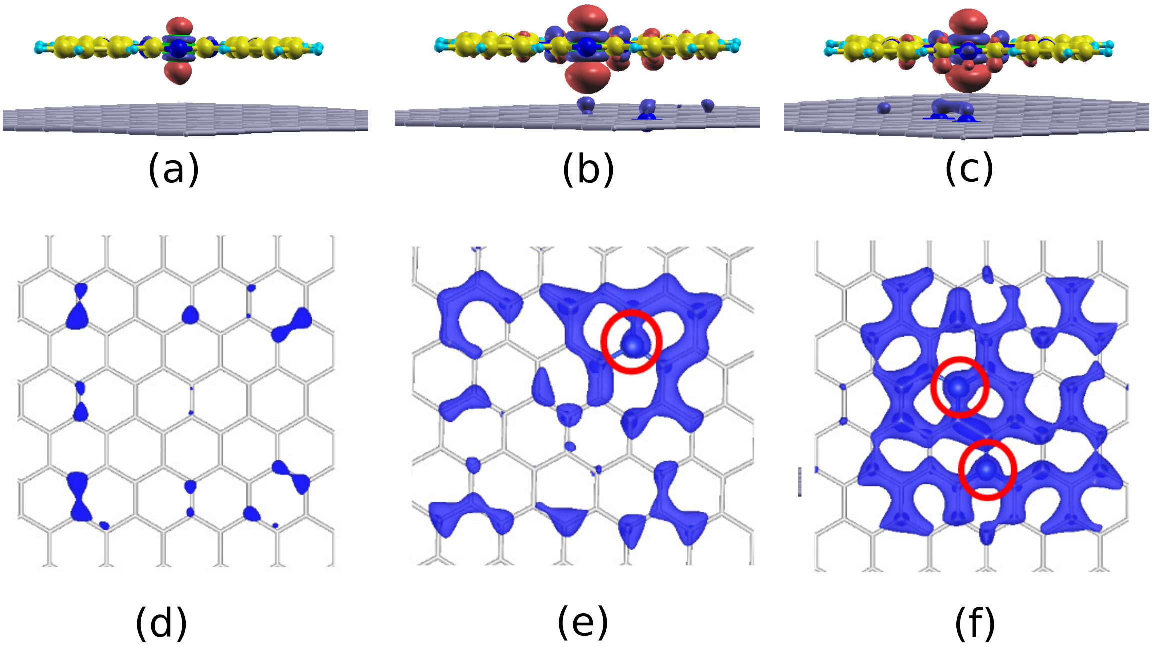

Figure 5.22: Charge redistribution that occurs on placing a CoPc molecule on (a),(d) pristine graphene, (b),(e) N-Gr, and (c),(f) 2N-Gr. Red and blue lobes represent electron gain and loss, respectively. The isosurfaces shown correspond to (a),(b)(c) 0.0015 e/Bohr^3 and (d),(e),(f) 0.00055 e/Bohr^3. Color code: C (yellow), blue (N), purple (Co), light blue (H). The red circles indicate the positions of dopant N atoms in the graphene substrate. The gray lines indicate nearest neighbor bonds between C atoms in graphene. The figures are reprinted with permission from Ref. 35.

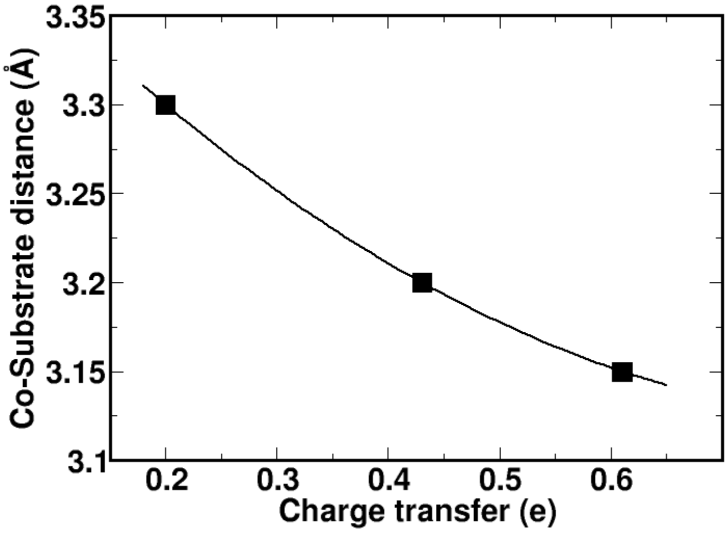

Figure 5.23: Distance between the Co atom (of CoPc) and the substrate as a function of charge transferred from the substrate to the molecule.

5.5 Conclusions

We have used density functional theory to tune the magnetism and charge of organic molecules deposited on graphene and N-doped graphene.

In the first part of this chapter, we have shown that one can induce magnetism in the F_4TCNQ/Gr system by applying an external electric field pointing in the direction from the molecule towards the graphene (negative electric field). Such a negative electric field causes enhanced charge transfer from the graphene to the molecule, which results in a sizeable magnetic moment in the system. Such a negative electric field splits the LUMO of the F_4TCNQ molecule into a SUMO and SOMO with opposite spin polarizations, and with partial filling of the SOMO, which induces the molecular magnetism. One can also develop a sizeable magnetic moment in the system by introducing nitrogen dopants in the substrate of the F_4TCNQ/Gr system. In this case, one need not apply an external electric field to get magnetism. N-doping in graphene of F_4TCNQ/Gr system itself induces magnetism, due to the transfer of a full electron from the N-site of the N-Gr to the molecule. Again, charge transfer from the substrate (N-Gr) to the LUMO splits the LUMO into SOMO and SUMO. We believe that our findings are interesting because they can conceivably have applications in the field of spintronics.

In the second part of this chapter, we have tuned the charge on a CoPc molecule deposited on pristine and N-doped graphene. Using DFT, we have shown that high charge transfer from N-pair of doped graphene to the CoPc helps us understand why the CoPc molecule gets reduced on a nitrogen pair, as a result of which the Co center goes from a neutral to a -1 state (it is important to note that this happens *only* on a N-pair, i.e., this reduction does not occur on a single N dopant or on the pristine Gr surface). In experiments, this reduction on the N-pair was signalled by the shift of the LUMO of the molecule to below the Fermi energy, for the CoPc on nitrogen pair. We have seen that the PDOS for CoPc on the nitrogen pair of the N-doped graphene agrees reasonably well with the dI/dV spectra measured experimentally for CoPc on N-pair.

Bibliography

[1] P. Avouris, "Graphene: electronic and photonic properties and devices," *Nano Lett.*, vol. 10, p. 4285, 2010.

[2] F. Schwierz, "Graphene transistors," *Nature Nanotechnol.*, vol. 5, p. 487, 2010.

[3] K. S. Novoselov, V. Fal, L. Colombo, P. Gellert, M. Schwab, K. Kim, *et al.*, "A roadmap for graphene," *Nature*, vol. 490, p. 192, 2012.

[4] J. H. Chen, C. Jang, S. Xiao, M. Ishigami, and M. S. Fuhrer, "Intrinsic and extrinsic performance limits of graphene devices on sio 2," *Nat. Nanotechnol*, vol. 3, p. 206, 2008.

[5] V. Gusynin and S. Sharapov, "Unconventional integer quantum hall effect in graphene," *Phys. Rev. Lett.*, vol. 95, p. 146801, 2005.

[6] Y. Zhang, Y.-W. Tan, H. L. Stormer, and P. Kim, "Experimental observation of the quantum Hall effect and Berry's phase in graphene," *Nature*, vol. 438, p. 201, 2005.

[7] K. S. Novoselov, A. K. Geim, S. V. Morozov, D. Jiang, Y. Zhang, S. V. Dubonos, I. V. Grigorieva, and A. A. Firsov, "Electric field effect in atomically thin carbon films," *Science*, vol. 306, p. 666, 2004.

[8] S. Zhou, G.-H. Gweon, J. Graf, A. Fedorov, C. Spataru, R. Diehl, Y. Kopelevich, D.-H. Lee, S. G. Louie, and A. Lanzara, “First direct observation of Dirac fermions in graphite,” *Nat. Phys.*, vol. 2, p. 595, 2006.

[9] K. S. Novoselov, A. K. Geim, S. Morozov, D. Jiang, M. I. Katsnelson, I. Grigorieva, S. Dubonos, and A. Firsov, “Two-dimensional gas of massless Dirac fermions in graphene,” *Nature*, vol. 438, p. 197, 2005.

[10] Y. W. Son, M. L. Cohen, and S. G. Louie, “Half-metallic graphene nanoribbons,” *Nature*, vol. 444, p. 347, 2006.

[11] Y. Zhang, T.-T. Tang, C. Girit, Z. Hao, M. C. Martin, A. Zettl, M. F. Crommie, Y. R. Shen, and F. Wang, “Direct observation of a widely tunable bandgap in bilayer graphene,” *Nature*, vol. 459, p. 820, 2009.

[12] H. Liu, Y. Liu, and D. Zhu, “Chemical doping of graphene,” *J. Mater. Chem.*, vol. 21, p. 3335, 2011.

[13] M. Garnica, D. Stradi, S. Barja, F. Calleja, C. Díaz, M. Alcamí, N. Martín, A. L. V. de Parga, F. I. Martín, and R. Miranda, “Long-range magnetic order in a purely organic 2D layer adsorbed on epitaxial graphene,” *Nat. Phys.*, vol. 9, p. 368, 2013.

[14] Q. H. Wang and M. C. Hersam, “Room-temperature molecular-resolution characterization of self-assembled organic monolayers on epitaxial graphene,” *Nat. Chem.*, vol. 1, p. 206, 2009.

[15] J. MacLeod and F. Rosei, “Molecular self-assembly on graphene,” *Small*, vol. 10, p. 1038, 2014.

[16] A. AlZahrani, “First-principles study on the structural and electronic properties of graphene upon benzene and naphthalene adsorption,” *Appl. Surf. Sci.*, vol. 257, p. 807, 2010.

[17] Y. Wang, Z. Xu, and Y. N. Moe, “On the performance of local density approximation in describing the adsorption of electron donating/accepting molecules on graphene,” *Chem. Phys.*, vol. 406, p. 78, 2012.

[18] S. M. Kozlov, F. Viñes, and A. Görling, “On the interaction of polycyclic aromatic compounds with graphene,” *Carbon*, vol. 50, p. 2482, 2012.

[19] K. Berland and P. Hyldgaard, “Analysis of van der waals density functional components: Binding and corrugation of benzene and C_{60} on boron nitride and graphene,” *Phys. Rev. B*, vol. 87, p. 205421, 2013.

[20] C. Lechner and A. F. Sax, “Adhesive forces between aromatic molecules and graphene,” *J. Phys. Chem. C*, vol. 118, p. 20970, 2014.

[21] S. Barja, M. Garnica, J. J. Hinarejos, A. L. V. de Parga, N. Martín, and R. Miranda, “Self-organization of electron acceptor molecules on graphene,” *Chem. Commun.*, vol. 46, p. 8198, 2010.

[22] D. Maccariello, M. Garnica, M. A. Nino, C. Navío, P. Perna, S. Barja, A. L. V. de Parga, and R. Miranda, “Spatially resolved, site-dependent charge transfer and induced magnetic moment in TCNQ adsorbed on graphene,” *Chem. Mater.*, vol. 26, p. 2883, 2014.

[23] I. F. Torrente, K. J. Franke, and J. I. Pascual, “Structure and electronic configuration of tetracyanoquinodimethane layers on a Au (1 1 1) surface,” *Int. J. Mass Spectrom.*, vol. 277, p. 269, 2008.

[24] M. Garnica, D. Stradi, F. Calleja, S. Barja, C. Díaz, M. Alcamí, A. Arnau, A. L. V. de Parga, F. Martín, and R. Miranda, "Probing the site-dependent Kondo response of nanostructured graphene with organic molecules.," *Nano Lett.*, vol. 14, p. 4560, 2014.

[25] V. D. Pham, S. Ghosh, F. Joucken, M. Pelaez-Fernandez, V. Repain, C. Chacon, A. Bellec, Y. Girard, R. Sporken, S. Rousset, Y. J. Dappe, *et al.*, "Selective control of molecule charge state on graphene using tip-induced electric field and nitrogen doping," *NPJ 2D Mater. Appl.*, vol. 3, no. 1, p. 1, 2019.

[26] A. Kumar, K. Banerjee, M. Dvorak, F. Schulz, A. Harju, P. Rinke, and P. Liljeroth, "Charge-transfer-driven nonplanar adsorption of F4TCNQ molecules on epitaxial graphene," *ACS Nano*, vol. 11, p. 4960, 2017.

[27] I. de Oliveira and R. Miwa, "Organic molecules deposited on graphene: A computational investigation of self-assembly and electronic structure," *J. Chem Phys.*, vol. 142, p. 044301, 2015.

[28] H. Pinto, R. Jones, J. Goss, and P. Briddon, "p-type doping of graphene with F4-TCNQ," *J. Phys: Condens. Matter*, vol. 21, p. 402001, 2009.

[29] G. F. Manbeck and E. Fujita, "A review of iron and cobalt porphyrins, phthalocyanines and related complexes for electrochemical and photochemical reduction of carbon dioxide," *J PORPHYR. PHTHALOCYA.*, vol. 19, p. 45, 2015.

[30] Z. Zhang, J. Xiao, X.-J. Chen, S. Yu, L. Yu, R. Si, Y. Wang, S. Wang, X. Meng, Y. Wang, *et al.*, "Reaction mechanisms of well-defined metal–n4 sites in electrocatalytic CO_2 reduction," *Angew. Chem. Int. Ed.*, vol. 57, p. 16339, 2018.

[31] D.-H. Nam, P. De Luna, A. Rosas-Hernández, A. Thevenon, F. Li, T. Agapie, J. C. Peters, O. Shekhah, M. Eddaoudi, and E. H. Sargent, "Molecular enhancement of heterogeneous co_2 reduction," *Nat. Mater.*, vol. 19, p. 266, 2020.

[32] M. Zhu, C. Cao, J. Chen, Y. Sun, R. Ye, J. Xu, and Y.-F. Han, "Electronic tuning of cobalt porphyrins immobilized on nitrogen-doped graphene for CO_2 reduction," *ACS Appl. Energy Mater.*, vol. 2, p. 2435, 2019.

[33] T. Atoguchi, A. Aramata, A. Kazusaka, and M. Enyo, "Electrocatalytic activity of coii tpp-pyridine complex modified carbon electrode for CO_2 reduction," *J. Electroanal. Chem.*, vol. 318, p. 309, 1991.

[34] H. Tanaka and A. Aramata, "Aminopyridyl cation radical method for bridging between metal complex and glassy carbon: cobalt (ii) tetraphenylporphyrin bonded on glassy carbon for enhancement of CO_2 electroreduction," *J. Electroanal. Chem.*, vol. 437, p. 29, 1997.

[35] M. Bouatou, S. Mondal, C. Chacon, F. Joucken, Y. Girard, V. Repain, A. Bellec, S. Rousset, S. Narasimhan, R. Sporken, Y. J. Dappe, and J. Lagoute, "Direct observation of the reduction of a molecule on nitrogen pairs in doped graphene," *Nano Lett.*, vol. 20, p. 6908, 2020.

[36] P. Giannozzi, S. Baroni, N. Bonini, M. Calandra, R. Car, C. Cavazzoni, Davide Ceresoli, G. L. Chiarotti, M. Cococcioni, I. Dabo, A. D. Corso, S. d. Gironcoli, S. Fabris, G. Fratesi, R. Gebauer, U. Gerstmann, C. Gougoussis, Anton Kokalj, M. Lazzeri, L. Martin-Samos, N. Marzari, F. Mauri, R. Mazzarello, Stefano Paolini, A. Pasquarello, L. Paulatto, C. Sbraccia, S. Scandolo, G. Sclauzero, A. P. Seitsonen, A. Smogunov, P. Umari, and R. M. Wentzcovitch, "QUANTUM ESPRESSO: a modular and open-source software project for quantum simulations of materials," *J. Phys.: Condens. Matter*, vol. 21, p. 395502, 2009.

[37] P. Giannozzi, O. Andreussi, T. Brumme, O. Bunau, M. B. Nardelli, M. Calandra, R. Car, C. Cavazzoni, D. Ceresoli, M. Cococcioni, *et al.*, "Advanced

capabilities for materials modelling with quantum espresso," *J. Phys.: Condens. Matter*, vol. 29, no. 46, p. 465901, 2017.

[38] D. Vanderbilt, "Soft self-consistent pseudopotentials in a generalized eigenvalue formalism," *Phys. Rev. B*, vol. 41, p. 7892, 1990.

[39] J. P. Perdew, K. Burke, and M. Ernzerhof, "Generalized gradient approximation made simple," *Phys. Rev. Lett.*, vol. 77, p. 3865, 1996.

[40] S. Grimme, "Semiempirical GGA-type density functional constructed with a long-range dispersion correction," *J. Comput. Chem*, vol. 27, p. 1787, 2006.

[41] K. Kunc and R. Resta, "External fields in the self-consistent theory of electronic states: a new method for direct evaluation of macroscopic and microscopic dielectric response," *Phys. Rev. Lett.*, vol. 51, p. 686, 1983.

[42] B. Kozinsky and N. Marzari, "Static dielectric properties of carbon nanotubes from first principles," *Phys. Rev. Lett.*, vol. 96, p. 166801, 2006.

[43] N. Marzari, D. Vanderbilt, A. De Vita, and M. C. Payne, "Thermal contraction and disordering of the Al(110) surface," *Phys. Rev. Lett.*, vol. 82, p. 3296, 1999.

[44] H. J. Monkhorst and J. D. Pack, "Special points for Brillouin-zone integrations," *Phys. Rev. B*, vol. 13, p. 5188, 1976.

[45] J. Tersoff and D. R. Hamann, "Theory of the scanning tunneling microscope," *Phys. Rev. B*, vol. 31, p. 805, 1985.

[46] R. Bader, *Atoms in Molecules, X-Ray Analyses and the Structure of Organic Molecules.* Clarendon Press: Oxford, UK, 1990.

[47] W. Tang, E. Sanville, and G. Henkelman, "A grid-based bader analysis algorithm without lattice bias," *J. Phys. Condens. Matter*, vol. 21, no. 8, p. 084204, 2009.

[48] P. A. Denis, "Chemical reactivity of electron-doped and hole-doped graphene," *J. Phys. Chem. C*, vol. 117, p. 3895, 2013.

[49] S. Ghosh, *Density Functional Theory and Descriptor-Based Strategies for Tailoring the Properties of Nanomaterials.* Jawaharlal Nehru Centre for Advanced Scientific Research, 2018.

[50] Z. Hou, X. Wang, T. Ikeda, K. Terakura, M. Oshima, M.-a. Kakimoto, and S. Miyata, "Interplay between nitrogen dopants and native point defects in graphene," *Phys. Rev. B*, vol. 85, p. 165439, 2012.

[51] H. J. Xiang, B. Huang, Z. Y. Li, S.-H. Wei, J. L. Yang, and X. G. Gong, "Ordered semiconducting nitrogen-graphene alloys," *Phys. Rev. X*, vol. 2, p. 011003, 2012.

[52] Y. Tison, J. Lagoute, V. Repain, C. Chacon, Y. Girard, S. Rousset, F. Joucken, D. Sharma, L. Henrard, H. Amara, *et al.*, "Electronic interaction between nitrogen atoms in doped graphene," *ACS Nano*, vol. 9, p. 670, 2015.

[53] M. Telychko, P. Mutombo, M. Ondracek, P. Hapala, F. C. Bocquet, J. Kolorenc, M. Vondracek, P. Jelinek, and M. Svec, "Achieving high-quality single-atom nitrogen doping of graphene/Sic (0001) by ion implantation and subsequent thermal stabilization," *ACS Nano*, vol. 8, p. 7318, 2014.

[54] R. Harsh, *Electronic interaction of organic molecules with low dimensional materials: a scanning tunneling microscopy study on graphene and black phosphorus.* Université de Paris, 2019.

Chapter 6

F_4TCNQ Molecules on Black Phosphorene

6.1 Introduction

Black phosphorene (BP), a monolayer of black phosphorus, has drawn much attention because of its fascinating electronic properties. In particular, its high charge carrier mobility, direct band gap semiconducting characteristics, and strong anisotropies in electro-optical and thermo-mechanical properties are opening up new opportunities for its application in electronics[1] and optical devices.[2] The structure of BP is shown in Fig. 6.1, in which the x and y axes represent the armchair and zigzag directions, respectively.

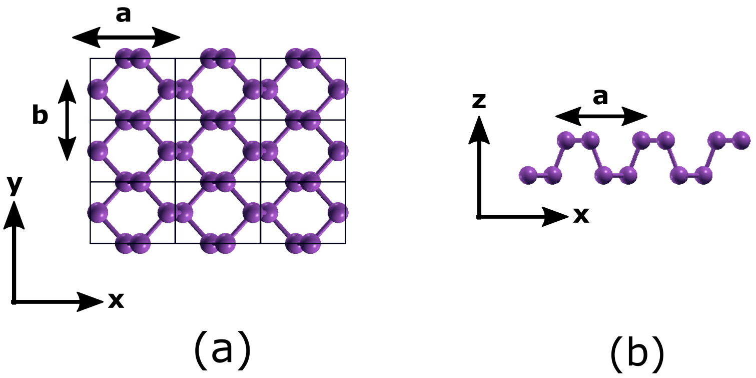

Figure 6.1: (a) and (b) are the top and side views of the black phosphorene (BP) 3x3 unit cell. **a** and **b** are the unit cell lattice parameters. The stacking along x-axis (armchair direction) is different from the y-axis (zigzag direction).

BP was first prepared by mechanical exfoliation by Lu *et al.*[3] The low structural stability of the BP and the low scalability of the exfoliation process are two shortcomings which limit experimental investigations and possible technological applications.[4;5] One solution to these problems is liquid exfoliation in organic solvents[6] or in ionic liquids.[7] Although this produces BP in high quantity, BP exfoliated using the liquid exfoliation method shows different characteristics than BP exfoliated mechanically.[8] Another answer to these problems is to increase the thickness, by increasing the number of atomic layers. Moreover, few-layer phosphorene shows unique characteristics because of its tunable band gap and charge carrier mobility with thickness. The band gap can be tuned from 0.3 eV[9] to 1.5 eV[10–12] by going down from the bulk to the monolayer. Also, one can tune the hole mobility from 640 – 700 cm^2 V^{-1} s^{-1} for monolayer (1L-BP) to 4800 – 6400 cm^2 V^{-1} s^{-1} for 5L-BP.[12]

Limitations in experimental investigations due to the chemical instability of BP encouraged people to study BP extensively using density functional theory. There are several theoretical studies which show that phosphorene is exceptional in several ways: it can exhibit a rather high band gap of 1.50 eV, and a very high hole mobility, which can reach up to 26,000 cm^2 V^{-1} s^{-1} (Ref. 12). The combination of these two properties makes BP a very promising candidate to be used in the semiconductor industry. Interestingly, the hole mobility in phosphorene shows high directional anisotropy: though the hole mobility can reach up to 26,000 cm^2 V^{-1} s^{-1} along the zigzag direction, it is only 640 – 700 cm^2 V^{-1} s^{-1} along the armchair direction.[12] One can tune the electronic properties of the BP by applying strain, creating defects, or doping with organic or gas molecules. A study by Carvalho *et al.* shows that compressive strain applied along the direction normal to the plane of the BP changes its band structure:[13] BP transforms from a direct band gap semiconductor to an indirect band gap semiconductor, semimetal, and finally metal, upon increasing compressive strain. Peng *et al.* showed that there are alternating direct to indirect band gap semiconductor transitions, as a function of uniaxial strain applied along the armchair or zigzag direction of the BP.[14] Similarly, defect engineering appears to be a promising technique to tune the electronic properties. Introducing a monovacancy can induce magnetism[15] in BP, and also make it a p-type semiconductor.[16] The divacancy reduces the carrier mobility in BP due to enhanced electron-hole recombination.[17]

The electronic properties of BP can also be tuned through chemical functionalization. We can broadly categorize such functionalization into two classes: (A) physisorption, i.e., non-covalent type of interaction between the adatom (or admolecule) with the substrate, and (B) chemisorption or covalent interaction between the adatom (or admolecule) and the substrate BP. Sometimes, chemisorption can break the host structure. For example, H, F, Cl, and the hydroxyl group (OH^-) can disintegrate BP. These chemical species act like scissors, cutting phosphorene into phosphorus chains and nanoribbons.[18;19] In contrast, physisorption of C,B,N, F, and O have been found to result in no damage to the host structure.[20] Of these species, B, N, C, and F reduce the band gap while the single O atom does not change the band gap. Li[21] and Na[22] metal adatoms cause a semiconductor to metal transition in BP. Moreover, Li ions show ultrafast diffusion along the zigzag direction on BP, which makes $Li_{0.042}P$ a promising candidate to be used in Li-ion batteries,[21] although a high concentration of Li can disintegrate BP.

Adsorption of small organic molecules or gas molecules results in a non-covalent interaction with BP, and does not damage the phosphorene's lattice structure like defect creation, strain engineering, and metal or non-metal adatoms. Often, the physisorption of organic molecules is referred to as “molecular doping” because they can change the electronic properties of BP (e.g., semiconductor to metal transition) like

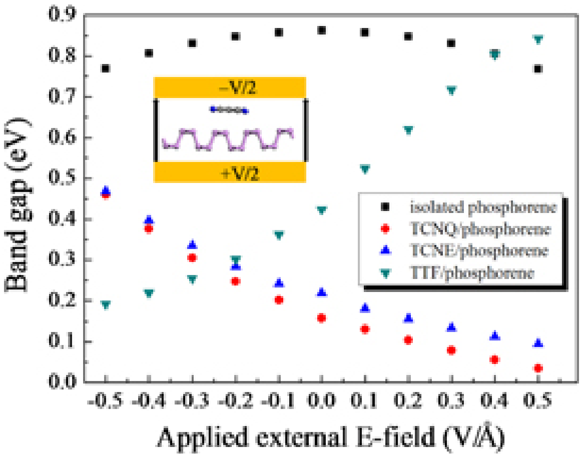

Figure 6.2: Field dependent band gaps of BP, TCNQ/BP, TCNE/BP, and TTF/BP. The direction of the applied positive E-field is labeled inside by taking TCNQ/BP as an example. Republished with permission of IOP Publishing Ltd, from 24; permission conveyed through Copyright Clearance Center, Inc.

other dopants. In this regard, a DFT study by Zhang *et al.* shows that tetracyano-p-quinodimethane (TCNQ), an electron acceptor-type molecule, causes *p*-type doping in BP, while tetrathiafulvalene (TTF), an electron donor-type molecule, introduces a deep donor state into the gap so that effective *n*-type doping cannot be realized.[23] However, one can make phosphorene into a *n*-type semiconductor by applying either in-plane strain or an external electric field. In another study, Jing *et al.* showed that the band gap of BP can be tuned by a combination of molecular doping and electric field.[24] TCNQ and tetracyanoethylene (TCNE), electron acceptor-type molecules, decrease the band gap of the combined system in a positive electric field (see Fig. 6.2), whereas TTF, an electron donor-type molecule, decreases the band gap in a negative electric field.

In this chapter, we have used density functional theory to study the change in electronic properties in BP due to molecular doping. We dope BP with an electron acceptor-type molecule, 2,3,5,6-tetrafluoro-7,7,8,8-tetracyano-quinodimethane (F_4TCNQ). Our DFT calculations show that a negative electric field can induce magnetism in the F_4TCNQ/BP system. This can be explained in terms of the splitting of the impurity band introduced by the molecule. We have also shown that the electronic and magnetic properties of this combined system will evolve in interesting ways as the temperature changes. These findings may be of interest for applications in spintronics.

Further, we show how that anisotropy in molecular diffusion barriers can be used to explain the unidirectional streaks observed in the experimental low-temperature scanning tunneling microscopy (STM) images. We discuss these experimental findings in the following section.

6.2 Experimental Background

In this section, we discuss the low temperature (4.6 K) STM experiments performed by our experimental collaborators Dr. Harsh & Dr. Lagoute in the MPQ laboratory of the University of Paris-Diderot.[25] In the experiments, they have used few-layer thick black phosphorene, rather than monolayer BP, due to the low structural stability of the latter. F_4TCNQ, at a very low concentration, has been deposited on few-layer phosphorene. This enables them to study the behaviour of single F_4TCNQ molecules on few-layer phosphorene, because the molecules are far apart from each other [see Fig. 6.3(b)] and the intermolecular interaction can therefore be neglected.

They have found that a few of the F_4TCNQ molecules are imaged as streaks during STM scanning [see Fig. 6.3(a)] and are mobile during scanning, which prevents them from taking the STS spectra. The mobility of the molecule during the process of scanning is shown in Fig. 6.3(b). The green shadow near the molecule was the initial position of the molecule before scanning; the molecule got shifted to a new position after scanning. We also note that the long axis of F_4TCNQ lies along the armchair direction with respect to the topmost layer of the few-layer phosphorene.

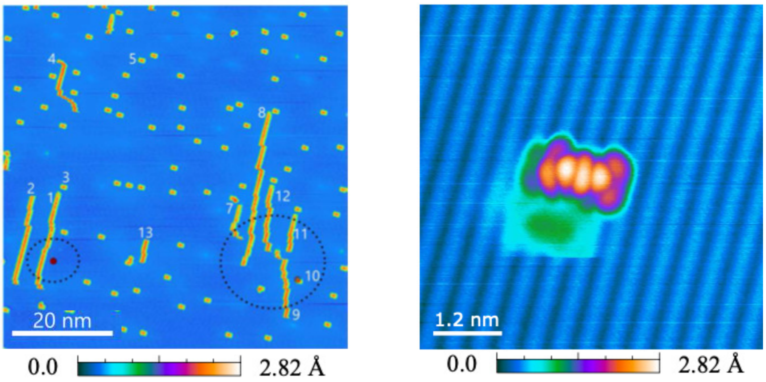

(a) (b)

Figure 6.3: (a) Experimental STM image of F_4TCNQ molecules deposited on few-layer black phosphorene at very low concentration. (b) Experimental STM image at a small length scale shows that single F_4TCNQ molecules are far apart from each other on few-layer black phosphorene. Both the STM images recorded at -2.0 V and I= 10 pA. White bars show the length scale of the STM images. The images are taken with permission from Ref 25.

Note that the "long axis" of the F_4TCNQ molecule is defined in Fig. 6.4. It shows that the long axis passes through those C atoms which are attached to the CN^- groups of the molecule.

6.3 Systems under study

In this section, we describe the systems we considered when performing our *ab initio* calculations. In this study, we considered two types of systems: (1) F_4TCNQ molecule on (monolayer) BP (also called 1L-BP), and (2) F_4TCNQ molecule on 3-layers thick phosphorene (3L-BP). Our primary focus is on the F_4TCNQ/BP system, and most of the calculations in this chapter have been performed on this system. However, in order to determine the favored adsorption geometry of the molecule on the substrate, and the adsorption geometry, we have also considered, in addition, F_4TCNQ/3L-BP.

In order to determine the adsorption geometry of a single F_4TCNQ molecule

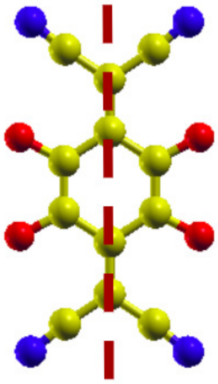

Figure 6.4: Optimized geometry of F_4TCNQ molecule in gas phase. Color code for atoms: red (F), yellow (C), and blue (N).The long axis of F_4TCNQ, which passes through C atoms attached to CN^- groups, is shown using a dark red dashed line.

on BP, we have used a $7\mathbf{a}\times 9\mathbf{b}$ supercell of BP, where **a** and **b** are the two in-plane primitive lattice vectors of the BP. Within this supercell, we adsorb a single molecule of F_4TCNQ; each molecule is then more than 22 Å apart from its neighbors in the xy plane. Guided by the STM images obtained by our collaborators, we have considered seven possible configurations for a F_4TCNQ molecule adsorbed on BP; these are shown in Figs. 6.5(a) – (g). These configurations differ from each other in terms of the position of the hexagonal ring of the F_4TCNQ molecule relative to the substrate. Note, however, that we always considered the long axis of the molecule to be oriented along the armchair direction of the BP, based on the experimental result shown in Fig. 6.3(b). We remark that an earlier DFT study by Zhang *et al.*[23] confirmed that for TCNQ (a sister molecule of F_4TCNQ) on BP too, the long axis of the molecule prefers to be oriented along the armchair direction of the substrate.

For F_4TCNQ/3L-BP, we considered seven configurations that are similar to those considered for the adsorption energy calculations on F_4TCNQ/BP, except for the fact that two extra layers of phosphorus are added at the bottom of the substrate. Only the side view of F_4TCNQ/3L-BP is shown in Fig. 6.6 for visual clarity.

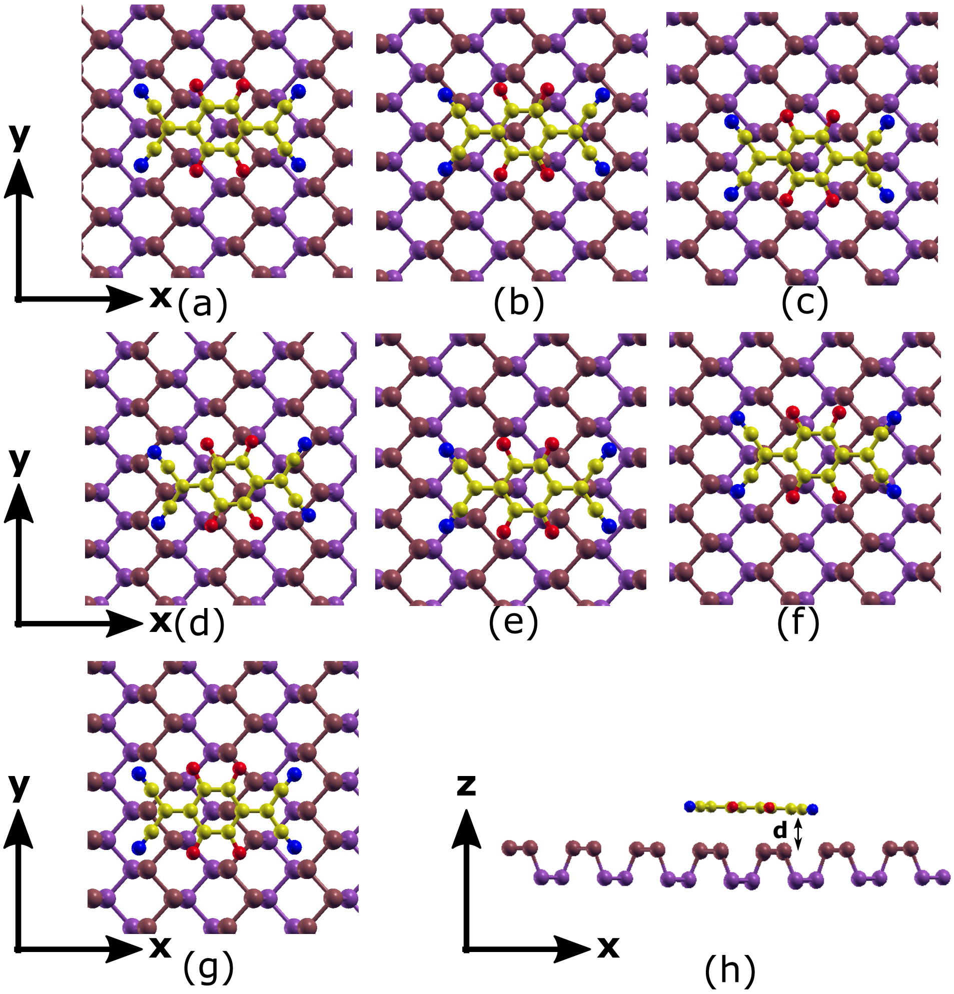

Figure 6.5: Optimized geometries of F_4TCNQ/BP systems, (a) to (g) are the top views of the seven configurations we considered. All the configurations are different from each other in terms of the position of hexagonal ring of the F_4TCNQ molecule on BP. (h) side view of F_4TCNQ/BP. Color code for atom is red (F), yellow (C), blue (N), maroon (P at the interface), purple (rest of the P).

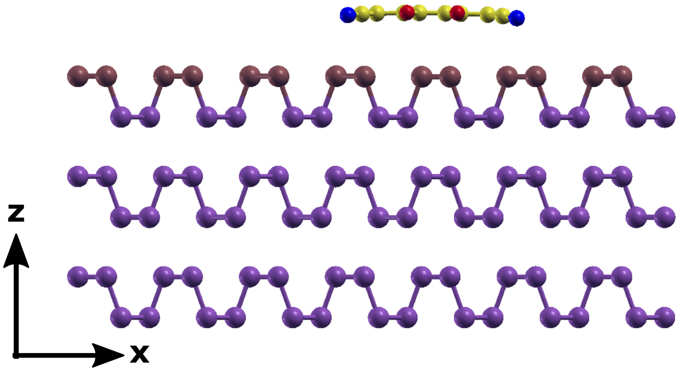

Figure 6.6: Side view of optimized geometry of F_4TCNQ/3L-BP. Two extra layers are added at the bottom of the F_4TCNQ/BP systems shown in Fig. 6.5(h). Color code for atom is red (F), yellow (C), blue (N), maroon (P at the interface), and purple (rest of the P).

6.4 Computational details

Our DFT calculations have been performed using both non-spin-polarized and spin-polarized density functional theory, as implemented in the Quantum ESPRESSO package.[26;27] The exchange-correlation potential is described using the Perdew-Burke-Ernzerhof (PBE) form of the generalized gradient approximation (GGA).[28] We have described the interactions between ion cores and valence electrons using ultrasoft pseudopotentials.[29] The Kohn-Sham equations have been expanded using a plane-wave basis set; the cutoff for the wave functions is chosen to be 35 Ry, and 350 Ry for the charge densities. We have used the semi-empirical DFT-D2 method[30] to include the long-range dispersion interactions.

We have adsorbed a single F_4TCNQ molecule within a $7\mathbf{a}\times 9\mathbf{b}$ supercell of BP or 3L-BP, when determining the lowest energy adsorption geometry. All the atomic coordinates are relaxed until the forces are less than 10^{-3} Ry/Bohr. However, during constrained optimization calculations performed to calculate the energy barrier for molecular diffusion, the four carbon atoms of the molecule that fall on the central long axis are held fixed at various positions. For calculations in the presence of an

Table 6.1: Lattice parameters for BP (1L-BP) and 3L-BP calculated using PBE+DFT-D2.

nL-BP	a (Å)		b (Å)	
	our calc.	prev calc.	our calc.	prev calc.
BP	4.56	4.56 [1b] 4.58 [1c]	3.31	3.32 [1b] 3.32 [1c]
3L-BP	4.48	4.47 [1b] 4.51 [1c]	3.32	3.32 [1b] 3.33 [1c]

[1b] Ref. 17
[1c] Ref. 12

external electric field, the electric field is applied via a sawtooth potential, which is directed perpendicular to the plane of the hybrid F_4TCNQ/BP system.[31;32]

Brillouin zone (BZ) sampling is restricted to the zone center for geometry optimization calculations. We have used Marzari-Vanderbilt[33] smearing to aid the convergence, with a width equal to 0.001 Ry. To generate the density of states (DOS), we have used a $3 \times 3 \times 1$ k-mesh to sample the BZ, using the Monkhorst-Pack scheme.[34]

The electronic charge associated with each atom is obtained by using the Bader method.[35;36]

6.5 Results and discussion

6.5.1 Benchmark calculations on monolayer and few-layer black phosphorene

We first carry out a few calculations on the black phosphorene substrates on which we will deposit the F_4TCNQ molecules.

We have computed the lattice parameters a and b of BP; we find good agreement with earlier reported values,[12;17] also computed using DFT, see Table 6.1.

We have also computed the electronic band structure and density of states (DOS)

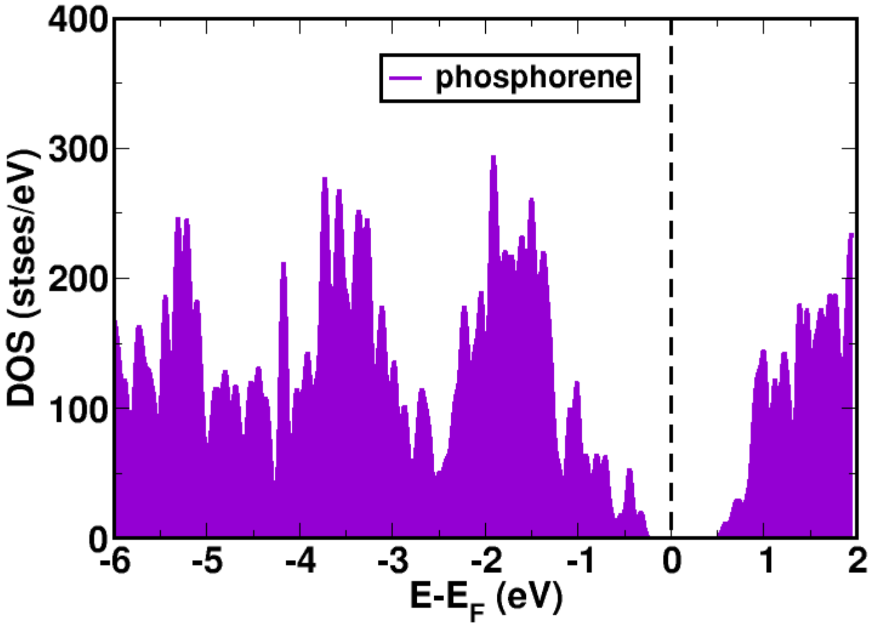

Figure 6.7: (a) Density of states (DOS) for the bare BP substrate. The black dashed line shows the position of the Fermi level.

for the bare phosphorene substrates, see Fig. 6.7. We find that the band gap for BP is 0.88 eV and that for 3L-BP is 0.20 eV. These values are in good agreement with values in the literature.[12;37]

6.5.2 Adsorption geometry and effect of thickness in determining the adsorption geometry

To determine the adsorption geometry of isolated F_4TCNQ molecules on BP and on few-layers phosphorene, we have compared the adsorption energies ($E_{\mathrm{ads}}^{\mathrm{nL\text{-}BP}}$) computed using the following formula:

$$E_{\mathrm{ads}}^{\mathrm{nL\text{-}BP}} = \left(E_{\mathrm{F4TCNQ/nL\text{-}BP}} - E_{\mathrm{nL\text{-}BP}}^{\mathrm{pris}} - E_{\mathrm{F4TCNQ}}^{\mathrm{iso}} \right). \tag{6.1}$$

Table 6.2: Adsorption energies (in eV) calculated using Eq. (6.1) for all the F_4TCNQ/nL-BP configurations shown in Fig. 6.5, for both monolayer and 3L phosphorene substrates. The boxed values correspond to the lowest energy configurations on the two substrates.

Configuration	$E_{\text{ads}}^{\text{BP}}$(eV)	$E_{\text{ads}}^{\text{3L-BP}}$ (eV)
Fig. 6.5(a)	-1.217	-1.508
Fig. 6.5(b)	-1.238	$\boxed{-1.534}$
Fig. 6.5(c)	-1.209	-1.499
Fig. 6.5(d)	$\boxed{-1.243}$	-1.509
Fig. 6.5(e)	-1.206	-1.523
Fig. 6.5(f)	-1.180	-1.299
Fig. 6.5(g)	-1.166	-1.309

Here n = 1 for BP and n = 3 for 3L-BP. $E_{\text{F4TCNQ}}^{\text{iso}}$, $E_{\text{nL-BP}}^{\text{pris}}$, and $E_{\text{F4TCNQ/nL-BP}}$ are the total energies of the isolated molecule in the gas phase, pristine substrate (nL-BP) and the combined system, respectively. In the case of BP, we use the notation $E_{\text{ads}}^{\text{BP}}$ throughout this chapter instead of $E_{\text{ads}}^{\text{1L-BP}}$, for notational simplicity. The second column of Table 6.2 lists our computed values for the adsorption energy of the F_4TCNQ/BP system, and the third column lists the values we obtain for the adsorption energy for F_4TCNQ/3L-BP. From this table, we see that the configuration Fig. 6.5(d) is the lowest energy configuration on BP. However, we note that this is almost degenerate with Fig. 6.5(b), we therefore believe that both these configurations may be found in low- temperature STM experiments. For F_4TCNQ/3L-BP, we see that Fig. 6.5(b) is the lowest-energy configuration, however Fig. 6.5(e), Fig. 6.5(d) and Fig. 6.5(a) all lie fairly close in energy. It is interesting to note that the lowest-energy configuration is different when the phosphorene is monolayer or three layers, though the energy differences between the various configurations are small.

We have found that the average distance between the molecule and BP changes from 3.15 Å for BP (1L-BP) to 3.34 Å in 3L-BP.

Based upon their STM images, which were performed on few-layer phosphorene, our collaborators deduced that they observe configurations corresponding to Fig. 6.5(b) as well as configurations corresponding to Fig. 6.5(d) in their experiments, with the former being more predominant. (However, we note that it is difficult to determine the position of the molecule precisely from STM images). We can, however, conclude that in general, there is good agreement between experiment and theory, though we note that the small energy differences between different adsorption configurations appear to be sensitive to the number of layers of phosphorene present. These small energy differences may also be sensitive to the precise treatment of dispersion interactions.

6.5.3 Charge transfer in F_4TCNQ/BP systems

We continue our study on F_4TCNQ/BP to see the effect of molecular doping on electronic properties. F_4TCNQ is expected to be an electron acceptor-type molecule that accumulates electron density from BP towards itself near the F_4TCNQ/BP interface. To get a better insight into the interfacial charge transfer in the combined F_4TCNQ/BP system, we compute the differential charge density, which is defined as:

$$\Delta\rho(\mathbf{r}) = \rho_{F4TCNQ/BP}(\mathbf{r}) - \rho_{F4TCNQ}(\mathbf{r}) - \rho_{BP}(\mathbf{r}), \tag{6.2}$$

where $\rho_{F4TCNQ/BP}(\mathbf{r})$, $\rho_{F4TCNQ}(\mathbf{r})$, and $\rho_{BP}(\mathbf{r})$ are the charge densities of the combined F_4TCNQ/BP system, isolated F_4TCNQ molecule, and bare BP, respectively. Note that the latter two quantities are evaluated in their geometries in the combined system. The quantity $\Delta\rho(\mathbf{r})$ is shown in Figs. 6.8(a) and 6.8(b). In this figure, purple color represents the electron accumulation (we see lobes of this color near the F_4TCNQ and at the F_4TCNQ/BP interface). Similarly, electron depletion

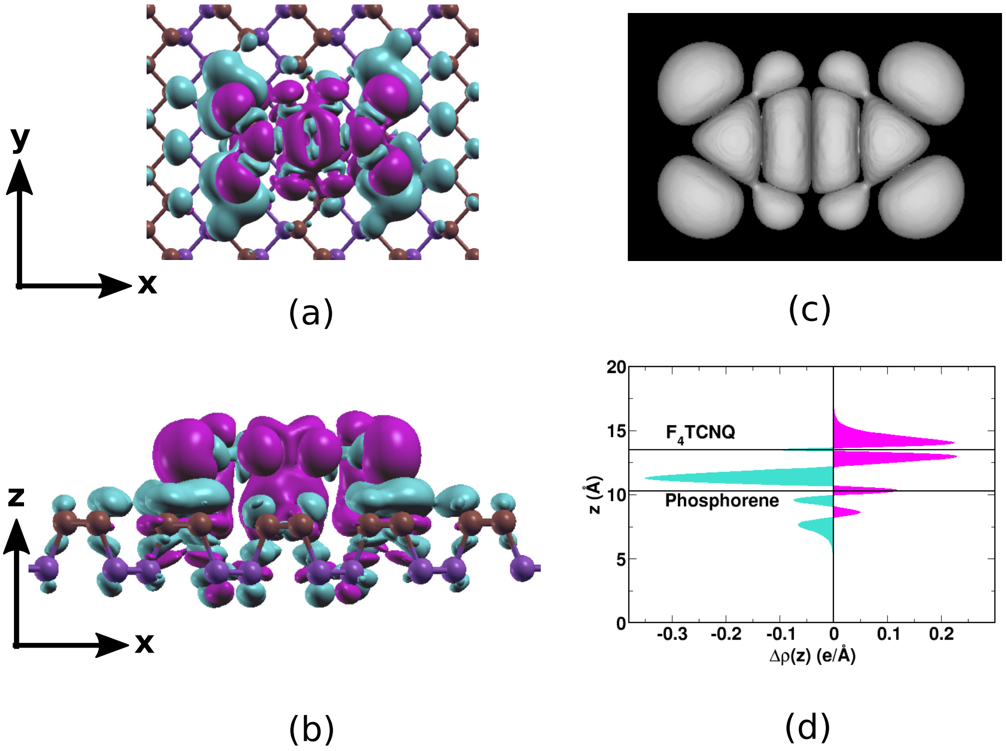
y
x
(a)
(c)
z
x
(b)
20
15
10
5
0
F4TCNQ
Phosphorene
z (Å)
-0.3
-0.2
-0.1
0
0.1
0.2
Δρ(z) (e/Å)
(d)

Figure 6.8: Calculated differential charge densities for Fig. 6.5(d) (a) top-view (b) side-view. (c) LUMO of the isolated F_4TCNQ molecule. To plot (a), (b) and (c) we have used iso-surface value of 0.00015 e-bohr^{-3}. (d) Planar averaged differential charge density, $\Delta\rho(z)$ is plotted as a function of z. Color code: purple (electron accumulation), and turquoise (electron depletion)

(turquoise color) occurs near the BP to maintain the charge neutrality. To further understand the charge redistribution, we have calculated the integral of $\Delta\rho(\mathbf{r})$ over the xy plane according to:

$$\Delta\rho(z) = \int_{xy} \Delta\rho(\mathbf{r}) dxdy; \tag{6.3}$$

here $\Delta\rho(z)$ is the planar average of the differential charge density $\Delta\rho(\mathbf{r})$. Note that the BP is normal to the z-axis. We find that $\Delta\rho(z)$ varies as a function of z, see Fig. 6.8(d). A negative value of $\Delta\rho(z)$ represents depletion of electron density, and a positive value represents the accumulation of electron density. Fig. 6.8(d) confirms the electron accumulation near the F_4TCNQ molecule and electron depletion near the BP at the F_4TCNQ/BP interface.

The transferred electrons are transferred from BP to the formerly empty lowest unoccupied molecular orbital (LUMO) of the F_4TCNQ molecule. This can be confirmed by noting the similarity in the shapes of the lobes of $\Delta\rho$ showing electron accumulation in Fig. 6.8(a) and the shape of the LUMO of the isolated molecule in the gas phase [see Fig. 6.8(c)]. To compute the total charge (electron) transfer ΔQ from BP to the molecule, we use the Bader analysis method.[35] We find that ΔQ is 0.59 e for Fig. 6.5(d).

6.5.4 Effect of electric fields: Magnetic moment at $T = 0$

Though F_4TCNQ/BP is non-magnetic in the absence of an external electric field, we have found that the application of an external electric field (ϵ) induces a non-magnetic to magnetic transition, see Fig. 6.9. The sign convention for the sign of the electric field is that it is positive ($\epsilon > 0$ V/Å) when it points along $+z$ and negative ($\epsilon < 0$ V/Å) when it points along -z. The directions of electric fields are shown pictorially in the corresponding insets of Fig. 6.9. In a positive electric field

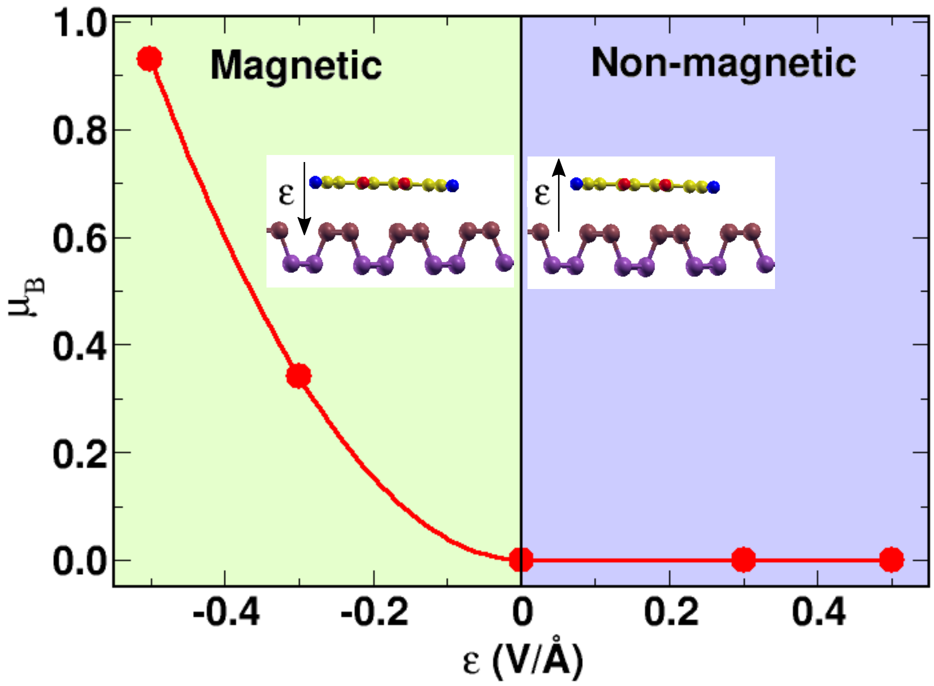

Figure 6.9: μ_B has been plotted as a function of external electric fields. Inset shows the direction of the electric field. Negative electric field pointed downwards—positive electric field pointed upwards, i.e., towards the molecule. The negative electric field ($\epsilon < 0$) gives rise to a stable magnetic phase in F_4TCNQ/BP system. Color code: pale green (magnetic phase) blue (non-magnetic phase).

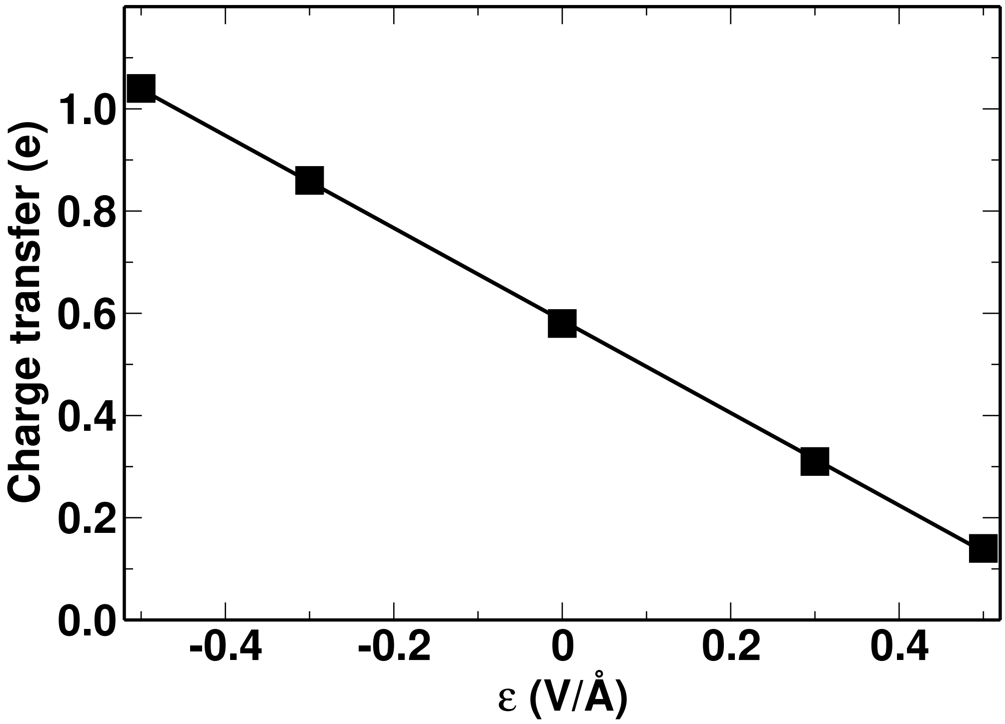

Figure 6.10: Charge transfer from BP to the molecule, as a function of the applied external electric field.

i.e., when $\epsilon > 0$ V/Å, the F_4TCNQ/BP combined system is found to be non-spin-polarized and has zero magnetic moment. However, when the polarity of the electric field is reversed ($\epsilon < 0$), the system becomes magnetic.

The electric-field-induced magnetism can be understood by looking at the charge transfer in the system. In Fig. 6.10, we have plotted the charge transferred from the BP to the molecule, as a function of the electric field. We note that we have used the Bader method[35] to partition the charge between the molecule and the BP substrate. We see that as the electric field is made more negative, this charge (electron) transfer ΔQ increases, in a linear fashion. The negative electric field pushes electrons from the BP into the molecule.

In Fig. 6.11, we have plotted μ_B (the total magnetic moment of the system) as a function of the charge (electron) transfer (ΔQ) from BP to the molecule . It is clear from Fig. 6.11 that the charge transfer induces the magnetic moment.

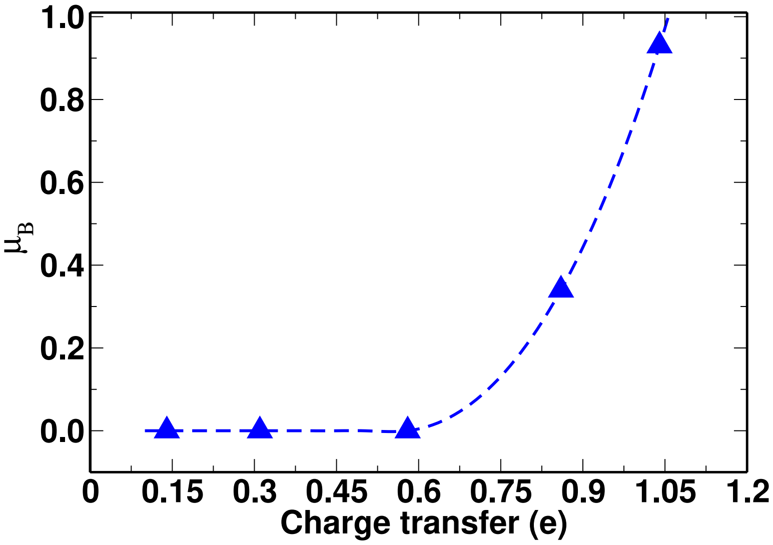

Figure 6.11: μ_B as a function of charge transfer from BP to the F_4TCNQ molecule.

In order to see how the spin polarization is distributed through the system, in Fig. 6.12 we have plotted the spin polarized charge density, i.e., the difference between the spin-up and spin-down charge densities $\left[n^{\uparrow}(\mathbf{r}) - n^{\downarrow}(\mathbf{r})\right]$ of F_4TCNQ/BP for $\epsilon = -\ 0.3$ V/Å and $\epsilon = -\ 0.5$ V/Å. We see that, at least at $T = 0$, the spin-polarization is localized primarily on the F_4TCNQ molecule.

We can also see where the magnetic moment is localized by computing the individual Bader charges q_i^{σ} on all the atoms in the system, where i indexes the atoms, and σ is a spin index. Then the net moment on the molecule or the substrate is given by $\sum_i (q_i^{\uparrow} - q_i^{\downarrow})$, where the summation runs over all the atoms in the molecule, or all the atoms in the phosphorene substrate. In this way, we find that when $\epsilon = -0.3$ V/Å, the moment on the F_4TCNQ molecule is 0.56 μ_B and that on the BP substrate is -0.21 μ_B. Similarly, when $\epsilon = -0.5$ V/Å, the moment on the F_4TCNQ molecule is 0.83 μ_B and that on the BP substrate is 0.10 μ_B. Thus, (at temperature $T = 0$) the the net spin polarization on the molecule and the substrate may be directed either oppositely or in the same direction, with the former being larger in magnitude. Note that the spin polarization in the substrate is spread out over many atoms, which is why it is not visible in Fig. 6.12.

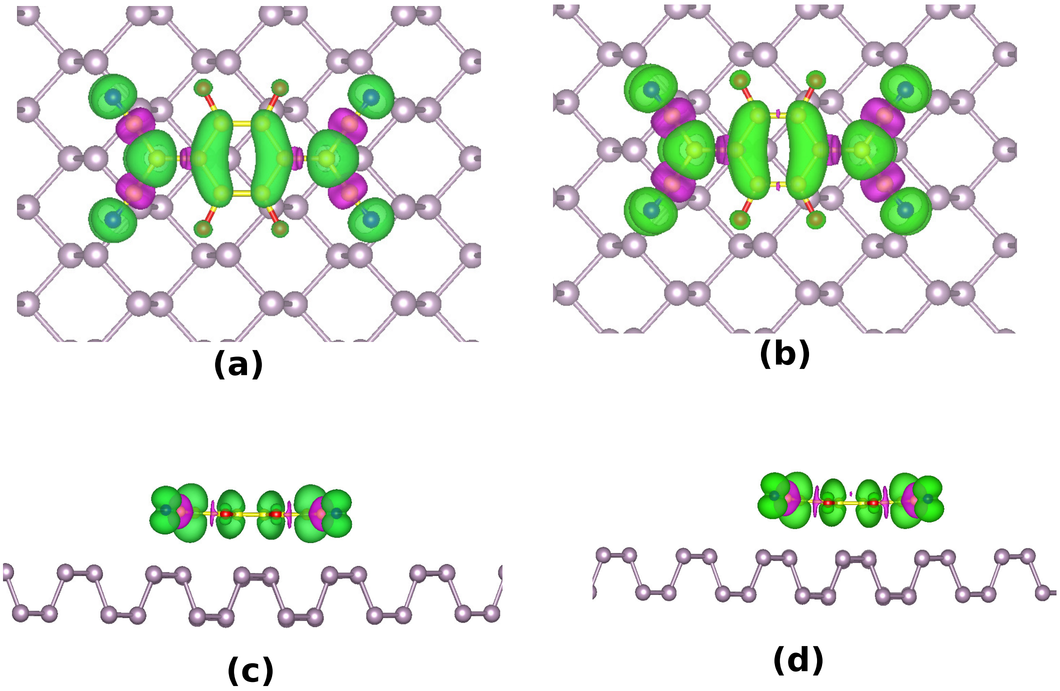

Figure 6.12: Top and side views of the F_4TCNQ/BP system, showing isosurfaces of the spin-polarized charge density $\left[n^{\uparrow}(\mathbf{r}) - n^{\downarrow}(\mathbf{r})\right]$, for (a),(c) $\epsilon = -0.3$ V/Å, and (b),(d) $\epsilon = -0.5$ V/Å. Green and purple lobes correspond to positive and negative values, respectively, i.e., green: $n^{\uparrow}(\mathbf{r}) > n^{\downarrow}(\mathbf{r})$ and purple: $n^{\uparrow}(\mathbf{r}) < n^{\downarrow}(\mathbf{r})$. Isosurface value 0.00046 e/bohr^3.

6.5.5 Effect of electric field on band structure

To gain further insight into the electric field induced magnetism in this system, we have plotted spin-polarized electronic band structures for different electric fields, see Fig. 6.13 and Fig. 6.14. One can see that the F_4TCNQ introduces a band (corresponding to the LUMO of the molecule) in the band gap of phosphorene. As the electric field is made progressively more negative, this band is pushed downward towards the valence band edge. Finally, at negative electric fields (when, in a non-spin-polarized calculation, the molecular LUMO lies very close to the valence band edge), a splitting of this band gap state occurs, into a spin-up state and a spin-down state.

By examining the electronic band structure of F_4TCNQ/BP [Fig. 6.13(c)] at $\epsilon = 0$, we find that bare BP, which shows a band gap of 0.88 eV [see Fig. 6.7], is converted into a *p*-type semiconductor after doping with F_4TCNQ. The Fig. 6.13(c) shows that F_4TCNQ introduces a state near the valence band edge of the BP and there are now impurity states 13 meV above the valence band edge. It is well-known that the introduction of an empty state near the valence band results in a *p*-type semiconductor. In this case, the energy of the LUMO of F_4TCNQ lies just above the valence band of the BP, resulting in *p*-type doping in the combined system. These results are similar to those obtained previously when TCNQ (another electron acceptor) was deposited on BP, resulting in *p*-type doping due to the molecular LUMO being position just above the valence band edge of the BP.[23] We note that the band gaps have been computed using the PBE+vdW functional; underestimation of band gaps is well-known to be a shortcoming of such ‘standard’ DFT calculations. However, we still believe that comparative changes in band gaps (as done here) can usefully be extracted using this technique.

In order to gain an understanding of how this molecular doping affects the electronic properties of the system, it is of interest to know to what extent these impurity

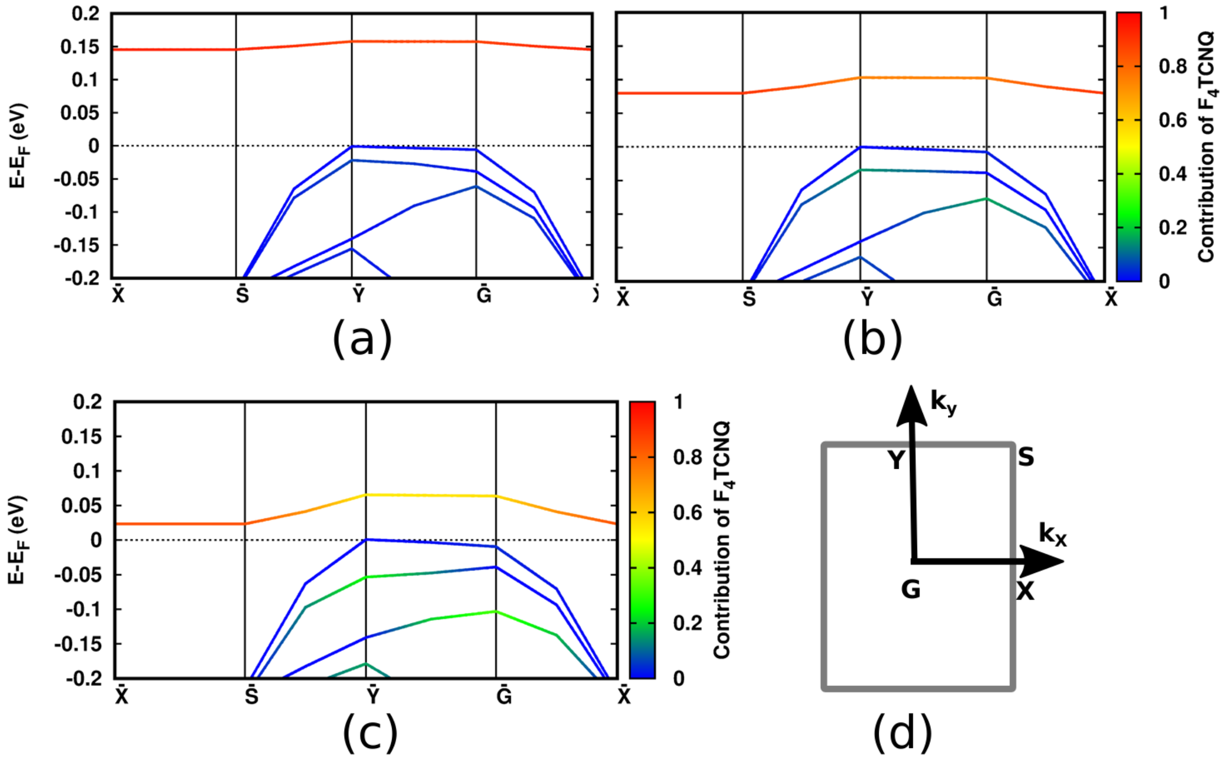

Figure 6.13: Projected band structures for F$_4$TCNQ/BP systems along the **k**-path $\overline{X}$–$\overline{S}$–$\overline{Y}$–$\overline{G}$–$\overline{X}$ at different external electric fields (a) $\epsilon= +0.5$ V/Å (b) $\epsilon= +0.3$ V/Å, (c) $\epsilon= 0.0$ V/Å. Note that we have projected the bands on the molecule. Color bar indicates the contribution from the molecule. Red color implies that full contribution of the molecule. Blue color indicates zero contribution of the molecule. Fermi energy has been drawn using black dashed line. (d) The full **k**-path inside the Brillouin zone.

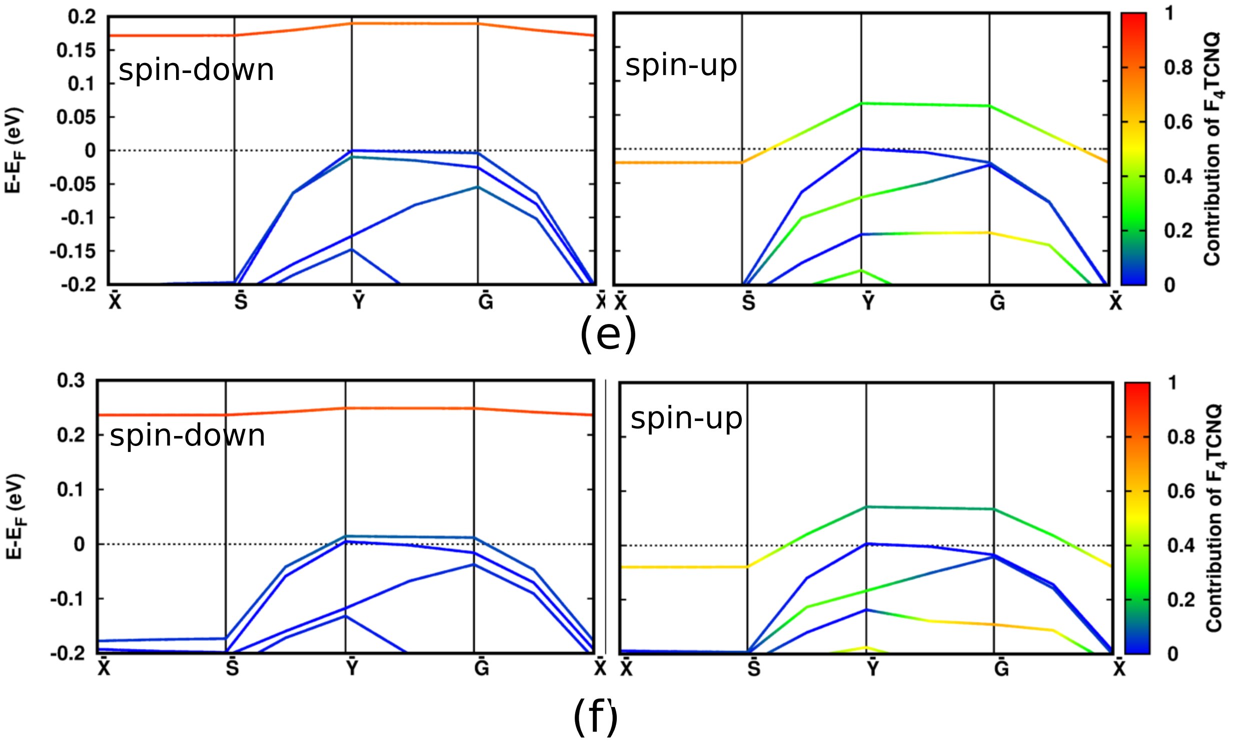

Figure 6.14: Projected spin polarized band structures for F$_4$TCNQ/BP systems along the **k**-path $\overline{X}$–$\overline{S}$–$\overline{Y}$–$\overline{G}$–$\overline{X}$ at (e) ϵ= -0.3 V/Å (f) ϵ= -0.5 V/Å. Note that we have projected the bands on the molecule. Color bar indicates the contribution from the molecule. Red color implies that full contribution of the molecule. Blue color indicates zero contribution of the molecule. Fermi energy has been drawn using black dashed line.

states are hybridized with the substrate. To see this, in Fig. 6.13 and Fig. 6.14, we have projected out the band structure so as to get the contribution from the molecule and the BP substrate, the color of the band indicates the relative contribution of the two. Red color indicates the full contribution from the molecule, whereas blue color indicates zero contribution of the molecule which means full contribution from the substrate BP. Intermediate colors indicate that the state has both molecular and BP character, due to hybridization between the two. From Fig. 6.13, we see that the impurity (molecular LUMO) state is positioned far above the valence band edge $\epsilon > 0$. At these positive electric fields, this state is seen to be fully red, i.e., it has purely molecular character. However, even at $\epsilon = 0$, we see that between $\bar{G}$ and $\bar{Y}$ (i.e., along the zigzag direction of the BP substrate), this acceptor band has partly substrate character. From Fig. 6.14, we see that at negative electric fields, this acceptor state gets split into, one unoccupied with spin down and one partially occupied one with spin up. These are the SUMO and SOMO that have been observed previously for similar systems; note however, that from the projected band structures, we see that this 'SOMO' does not have purely molecular character. With increasing electric field, it acquires increasing substrate character; again this character is most pronounced between $\bar{G}$ and $\bar{Y}$.

As a result of this band structure at negative electric fields, the electronic and magnetic properties of this system will evolve in interesting ways as the temperature is increased. Because there are two spin polarized acceptor states at two different energies, electrons from the valence band will be preferentially excited to the lower (spin-up) acceptor state. As a result, the BP will start exhibiting spin polarized conduction along the zigzag direction.

The magnetic moment of the system will first increase (as more carriers are preferentially excited to the spin-up lower acceptor band) and then start decreasing (as the higher spin-down acceptor band also starts getting occupied). The magnetic

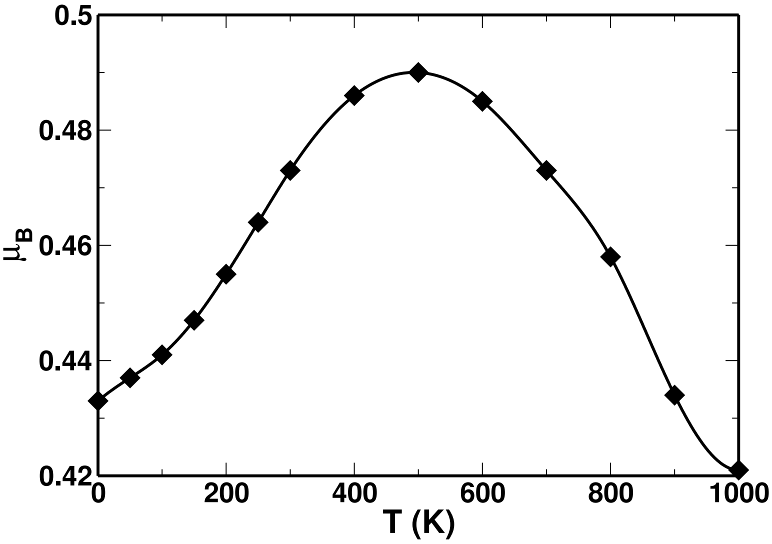

Figure 6.15: Magnetic moment of the F_4TCNQ/BP system as function of temperature T.

moment and temperature T can then be estimated using the following equation:

$$\mu_B(T) = \int_{-\infty}^{\infty} [g^{\uparrow}(E) - g^{\downarrow}(E)] f(E,T) dE \tag{6.4}$$

where $g^{\uparrow}(E)$ an $g^{\downarrow}(E)$ are the density of states corresponding to the up- and down-spin channels, respectively. $f(E,T)$ is the Fermi-Dirac distribution function, which is given by:

$$f(\epsilon) = \frac{1}{\exp(\frac{E-E_F}{k_B T}) + 1} \tag{6.5}$$

where, E_F and k_B are the Fermi energy and Boltzmann's constant, respectively.

6.5.6 Directional anisotropy in molecular diffusion

To explain the experimental observation of streaks in STM images during the course of a scan Fig. 6.16(b), we have considered the optimized geometry of Fig. 6.5(d) and calculated the diffusion barrier for the molecule along both the armchair and zigzag directions. In order to compute the diffusion barrier along the armchair direction, we have moved the molecule to its next equivalent site, indicated in Fig. 6.16(a) by the magenta arrow. The distance covered by the molecule to go to its nearest equivalent sites is 4.56 Å which is equal to the lattice parameter **a**. Twelve equidistant images are interpolated between the initial (tail of the magenta arrow) and the final (head of the magenta arrow) positions. We have calculated the total energies of the images using a constrained optimization method. Similarly, we have generated the images and computed the total energies along the zigzag direction. However, the distance molecule traveled along zigzag is different from the armchair direction. It is 3.31 Å,i.e., equal to the lattice parameter **b**.

Fig. 6.16(c) shows the variation of total energies as a function of the d_{path}, which is the lateral distance moved by the molecule on the BP surface. d_{path} is 4.56 Å and 3.31 Å for the final images along with armchair and zigzag directions, respectively. EB_1 (energy barrier for the first transition state) and EB_2 (energy barrier for the second transition state) are 0.107 eV and 0.204 eV for armchair direction and EB_1 is 0.05 eV for zigzag direction. The high diffusion barrier for armchair direction hinders the molecule to move along armchair direction. In contrast, the barrier is low for zigzag direction, and the molecule is expected to move, which is responsible for forming a streak along zigzag direction. The experimental STM image is shown in Fig. 6.16(c), which confirms the same.

6.6 Conclusions

We have shown that molecular doping is an effective way to control the electronic properties of two-dimensional materials like BP. Doping with F_4TCNQ causes high charge transfer from the substrate BP to the molecule. Charge transfer can further be tuned by applying external electric fields. We have found that a negative electric field can also induce magnetism in the F_4TCNQ/BP system. This can be explained in terms of the splitting of the impurity band introduced by the molecule. F_4TCNQ

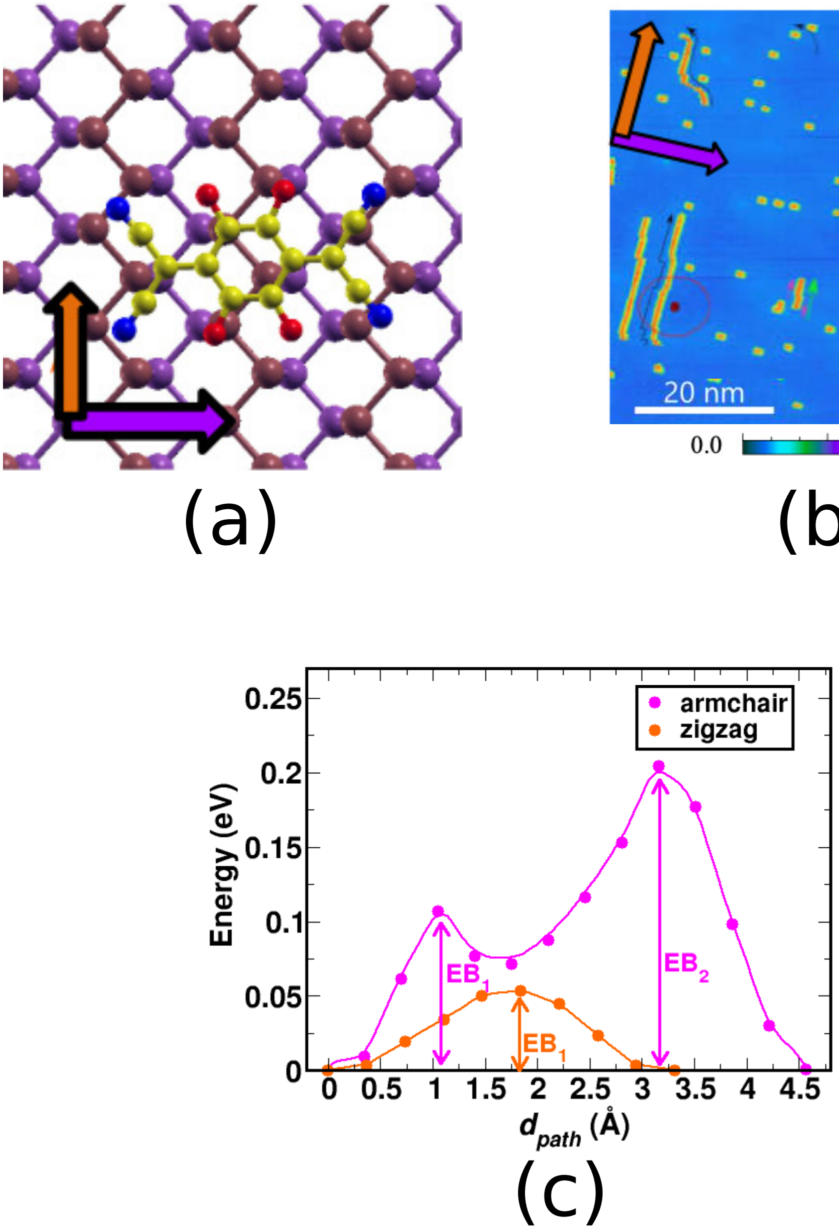

Figure 6.16: (a) Diffusion of the molecule along the armchair (magenta arrow) and along the zigzag direction (orange arrow). (b) Experimental STM image shows streaks along zigzag direction. The STM recorded at -2.0 V bias voltage and at I= 10 pA. The image is taken with permission from Ref 25. (c) Barrier heights for both the directions calculated using constrained optimization method. To calculate the diffusion barrier, we have interpolated equidistant images between two equivalent sites. Plot shows the variation of the total energy of the images as a function of d_{path}.

creates p-type doping in the BP by introducing a band (corresponding to its LUMO) in the band gap of BP which gets split into one unoccupied spin down (SUMO) band and one partially occupied spin up (SOMO) band at negative electric fields. We have also shown that the electronic and magnetic properties of this system will evolve in interesting ways as the temperature changes.

The previous results are theoretical predictions which await experimental confirmation; they are of considerable interest because of possible applications in spintronics. In addition we explained the experimental observation of streaks in STM images, as being due to anisotropic diffusion of the molecules. We find that the diffusion barrier is high for molecular motion along the armchair direction, which prevents the molecule from moving along the armchair direction. F_4TCNQ moves along the zigzag direction, because of the low energy barrier, resulting in the observation of the streaks in zigzag direction of the STM image.

Bibliography

[1] L. Li, Y. Yu, G. J. Ye, Q. Ge, X. Ou, H. Wu, D. Feng, X. H. Chen, and Y. Zhang, “Black phosphorus field-effect transistors,” *Nat. Nanotechnol*, vol. 9, p. 372, 2014.

[2] M. Buscema, D. J. Groenendijk, G. A. Steele, H. S. Van Der Zant, and A. Castellanos-Gomez, “Photovoltaic effect in few-layer black phosphorus pn junctions defined by local electrostatic gating,” *Nat. Commun.*, vol. 5, p. 4651, 2014.

[3] W. Lu, H. Nan, J. Hong, Y. Chen, C. Zhu, Z. Liang, X. Ma, Z. Ni, C. Jin, and Z. Zhang, “Plasma-assisted fabrication of monolayer phosphorene and its raman characterization,” *Nano Res.*, vol. 7, p. 853, 2014.

[4] H. Liu, A. T. Neal, Z. Zhu, Z. Luo, X. Xu, D. Tománek, and P. D. Ye, “Phosphorene: an unexplored 2d semiconductor with a high hole mobility,” *ACS Nano*, vol. 8, p. 4033, 2014.

[5] A. Castellanos-Gomez, L. Vicarelli, E. Prada, J. O. Island, K. Narasimha-Acharya, S. I. Blanter, D. J. Groenendijk, M. Buscema, G. A. Steele, J. Alvarez, *et al.*, “Isolation and characterization of few-layer black phosphorus,” *2d Mater.*, vol. 1, p. 025001, 2014.

[6] A. H. Woomer, T. W. Farnsworth, J. Hu, R. A. Wells, C. L. Donley, and S. C. Warren, "Phosphorene: synthesis, scale-up, and quantitative optical spectroscopy," *ACS Nano*, vol. 9, p. 8869, 2015.

[7] W. Zhao, Z. Xue, J. Wang, J. Jiang, X. Zhao, and T. Mu, "Large-scale, highly efficient, and green liquid-exfoliation of black phosphorus in ionic liquids," *ACS Appl. Mater. Interfaces*, vol. 7, p. 27608, 2015.

[8] F. Xu, B. Ge, J. Chen, A. Nathan, L. L. Xin, H. Ma, H. Min, C. Zhu, W. Xia, Z. Li, *et al.*, "Scalable shear-exfoliation of high-quality phosphorene nanoflakes with reliable electrochemical cycleability in nano batteries," *2d Mater.*, vol. 3, p. 025005, 2016.

[9] A. Morita, "Semiconducting black phosphorus," *Appl. Phys. A*, vol. 39, p. 227, 1986.

[10] A. N. Rudenko, S. Yuan, and M. I. Katsnelson, "Toward a realistic description of multilayer black phosphorus: From *gw* approximation to large-scale tight-binding simulations," *Phys. Rev. B*, vol. 92, p. 085419, 2015.

[11] Y. Cai, G. Zhang, and Y.-W. Zhang, "Layer-dependent band alignment and work function of few-layer phosphorene," *Sci. Rep.*, vol. 4, p. 6677, 2014.

[12] J. Qiao, X. Kong, Z.-X. Hu, F. Yang, and W. Ji, "High-mobility transport anisotropy and linear dichroism in few-layer black phosphorus," *Nat. Commun.*, vol. 5, p. 4475, 2014.

[13] A. Carvalho, A. S. Rodin, A. H. Castro Neto, and A. H. C. Neto, "Phosphorene nanoribbons cornell univ," 2014.

[14] X. Peng, Q. Wei, and A. Copple, "Strain-engineered direct-indirect band gap

transition and its mechanism in two-dimensional phosphorene," *Phys. Rev. B*, vol. 90, p. 085402, 2014.

[15] T. Hu and J. Dong, "Geometric and electronic structures of mono-and di-vacancies in phosphorene," *Nanotechnology*, vol. 26, p. 065705, 2015.

[16] Y. Guo and J. Robertson, "Vacancy and doping states in monolayer and bulk black phosphorus," *Sci. Rep.*, vol. 5, p. 14165, 2015.

[17] V. Wang, Y. Kawazoe, and W. Geng, "Native point defects in few-layer phosphorene," *Phys. Rev. B*, vol. 91, p. 045433, 2015.

[18] X. Peng and Q. Wei, "Chemical scissors cut phosphorene nanostructures," *Mater. Res. Express*, vol. 1, p. 045041, 2014.

[19] D. W. Boukhvalov, A. N. Rudenko, D. A. Prishchenko, V. G. Mazurenko, and M. I. Katsnelson, "Chemical modifications and stability of phosphorene with impurities: a first principles study," *Phys. Chem. Chem. Phys*, vol. 17, p. 15209, 2015.

[20] G. Wang, R. Pandey, and S. P. Karna, "Effects of extrinsic point defects in phosphorene: B, c, n, o, and f adatoms," *Appl. Phys. Lett.*, vol. 106, p. 173104, 2015.

[21] W. Li, Y. Yang, G. Zhang, and Y.-W. Zhang, "Ultrafast and directional diffusion of lithium in phosphorene for high-performance lithium-ion battery," *Nano Lett.*, vol. 15, no. 3, p. 1691, 2015.

[22] V. V. Kulish, O. I. Malyi, C. Persson, and P. Wu, "Phosphorene as an anode material for na-ion batteries: a first-principles study," *Phys. Chem. Chem. Phys.*, vol. 17, p. 13921, 2015.

[23] R. Zhang, B. Li, and J. Yang, "A first-principles study on electron donor and acceptor molecules adsorbed on phosphorene," *J. Phys. Chem. C*, vol. 119, p. 2871, 2015.

[24] Y. Jing, Q. Tang, P. He, Z. Zhou, and P. Shen, "Small molecules make big differences: molecular doping effects on electronic and optical properties of phosphorene," *Nanotechnology*, vol. 26, p. 095201, 2015.

[25] R. Harsh, *Electronic interaction of organic molecules with low dimensional materials: a scanning tunneling microscopy study on graphene and black phosphorus.* Université de Paris, 2019.

[26] P. Giannozzi, S. Baroni, N. Bonini, M. Calandra, R. Car, C. Cavazzoni, Davide Ceresoli, G. L. Chiarotti, M. Cococcioni, I. Dabo, A. D. Corso, S. d. Gironcoli, S. Fabris, G. Fratesi, R. Gebauer, U. Gerstmann, C. Gougoussis, Anton Kokalj, M. Lazzeri, L. Martin-Samos, N. Marzari, F. Mauri, R. Mazzarello, Stefano Paolini, A. Pasquarello, L. Paulatto, C. Sbraccia, S. Scandolo, G. Sclauzero, A. P. Seitsonen, A. Smogunov, P. Umari, and R. M. Wentzcovitch, "QUANTUM ESPRESSO: a modular and open-source software project for quantum simulations of materials," *J. Phys.: Condens. Matter*, vol. 21, p. 395502, 2009.

[27] P. Giannozzi, O. Andreussi, T. Brumme, O. Bunau, M. B. Nardelli, M. Calandra, R. Car, C. Cavazzoni, D. Ceresoli, M. Cococcioni, *et al.*, "Advanced capabilities for materials modelling with quantum espresso," *J. Phys.: Condens. Matter*, vol. 29, no. 46, p. 465901, 2017.

[28] J. P. Perdew, K. Burke, and M. Ernzerhof, "Generalized gradient approximation made simple," *Phys. Rev. Lett.*, vol. 77, p. 3865, 1996.

[29] D. Vanderbilt, "Soft self-consistent pseudopotentials in a generalized eigenvalue formalism," *Phys. Rev. B*, vol. 41, p. 7892, 1990.

[30] S. Grimme, “Semiempirical gga-type density functional constructed with a long-range dispersion correction,” *J. Comput. Chem*, vol. 27, p. 1787, 2006.

[31] K. Kunc and R. Resta, “External fields in the self-consistent theory of electronic states: a new method for direct evaluation of macroscopic and microscopic dielectric response,” *Phys. Rev. Lett.*, vol. 51, p. 686, 1983.

[32] B. Kozinsky and N. Marzari, “Static dielectric properties of carbon nanotubes from first principles,” *Phys. Rev. Lett.*, vol. 96, p. 166801, 2006.

[33] N. Marzari, D. Vanderbilt, A. De Vita, and M. C. Payne, “Thermal contraction and disordering of the al(110) surface,” *Phys. Rev. Lett.*, vol. 82, p. 3296, 1999.

[34] H. J. Monkhorst and J. D. Pack, “Special points for brillouin-zone integrations,” *Phys. Rev. B*, vol. 13, p. 5188, 1976.

[35] R. Bader, *Atoms in Molecules, X-Ray Analyses and the Structure of Organic Molecules.* Clarendon Press: Oxford, UK, 1990.

[36] W. Tang, E. Sanville, and G. Henkelman, “A grid-based bader analysis algorithm without lattice bias,” *J. Phys. Condens. Matter*, vol. 21, no. 8, p. 084204, 2009.

[37] V. Tran, R. Soklaski, Y. Liang, and L. Yang, “Layer-controlled band gap and anisotropic excitons in few-layer black phosphorus,” *Phys. Rev. B*, vol. 89, p. 235319, 2014.

Chapter 7

Defects in Few-layer Black Phosphorene

7.1 Introduction

Black phosphorus is the most stable form of elemental phosphorus. Black phosphorus can be viewed as having an orthorhombic crystal structure[1] (see Fig. 7.1) where a relatively strong van der Waals interaction stacks the layers, as in graphite. Black phosphorene (BP), a monolayer of black phosphorus, can be obtained by mechanical cleavage[2] and liquid exfoliation.[3;4] Few-layer black phosphorene has drawn enormous attention in recent years. It is appealing for its tunable bandgap, which can be varied from 0.3 eV (for bulk)[1] to 1.5 eV (for BP)[5–7] by changing the thickness (the number of layers). There is also a strong directional anisotropy in the charge carrier mobility. Hole mobility in BP can reach up to 10,000 – 26,000 cm^{2}V^{-1}s^{-1} along the zigzag direction, compared to 640 – 700 cm^{2}V^{-1}s^{-1} along the armchair direction.[6] This hole mobility can be further tuned by changing the number of layers; for example, along the armchair direction, the hole mobility varies from 640 – 700 cm^{2}V^{-1}s^{-1} for BP to 4800 – 6400 cm^{2}V^{-1}s^{-1} for five-layer black phosphorene (5L-BP).[6] The tunable band gap and charge carrier mobility make few-layer phosphorene very unique in the sense that the combination of these two properties is rarely observed. For example, graphene shows a high electrical conductivity of

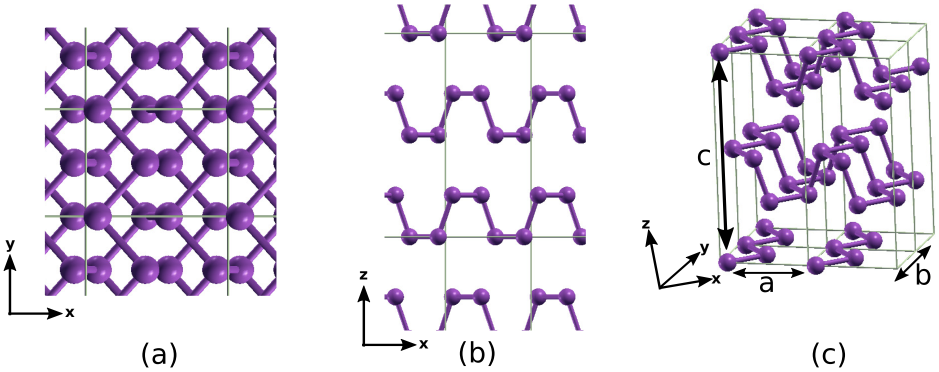

Figure 7.1: Orthorhombic crystal structure of bulk black phosphorus (a) top view of x-y plane, (b) side view of x-z plane, and (c) side view of x-z plane slightly tilted along y-direction for better visual clarity of lattice vectors **a**, **b** and **c**. It can be seen that **a** is the lattice vector along the armchair (x) direction, **b** is the lattice vector along the zigzag (y) direction , and **c** represents the lattice vector along the z direction. Phosphorus atoms are indicated by purple spheres.

$2{\times}10^5$ cm^{2}V^{-1}s^{-1},[8;9] but zero band gap, and MoS_2 shows a sizeable band gap of 1.2 – 1.8 eV[10] but a low carrier mobility of 10 – 200 cm^{2}V^{-1}s^{-1}.[11] For the above reasons, few-layer phosphorene can potentially be used in electronic and photonic devices such as field-effect-transistors,[12] photovoltaic p-n junctions[13], and thin-film solar cells.[14]

Defects are an inevitable presence in any crystalline material. These defects can be of different types and have different origins. Missing atom/atoms create so-called intrinsic defects, whereas substitution or intercalation of an atom/atoms other than that of native elements results in extrinsic defects. For example, monovacancies, divacancies, and Stone-Wales defects are some of the common intrinsic defects found in graphene and silicene.[15–20] The presence of different defects causes different changes in the properties of the materials, and hence in their possible applications. There are several examples in the materials science literature where the introduction of defects in a material leads to stark differences in its properties, such as from being an insulator to a conductor or even a superconductor, magnetic to non-magnetic, non-spin polarized to spin-polarized and so on. In the case of BP, it is known that the presence of monovacancies leads to a non-magnetic to magnetic transition,[21] and also makes it a p-type semiconductor.[22] On the other hand, divacancies in BP reduce the carrier mobility due to increased electron-hole recombination, thus impairing the performance of electronic devices making use of such defected BP.[23] Therefore, it is essencial to understand the nature and impact of different kinds of defects in a particular material.

There exist several previous DFT studies on intrinsic as well as extrinsic defects in BP.[24–26] The main kinds of intrinsic defects that have been studied earlier are monovacancy (MV), divacancy (DV), and Stone-Wales defect (SW). It has been found that among all these intrinsic defects, the DV is the most energetically favored.[24] It has also been reported that two MVs diffuse towards each other and coalesce to form a DV.[24] In addition, extrinsic defects created by substitution, addition, and intercalation between two layers by Sn, Ni, Zn, Fe, Cu, O and I atoms have also been studied.[26]

More recently, there has been an experimental scanning tunneling microscopy (STM) study of few-layer BP by Kiraly et al.[27] They have observed dumbbell-shaped features which extended over a few nm, see Figs. 7.2(a) and (b). Since the few-layer BP surface used in the experiment was cleaved in ultra-high vacuum, they ruled out the possibility of any extrinsic impurity at the surface and, therefore, associated the presence of dumbbell-like features with native defects of BP. They speculated that the monovacancy point defect might have caused this kind of shape. They used the tight binding model (TBM) to simulate charge densities for the monovacancy point defects A [see insets of the Fig. 7.2(b)]. The TBM calculations yielded highly anisotropic charge densities that looked like a dumbbell in shape [see Fig. 7.2(b)],

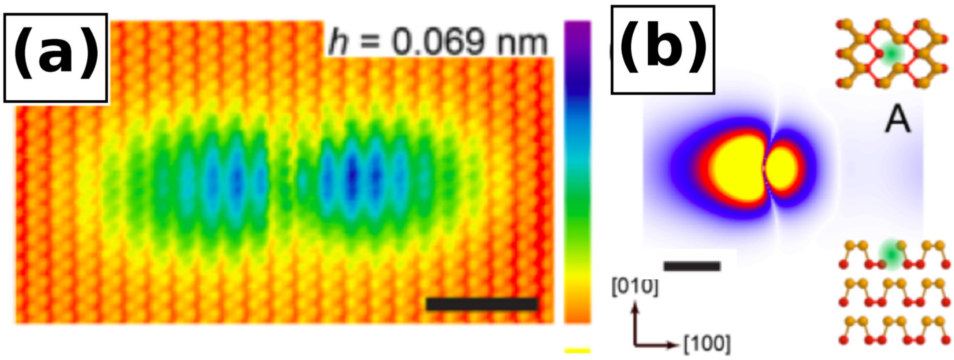

Figure 7.2: Experimental STM images of few-layer phosphorene from Kiraly et al.[27] (a) is the constant-current STM image for the monovacancy A which has been shown in the insets of the (b). The point defect A has been created by removing single P atom from the upper sublayer of the topmost layer of the three-layer black phosphorene (3L-BP). The STM image recorded at −0.1 V bias voltage. scale bar = 2 nm. (b) is charge density plots for A simulated using a tight binding model, scale bar = 1 nm. Reprinted with permission from Ref. 27©2017 American Chemical Society.

centered at the position of the monovacancy.

Qiu *et al.*[28] also found a dumbbell shaped feature in their STM topography experiment (see Fig. 7.3) on the black phosphorus surface. The STM images show an oval-shaped feature at positive bias and a dumbbell shape at negative bias. To understand the origin of this feature, they carried out elemental analysis using x-ray photoelectron spectroscopy (XPS), which showed the existence of Sn as an impurity. We note that is very common to find Sn as impurity in BP systems,[29] since Sn is often used as a catalyst during the synthesis of black phosphorous. They have speculated that either a Sn substitutional defect or a monovacancy point defect may be responsible for the dumbbell shapes.

There have also been other studies where density functional theory (DFT) has been used to obtain simulated STM images of various intrinsic and extrinsic defects in BP,[24;25] but none of them reported dumbbell-shaped features extending over a few nanometers. Although the two experiments mentioned above (Qiu *et al.*[28] and Kiraly *et al.*[27]) have shown the existence of dumbbell shaped features in the STM

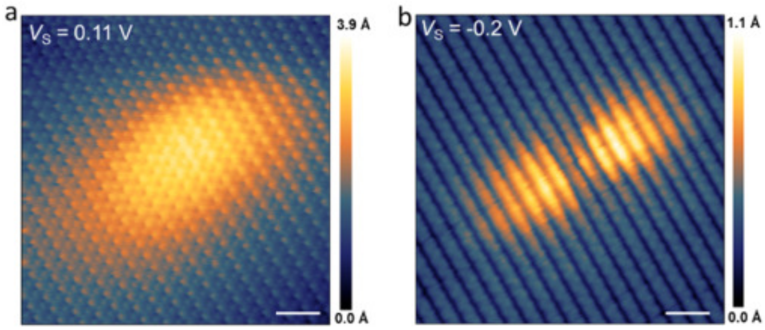

Figure 7.3: Experimental constant current STM images of black phosphorus surface recorded at (a) 0.11 V and (b) −0.2 V, scale bar = 1 nm. Reprinted with permission from Ref. 28 ©2017 American Chemical Society.

images of few-layer black phosphorene, the origin of such features is still unclear, and a satisfactory theoretical explanation is lacking. In this chapter, we investigate the origin of the dumbbell-shaped feature using *ab initio* density functional theory (DFT). We find that the presence of one particular type of extrinsic defect (Sn substitution in the lower sub-layer of the topmost layer of phosphorene) is the source of the dumbbell-shaped feature. We also explain another experimental observation: our experimental colleagues have shown that an applied electric pulse can switch a feature that is initially imaged by STM as a bright circular spot to a dumbbell-shaped feature after the application of the pulse. Our calculations show that this can be explained in terms of an initial configuration corresponding to Sn-int (Sn intercalated between top & middle layer of the 3L-BP) being converted to Sn-2 + P-adatom (Sn substituted in the lower sub-layer of the topmost layer + a P atom adsorbed on the upper sub-layer over the Sn atom)

7.2 Experimental results

Low temperature (4 K) STM experiments on few-layer thick black phosphorene were performed by our experimental collaborators in the MPQ laboratory of the University of Paris - Diderot. A bright dumbbell shape has been observed in the

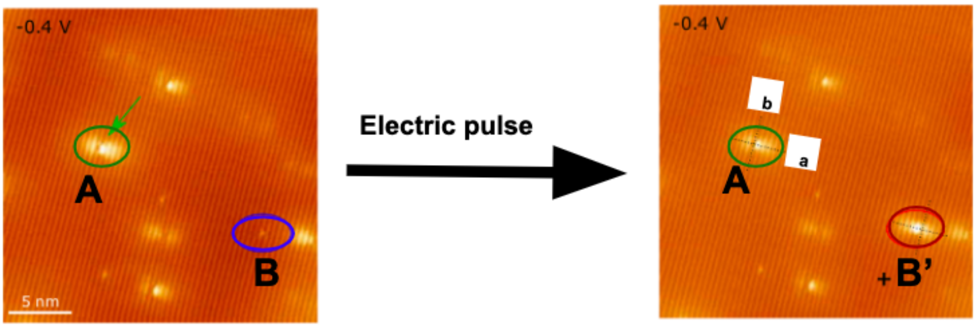

Figure 7.4: Experimental STM images recorded for the same area on the surface of few-layer black phosphorene before (left) and after (right) applying an electric pulse at bias voltage of -0.4 V and $I = 100$ pA. scale bar = 5 nm. Feature **A** remains unchanged after application of the electric pulse. However, feature **B** is transformed into **B'** after the electric pulse is applied. **a** and **b** represent the armchair and zigzag directions of the few-layer BP. The colored ellipses have been drawn to highlight the features of interest. The figures are reprinted with permission from Ref. 30.

STM topography, which we have marked as feature **A** (surrounded by a green oval) in Fig. 7.4(a). One can note that feature **A** remains the same after applying an electric pulse [see the feature surrounded by a green oval in Fig. 7.4(b)]. However, another feature **B**, which has a bright circular shape [see the feature surrounded by a blue oval in Fig. 7.4(a)], changed to feature **B'** [see the feature surrounded by a red oval in Fig. 7.4(b)] once they applied the electric pulse. Feature **B'** resembles feature **A** in some respects, i.e., both have very extended dumbbell shapes, and they have bright contrast. One can get an idea of the dimensions of the dumbbell-shaped features by looking at the scale bar shown in Fig. 7.4. The extension is roughly 3 nm, and it is along the armchair direction (the long axis of the dumbbell is oriented along the lattice vector **a** in the right-hand-side image of Fig. 7.4, where **a** represents the lattice vector of the BP lattice along the armchair direction). However, a closer examination reveals that there are also differences between the features **A** and **B'**: feature **A** has almost zero brightness at the center of the dumbbell, whereas feature **B'** has the highest brightness at the center of the dumbbell.

This difference between feature **A** and feature **B'** is also clearly apparent in

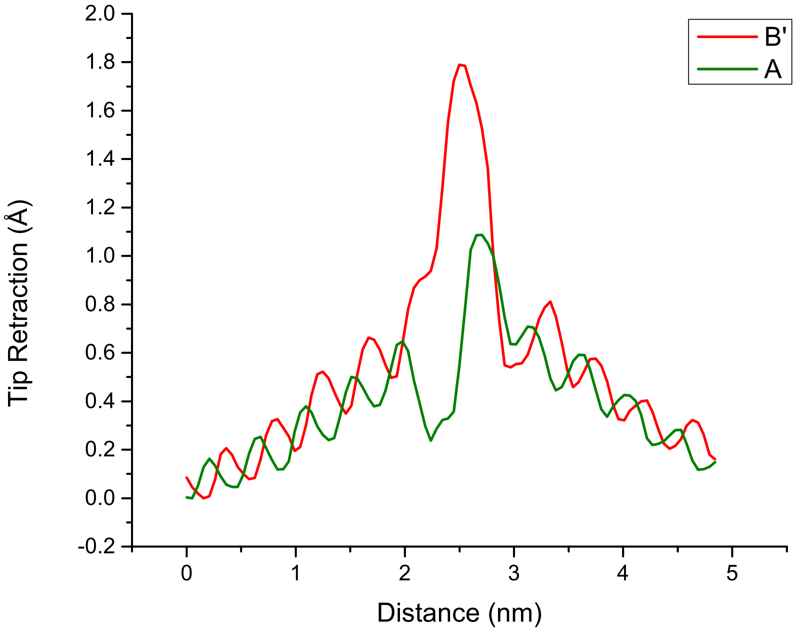

Figure 7.5: Line scan profile for the features **A** (green line) and **B'** (red line). Scanning for both the features has been performed along the axis **a** shown in the right-hand side of Fig. 7.4. This image is reused with permission from Ref. 30.

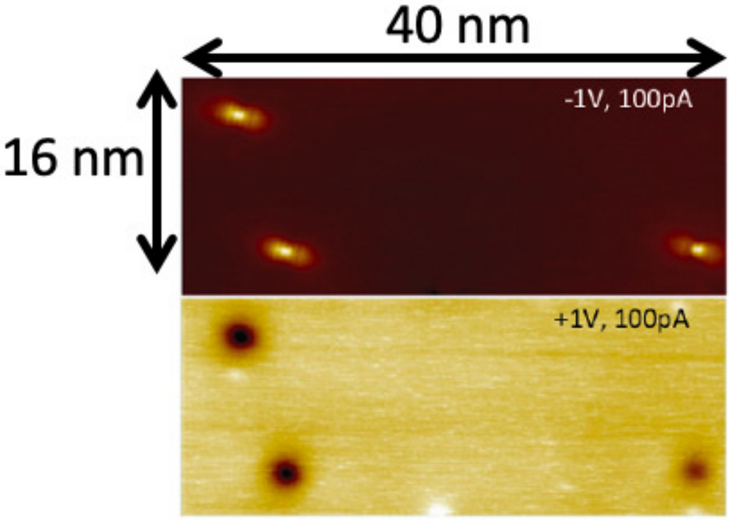

Figure 7.6: Experimental STM images for feature **A**. The top panel shows STM image recorded at -1.0 V bias voltage and I $=$ 100 pA. The bottom panel is the STM image recorded at $+1.0$ V bias voltage and I $=$ 100 pA. Dumbbell shape can be observed at negative bias (top panel), and dumbbell changes to a dark circle at positive bias (bottom panel) This figure is reprinted with permission from Ref. 30.

Fig. 7.5, where we have plotted experimentally obtained line profiles for the two features. We have used a green line for feature **A** and red line for feature **B'**, maintaining the same color convention as was used to draw the ovals surrounding the features in Fig. 7.4. Fig. 7.5 shows that the STM tip is retracted more (in order to maintain a constant current) over the center of feature **B'** than over the center of feature **A**, suggesting that either atom(s) at the center of feature **B'** are at a greater height, or the local electron density there is considerably larger. Our colleagues have also found out that the change from feature **B** to feature **B'** is irreversible, i.e., once the the electrical pulse is turned off, **B'** does not revert back to **B**.

Their experiments also showed that feature **A** changes in shape and contrast with the inversion of bias voltage. The bright dumbbell shape seen at negative bias (see top panel of Fig. 7.6), changed to a dark circular spot at positive bias voltage (see the bottom panel of Fig. 7.6). However, feature **B** remains unchanged even if they reversed the bias voltage.

7.3 Systems under study

We studied intrinsic and extrinsic defects in trilayer black phosphorene (3L-BP) because of the earlier speculations[27;28] that say defects in a few-layer black phosphorene could explain the dumbbell shape observed in the STM image. For all our calculations, we have used a (7 × 9) supercell of 3L-BP, within which we have created defects. Before going into details of the defect creation in the (7 × 9) supercell, we discuss the geometries of the (3 × 3) unit cell of the monolayer (BP), bilayer (2L-BP), and trilayer (3L-BP) of black phosphorene [see Figs. 7.7(a)-(f)], for better understanding. Figs. 7.7(a) and 7.7(d) show the top view and side view of the BP. **a** and **b** represent the lattice vectors along the armchair direction, and along the zigzag direction of the corresponding (1 × 1) unit cell, respectively. In the cases of 2L-BP and 3L-BP, layers are stacked along the **c** lattice vector, see Figs. 7.7(e) and 7.7(f). The (7 × 9) supercell of 3L-BP is generated by repeating 7 primitive unit cells along the armchair direction and 9 along the zigzag direction.

7.3.1 Intrinsic Defects

We have considered five different types of intrinsic defects: three monovacancies (MV), as well as one divacancy (DV), and one Stone-Wales defect (SW). These are the intrinsic defects (see Fig. 7.8) that are commonly observed in phosphorene and have the lowest formation energies.[24;26] One should note that we have shown only the topmost layer of the 3L-BP in the figures showing top views, in Fig. 7.8. Note also that we have used yellow color for the P atoms near the vacancy, so as to show the vacancy more clearly.

The three types of monovacancies we have studied are labeled as 59-MV, 5656-MV-1 and 5656-MV-2. The 59-MV is shown in Fig. 7.8(a). It can be created by removing one P atom from the SL-1 [upper sublayer of the topmost layer, see

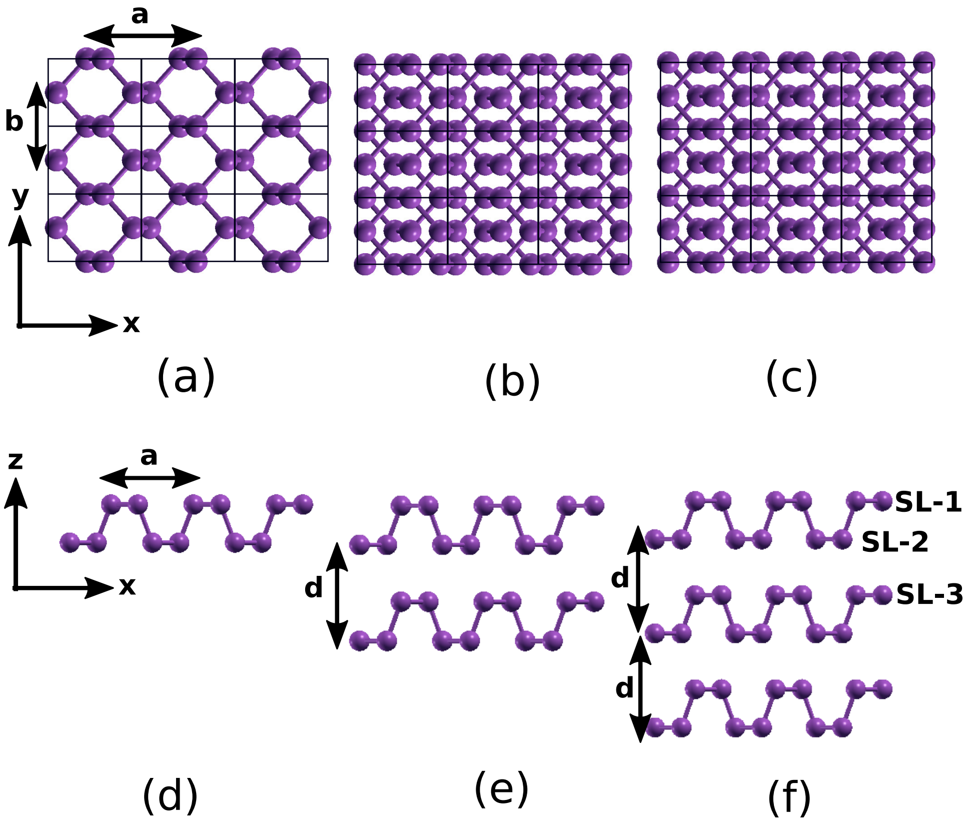

Figure 7.7: Top and side views of (3×3) unit cell of (a),(d) monolayer (BP), (b),(e) bilayer (2L-BP), and (c),(f) trilayer (3L-BP) of black phosphorene, respectively. a and b are the lattice parameters, and d is the interlayer distance between two consecutive layers. SL-1 and SL-2 are the upper and lower sublayers of the topmost BP layer. SL-3 is the upper sublayer of the second BP layer. Purple spheres indicate phosphorus atoms. The rectangles in (a), (b) and (c) indicate the boundaries of (1×1) cells.

Fig. 7.7(f)] of the 3L-BP and constructing five-member and nine-member shared rings by distorting the neighbouring atoms near the vacancy. Note that constructing the 59-MV by distorting the neighbouring atoms of the vacancy allow the atoms of the SL-2 (lower sub-layer of the topmost layer) to come and lie on the same plane as SL-1.

The 5656-MV-1 monovacancy can be created by removing a single P atom from SL-1, see Fig. 7.8(e). Similarly, we have created the 5656-MV-2 monovacancy [see Fig. 7.8(f)] by removing a single P atom from SL-2 of 3L-BP. The two sublayers SL-1 and SL-2 of the topmost phosphorene layer for the 3L-BP have been shown in Fig. 7.7(f).

The divacancy DV [see Fig. 7.8(b)], can be created by removing two atoms from the topmost phosphorene layer: one from SL-1 and another from SL-2. We have created 5757-ring in DV by joining the neighbouring atoms near the vacancy.

Fig. 7.8(c) shows the SW defect. One should note that SW is not a vacancy defect. One can form the 5757-SW defect by twisting one P-P bond through an angle of 90°.

7.3.2 Extrinsic Defects

For extrinsic defects, we have considered defects in 3L-BP due to substitution or intercalation with foreign atoms. In substitutional defects, we studied Sn and Au substitutions in different layers of 3L-BP. One should note that we have used Sn substitutional/intercalation defects because Sn is often used as a catalyst to grow the black phosphorus crystal.[28] One can therefore assume that there may be a relatively high probability of finding Sn as an impurity in the black phosphorus crystal. The same is true for Au, though the use of Au is limited because of its high cost.

Substitution of one P atom in SL-1 by one Sn atom results in the defect type that

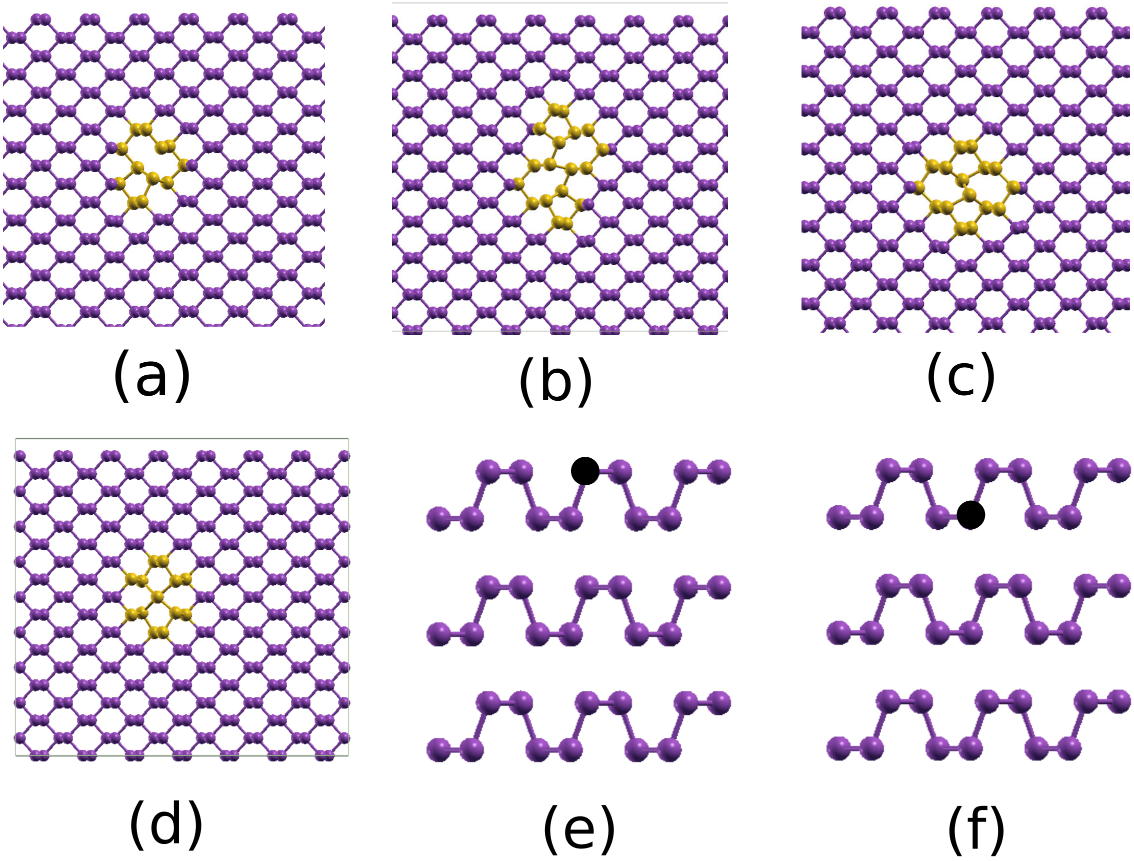

Figure 7.8: Optimized geometries of intrinsic defects in 3L-BP: Top views of (a) 59-MV, (b) 5757-DV, (c) 5757-SW, (d) 5656-MV-1/2. Note that we have shown one geometry for both the top views of 5656-MV-1 and 5656-MV-2 because they look the same. (e) and (f) are the side views of 5656-MV-1 and 5656-MV-2. Filled black circle in (e) and (f) represents the position of the single vacancy in the case of 5656-MV-1/2. Color code: purple (P), we have used yellow for the P atoms near vacancy to show the vacancy more clearly.

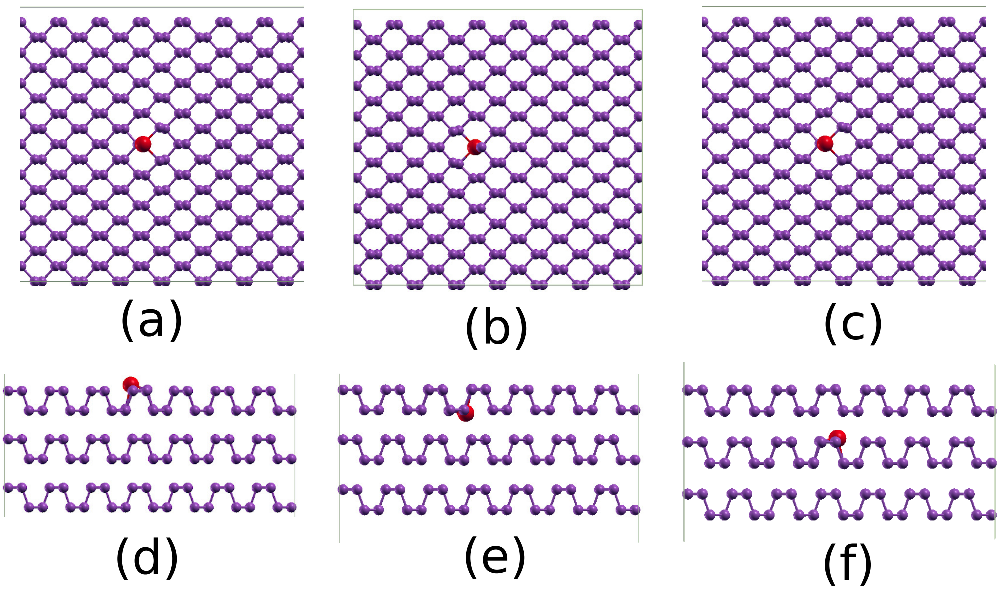

Figure 7.9: Optimized geometries of extrinsic defects in 3L-BP: (a) and (d) are the top view and side view of Sn-1, (b) and (e) are the top view and side view of Sn-2, (c) and (f) are top view and side view of Sn-3. For the top views shown in (a) and (b) we have shown only the top layer of the 3L-BP for visual clarity. Similarly, for (c) we have shown the middle layer of the 3L-BP to show the substitution in SL-3. Color code: purple (P) and red (Sn).

we label as Sn-1 [see Figs. 7.9(a) and 7.9(d)]. Similarly, to obtain the defect that we label as Sn-2, we substituted one P atom from SL-2 by one Sn [see Fig. 7.9(b) and 7.9(e)]; the substitution of one P by Sn atom in the SL-3 layer [see Figs. 7.9(c) and 7.9(f)] gives the Sn-3 defect. In the case of Au substitution, we have considered only one configuration, Au-2, where one P atom of the SL-2 layer is substituted by a Au atom [see Figs. 7.10(a), and 7.10(c)].

Finally, we added one Sn atom in between the top layer and middle layer of 3L-BP to create Sn intercalation, we label this as the Sn-int defect [see Figs. 7.10(b), and 7.10(d)].

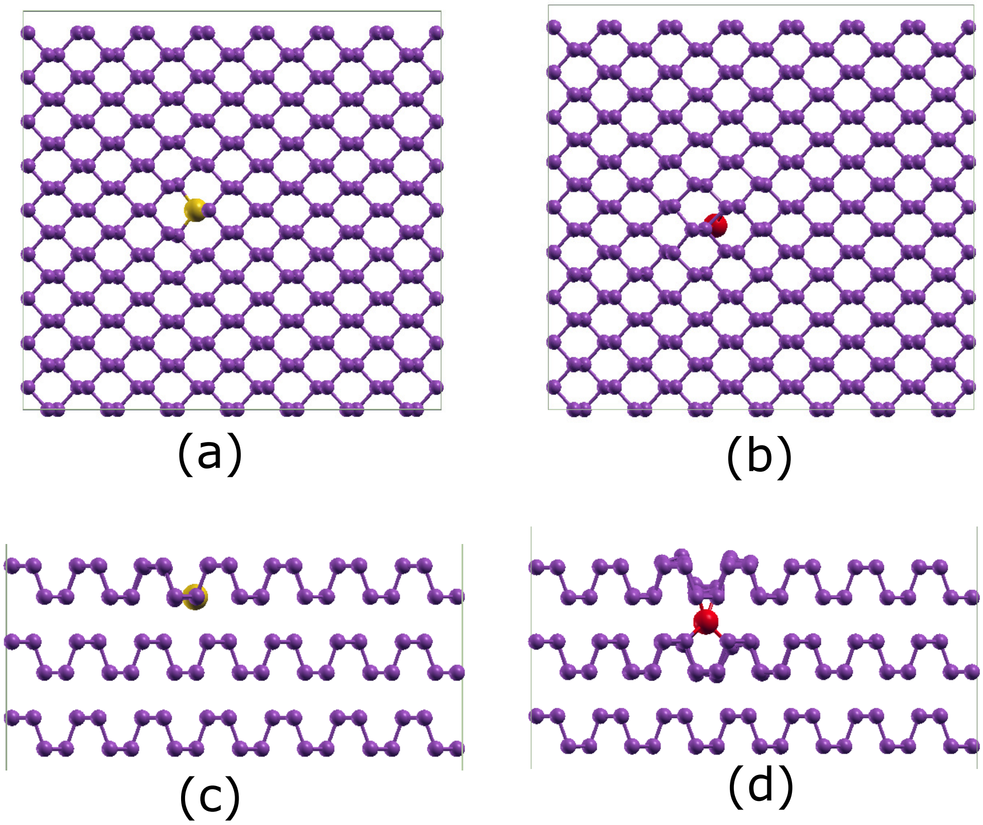

Figure 7.10: Optimized geometries of extrinsic defects in 3L-BP: (a) and (c) are top view and side view of Au-2. (b) and (d) are top view and side view of Sn-int. For the top views shown in (a) and (b), we have shown only the top layer of the 3L-BP for visual clarity. Color code: purple (P), red (Sn) and golden yellow (Au).

7.4 Computational details

Our calculations have been performed within the framework of spin polarized density functional theory, using the Quantum ESPRESSO package.[31;32] The exchange-correlation potential is treated with the Perdew-Burke-Ernzerhof (PBE) form of the generalized gradient approximation (GGA).[33] We used ultrasoft pseudopotentials to describe the interactions between the ionic cores and valence electrons.[34] The Kohn-Sham orbitals are expanded in a plane-wave basis set, using the cutoffs set to 35 Ry for wavefunctions and 350 Ry for charge densities. Long-range dispersion interactions have been incorporated using the semiemipirical DFT-D2 technique.[35]

We have used a three layer slab model with dimensions $7\mathbf{a} \times 9\mathbf{b}$, and three layers are stacked along the $\mathbf{c}$ lattice vector, of which the bottommost layer is held fixed. All other atomic coordinates are relaxed until the forces are less than 10^{-3} Ry/Bohr. Brillouin zone (BZ) sampling is restricted to the zone center for the geometry optimization calculations. To generate the density of states (DOS) plots and STM images, we have used a $3 \times 3 \times 1$ $\mathbf{k}$-mesh to sample the Brillouin zone, using the Monkhorst-Pack scheme.[36] For all the calculations, convergence is aided by using Marzari-Vanderbilt[37] smearing of width 0.001 Ry. All the constant current STM images are simulated using the Tersoff-Hamann approach.[38]

7.5 Results and Discussion

We divide this section into five parts. In the first part, we discuss the electronic structure and properties of pristine few-layer black phosphorene and then compare our results with the previous literature. In the second part, we discuss the energetics of intrinsic and extrinsic defects in 3L-BP. In the next section, we present our simulated STM images for all the kinds of defects we considered by us, and compare these with the experimentally obtained STM images of defects in few-layer

Table 7.1: Lattice parameters of bulk and few layer of black phosphorene (nL-BP, where n = 1, 2, and 3) calculated using PBE + DFT-D2.

nL-BP	a (Å)		b (Å)		c (Å)	
	our calc.	prev calc.	our calc.	prev calc.	our calc.	prev calc.
BP	4.56	4.56 [1b] 4.58 [1c]	3.31	3.32 [1b] 3.32 [1c]	NA	NA
2L-BP	4.50	4.50 [1b] 4.52 [1c]	3.315	3.32 [1b] 3.33 [1c]	NA	NA
3L-BP	4.48	4.47 [1b] 4.51 [1c]	3.32	3.32 [1b] 3.33 [1c]	NA	NA
Bulk [1a]	4.42	4.41 [1b]	3.32	3.31 [1b]	10.46	10.46 [1b]

[1a] Experimental lattice parameters; a= 3.31Å, b= 10.37Å, c= 4.38Å[39]
[1b] Ref. 23
[1c] Ref. 6

phosphorene. In the fourth and fifth parts, we present what we believe to be the two types of defects that correspond to the features **A** and **B** seen in experiments. We also explain the change in contrast seen on reversing bias in feature **A**, and why, on applying an electric pulse, feature **B** is transformed into feature **B'**.

7.5.1 Benchmark calculations: lattice parameters and band gap of pristine few-layer black phosphorene

We have performed 'variable cell optimization' to get the optimized lattice parameters for BP to 3L-BP. The optimized structures of the BP, 2L-BP, and 3L-BP are shown in Fig. 7.7. Our results for lattice parameters presented in Table 7.1 show that the lattice parameter **a** decreases when the thickness (number of layers) increases, although **b** remains unchanged upon increasing the thickness. The lattice parameters **a** = 4.48 Å and **b** = 3.32 Å of the 3L-BP have been used to construct a 7**a** × 9**b** supercell, which we used further to study the defects.

We have also computed the band gaps of few-layer black phosphorene systems, and compared our results with those of previous studies, these results are presented

Table 7.2: DFT results for calculated band gap (E_g) of few-layer black phosphorene and bulk black phosphorus. The second column contains our results computed using PBE + DFT-D2, the remaining columns contain previous values in the literature obtained using different techniques. The experimental values for the band gap in bulk black phosphorus range from 0.31 to 0.35 eV.[40–43]

	E_g (eV)			
Number of layers	our calc.	PBE [2a]	HSE06 [2b]	GW0 [2b]
1L	0.88	0.85	1.51	1.53
2L	0.41	0.50	1.02	1.01
3L	0.20	0.33	0.79	0.73
Bulk	0.0	0.0	0.15	0.27

[2a] Ref. 44
[2b] Ref. 6

in Table 7.2. We get good agreement with earlier calculations also performed using the PBE functional. It is well known that calculations performed using PBE or PBE+DFT-D2 can be expected to underestimate the band gaps (E_g) with respect to experiment. However, such calculations are still expected to be reliable for obtaining geometric structures, and also for comparative studies, e.g., comparing defect formation energies between various types of defects.

7.5.2 Defect Formation Energies

The defect formation energy (E_{DFE}) of defected systems can be calculated using the following formula:

$$E_{\mathrm{DFE}} = -\left(E_{\mathrm{pristine}} - \sum_i n_i \mu_i + \sum_j m_j \mu_j - E_{\mathrm{defect}}\right), \tag{7.1}$$

where E_{pristine} is the total energy of the pristine three-layer phosphorene (3L-BP), and E_{defect} is the total energy of the of defected system. n_i is the number of missing atoms (in this case P) from the system due to intrinsic or extrinsic defects, and m_i is the number of substituted/adatoms (e.g., Sn, Au) which cause extrinsic defects. μ_i

and μ_j are the chemical potentials of i^{th} and j^{th} types of atoms. μ_i for P is calculated by dividing the total energy of pristine 3L-BP by the total number of atoms present in the system. In the case of a transition metal like Sn or Au substituted or added to the systems, μ_j is the total energy calculated for an isolated atom of that species in vacuum.

The calculated values of E_{DFE} for all the defects we have considered are listed in Table 7.3. A positive value of E_{DFE} suggests that defect formation is unfavorable, whereas a negative value of E_{DFE} suggests defect formation is favorable. The more negative the value of E_{DFE}, the higher the probability of defect formation is. On the contrary, the higher the positive value of E_{DFE}, the lower the chance of defect formation is. By examining these values, we see that DV is more feasible to form over SW and MV in the case of intrinsic defects. We also see that any extrinsic defect due to a Sn or Au impurity is energetically more favorable than any of the kinds of intrinsic defects. One can also note that substitution of Sn is more favorable than intercalation. This is because of the fact that intercalation of a large atom like Sn weakens the interlayer van der Waals interactions by increasing the distance between the layers.

7.5.3 Simulated constant-current STM images for intrinsic and extrinsic defects in 3L-BP

We have used the Tersoff-Hamann[38] approach to simulate constant-current STM images for all the intrinsic and extrinsic defects we have considered.

Figs. 7.11(a)–(j) show the constant current STM images for all the intrinsic defects we have considered. The simulated STM images for the intrinsic defects do not show much resemblance with the experimental STM images presented above in Fig. 7.4 and Fig. 7.6. We have considered two bias voltages, one below the Fermi

Table 7.3: Calculated values of defect formation energy for all the types of intrinsic and extrinsic defects in 3L-BP considered by us. The positive E_{DFE} value of intrinsic defects suggests that formation of these defects is energetically unfavorable, whereas the negative E_{DFE} value of extrinsic defects suggests that formation of these defects is energetically favorable.

Systems	E_{DFE} (eV)
Pristine	0.0
59-MV	1.46
5757-DV	1.31
5757-SW	1.91
5656-MV-1	1.44
5656-MV-2	1.53
Sn-1	-3.04
Sn-2	-3.10
Sn-3	-3.20
Au-2	-2.63
Sn-int	-0.97

energy (negative bias) and another above the Fermi energy (positive bias), in order to check for a change in contrast as was observed in the experimental images of feature **A**.

Close examination of the simulated STM images shown in Fig. 7.11 reveals that STM images of the 59-MV and DV do not match the experimental observations at all. The SW leads to an extended feature at negative bias but fails to explain the dumbbell shape. For 5656-MV-1 and 5656-MV-2, we see an extended feature at negative bias, see Figs. 7.11(g) and 7.11(i). However, we do not see a bright dumbbell shape in the simulated images for any of the intrinsic defects considered. Note that this is in disagreement with the already mentioned work of Kiraly et al.,[27] who had speculated that the dumbbell type feature arose from a monovacancy of type 5656-MV-1. At positive bias, we see circular dark spots for both 5656-MV-1 and 5656-MV-2, see Fig. 7.11(h), and 7.11(j). However, for both 5656-MV-1 and 5656-MV-2, the features remain dark at both positive and negative bias voltages, which cannot explain the change of contrast on the reversal of bias potential observed in the experiment.

Therefore, none of the intrinsic defects considered here can explain the origin of the feature **A**. Similarly, none of the simulated STM images show a match with feature **B** and feature **B'**.

In Fig. 7.12, and Fig. 7.14, we have plotted simulated constant-current STM images for all the types of extrinsic defects considered by us. Upon examination, we conclude that Figs. 7.12(b) and 7.12(d) show the best match with the experimentally obtained images of feature **A**; these are the STM images for Sn-2 [see Figs. 7.9(b) and 7.9(e)]. We can see that the theoretically obtained STM images of Sn-2 show an extended dumbbell shape at negative bias and dark circular spot at positive bias (the full shape of the dumbbell cannot be seen because of the finite size of the supercell used in our simulations; a larger supercell would presumably show the whole dumbbell, but is unfeasible due to computational limitations). All these characteristics are in accordance with the experimental observations on feature **A**. Fig. 7.13 shows the comparison between theoretical and experimental STM images. One can look at the scale bars shown in Fig. 7.13(a) and 7.13(b) and can confirm that in both cases, we get the extended dumbbell shapes at negative bias. It can also be confirmed from both the experiment and theory that the bright dumbbell changes into a dark circular spot at positive bias.

Figs. 7.14(a) and 7.14(d) are theoretically obtained STM images for the Sn-3 defect at both polarities. They show similar features like Sn-2. The only difference is their brightness. At negative bias, the bright features in the image of Sn-2 are brighter than those in the image of Sn-3; this is presumably because of the fact that the Sn atom in the Sn-3 defect is buried under the topmost layer of P atoms, see 7.9(f). For both the cases i.e., for Sn-2 and Sn-3, a change of contrast can be observed on the reversal of the bias voltage. One can also note that Au-2 also shows

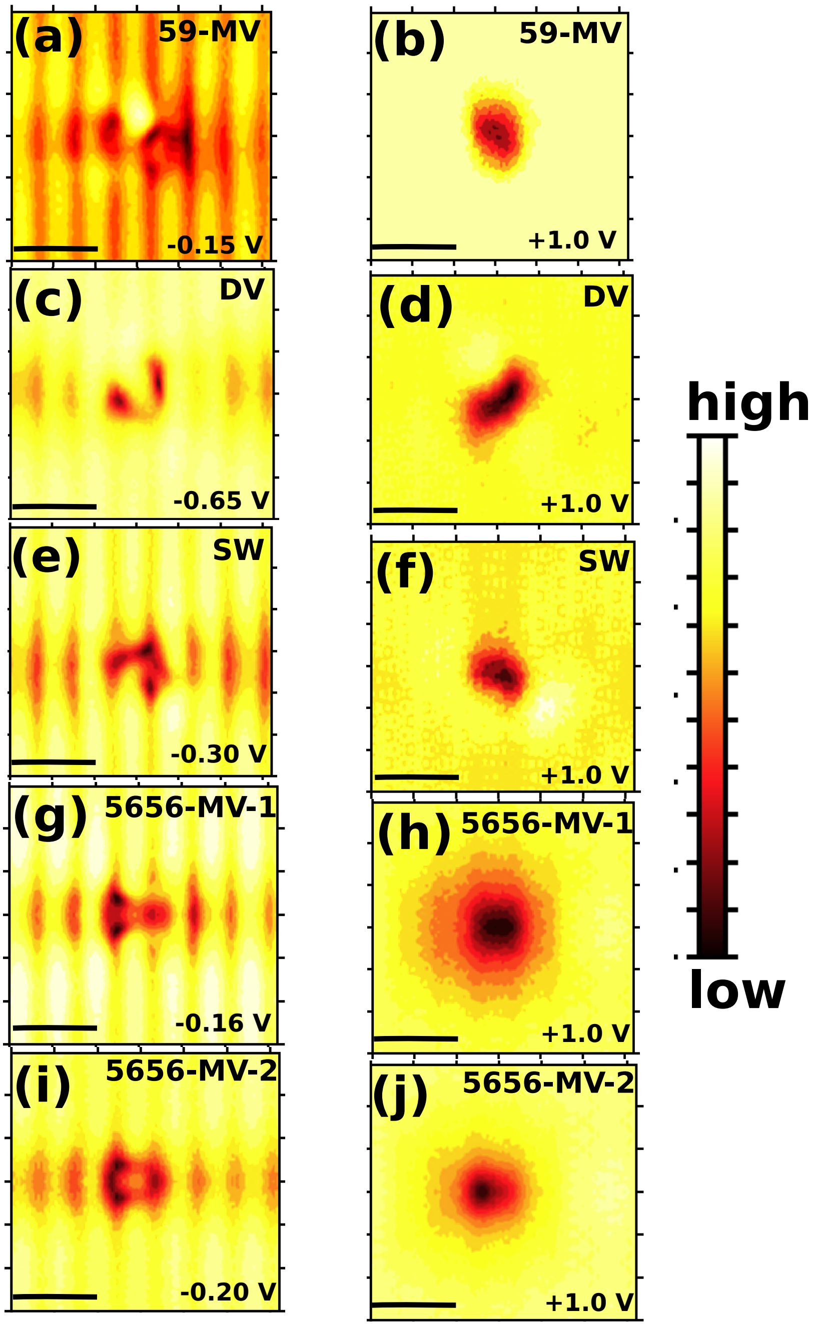

Figure 7.11: Simulated constant current STM images: (a) and (b) for 59-MV at bias voltage -0.15 V and $+1.0$ V, (c) and (d) for DV at bias voltage -0.65 V and $+1.0$ V, (e) and (f) for SW at bias voltage -0.3 V and $+1.0$ V, (g) and (h) for 5656-MV-1 at bias voltage -0.16 V and $+1.0$ V, (i) and (j) 5656-MV-2 at bias voltage -0.20 V and $+1.0$ V. We have fixed the isosurface value at 1×10^{-8} e/Bohr^3 to plot STM images. Scale bar = 1 nm

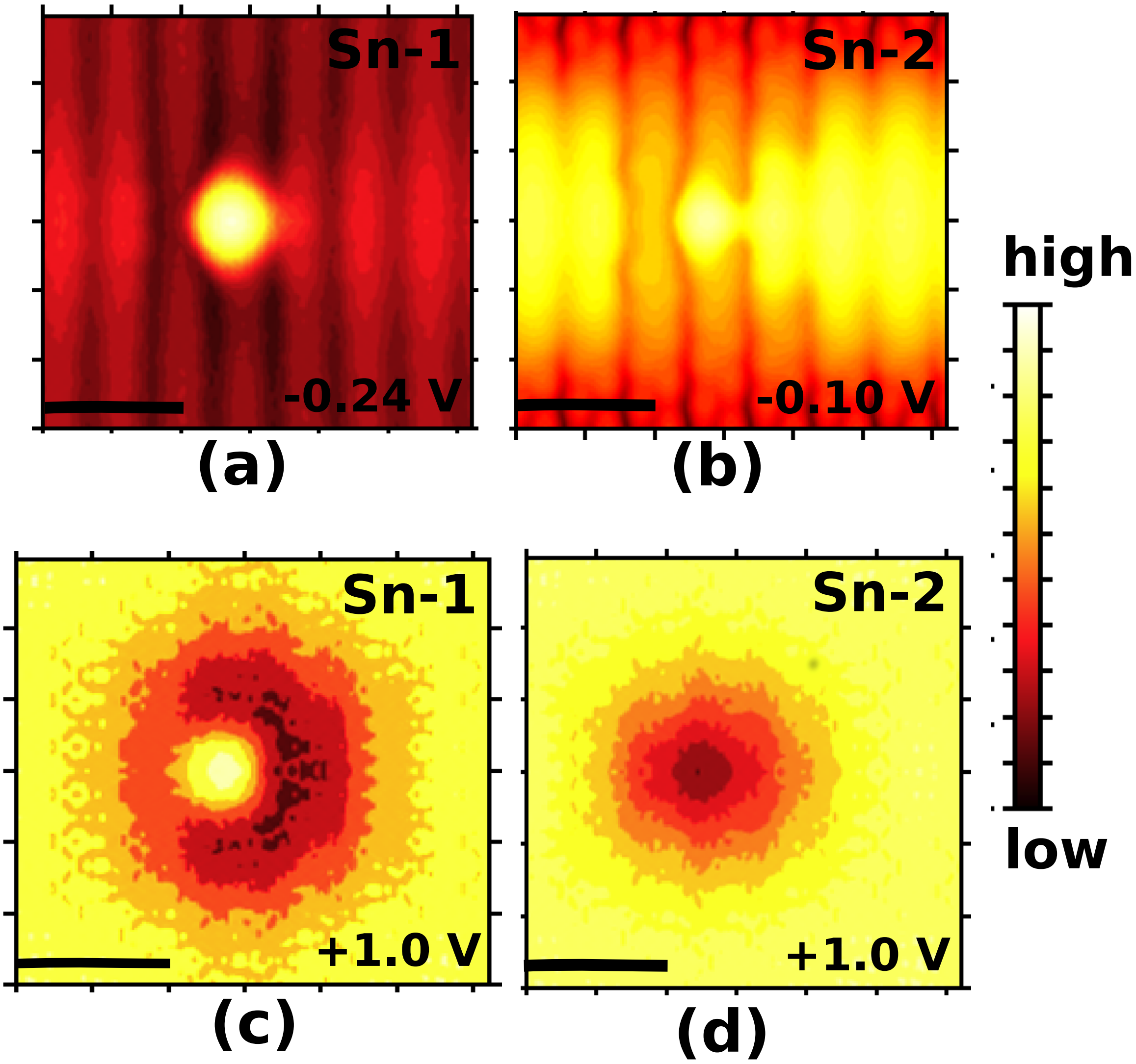

Figure 7.12: Simulated constant-current STM images: (a) and (c) for Sn-1 at bias voltage −0.24 V and +1.0 V, (b) and (d) for Sn-2 at bias voltage −0.10 V and +1.0 V. We have fixed the isosurface value at 1×10^{-8} e/Bohr^3 to plot STM images. Scale bar = 1 nm

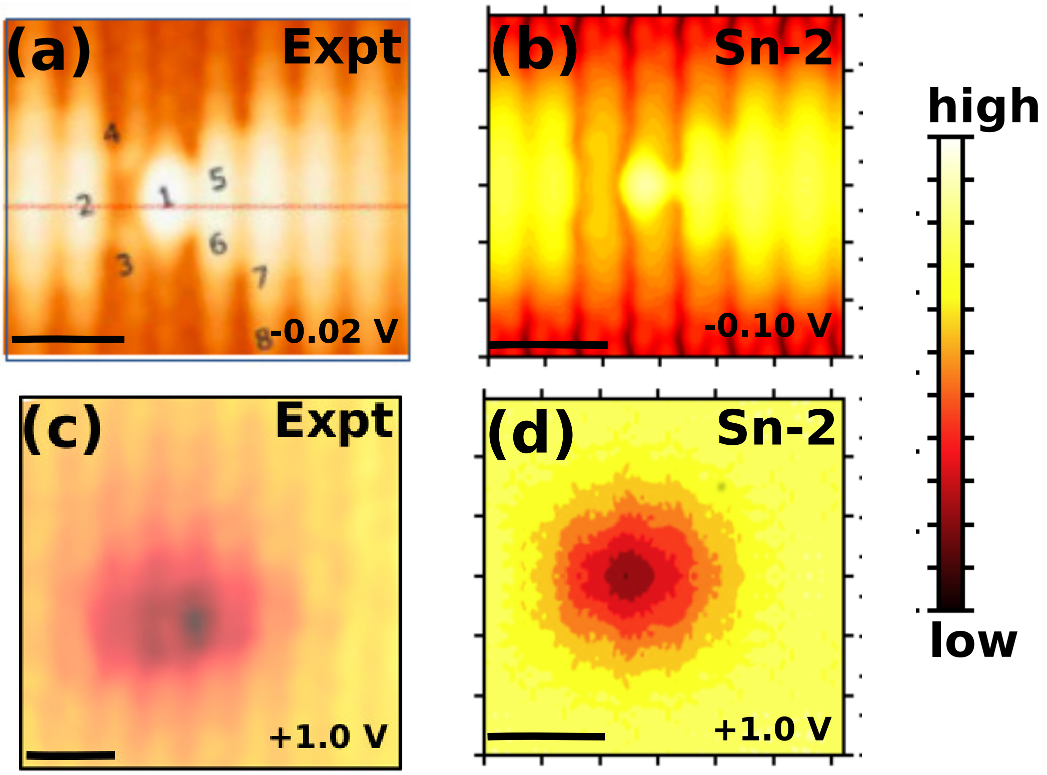
(a)
Expt
4
2
1
5
3
6
7
8
-0.02 V
(b)
Sn-2
-0.10 V
high
low
(c)
Expt
+1.0 V
(d)
Sn-2
+1.0 V

Figure 7.13: (a) and (c) are experimental STM images at V = −0.022 V, I = 200 pA and V = +1.0 V, I = 400 pA, respectively (b) and (d) are simulated STM images for Sn-2 at bias voltage −0.10 V and +1.0 V. We have fixed the isosurface value at $1{\times}10^{-8}$ e/Bohr^3 to plot (b) and (d). scale bar = 1 nm.

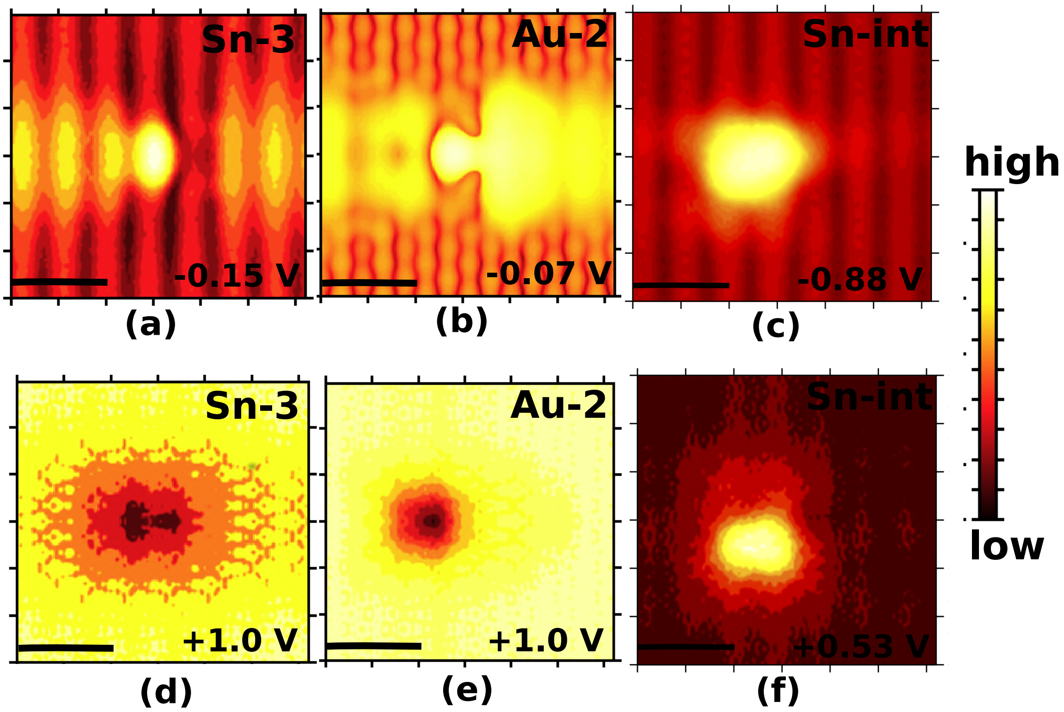

Figure 7.14: Simulated constant-current STM images: (a) and (d) for Sn-3 at bias voltage −0.15 V and +1.0 V, (b) and (e) for Au-2 at bias voltage −0.07 V and +1.0 V, (c) and (d) for Sn-int at bias voltage −0.88 V and +0.53 V. We have fixed the isosurface value at 1×10^{-8} e/Bohr^3 to plot the STM images. Scale bar = 1 nm.

the change of contrast, see Figs. 7.14(b), and 7.14(e) but the shape looks different than dumbbell at negative bias.

Simulated STM images for Sn-int have been shown in Figs. 7.14(c), and 7.14(f). We note that they consist of bright circular spots at both polarities. This agrees well with feature **B**.

Therefore, our results suggest that the origin of the feature **A** may be due to Sn-2 (a substitutional Sn defect in the lower sublayer of the topmost phosphorene layer), and the origin of feature **B** may be due to Sn-int (an intercalated Sn atom between the first and second phosphorene layers).

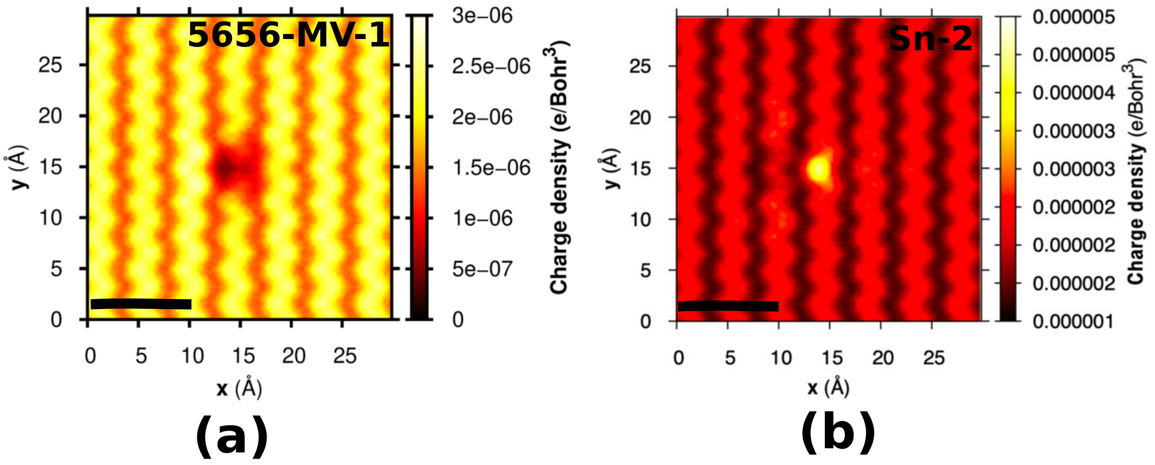

Figure 7.15: Charge density plot for (a) 5656-MV-1, and (b) Sn-2. The variation of the isosurface is shown for the plane placed at 2.57 Å above from the topmost layer. Scale bar = 1nm.

7.5.4 Origin of the shape and contrast in feature A and feature B

In this section, we attempt to explain two observations found in feature **A** using our DFT results: (1) why we see an extended dumbbell shape at negative bias voltage for feature **A** (Sn-2) and (2) why we see that the bright dumbbell changes to a dark circular spot at positive bias. We also attempt to explain why we see bright spots at both the positive and negative bias voltages for feature **B** (Sn-int). In other words, we want to understand the reason behind the shapes and contrast for the features **A** and **B**.

One possible way to explain this shape might be to examine the charge density distribution around the defect. First, we have plotted charge density of 5656-MV-1 [see Fig. 7.15(a)] and compared our result with the previous study done by Kiraly *et al.*[27] We see that in disagreement with their result, we do not find an extended dumbbell shape in the charge density plot for this defect. We do not completely understand the reason for this discrepancy, but we note that our result has been

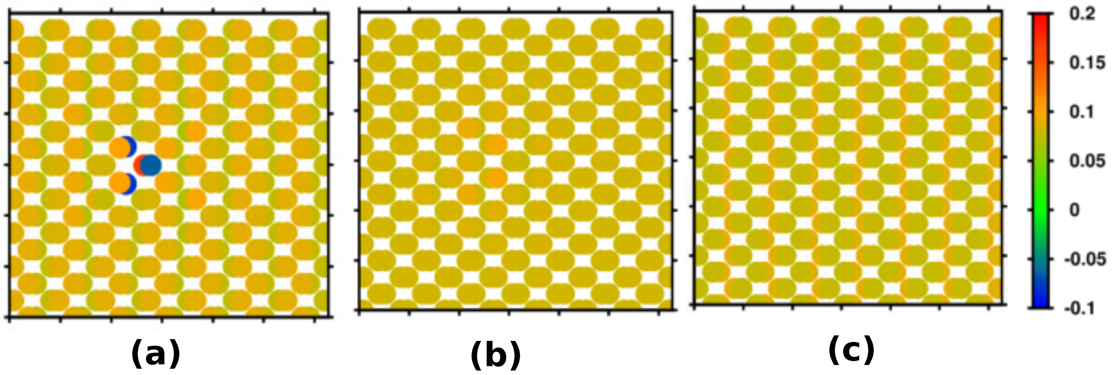

Figure 7.16: Distribution of atomic charges in the Sn-2 system, i.e., a 3L-BP system with a Sn atom substituted in the lower sublayer of the topmost BP layer. The atoms are colored according to the value of the calculated Löwdin charge (Q_i^L) computed according to Eq. (7.4), for (a) top layer, (b) middle layer, and (c) bottom layer.

obtained using DFT, whereas theirs was calculated using the tight binding approximation.

Next, we have plotted the charge density for the Sn-2 defect, in Fig. 7.15(b). From this figure, we see that also for this defect, we do not obtain an extended dumbbell shape, i.e., the charge density profile cannot explain the extended dumbbell shape of the feature **A** that is seen in STM images.

Another possible way to try and understand why we see a dumbbell shape is to look at the spatial distribution of atomic charges. For this purpose, we have computed the Löwdin charges. We have calculated the Löwdin charge on the i^{th} atom (Q_i^L) using the following relations:

$$P_{i,j}(\epsilon) = \sum_n \langle \psi_n | \phi_i^j \rangle \langle \phi_i^j | \psi_n \rangle \delta\big(\epsilon - \epsilon_n\big), \tag{7.2}$$

$$\pi_i = \sum_j P_{i,j}(\epsilon), \tag{7.3}$$

$$Q_i^L = Z_i - \int_{\epsilon_{min}}^{\epsilon_F} \pi_i(\epsilon) d\epsilon, \tag{7.4}$$

where i is an atomic index, and Z_i is the ionic charge of the i^{th} atom. $P_{i,j}(\epsilon)$ represents the density of states projected on the j^{th} orbital of the i^{th} atom. π_i is the total projected density of states (PDOS) summed over all the orbitals for the i^{th} atom. ψ_n is the n^{th} Kohn-Sham orbital and ϕ_i^j is j^{th} atomic orbital of the atom with atomic index i. In Figs. 7.16(a)-(c) we have plotted our results for the Löwdin charge for the Sn-2 system, plotted for each of the three layers that constitute the system. We see that the Löwdin charge is highest on the Sn atom, but we do not find a continuous variation of charge, which can give a shape like a dumbbell.

Although both the charge density and the Löwdin charge do not show signatures of the dumbbell-like shape seen at negative bias in feature **A**, we introduce two quantities Δ_i and $D_{i,j}$ that we find can be meaningful in this regard. These quantities are defined in the following way:

$$\Delta_i = \int_{\epsilon_F}^{\epsilon_F + eV} \pi_i(\epsilon) d\epsilon, \tag{7.5}$$

$$D_{i,j} = \int_{\epsilon_F}^{\epsilon_F + eV} P_{i,j}(\epsilon) d\epsilon, \tag{7.6}$$

where ϵ_F is the Fermi energy and V is the bias potential we use for STM. One should note that Eqs. (7.5) and (7.6) compute Δ_i and $D_{i,j}$ making use of an energy window of ϵ_F to $\epsilon_F + eV$ using the same logic proposed by Tersoff and Hamann.[38] However, Tersoff and Hamann's approach calculates the local density of states (integrated inside the energy window of ϵ_F to $\epsilon_F + eV$) which is different from the quantities $D_{i,j}$ and Δ_i. Our approach is novel because these quantitites are faster to compute than the simulated STM images obtained using the Tersoff-Hamann approach, yet they can accurately predict the shape of features seen in STM and phenomena such as a change of contrast upon changing bias voltage. In addition, they lend themselves to easy interpretation about which orbitals are responsible for the features and

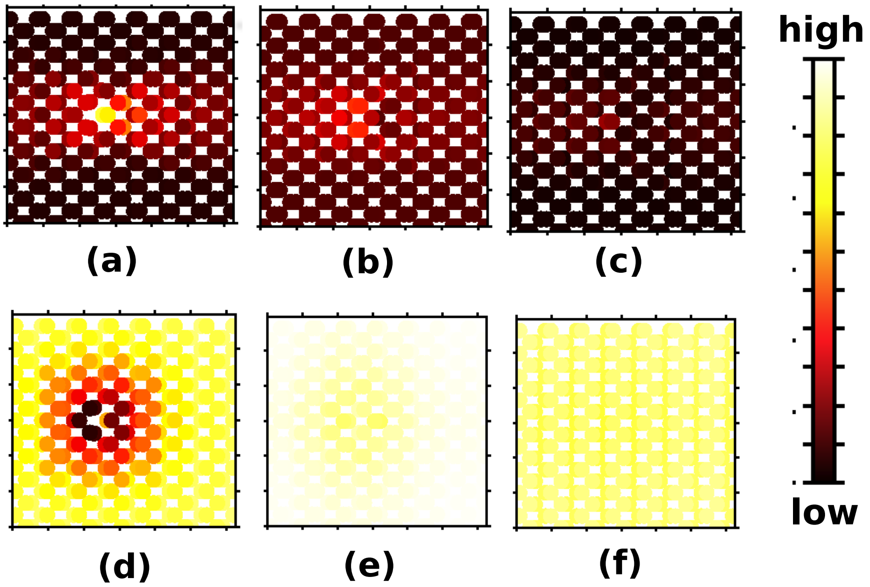

Figure 7.17: $\log(\Delta_i)$ for the atoms in (a) top layer, (b) middle layer, and (c) bottom layer of the Sn-2 system for the energy window ϵ_F to $\epsilon_F - 0.10$ eV. $\log(\Delta_i)$ for the atoms in (d) top layer, (e) middle layer, and (f) bottom layer of the Sn-2 system for the energy window ϵ_F to $\epsilon_F + 1.0$ eV.

phenomena observed.

We have plotted the quantity Δ_i for the atoms present in the different layers of the Sn-2 system, see Figs. 7.17(a)-(f). For the energy window from ϵ_F to $\epsilon_F -$ 0.10 eV (negative bias), atoms aligned with the impurity Sn atom along the armchair direction contribute maximum to Δ_i, we see a bright dumbbell, see Fig. 7.17(a). One should note that the atoms' contribution from the middle and bottom layers are less compared to the top layer. On the other hand, top layer atoms near the Sn atom of the Sn-2 system has the least contribution if we choose the energy window from ϵ_F to ϵ_F + 1.0 eV (positive bias), see Fig. 7.17(d). The least contributing (black/red points) atoms near the Sn impurity form a dark circle and are responsible for the change of contrast at the positive bias.

In the same way, we have plotted $D_{i,j}$ for both the negative and positive bias voltages. The quantity $D_{i,j}$ represents the projection of the Δ_i on the j^{th} orbital of the atom with the index i. Therefore, $D_{i,j}$ is the orbital decomposition of the

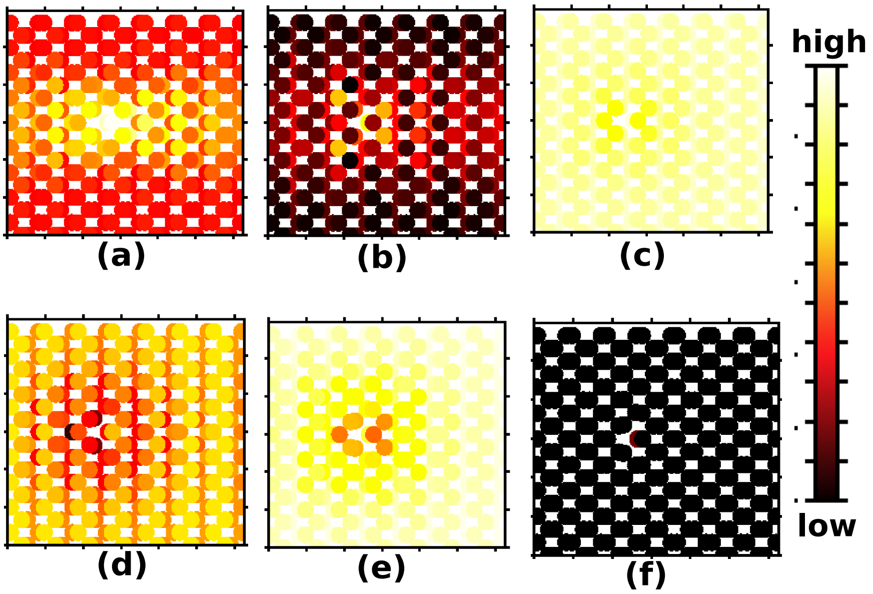

Figure 7.18: $\log(D_{i,j})$ for (a) p_z, (b) p_x+p_y, and (c) s orbitals of the atoms present in top layer layer of the Sn-2 system for the energy window ϵ_F to $\epsilon_F - 0.10$ eV. $\log(D_{i,j})$ for (d) p_z, (e) p_x+p_y, and (f) s orbitals of the atoms present in top layer layer of the Sn-2 system for the energy window ϵ_F to $\epsilon_F + 1.0$ eV.

quantity Δ_i. We have decomposed Δ_i on p_z, p_x+p_y, and s orbitals to see the contributions of those orbitals in Δ_i, in Fig. 7.18. One can notice that p_z orbitals participate significantly in both the cases i.e., forming the bright dumbbell at negative bias and forming the dark circular spot at positive bias. One can see a bright dumbbell at negative bias and a dark circular spot at positive bias because of the fact that the STM tip, which is normal to the BP layers (i.e., along the z-axis) is primarily sensitive to the p_z orbitals during the scanning.

A similar analysis can be done for the Sn-int defect. We have plotted the quantity Δ_i for the Sn-int system in Fig. 7.19 and $D_{i,j}$ in Figs. 7.20–7.21. Figs. 7.19(a)-(c) show the atomic contribution to the quantity Δ_i within the energy window from ϵ_F to $\epsilon_F - 0.88$ eV (negative bias) for the atoms present in the top, middle and bottom layer of the Sn-int system, respectively. One can note that both the top and middle layers have contributed to the quantity Δ_i to form the bright spot at negative bias. This is in contrast to our findings for the Sn-2 system, where we found the top layer

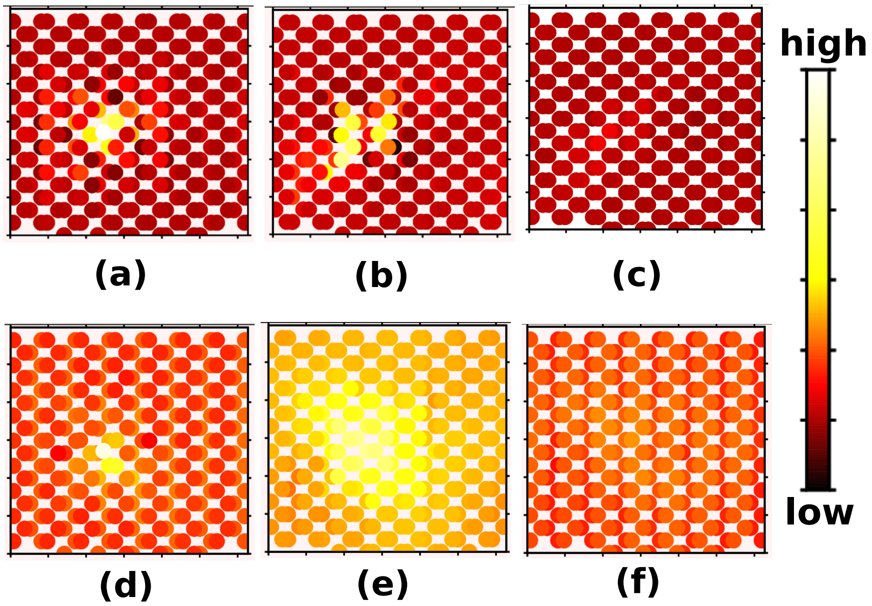

Figure 7.19: log(Δ_i) for the atoms in (a) top layer, (b) middle layer, and (c) bottom layer of the Sn-int system for the energy window ϵ_F to ϵ_F -0.88 eV. log(Δ_i) for the atoms in (d) top layer, (e) middle layer, and (f) bottom layer of the Sn-int system for the energy window ϵ_F to ϵ_F $+0.53$ eV.

has a maximum contribution to Δ_i. However, the middle layer has contributed the maximum to the Δ_i for positive bias, i.e., inside the energy window, ϵ_F to $\epsilon_F + 0.53$ eV, see Figs. 7.19(d)-(f). In comparison to Sn-2 (where the defect is present in the top layer), the defect in the Sn-int is owing to the intercalated (inserted) Sn atom between the top and the middle layer, which may explain the contribution of both the top and middle layers to the Δ_i in case of Sn-int.

To see the orbital contributions from each layer, we have plotted $D_{i,j}$ for both the top and middle layers of the Sn-int. One should note that we have plotted $D_{i,j}$ only for the p_z, and s orbitals for both the layers because of the fact that the STM tip, which is normal to the BP layers (i.e., along the z-axis) is also sensitive to the s orbitals (due to their spherical shape) in addition to p_z orbitals. Figs. 7.20(a)-(d) show the orbital contribution of p_z at both the negative [Figs. 7.20(a)-(b)] and positive [Figs. 7.20(c)-(d))] bias voltages. Similarly, Figs. 7.21(a)-(d) show the contribution of s orbitals at both negative and positive bias voltages. A closer examination of

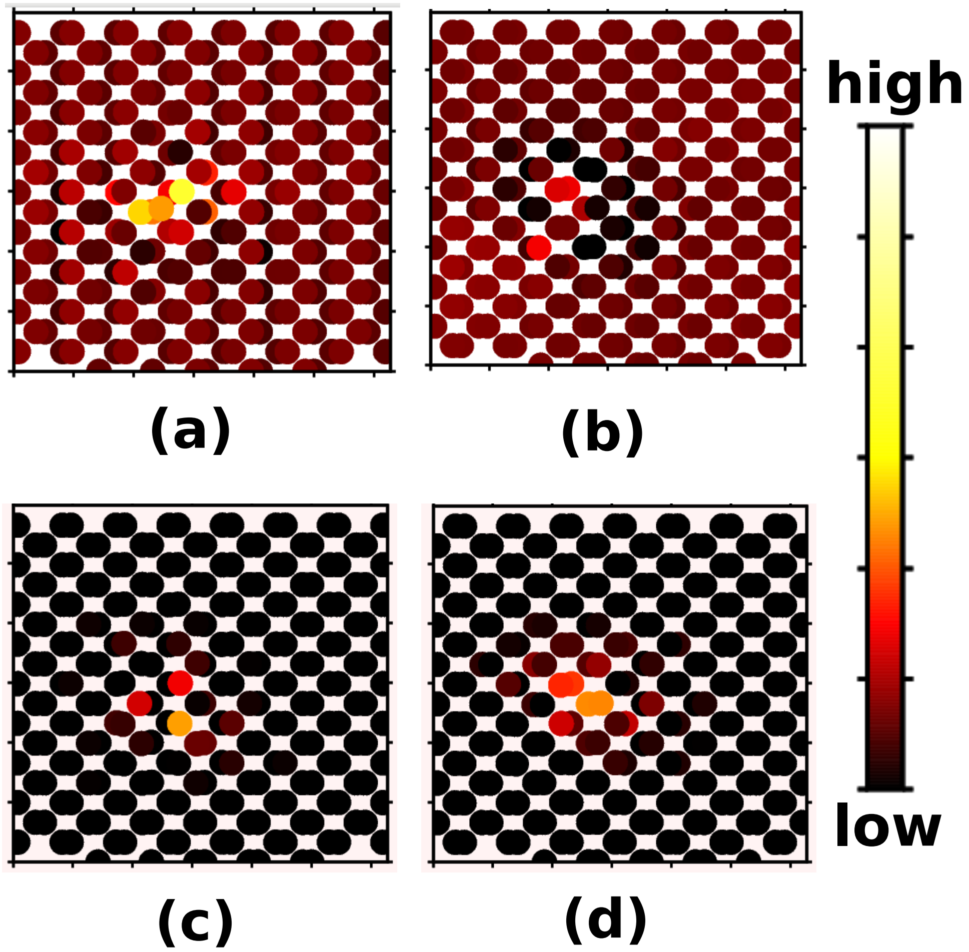

Figure 7.20: log(Δ_i) for the p_z orbitals of the atoms in (a) top layer and (b) middle layer of the Sn-int system for the energy window ϵ_F to $\epsilon_F - 0.88$ eV. log(Δ_i) for the p_z orbitals of the atoms in (c) top layer and (d) middle layer of the Sn-int system for the energy window ϵ_F to $\epsilon_F + 0.53$ eV.

Fig. 7.20 and Fig. 7.21 reveals that p_z orbitals of the top layer have the maximum contribution to form the bright spot at negative bias, and both p_z and s orbitals of the middle layer have contributed the maximum to form the bright spot at positive bias.

7.5.5 Effect of the electric pulse

In the previous section, we have shown that the Sn-2 and Sn-int defects are the origins of the feature **A** and feature **B** respectively, by comparing our DFT results

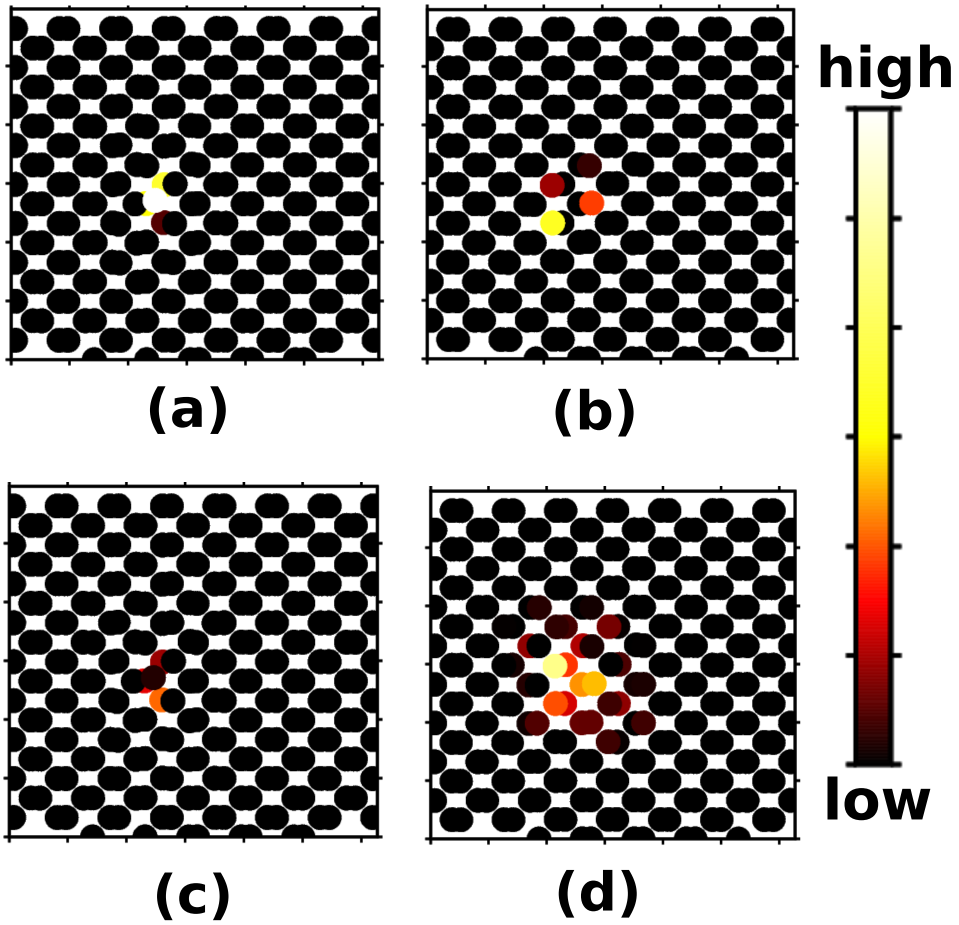

Figure 7.21: log(Δ_i) for the s orbitals of the atoms in (a) top layer and (b) middle layer of the Sn-int system for the energy window ϵ_F to $\epsilon_F - 0.88$ eV. log(Δ_i) for the s orbitals of the atoms in (c) top layer and (d) middle layer of the Sn-int system for the energy window ϵ_F to $\epsilon_F + 0.53$ eV.

with the STM experiments. In this section, we discuss the origin of feature **B'**, which means we want to understand what happens to feature **B** under the application of the external electric pulse. From the experiments, we can guess that Sn-int has switched to another defect, which gives a dumbbell-like shape with a bright spot in its centre. To verify our guess, we have considered three possibilities for what could happen to the interstitial Sn atom when an electric pulse is applied, see Figs. 7.22(a)-(c). In this section, we show, using DFT, that one of these three ways can explain the switchover process. For this purpose, we have simulated STM images for all the three final configurations (i.e., configuration we got after applying electric pulse) shown in Fig. 7.22 and compared the experimental STM images of feature **B'**. In addition, we have compared the thermodynamic feasibility by computing enthalpy (ΔH) for all the three switch-over paths to select the most favorable scenario among the three considered.

In Fig. 7.22(a) we have shown that the electric pulse breaks the Sn-P bond in Sn-int and helps Sn-int switch into Sn-2 + P-vac, where the P atom that has now been substituted by a Sn atom has gone far into the vacuum i.e., away from the surface. We can consider this Sn-2 + P-vac as Sn-2 when simulating STM images because of the fact that the removed P atom has gone very far from the surface. In the second case, we have considered Sn-int to Sn-2 + P-adatom switchover where P is bonded to the substrate in this case instead of going far in the vacuum, see Fig. 7.22(b). Lastly, we have considered that an electric pulse could perhaps flip the Sn-P bond in Sn-int, which results in Sn-2 + P-int, where P is intercalated between the top and middle layers, see Fig. 7.22(c). One should note that we have considered these three possibilities where defects are at the top of the surface or at the top layer based on the experimental finding shown in Fig. 7.5, which suggests that feature **B'** should have atoms at a greater height than they are in feature **A**, which is already at the top layer.

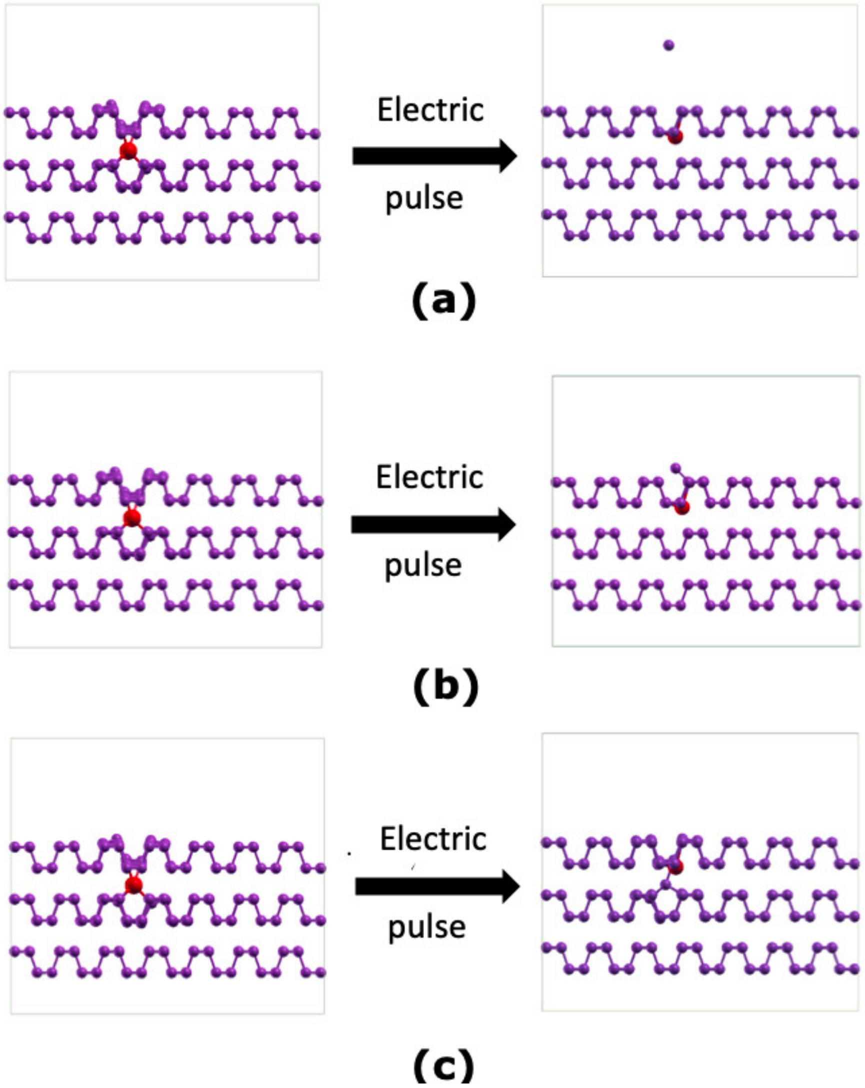
Electric
pulse
(a)
Electric
pulse
(b)
Electric
pulse
(c)

Figure 7.22: Three possible scenarios considered for effect of electric pulse on the Sn interstitial defect: (a) Sn-int switches to Sn-2 + P-vac (or Sn-2), (b) Sn-int switches to Sn-2 + P-adatom, (c) Sn-int switches to Sn-2+P-int. Color code: purple (P), red (Sn)

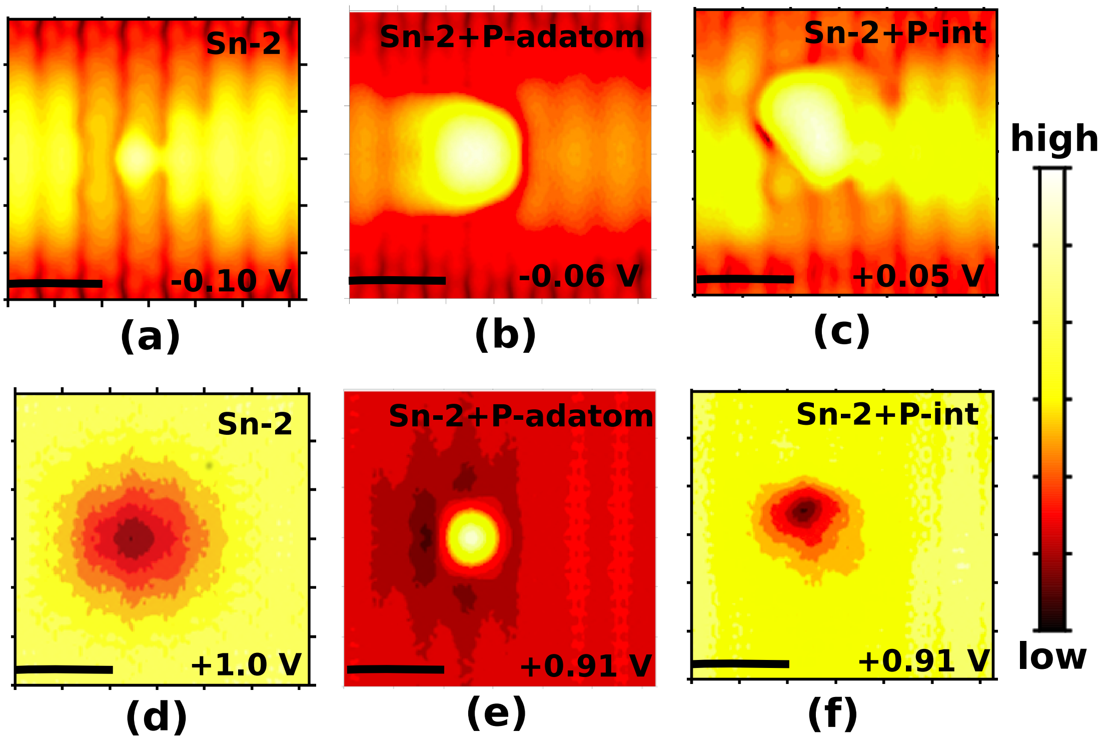

Figure 7.23: Simulated constant-current STM images: (a) and (d) for Sn-2 + P-vac (or Sn-2) at at bias voltages −0.10 V and +1.0 V, (b) and (e) for Sn-2 + P-adatom at bias voltages −0.06 V and +0.91 V, (c) and (f) for Sn-2 + P-int at bias voltages +0.05 V and +0.91 V. Scale bar = 1nm

Comparison of STM images for Sn-2 + P-vac, Sn-2 + P-adatom and Sn-2 + P-int

We have already shown the simulated STM images for Sn-2 + P-vac (i.e., for the Sn-2 defect) in Figs. 7.12(b) and 7.12(d). However, we have repeated them in Fig. 7.23(a) [as in Fig. 7.12(b)] and Fig. 7.23(d) [as in Fig. 7.12(d)] for the ease of reference. Figs. 7.23(b) and 7.23(e) show the simulated STM images for Sn-2+P-adatom. Similarly, STM images for Sn-2+P-int are shown in Fig. 7.23(c) and 7.23(f). By examining these figures, one can conclude that Sn-2+P-int is not the best match for feature **B'** because it leads to a distorted dumbbell-like feature at negative bias, as opposed to the symmetric dumbbell seen in the experimental images of feature **B'** So, we can already conclude that the switchover path shown in Fig. 7.22(c) is unlikely to correspond to the experimental scenario. Among the two remaining choices, i.e., between the pathways shown in Fig. 7.22(a) and Fig. 7.22(b), we believe the latter, i.e., that shown in Fig. 7.22(b), is correct rather than the former, because only Sn-2+P-adatom give rise to an STM image which is a dumbbell shape with a bright spot in its center at negative bias volatge, which we have also seen in the experiment, see Fig. 7.4.

However, we couldn't compare the STM image of the Sn-2+P-adatom simulated at +0.91 V with the experiment due to the lack of experimental data for feature **B'** at positive bias.

We note also that the Sn-2+P-adatom configuration has a P adatom adsorbed on the topmost layer of the 3L-BP system, which can explain also the height profile shown in Fig. 7.5, which suggests that there is one atom at a much greater height than the surrounding atoms, in this configuration.

Comparison of the energetics among the paths shown in Fig. 7.22

It is important to compare the defect formation energies (E_{DFE}) for all the defects shown in Fig. 7.22. We have computed that E_{DFE} for the initial state, Sn-int is −0.97 eV. We find that all three final states considered have a lower energy than this. Calculated E_{DFE} for the Sn-2+P-adatom is −5.24 eV, which is much lower compared to Sn-2 (−3.10 eV) and Sn-2+P-int (−4.98 eV). This already indicates the feasibility of the formation of the Sn-2+P-adatom defect from Sn-int. Note that the E_{DFE} for all these three extrinsic defects is negative, in contrast to the intrinsic defects considered earlier, where the E_{DFE} was positive; this is in accordance with the results of previous authors.[26]

To summarize the thermodynamic feasibilities of the three paths considered in Figs. 7.22(a)–(c), we have drawn a diagram (see Fig. 7.24) showing the change in enthalpy (ΔH) of each possible path. This makes the process shown in Fig. 7.22(b) (i.e. switchover of Sn-int to Sn-2 + P-adatom) more likely to occur (based on

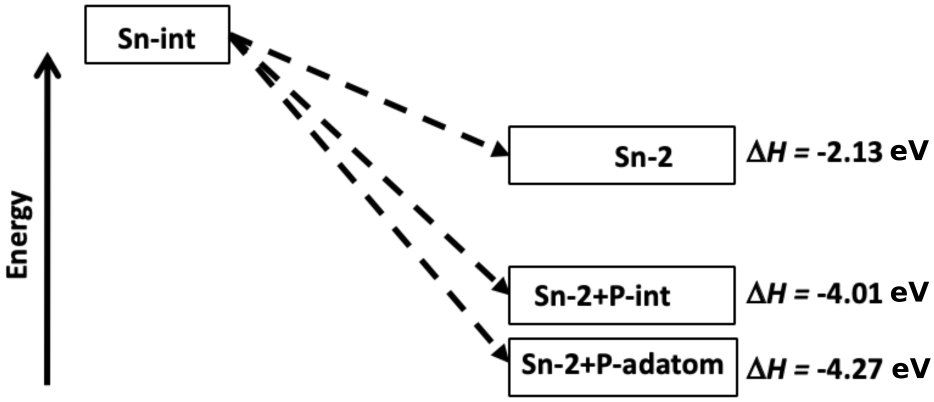

Figure 7.24: Change in enthalpy for the three switchover paths discussed in Figs. 7.22(a)–(c).

thermodynamic considerations) than the other two. So, both comparison of experimental and theoretical STM images and energetic considerations suggest that the electric pulse switches Sn-int defect to Sn-2+P-adatom. Hence, we conclude that the configuration Sn-2+P-adatom is the origin of feature **B'**.

7.6 Conclusions

We have used DFT to investigate and explain the origin of three different features observed in STM experiments performed on few-layer black phosphorene by our collaborators in the MPQ Laboratory of the University of Paris-Diderot. Our results suggest that defects due to Sn impurities are responsible for these features. The defect that we call Sn-2 (Sn substitution in the lower sublayer of the topmost phosphorene layer) shows up in STM images as a dumbbell shape at negative bias and a dark circular spot at positive bias; this is called feature **A** by us. The dumbbell is of very large extent, of the order of a few nm. We are the first one to report the origin of the extended nature of the dumbbell shape as well as the change of contrast on the reversal of the bias polarity. Similarly, we have shown that what we call the Sn-int defect (an interstitial Sn atom between the first and second phospherene layers) shows up as bright spots at both polarities and is the origin of feature that we call **B**.

DFT is also successful explaining the effect of an electric pulse on these defects due to Sn impurities. An electric pulse has no effect on Sn-2 because it has a very low E_{DFE} (-3.10 eV), which makes this defect stable. However, an electric pulse can convert the comparatively less stable defect Sn-int (with E_{DFE} = -0.97 eV) to another defect, which we called Sn-2-P-adatom. This latter identification is made on the basis of both energetics (ΔH of the switchover process) and STM images (comparison of experiment vs. theory). Both the Sn-2 and Sn-2-P-adatom defects lead to dumbbell-like features in STM images. However, the Sn-2-P-adatom defect shows a dumbbell with a bright spot in its centre, whereas the Sn-2 defect shows a dumbbell with a dark spot in the centre. We have successfully distinguished three defects: Sn-2 = feature **A**, Sn-int = feature **B**, and Sn-2 + P-adatom = feature **B'**.

Bibliography

[1] A. Morita, “Semiconducting black phosphorus,” *Appl. Phys. A*, vol. 39, p. 227, 1986.

[2] W. Lu, H. Nan, J. Hong, Y. Chen, C. Zhu, Z. Liang, X. Ma, Z. Ni, C. Jin, and Z. Zhang, “Plasma-assisted fabrication of monolayer phosphorene and its raman characterization,” *Nano Res.*, vol. 7, p. 853, 2014.

[3] A. Castellanos-Gomez, L. Vicarelli, E. Prada, J. O. Island, K. Narasimha-Acharya, S. I. Blanter, D. J. Groenendijk, M. Buscema, G. A. Steele, J. Alvarez, *et al.*, “Isolation and characterization of few-layer black phosphorus,” *2d Mater.*, vol. 1, p. 025001, 2014.

[4] H. Liu, A. T. Neal, Z. Zhu, Z. Luo, X. Xu, D. Tománek, and P. D. Ye, “Phosphorene: an unexplored 2d semiconductor with a high hole mobility,” *ACS Nano*, vol. 8, p. 4033, 2014.

[5] Y. Cai, G. Zhang, and Y.-W. Zhang, “Layer-dependent band alignment and work function of few-layer phosphorene,” *Sci. Rep.*, vol. 4, p. 6677, 2014.

[6] J. Qiao, X. Kong, Z.-X. Hu, F. Yang, and W. Ji, “High-mobility transport anisotropy and linear dichroism in few-layer black phosphorus,” *Nat. commun.*, vol. 5, p. 4475, 2014.

[7] A. N. Rudenko, S. Yuan, and M. I. Katsnelson, "Toward a realistic description of multilayer black phosphorus: From *gw* approximation to large-scale tight-binding simulations," *Phys. Rev. B*, vol. 92, p. 085419, 2015.

[8] K. Bolotin, K. Sikes, Z. Jiang, M. Klima, G. Fudenberg, J. Hone, P. Kim, and H. Stormer, "Ultrahigh electron mobility in suspended graphene," *Solid State Communications*, vol. 146, p. 351, 2008.

[9] K. I. Bolotin, K. J. Sikes, J. Hone, H. L. Stormer, and P. Kim, "Temperature-dependent transport in suspended graphene," *Phys. Rev. Lett.*, vol. 101, p. 096802, 2008.

[10] A. Kara, H. Enriquez, A. P. Seitsonen, L. L. Y. Voon, S. Vizzini, B. Aufray, and H. Oughaddou, "A review on silicene—new candidate for electronics," *Surf. Sci. Rep.*, vol. 67, p. 1, 2012.

[11] Q. Wang, K. Kalantar-Zadeh, A. Kis, J. Coleman, and M. Strano, "Electronics and optoelectronics of two-dimensional transition metal dichalcogenides," *Nature Nanotechnol*, vol. 7, p. 699, 2012.

[12] L. Li, Y. Yu, G. J. Ye, Q. Ge, X. Ou, H. Wu, D. Feng, X. H. Chen, and Y. Zhang, "Black phosphorus field-effect transistors," *Nat. Nanotechnol*, vol. 9, p. 372, 2014.

[13] M. Buscema, D. J. Groenendijk, G. A. Steele, H. S. Van Der Zant, and A. Castellanos-Gomez, "Photovoltaic effect in few-layer black phosphorus pn junctions defined by local electrostatic gating," *Nat. Commun.*, vol. 5, p. 4651, 2014.

[14] J. Dai and X. C. Zeng, "Bilayer phosphorene: effect of stacking order on bandgap and its potential applications in thin-film solar cells," *J. Phys. Chem. Lett.*, vol. 5, p. 1289, 2014.

[15] A. Hashimoto, K. Suenaga, A. Gloter, K. Urita, and S. Iijima, “Direct evidence for atomic defects in graphene layers,” *Nature*, vol. 430, p. 870, 2004.

[16] F. Banhart, J. Kotakoski, and A. V. Krasheninnikov, “Structural defects in graphene,” *ACS Nano*, vol. 5, p. 26, 2010.

[17] R. G. Amorim, A. Fazzio, A. Antonelli, F. D. Novaes, and A. J. da Silva, “Divacancies in graphene and carbon nanotubes,” *Nano Lett.*, vol. 7, no. 8, p. 2459, 2007.

[18] L. Kou, C. Tang, W. Guo, and C. Chen, “Tunable magnetism in strained graphene with topological line defect,” *ACS Nano*, vol. 5, p. 1012, 2011.

[19] J. Gao, J. Zhang, H. Liu, Q. Zhang, and J. Zhao, “Structures, mobilities, electronic and magnetic properties of point defects in silicene,” *Nanoscale*, vol. 5, p. 9785, 2013.

[20] H. Sahin, J. Sivek, S. Li, B. Partoens, and F. M. Peeters, “Stone-wales defects in silicene: Formation, stability, and reactivity of defect sites,” *Phys. Rev. B*, vol. 88, p. 045434, 2013.

[21] T. Hu and J. Dong, “Geometric and electronic structures of mono-and divacancies in phosphorene,” *Nanotechnology*, vol. 26, p. 065705, 2015.

[22] Y. Guo and J. Robertson, “Vacancy and doping states in monolayer and bulk black phosphorus,” *Sci. Rep.*, vol. 5, p. 14165, 2015.

[23] V. Wang, Y. Kawazoe, and W. Geng, “Native point defects in few-layer phosphorene,” *Phys. Rev. B*, vol. 91, p. 045433, 2015.

[24] Y. Cai, Q. Ke, G. Zhang, B. I. Yakobson, and Y.-W. Zhang, “Highly itinerant atomic vacancies in phosphorene,” *J. Am. Chem. Soc.*, vol. 138, p. 10199, 2016.

[25] W. Hu and J. Yang, “Defects in phosphorene,” *J. Phys. Chem. C*, vol. 119, p. 20474, 2015.

[26] J. Gaberle and A. L. Shluger, “Structure and properties of intrinsic and extrinsic defects in black phosphorus,” *Nanoscale*, vol. 10, p. 19536, 2018.

[27] B. Kiraly, N. Hauptmann, A. N. Rudenko, M. I. Katsnelson, and A. A. Khajetoorians, “Probing single vacancies in black phosphorus at the atomic level,” *Nano Lett.*, vol. 17, p. 3607, 2017.

[28] Z. Qiu, H. Fang, A. Carvalho, A. Rodin, Y. Liu, S. J. Tan, M. Telychko, P. Lv, J. Su, Y. Wang, *et al.*, “Resolving the spatial structures of bound hole states in black phosphorus,” *Nano Lett.*, vol. 17, p. 6935, 2017.

[29] C. C. Mayorga-Martinez, Z. Sofer, D. Sedmidubskỳ, J. Luxa, B. Kherzi, and M. Pumera, “Metallic impurities in black phosphorus nanoflakes prepared by different synthetic routes,” *Nanoscale*, vol. 10, p. 1540, 2018.

[30] R. Harsh, *Electronic interaction of organic molecules with low dimensional materials: a scanning tunneling microscopy study on graphene and black phosphorus.* Université de Paris, 2019.

[31] P. Giannozzi, S. Baroni, N. Bonini, M. Calandra, R. Car, C. Cavazzoni, Davide Ceresoli, G. L. Chiarotti, M. Cococcioni, I. Dabo, A. D. Corso, S. d. Gironcoli, S. Fabris, G. Fratesi, R. Gebauer, U. Gerstmann, C. Gougoussis, Anton Kokalj, M. Lazzeri, L. Martin-Samos, N. Marzari, F. Mauri, R. Mazzarello, Stefano Paolini, A. Pasquarello, L. Paulatto, C. Sbraccia, S. Scandolo, G. Sclauzero, A. P. Seitsonen, A. Smogunov, P. Umari, and R. M. Wentzcovitch, “QUANTUM ESPRESSO: a modular and open-source software project for quantum simulations of materials,” *J. Phys.: Condens. Matter*, vol. 21, p. 395502, 2009.

[32] P. Giannozzi, O. Andreussi, T. Brumme, O. Bunau, M. B. Nardelli, M. Calandra, R. Car, C. Cavazzoni, D. Ceresoli, M. Cococcioni, *et al.*, "Advanced capabilities for materials modelling with quantum espresso," *J. Phys.: Condens. Matter*, vol. 29, p. 465901, 2017.

[33] J. P. Perdew, K. Burke, and M. Ernzerhof, "Generalized gradient approximation made simple," *Phys. Rev. Lett.*, vol. 77, p. 3865, 1996.

[34] D. Vanderbilt, "Soft self-consistent pseudopotentials in a generalized eigenvalue formalism," *Phys. Rev. B*, vol. 41, p. 7892, 1990.

[35] S. Grimme, "Semiempirical gga-type density functional constructed with a long-range dispersion correction," *J. Comput. Chem.*, vol. 27, p. 1787, 2006.

[36] H. J. Monkhorst and J. D. Pack, "Special points for Brillouin-zone integrations," *Phys. Rev. B*, vol. 13, p. 5188, 1976.

[37] N. Marzari, D. Vanderbilt, A. De Vita, and M. C. Payne, "Thermal contraction and disordering of the Al(110) surface," *Phys. Rev. Lett.*, vol. 82, p. 3296, 1999.

[38] J. Tersoff and D. R. Hamann, "Theory of the scanning tunneling microscope," *Phys. Rev. B*, vol. 31, p. 805, 1985.

[39] A. Brown and S. Rundqvist, "Refinement of the crystal structure of black phosphorus," *Acta Crystallographica*, vol. 19, p. 684, 1965.

[40] R. W. Keyes, "The electrical properties of black phosphorus," *Phys. Rev.*, vol. 92, p. 580, 1953.

[41] Y. Maruyama, S. Suzuki, K. Kobayashi, and S. Tanuma, "Synthesis and some properties of black phosphorus single crystals," *Physica B+C*, vol. 105, p. 99, 1981.

[42] Y. Akahama, S. Endo, and S.-i. Narita, “Electrical properties of black phosphorus single crystals,” *J. Phys. Soc. of Jpn*, vol. 52, p. 2148, 1983.

[43] D. Warschauer, “Electrical and optical properties of crystalline black phosphorus,” *J. Appl. Phys*, vol. 34, no. 7, p. 1853, 1963.

[44] V. Tran, R. Soklaski, Y. Liang, and L. Yang, “Layer-controlled band gap and anisotropic excitons in few-layer black phosphorus,” *Phys. Rev. B*, vol. 89, p. 235319, 2014.

Chapter 8

Summary & Future Outlook

In this chapter, we summarize our main findings from each chapter of this thesis and present a brief outlook for the possible future directions of research.

The general theme that we followed in this thesis is to tailor the properties of two-dimensional systems by adsorbing organic molecules and by defect engineering. Another objective of this thesis was to provide explanations to certain puzzles that arose from experimental observations. This thesis focused on two types of systems: organic molecules on surfaces, and two-dimensional systems with impurities or defects.

We started with organic molecules on the surfaces. In **Chapter 3**, we studied the spin crossover molecule $Fe((3, 5\text{-}(CH_3)_2C_3N_2H)_3BH)_2$ (or IPB) on Au(111). We found that in this system, the IPB molecules form an ordered spin superlattice, with a 2:1 ratio of high-spin and low-spin states molecules, arranged in a $S_{1/3}$ unit cell. We are the first to report such a two-dimensional ordered mixed spin phase of spin crossover molecules. We have shown that both the Hubbard U parameter and epitaxial strain play an important role in determining the mixed spin phase on Au(111). We showed that a mechano-elastic model fitted to DFT data could explain the phenomenon of epitaxial strain-induced spin crossover. This finding shows how to control the spin states of such spin crossover molecules at metallic interfaces by tuning the epitaxial strain, which arises because of lattice mismatch between the molecular monolayer and the substrate. Future work needs to be carried out on different metallic interfaces, which can give a better understanding of epitaxial strain-induced spin crossover of IPB molecules in a controlled way. It would also be interesting to study how the properties of such systems evolve with an increase in temperature; we have studied only the low-temperature structure here. Experiments have shown that at room temperature, the IPB/Au(111) system changes its structure to one with a $S_{1/2}$ unit cell, where all the molecules are in the high spin state.

In **Chapter 4**, we studied the electron acceptor type F_4TCNQ molecule on twisted bilayer graphene (TBLG). We found that, counter-intuitively, a single (isolated) F_4TCNQ molecule avoids sitting on the electron-rich AA-stacked region of the Moiré pattern of TBLG. A weal van der Waals interactions between the molecule and the locally convex surface near the AA-stacked region disfavors adsorption of the molecule in these regions. Our DFT calculations have also shown that at higher molecular coverage, F_4TCNQ forms a 1D-linear chain that avoid AA-stacked regions of TBLG, rather than forming a 2D-monolayer. Our calculations have validated the experimental findings of the 1D-linear chain of F_4TCNQ molecules on the Moiré. We have found that the binding energy landscape for a charged dimer of F_4TCNQ molecules can explain the strong intermolecular interactions among the F_4TCNQ molecules along a particular direction, leading to the formation of a one-dimensional F_4TCNQ chain on TBLG at higher coverage. This raises the possibility of making a molecular wire out of these molecules. Future work could be to study the electron transport through the 1D-chain. It would also be of interest to perform similar calculations on other substrates, and to check whether the controlling parameter that determines whether a 1D chain or 2D island is formed is the charge transfer between the substrate and molecule.

In **Chapter 5**, we have tuned the magnetism and the charge of organic molecules deposited on graphene. In the first part of this chapter, we have tuned the molecular magnetism of the F_4TCNQ molecule deposited on graphene by applying an external electric field to the system, or by doping the graphene substrate with nitrogen. Adding magnetism to the F_4TCNQ-graphene system could possibly open the gate for such systems to be used in spintronic devices. It is expected that experimental data will soon be available on this system, and it would be good to compare this with our results. In the second part of this chapter, we have tuned the charge of the organometallic catalyst CoPc (cobalt phthalocyanine) on nitrogen-doped graphene. We have shown that high charge transfer from nitrogen pairs in the doped substrate to the CoPc molecule can shift the LUMO of the CoPc below the Fermi level; such a shift occurs only over N-pairs and not over single N atoms. This is in agreement the experimental $\mathrm{d}I/\mathrm{d}V$ spectra, which show the signature of a reduction reaction for the CoPc on nitrogen pairs. CoPc is a potential catalyst for the CO_2 reduction reaction. It is expected to show enhanced catalytic performance in its reduced state. One could possibly extend this work to study the catalytic activity of CoPc on N-pairs, and compare it with the activity on pristine graphene or over a single N dopant.

In **Chapter 6**, we have shown that one can tune the electronic and magnetic properties of black phosphorene (BP) by using molecular doping combined with the application of an external electric field. F_4TCNQ creates p-type doping in the BP by introducing a band (corresponding to its LUMO) in the band gap. Our results show that impurity state (band) introduced by the molecule is not pure molecular state, but is hybridized with the phosphorene substrate which gets split into one unoccupied spin down SUMO and one partially occupied spin up SOMO states at negative electric fields. These states act as spin polarized acceptor states for the system: a spin-up (say) lower acceptor state and a spin-down upper acceptor state.

As these get differentially filled as the temperature is increased, the system gets spin polarized in a temperature-dependent manner. The charge carriers in the vicinity of the Fermi level are spin polarized; the amount of these charge carriers and their degree of spin polarization is temperature dependent. Their spatial distribution in the phosphorene substrate is also highly anisotropic. Thus, the degree of spin polarization can be controlled by both the electric field and the temperature. These findings suggest that the system will have interesting spin-polarized transport properties; we plan to carry out such calculations in the future. We hope that our work will stimulate experiments on these systems. In addition, we have found that the diffusion barrier for F_4TCNQ on phosphorene is highly anisotropic, being low/high along the zigzag/armchair directions. This can explain a puzzle regarding the origin of streaks found in experimental STM images of this system. These streaks are found to occur along the zigzag direction but not the armchair direction. Our theoretical findings suggest that during the scan time, the F_4TCNQ molecule moves along the zigzag direction (due to the low diffusion barrier along this direction), and is therefore imaged as a streak. Note that in this chapter, we had used the electron acceptor F_4TCNQ to study the effect of molecular doping on BP, in combination with an external electric field. As a next step, we can study the adsorption of nucleophilic molecules on BP in combination with the external electric field to see the effect of nucleophilic molecules on the electronic properties of BP.

In **Chapter 7**, we have investigated and explained the origin of three different features observed in STM images of few-layer black phosphorene. Our DFT calculations suggest that defects due to Sn impurities are responsible for these features. The defect that we call Sn-2 (Sn substitution in the lower sublayer of the topmost phosphorene layer) shows up in STM images as an extended (a few nm) dumbbell shape at negative bias and a dark circular spot at positive bias, which we refer to as feature **A**. To the best of our knowledge, we are the first to show, by simulating

STM images, that this defect results in both the extended nature of the dumbbell shape of feature **A** as well as its change of contrast on the reversal of the bias polarity. Similarly, we have shown that what we call the Sn-int defect (an interstitial Sn atom between the first and second phosphorene layers) shows up in STM images as bright spots at both polarities, and is the origin of the feature that we call **B**. We were also successful in explaining the effect of an electric pulse on the Sn impurity defects. We have shown that an electric pulse can convert the Sn-int defect to another defect, which we call Sn-2-P-adatom (referred to also as feature **B'** in the experimental images). The identification of this defect is made on the basis of energetics, as well as by comparing the simulated STM images for various possiblities with the experimental image for feature **B'**. Both the Sn-2 and Sn-2-P-adatom defects lead to dumbbell-like features in STM images. However, the Sn-2-P-adatom defect shows a dumbbell with a bright spot in its centre, whereas the Sn-2 defect shows a dumbbell with a dark spot in the centre. We have not studied, in great detail, how these defects affect the properties of the phosphorene. It would be good to explore this aspect further in future work.